2017

Investigating Key Techniques to Leverage the Functionality of Ground/Wall Penetrating Radar

Yu Zhang
University of Vermont

INVESTIGATING KEY TECHNIQUES TO LEVERAGE THE FUNCTIONALITY OF GROUND/WALL PENETRATING RADAR

A Dissertation Presented

by

Yu Zhang

to

The Faculty of the Graduate College

of

The University of Vermont

In Partial Fulfillment of the Requirements
for the Degree of Doctor of Philosophy
Specializing in Electrical Engineering

October, 2017

Defense Date: August 14, 2017
Dissertation Examination Committee:

Tian Xia, Ph.D., Advisor
Dryver R. Huston, Ph.D., Chairperson
Kurt E. Oughstun, Ph.D.
Mads R. Almassalkhi, Ph.D.
Cynthia J. Forehand, Ph.D., Dean of the Graduate College

ABSTRACT

Ground penetrating radar (GPR) has been extensively utilized as a highly efficient and non-destructive testing method for infrastructure evaluation, such as highway rebar detection, bridge decks inspection, asphalt pavement monitoring, underground pipe leakage detection, railroad ballast assessment, etc. The focus of this dissertation is to investigate the key techniques to tackle with GPR signal processing from three perspectives: (1) Removing or suppressing the radar clutter signal; (2) Detecting the underground target or the region of interest (RoI) in the GPR image; (3) Imaging the underground target to eliminate or alleviate the feature distortion and reconstructing the shape of the target with good fidelity.

In the first part of this dissertation, a low-rank and sparse representation based approach is designed to remove the clutter produced by rough ground surface reflection for impulse radar. In the second part, Hilbert Transform and 2-D Renyi entropy based statistical analysis is explored to improve RoI detection efficiency and to reduce the computational cost for more sophisticated data post-processing. In the third part, a back-projection imaging algorithm is designed for both ground-coupled and air-coupled multistatic GPR configurations. Since the refraction phenomenon at the air-ground interface is considered and the spatial offsets between the transceiver antennas are compensated in this algorithm, the data points collected by receiver antennas in time domain can be accurately mapped back to the spatial domain and the targets can be imaged in the scene space under testing. Experimental results validate that the proposed three-stage cascade signal processing methodologies can improve the performance of GPR system.

CITATIONS

Material from this dissertation has been published in the following form:

Zhang, Y. and Xia, T.. (2016). In-Wall Clutter Suppression based on Low-Rank and Sparse Representation for Through-the-Wall Radar. IEEE Geoscience and Remote Sensing Letters, 13(5), 671-675.

Zhang, Y., Venkatachalam, A. S. and Xia, T.. (2015). Ground-penetrating radar railroad ballast inspection with an unsupervised algorithm to boost the region of interest detection efficiency. SPIE Journal of Applied Remote Sensing, 9(1), 1-19.

Zhang, Y., Candra, P., Wang, G. and Xia, T.. (2015). 2-D Entropy and Short-Time Fourier Transform to Leverage GPR Data Analysis Efficiency. IEEE Transactions on Instrumentation and Measurement, 64(1), 103-111.

AND

Material from this dissertation has been submitted for publication to IEEE Transactions on Geoscience and Remote Sensing on August 07, 2017 in the following form:

Zhang, Y., Burns, D., Orfeo, D., Huston, D. and Xia, T.. Air Coupled Ground Penetrating Radar Clutter Mitigation for Rough Surface Sensing. IEEE Transactions on Geoscience and Remote Sensing.

ACKNOWLEDGEMENTS

First, I would like to express my deepest gratitude to my PhD advisor, Dr. Tian Xia. For the past five years, he has been not only an advisor in research, but also a mentor and a good friend in life. Without his generous mentorship, guidance, encouragement and support, I could not achieve so much. His inexhaustible passion in research and dedication to students have set up an inspirational model for me.

Second, a special thanks to Dr. Dryver Huston, my co-advisor and committee chairperson, for his continuous guidance and insightful suggestions during our five years' collaborative research. I can always learn great ideas from him on our group meeting every Friday morning. I would like to extend my gratitude to my dissertation committee, Dr. Kurt Oughstun and Dr. Mads Almassalkhi, for their precious time in reviewing my dissertation and their valuable suggestions. I would also like to thank Dr. Gagan Mirchandani, for serving on my PhD comprehensive exam committee and teaching the philosophy of matrix theory in his course. I would also like to thank Dr. Yuanchang Xie, for his help on our collaborative research and GPR field testing in Summer 2013.

Third, I would like to thank my colleagues, especially Dr. Dylan Burns, Dan Orfeo, Wenzhe Chen, Lixi Tao, Amr Ahmed, and Taian Fan. Thank you for all the help and friendship during my five years' PhD journey. A special thanks to Anbu Venkatachalam, the best officemate, badminton partner and friend for generous help on both research and life when I was a freshman at UVM. Again, to all my colleagues, it was an honor working with all of you at UVM and I really hope that our roads will cross again in future.

Fourth, I would like to express my gratitude to the people who offered their help during my job-hunting period. Thanks to Mr. John Carulli for his "tips & tricks" on preparing the resume and insightful suggestions on choosing career path from the perspective of a UVM alumni. Thanks to Dr. Hamid Ossareh for his insightful advices on negotiating the job offer in automotive industry.

Fifth, I would like to thank the staff members of the College of Engineering and Mathematical Sciences, especially Karen Bernard, Katarina Khosravi, Pattie McNatt, and Sharon Sylvester, and the staff members of Graduate College, especially Kimberly Hess, Sean Milnamow and Bethany Sheldon, for all the help they provided over these years.

Finally, I would love to thank my parents. Their unconditional love and support are invaluable to me. I am proud to be their son. I would also express my deep gratitude to my girlfriend, Dr. Tianxin Miao, who is going to be another Dr. Zhang soon. We built our first home together at UVM Apartment Family Housing with all our plush animal friends. She has been giving me bottomless love and infinite tolerance of my increasing collection of transformer action figures.

TABLE OF CONTENTS

LIST OF TABLES

Table Page

LIST OF FIGURES

Figure Page

CHAPTER 1: INTRODUCTION

1.1. Non-destructive Testing Problem

According to a 2012 Federal Transit Administration report [1], one-third of the nation's transit assets are at or have exceeded their expected useful life. More than 40% of bus assets and 25% of rail transit assets are in marginal or poor conditions. The level of capital investment required to attain a state of good repair in the nation's transit assets is projected to be $77.7 billion. Rail transit assets exceeding their useful life can result in asset failures, which can increase the risk of catastrophic accidents, disrupt service, and strain maintenance departments.

The United States also contains a road network dating to 1940 with more than 570,000 bridges in service. With 3.8 trillion vehicle-kilometers per year, the US roadway infrastructure is considered one of the largest in the world [2]. The average interstate bridge is roughly 40 years old while most bridges are more than 50 years old. In 2013 American Society of Civil Engineering (ASCE) report [3], the accumulated GPA of America's Infrastructure is rated as D + only, which indicates that "the infrastructure is in poor to fair condition and mostly below standard, with many elements approaching the end of their services life. A large portion of the system exhibits significant deterioration. Condition and capacity are of significant concern with strong risk of failure". It is also reported that one in nine of the nations' bridges are rated as structurally deficient. By 2030, that number will double without substantial bridge replacement. The Federal Highway Administration (FHWA) estimates that to eliminate the nation's bridge deficient backlog by 2028, $20.5 billion annually investment is needed, while only $12.8

billion is being spent currently. For roads improvements, $170 billion in capital investment would be needed on an annual basis, while the current level is only $91 billion.

Infrastructure can suffer from various defects, such as cracks, spalling, scaling, honeycomb, voids, delamination, insufficient cover, corrosion of rebar, etc. Early and accurate detection, localization and assessment of damages or defects in infrastructure are of great values for scheduling maintenance and rehabilitation activities, and can significantly reduce the damage progression and maintenance costs. To secure the transportation infrastructure safety and cut the maintenance cost, it is critically important to develop effective and efficient testing technologies for the infrastructure structural condition inspections.

Conventional techniques for infrastructure condition assessment, including drilling testing, core sampling, corrosion (half-cell) potentials, acoustic/hammer testing and chloride ion measurements, etc., are destructive, low efficient, low coverage, labor intensive, time consuming, and disturbing to normal traffic. These drawbacks limit their applications for infrastructure inspection during the construction and lifetime maintenance.

Presently, innovative non-destructive testing (NDT) technologies are increasingly adopted by many transportation agencies. Among all non-destructive testing (NDT) techniques, Ground Penetrating Radar (GPR) is deemed as one of the most effective and promising tools enabling subsurface structural characterizations [4]-[5]. As an easily deployed and highly efficient NDT methodology, GPR has been explored in various case studies, such as rebar detection [6]-[7], bridge deck inspection [8]-[9], soil moisture assessment [10]-[11], railroad ballast monitoring[12]-[14], underground utility mapping [15]-[16], asphalt pavement inspection [17]-[18], etc. Figure 1.1 shows some testing scenarios of GPR applications for transportation infrastructure inspection.

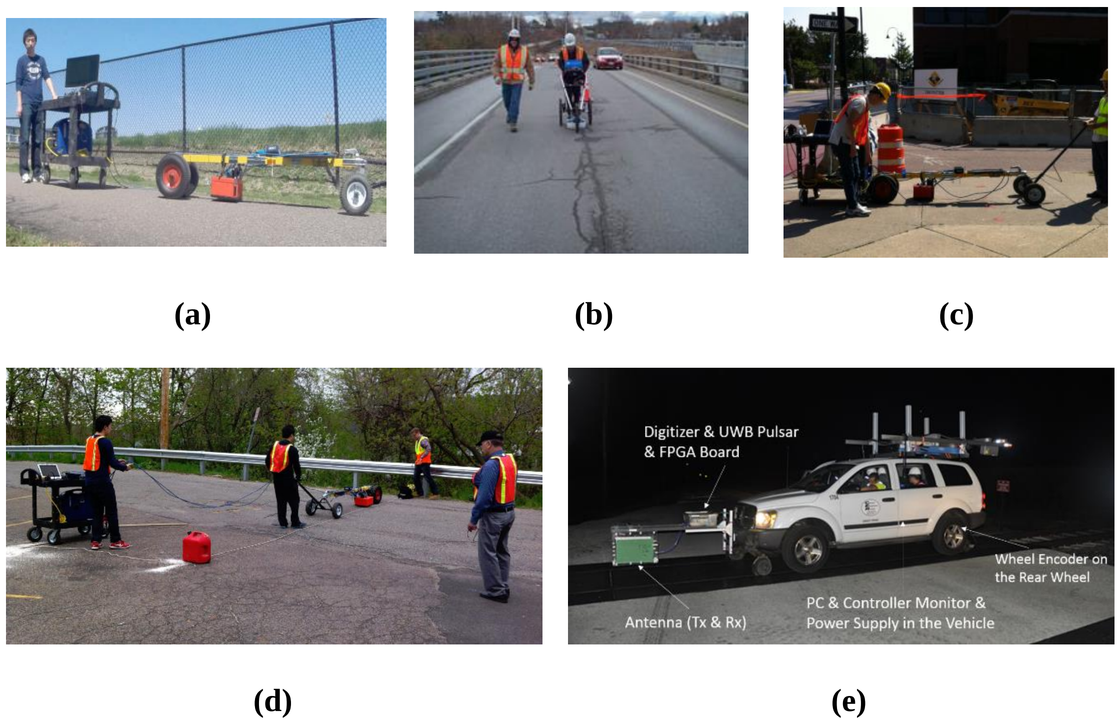

Figure 1.1: GPR explored in various case studies for non-destructive underground infrastructure inspection: (a) asphalt pavement inspection; (b) bridge deck inspection [19]; (c) rebar detection; (d) underground utilities mapping for smart city; (e) railroad ballast condition assessment.

1.2. Background of Ground Penetrating Radar

1.2.1. History and Applications

GPR is a geophysical method that uses radar pulses to image the subsurface [20]. The most common form of GPR measurements deploys a transmitter and a receiver in a fixed geometry, which are moved over the surface to detect reflections from subsurface features [4].

The first use of electromagnetic signals to determine the presence of remote terrestrial metal objects is generally attributed to Hiilsmeyer in 1904. The first patent for a system designed to use continuous-wave radar to locate buried objects was submitted by Leimbach, G. and Löwy, H. in 1910 [21]. A patent for a system using pulsed techniques rather than continuous waves was filed in 1926 by Hülsenbeck [22], leading to improved depth resolution. A glacier's depth was measured using GPR in 1929 by Stern, W. [23].

Pulsed radar were further developed from the 1930s as a subsurface sensing methodology for glacier [24], ice [25], salt deposits [26], desert formation [27], tunnel rocks [28] and coal layer [29]. Renewed interests and developments in this field were generally starting from the 1970s, when military applications began driving research and the lunar investigations were in progress. From the 1970s until the present day, the range of applications has been expanding steadily. Commercial applications followed and the first affordable consumer equipment was sold in 1985 [23].

Recent research progress has been continuously driving and expanding the applications of GPR. Now the GPR techniques and methodologies have been used widely in the following applications: archaeological investigations [30], borehole inspection [31], bridge deck analysis [32], building condition assessment [33], detection of buried mines (anti-personnel and anti-tank) [34]-[37], evaluation of reinforced concrete [38], geophysical investigations [39], earthquake and snow avalanche victims detection [40]-[42], underground utilities detection and mapping [43]-[46], planetary exploration [47], rail track and bed inspection [48], road condition survey[49], security applications [50]-[51], snow, ice and glacier [52]-[53], timber condition [54], tunnel linings [55], etc.

1.2.2. Operating Mechanism

In GPR's operation, the GPR transmitter antenna radiates the electromagnetic (EM) wave into the subsurface structure under testing. The EM wave traveling velocity in the structure is determined primarily by the permittivity or dielectric constant of the subsurface material. When the EM wave hits features or objects that have electrical properties differing from the surrounding medium, it will be reflected and received by the receiver antenna. The reflection coefficient at the interface of two media is R_{21}, which equals the ratio of the electrical fields of the reflection wave and the incident wave. The R_{21} value is determined by the following equation [5]:

$$R_{21} = \frac{\sqrt{\varepsilon_1}-\sqrt{\varepsilon_2}}{\sqrt{\varepsilon_1}+\sqrt{\varepsilon_2}} \tag{1.1}$$

where ε_1 is the dielectric constant of the upper media and ε_2 is the dielectric constant of the lower media. The dependence of signal traveling velocity and amplitude on the material electrical properties will result in different reflection waveforms. By analyzing the reflection signals, the subsurface structural features can be effectively characterized.

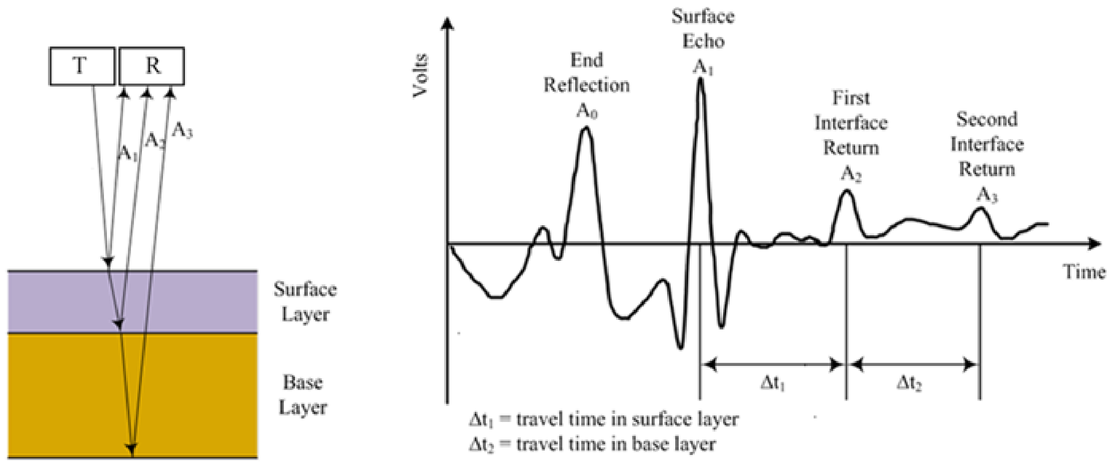

Figure 1.2: Model depicting the various scattered signals in impulse ground penetrating radar and the scattered signals shown in time domain [56]

An example is illustrated in Figure 1.2. GPR signal transmitted from a transmitter antenna penetrates into the underground media consisting of two layers, a surface layer and a base layer. The reflection signal back from the media is picked up by a receiver antenna. At each interface between two adjacent layers, some of the signal is reflected, while some of the signal penetrates into the next layer. The reflection signal in this example comprises of following four types of echoes:

- A_0: the signal directly propagates from the transmitter antenna to the receiver antenna, which is called direct coupling signal or end reflection signal.
- A_1: the signal reflected from the top surface of the first layer or the surface layer.
- A_2: the signal reflected from the interface between the surface layer and the base layer.
- A_3: the signal reflected from the bottom surface of the base layer.

The amplitude and the time delay of the various reflection pulses A_1, A_2 and A_3 are determined by the dielectric constant and thickness of the media. Therefore, by measuring the amplitude and time delay of different echoes, the dielectric constant of the material, thickness of the layer and depth of the target can be calculated.

During the GPR inspection, the transmitter antenna and receiver antenna move over the underground target. At each scanning position, the receiver antenna collects a 1-D signal. This 1-D signal is called A-Scan trace. As the GPR inspection goes on, a group of A-Scan traces is collected along the scanning direction. Upon assembling all the A-Scan traces, a B-Scan image is produced. Finally, if multiple parallel B-Scan images are collected when moving the antennas over a regular grid, a 3-D data matrix can be recorded, which is called a C-Scan.

1.2.3. System Architecture: Impulse Radar, SFCW Radar and FMCW Radar

From GPR imaging scheme aspect, impulse radar, stepped frequency continuous wave (SFCW) radar and frequency modulation continuous wave (FMCW) radar are three typical architectures for GPR system [56].

Figure 1.3 shows a basic diagram of an impulse radar system. An ultra-wideband (UWB) pulse is generated by UWB pulse generator and transmitted out of the transmitter antenna (TX). The pulse penetrates into the ground and reaches out to the target. Some of this pulse scatters back from the target and travels back to the receiver antenna (RX). The received pulse is amplified by a low noise amplifier (LNA) and sampled by an analog-to-digital converter (ADC) unit, such as oscilloscope or digitizer. The digital GPR pulse is then stored and processed by a host computer. By measuring the time difference between the time instances of transmitting the pulse and receiving the pulse, the down range of the target can be calculated.

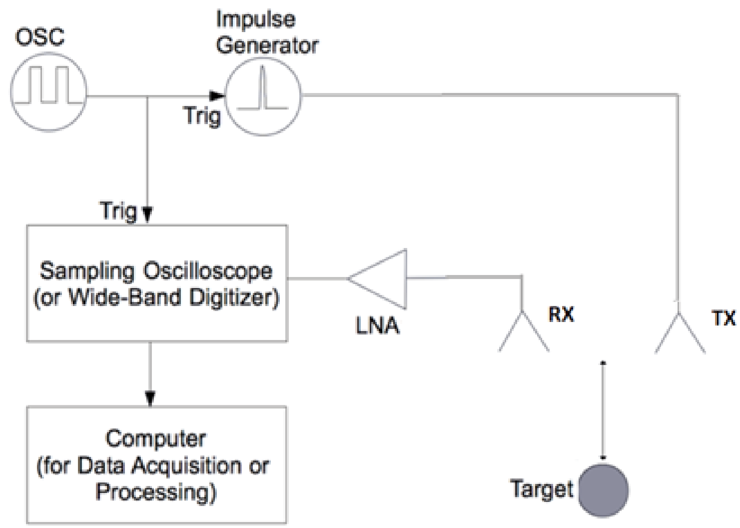

Figure 1.3: Block diagram of basic impulse GPR system [57].

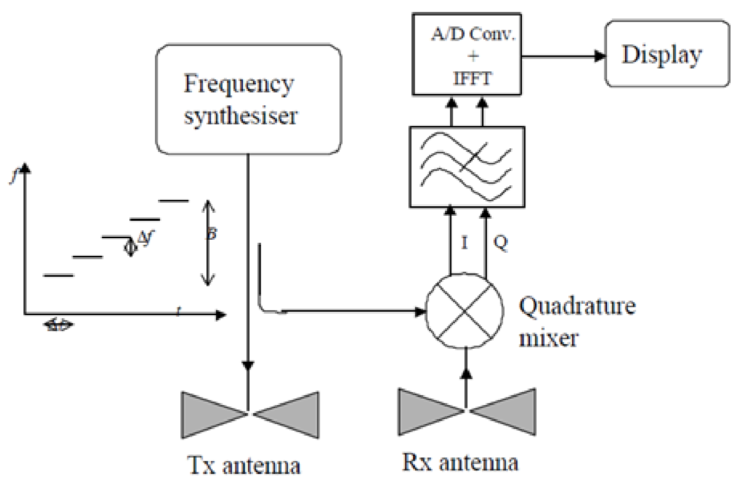

Figure 1.4: Block diagram of SFCW radar system [58].

Figure 1.4 illustrates the block diagram of SFCW radar system. Continuous wave radar transmits a frequency sweep over a fixed bandwidth. In frequency domain, the continuous wave changes by fixed step Δf. The received signal is acquired as a function of frequency by the data acquisition unit. To achieve an ultra-wide bandwidth, all the frequencies are swept from a set beginning to an end frequency. The amplitude and phase of the received signal at each frequency tone are compared with the transmitted signal to obtain the frequency response of the underground targets. Then the frequency response data is processed by a window function and transformed to time domain signal by inverse Fourier transformation.

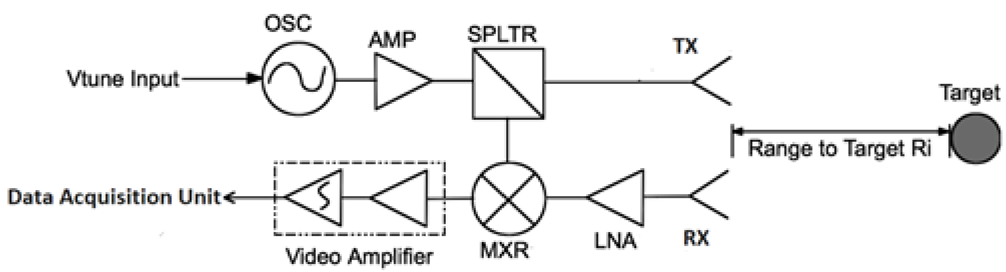

Figure 1.5: Simplified block diagram of a coherent linear FMCW radar system [57].

Figure 1.5 depicts the simplified block diagram of a FMCW radar system. The FMCW radar transmits the continuous wave which is frequency modulated with a linear sweep. The sweeping carrier frequency is controlled by a voltage-controlled oscillator (VCO) over a chosen frequency range. At the receiver end, the backscattered wave is mixed with the emitted wave. The difference in frequency between the transmitted and received wave is a function of the depth of the target. By characterizing the frequency difference, the range to the target can be calculated.

1.2.4. Height of Antenna: Ground-Coupled GPR and Air-Coupled GPR

From the height of antennas aspect, GPR system can be classified as ground-coupled GPR and air-coupled GPR.

For the ground-coupled GPR system, antennas are installed at close proximity to the ground surface. For this type of GPR, it has higher detecting sensitivity and low signal loss. However, the antennas may hit the ground obstacles and even may not be deployable for hazardous areas like landmine detection scenario. Figure 1.6(a) shows the GSSI SIR-30 GPR system [59] under ground-coupled configuration as an example of ground-coupled GPR.

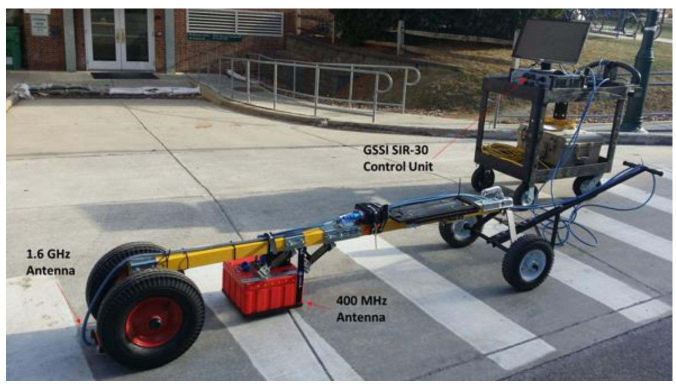

(a)

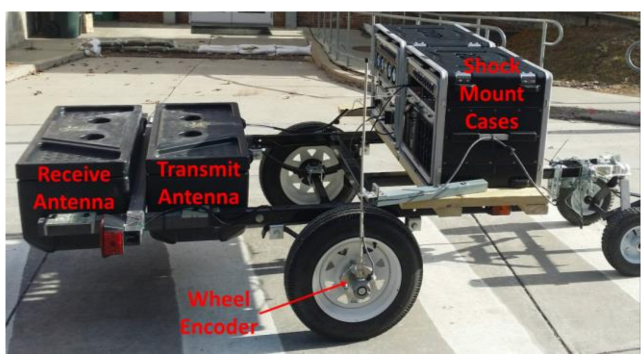

(b)

Figure 1.6: GPR antenna configuration: (a) GSSI SIR-30 ground-coupled GPR system; (b) UVM air-coupled impulse GPR system.

For the air-coupled GPR system, large standoff distance exists between the antennas and ground surface. Such configuration makes the system's movement has higher flexibility, so the air-coupled GPR is easily deployed and good for high-speed survey. Moreover, since the antennas do not touch the ground, the risk of entering dangerous or hazardous areas for radar operators is reduced. However, due to the large standoff distance above the ground surface, the signal loss is large during the propagation in the air. Figure 1.6(b) provides an example of air-coupled GPR system, an air-coupled high-speed dual-channel impulse ground penetrating radar [60] designed by UVM.

1.2.5. Spatial Offset between Antennas: Monostatic, Bistatic and Multistatic

From the number of antennas and separation distance between antennas aspect, the GPR system can be categorized as monostatic GPR, bistatic GPR and multistatic GPR.

Figure 1.7 illustrates the antenna configuration of those three types of GPR systems. Monostatic GPR is a GPR system in which the transmitter and receiver are collocated [61]. Bistatic radar is the GPR system comprising a transmitter antenna and a receiver antenna that are separated by a distance [62]. The separation distance should be comparable to the expected target distance, otherwise such bistatic GPR can be simplified to a monostatic GPR. Multistatic GPR system contains multiple spatially diverse monostatic radar or bistatic radar components with a shared area of coverage [63]. For example, the multistatic GPR shown in Figure 1.7 has two transmitter antennas and two receiver antennas, so it contains $2 \times 2 = 4$ components pairs. Each of the components pairs involves a different bistatic angle and target radar cross section. Upon the data fusion between each component pair, the spatial diversity afforded by the multistatic GPR system allows for different aspects of a target being viewed simultaneously. Information gained from various antenna pairs and multiple radar cross sections can give rise to a number of advantages over conventional monostatic or bistatic GPR systems [64], such as higher signal-to-noise ratio (SNR), lower shadowing effects, high detection rate, better robustness, etc.

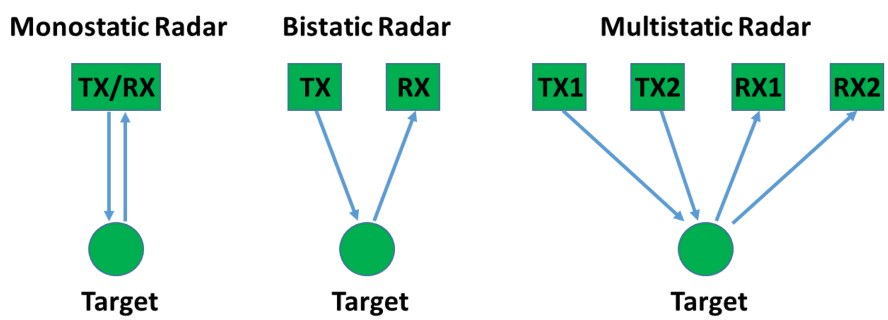

Figure 1.7: Antenna configuration of monostatic GPR, bistatic GPR and multistatic GPR.

1.2.6. Critical Specifications

Range resolution and penetrating depth are two critical specifications for a GPR system.

Range resolution for a GPR system is defined as the minimum detectable or observable distance difference between two targets [57]. For the impulse radar system, targets separated by half of the pulse width time T_p can be distinguished. The theoretical range resolution of an impulse GPR system can be calculated by:

$$\rho_r = \frac{velocity \times T_p}{2} = \frac{cT_p}{2\sqrt{\varepsilon_r}} \tag{1.2}$$

where c is the speed of light in air and ε_r is the dielectric constant of the subsurface media. Therefore, the narrower the width of the pulse is, the better range resolution an impulse GPR system has.

For a continuous wave (SFCW or FMCW) GPR system, the range resolution is determined by the bandwidth BW_{tx} of the transmitting signal instead of the pulse width, which can be calculated by the following equation:

$$\rho_r = \frac{velocity}{2BW_{tx}} = \frac{c}{2BW_{tx}\sqrt{\varepsilon}} \tag{1.3}$$

Therefore, a GPR system with larger signal bandwidth has a better range resolution.

Furthermore, according to Eq. (1.2) and Eq. (1.3), for a specific GPR system, the same transmitting signal has a better resolution when the subsurface media has a larger dielectric constant. Thus, when scanning a subsurface region with larger dielectric constant, to decrease the hardware cost while achieve the certain range resolution, a GPR system with smaller bandwidth can be deployed.

The second critical specification of a GPR system is the penetrating depth, which is determined by central frequency of the GPR system. According to EM wave theory, if the GPR signal's frequency is high, the penetrating depth is low. On the contrary, if the GPR signal's frequency is low, the penetrating depth increases. Therefore, the tradeoff between the range resolution and penetrating depth exists when choosing the GPR signal and antennas.

The higher the frequency of the GPR signal and the antenna, the shallower into the ground it will penetrate, while it can see smaller targets, for instance, the rebar in bridge deck. Conversely, a GPR system with low frequency signal and antenna is good for deep but big targets, such as underground utility pipes. Thus, choice of antenna and signal frequency is one of the most important factors in GPR survey design. Table 1.1 provides a reference for various transportation infrastructure applications and corresponding appropriate choices of GPR signal and antenna.

Table 1.1: Antenna frequency, approximate depth penetration and appropriate application [66].

Appropriate Application	Primary Antenna Choice	Secondary Antenna Choice	Depth Range (Approximate)
Structural Concrete, Roadways, Bridge Decks	2600 MHz	1600 MHz	0-0.3 m (0-1.0 ft)
Structural Concrete, Roadways, Bridge Decks	1600 MHz	1000 MHz	0-0.45 m (0-1.5 ft)
Structural Concrete, Roadways, Bridge Decks	1000 MHz	900 MHz	0-0.6 m (0-2.0 ft)
Concrete, Shallow Soils, Archaeology	900 MHz	400 MHz	0-1 m (0-3 ft)
Shallow Geology, Utilities, UST's, Archaeology	400 MHz	270 MHz	0-4 m (0-12 ft)
Geology, Environmental, Utility, Archaeology	270 MHz	200 MHz	0-5.5 m (0-18 ft)
Geology, Environmental, Utility, Archaeology	200 MHz	100 MHz	0-9 m (0-30 ft)
Geologic Profiling	100 MHz	MLF (16-80 MHz)	0-30 m (0-90 ft)
Geologic Profiling	MLF (16-80 MHz)	None	Greater than 30 m (90 ft)

1.3. GPR Signal Processing Problems and Methodologies

In this section, general and conventional GPR signal processing problems and methodologies are introduced. Methodologies that are more sophisticated will be described and discussed in further chapters when specific GPR signal processing problems are addressed and investigated.

Cassidy, N. J. in 2009 [67] summarized the typical GPR data processing flow by 11 steps. Considering the GPR research has kept progressing since 2010s and the focus of this dissertation is GPR signal processing instead of general data processing, we emphasized a few of the steps in Cassidy's flow, added some new steps into it and reorganized the sequence with each of the steps in their most relevant order as: (1) Editing and Rubber-banding; (2) Dewow; (3) Time-zero correction; (4) Range Filtering and Cross-Range Filtering; (5) Deconvolution; (6) Migration; (7) Attribute analysis; (8) Gain Adjustment; (9) Image analysis; (10) Region of Interest Detection. Each of these signal processing steps will be elaborated in this chapter.

1.3.1. Trace Editing and Rubber-banding

In GPR survey, caused by overenthusiastic triggering, external noise sources, equipment failure or malfunction, occasional traces may be corrupted or missed. Existence of bad traces will impair the processing results of further GPR signal processing steps. The "editing" is to correct the bad or poor data and reorganize the A-Scan traces in the data file. Interpolation between good traces is often performed to compensate the missed traces or replace the corrupted traces [68]-[69].

Similarly to trace editing, rubber-banding is also a process to modify the A-Scan traces, which corrects the GPR data to ensure spatially uniform increments in GPR scanning direction. For distance triggered GPR system, equidistant data collection is required for subsequent signal processing steps, such as migration. To ensure the good data registration, a series of marker points at know distances are recorded during the GPR survey. If the traces corruption or missing happens, the corrupted section is interpolated between to known marker points and then resampled to produce a good section with equally spaced traces [70]-[72].

1.3.2. Dewow

'Wow' is caused by the swamping or saturation of the recorded signal by the strong direct coupling wave or air-ground surface reflection signal. If the DC signal bias exists in the A-Scan trace, the low-frequency component will distort the spectrum of the A-Scan in frequency domain, which affects the subsequent spectral processing steps in frequency domain [73]. Dewowing step reduces the DC bias or the low-frequency components from the GPR signal and adjusts the mean of the A-Scan trace to zero. This process can be implemented in two ways. In the first way, the DC bias or component is calculated as the average of the data points on the A-Scan trace and then subtracted from the A-Scan trace. Alternatively, a high-pass filter with a cut-off frequency that is below the bandwidth of the recorded signal is performed to filter out the low frequency or DC component in the A-Scan trace [74]-[75].

1.3.3. Time-zero correction

If the antenna platform is fixed, the arrival time instance of direct coupling signal in each A-Scan trace should be identical. However, thermal drift, electronic instability, cable length differences and variations in antenna air-gap can cause shifting in the time instance of direct coupling signal [76]. The misalignment of the time-zero correction has an effect on the position of the ground surface reflection and the target reflection, thus, it is necessary to adjust the A-Scan traces to a common time-zero position before subsequent processing steps are performed. Typically, the direct coupling signal in one A-Scan trace is chosen as the reference. The time shifting between the direct coupling waves in different A-Scan traces are calculated by cross-correlation [77]-[78]. Then the time shifting is compensated to each A-Scan trace so that all the A-Scan traces are matching with a common time-zero position.

1.3.4. Range Filtering and Cross-Range Filtering

Generally, GPR filtering can be classified into two types: range filtering along individual A-Scan trace and cross range filtering across a number of A-scan traces.

The goal of the range filtering is removing the noises in A-Scan traces to improve the SNR of GPR signal. Moving average filter [79] is one of the typical temporal filters. The moving average is calculated as the weighted mean of data points within a specified window. The moving average filter is good for removing excessive higher-frequency noise from the data such as radio frequency interference from communication devices [67]. Median filter [80]-[82] is a nonlinear digital filtering technique, often used to remove spikes and salt and pepper noise from GPR A-Scan trace. The median filter runs through the signal point by point, replacing each data point with the median of its neighboring data points across a specified window. While moving average filter and median filter are both attempted in time domain, low-pass filter (LPF), high-pass filter (HPF) and band-pass filter (BPF) are the other type of range filter along A-Scan traces performing in frequency domain [83]-[86]. The LPF can remove the high-frequency noise, and the HPF can suppress the DC bias and low frequency noise. The BPF can be considered a cascade combination of the LPF and HPF performing on the GPR A-Scan signal. The cutoff frequency of each filter can be determined based on bandwidth of the transmitting signal. Joint time-frequency (JTF) analysis [87]-[88] is also applied to suppress the noise components in GPR A-Scan trace. As one of the JTF analysis methods, wavelet transform [89] decomposes the GPR A-Scan into the combination of various signal atoms, eliminates the noise components and reconstructs the GPR signal with the residual signal components.

Radar clutter is the undesired receiving signal other than the scattering signal from the target. Cross-range filtering is aiming to improve the signal-to-clutter ratio (SCR) of GPR signal by suppressing the radar clutter in GPR image. Time gating [90]-[92] is one of the earliest clutter removal methods. In the time gating method, a windowing function is defined to null the signal segments over the time intervals where different signal traces exhibit a high similarity, which facilitates clutter signal removal. Average (or background) subtraction [93]-[94] is a widely used method to remove the ground reflection. Assuming the clutter in each A-Scan shows high similarity, the average subtraction method calculates the average of the first several A-Scan waveforms as the background and then subtracts this average value from the B-Scan image. Spatial filtering method [95]-[96] utilizes the same assumption to filter out the clutter data corresponding to the ground surface reflection. Considering the reflection signal from the buried object with limited spatial extent varies in different A-scan traces, a spatial filter is thus applied along the antenna moving direction to mitigate the spatial zero-frequency and low-frequency components corresponding to clutter. Principal component analysis (PCA) [97]-[99] and independent component analysis (ICA) [100]-[101] are also conventional clutter removal methods. PCA and ICA uses the mathematical modeling principle to decompose the signal into different components, and then finds out the components corresponding to object and clutter respectively. The subspace projection approach [102] is based on the reflection energy difference between the ground surface and the buried object. Singular value decomposition (SVD) is performed on the data matrix to identify and remove the ground surface electromagnetic signature.

Differing from the aforementioned GPR signal processing steps (editing, rubber-banding, dewow, time-zero correction and range filtering) which already have well-developed conventional methodologies, the cross-range filtering or clutter removal filtering is still an open research problem. On the other hand, since the SCR of the GPR data is the key to target detection, while GPR signal is heavily contaminated by clutter, clutter removal is also one of the primary objectives in GPR signal processing [21]. Therefore, exploring of clutter removal methodologies that can efficiently and effectively eliminate or suppress the clutter signal component under complex GPR testing scene is still a challenge research topic.

1.3.5. Deconvolution

Deconvolution is a temporal process that removes the effect of the source wavelet from the recorded A-Scan trace and compresses the recorded GPR wavelet into a narrow and distinct form [103]-[105], which is similar to the idea of pulse compression in general radar signal processing [106]. The deconvolution can effectively improve the resolution of the reflection signal if two primary assumptions can be met extremely. The first assumption is the subsurface is horizontally layered and homogeneous. The second one is the propagating signal should be plane-wave. For GPR testing scene, these are very restricting assumptions as the subsurface is complex and usually inhomogeneous. Moreover, the GPR is a short-range system [57] when scanning some shallowly buried targets, so the GPR signal propagates in near field and can not be modeled as plane-wave. Therefore, the effectiveness of deconvolution technique is not assured if no special handling is performed [107]-[108]. Regularized deconvolution with calibration testing on directly coupling signal [109], metal plate reflection signal in free space [110], and attenuation model [111] is more practical for GPR inspection scene.

1.3.6. Migration

Since the GPR antenna receives the field scattering while moving above the buried object along the inspection direction, the EM waves reflecting back from the same object have different travel times to the GPR antennas at different positions. For instance, as demonstrated in Figure 1.8, for a ground-coupled monostatic GPR system, when the antenna is at location 1, the distance between the target and the antenna is R_1. Correspondingly, the two-way travel time for the EM wave is $t_1 = 2R_1/v$, where $v =$

$c/\sqrt{\varepsilon_r}$ is the propagation velocity of the EM wave in subsurface media. While antenna moves to the position right above the target, its range to the target is R_2 and the two-way signal travel time is $t_2 = 2R_2/v$. In GPR B-scan image, the object pattern shows a hyperbolic distortion, which impairs the shape of buried target and decreases the cross-range resolution of the GPR B-Scan image. Therefore, one of the most important GPR signal processing steps is to migrate the distorted GPR image to a focused one and reconstruct the true shapes and locations of buried targets.

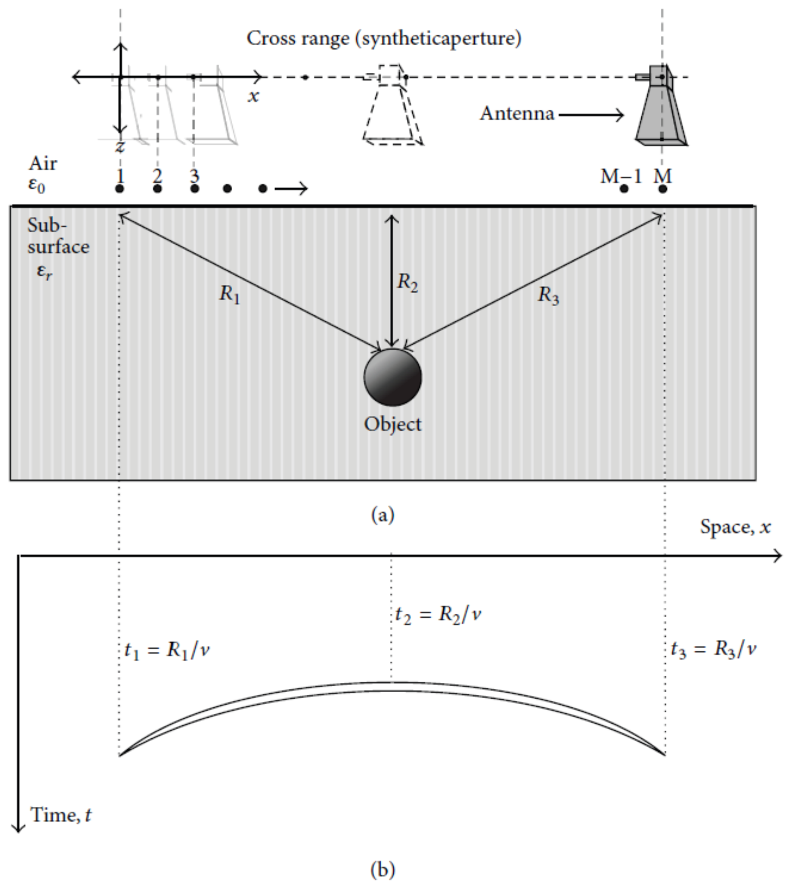

Figure 1.8: Hyperbolic distortion in GPR image: (a) geometrical layout of GPR inspection; (b) hyperbolic distortion in GPR B-Scan image [112].

The concept of migration was originally proposed for processing seismic images [113]-[114], and introduced to the GPR imaging thanks to the likenesses between the acoustic and EM wave equations [112]. Conventional migration methods for GPR imaging include the hyperbolic summation, Kirchhoff's migration, phase-shift migration, frequency-wavenumber (ω-k) migration, and back-projection migration.

Hyperbolic summation (HS) migration [115] is a GPR version of the diffraction summation method [116] that has been successfully applied in seismic data processing. The HS migration method assumes the B-Scan image can be modeled as the contribution of finite number of hyperbolas that correspond to different points on the targets. It is implemented as a summation of the diffraction energies along a hyperbolic trajectory operating on spatial domain [117].

Kirchhoff's migration [118] is also known as reverse-time wave equation migration whose aim is to find the Kirchhoff solution of the wave equation within the propagating medium based on Huygen's principle [119]-[120]. The Kirchhoff's migration can produce a good reconstructed radar image for monostatic GPR setup. However, the Kirchhoff's migration is derived from the zero-offset exploding reflector model [121], so it does not account for the spatial offset between the transmitter antenna and receiver antenna, which make it infeasible for bistatic GPR or multistatic GPR.

Phase-shift migration [122] method iteratively compensates a phase-shift to migrate the wave field to the exploding time of $t = 0$ such that all the scattered waves are mapped back to target scene. The main objective of the phase-shift migration method is to calculate the wave field at $t = 0$ by extrapolating the EM wave in range direction with a phase factor [112]. The concept and assumption of the phase-shift migration is similar to Kirchhoff's migration [123], therefore, it is only designed to work for monostatic GPR configuration.

Frequency-wavenumber (ω-k) migration technique is based on the phase-shift migration algorithm, which was first proposed for seismic imaging applications [124] and then adapted to the synthetic aperture radar (SAR) imaging [125]-[130]. This algorithm is also called as seismic migration algorithm, f-k migration algorithm, or Stolt migration algorithm (SMA) by different researchers. For simplicity, we call it SMA in this dissertation. The main idea of the SMA is the interpolation operation in the wavenumber-wavenumber domain to obtain the reconstructed image in the scene space. The SMA works faster than the aforementioned migration techniques. Unfortunately, the traditional SMA also fails to consider the spatial offset between the transmitter antenna and receiver antenna, so it can only work for monostatic GPR imaging. Some modified or improved SMAs were proposed in [131]-[132] for multiple-input multiple output (MIMO) radar system claiming the separation between the transmitter antenna and receiver antenna was considered, nevertheless, those modified SMAs are formulated from the models of transmitted signals in air or free space medium. Thus, they do not perform well in subsurface lossy medium [133] for GPR applications.

Back-projection algorithm (BPA) was first introduced as a seismic migration method [113] and then further developed for SAR imaging applications [134]-[137]. The BPA algorithm characterizes the differences in the two-way EM wave propagating distance at different antenna locations and projects the collected data points from the recorded time instances back to their true spatial locations in scene space. The primary advantage of BPA is its flexibility in handling the configuration of radar systems. Theoretically, once the exact location of the antenna is measured and the propagating path of the EM wave is determined, BPA can reconstructed the target from the radar image. Therefore, BPA has the potential to be extended to air-coupled bistatic and multistaic GPR system. Secondly, since each of the A-Scan traces is serially processed and back-projected to the entire GPR image independently, the BPA does not require a straight and uniformly sampled synthetic scan aperture [112]. This "independently processing" property of BPA also implies its capability of the real-time imaging as the GPR scanning is undergoing. Thirdly, the BPA can project the GPR time-domain data points back to a specific sub-region of the scene space. For GPR applications where the approximate location of the buried target or the region of interest (RoI) is a priori-knowledge, the BPA can directly imaging the RoI instead of the whole subsurface region. Therefore, using some RoI detection algorithms as the pre-processing, the GPR imaging efficiency of BPA can be improved dramatically.

1.3.7. Attribute Analysis

Attribute analysis extracts the information about the relative reflectivity, amplitude, frequency, phase relationships and statistical features to aid GPR data interpretation.

The basic attribute analysis is performed on the whole A-Scan signal, e.g. mean amplitude, peak amplitude and time delay between two peaks, which can be used for many GPR applications, such as, estimating the dielectric constant of the subsurface media [5], [138], the density of the asphalt pavement [139]-[141], the thickness of the asphalt pavement [142]-[143]. Some attribute analysis methods operate on the data points within a time window, e.g. instantaneous amplitude, instantaneous phase and instantaneous frequency. Those instantaneous features have been utilized for estimation of water content [144], detection of subsurface contaminant [145]-[146], detection of fouling railroad ballast [147], etc. Recently, joint time-frequency techniques considering both the temporal features and frequency features have been explored for analyzing and interpreting GPR data, which include empirical mode decomposition (EMD) [148]-[151], short-time Fourier Transform (STFT) [152]-[154], wavelet transform [155]-[157] and curvelet transform [158]-[159], etc.

1.3.8. Gain Adjustment

Gain adjustment modifies the signal amplitude to improve the visualization of the GPR image. Since the data values are manipulated, the relative amplitudes information or phase relationships within the GPR image are changed. Therefore, we would like to perform the gain adjustment as the last GPR signal processing step.

To eliminate the signal attenuation during transmitting in subsurface media and enhance the target scattering signal, a scaling function $A(d)$ is multiplied to the amplitudes of received signal at different depths. Typically, a deeper d corresponds to a larger value of $A(d)$. Theoretically, for the visual purpose, the scaling function $A(d)$ can be arbitrary function defining by the GPR operator or user. However, we have to admit that gain adjustment manipulates the data values, so the bias from GPR operator is inevitable. Moreover, since the gain is applied to all the data points in the GPR image, both the target signal and noises are amplified simultaneously in an indiscriminate way.

Here, a practical gain function based on characterizing the signal propagating loss in the subsurface media [10], [13] is described as an example. For the signal penetration in a uniform or homogeneous media, the attenuation is linearly proportional to the penetrating depth. The gain function of signal transmitted in the media can be characterized as

$$g(m) = g(1) + \frac{g(M) - g(1)}{M - 1}(m - 1),\ m = 1,2,\dots,M \tag{1.4}$$

where m represents the index of the sample along the range direction (penetrating depth) in B-Scan image while $g(m)$ (unit: dB) indicates signal attenuation. Assuming the incident signal voltage amplitude at the ground surface is $V(0)$ and the voltage amplitude at depth d is $V(d)$, we have

$$20\log\left(\frac{V(0)}{V(d)}\right) = \alpha \cdot d \tag{1.5}$$

where α is the attenuation coefficient (unit dB/meter) and d is the penetrating depth. $V(d)$ can be derived as

$$V(d) = V(0) \times 10^{-\frac{\alpha \cdot d}{20}} \tag{1.6}$$

The value of α can be determined by [160]:

$$\alpha = \omega\sqrt{\varepsilon\mu}\left\{\frac{1}{2}\left[\sqrt{1 + \left(\frac{\sigma}{\omega\varepsilon}\right)^2} - 1\right]\right\}^{1/2} \tag{1.7}$$

where σ is the electrical conductivity of the media, μ is the permeability of the media, $\mu = \mu_0 = 4\pi \times 10^{-7}\mathrm{henry/m}$, $\omega = 2\pi f$, ε is the dielectric permittivity.

When the penetrating depth increases by d meters, the signal round trip transmission distance increases by $2d$ meters. If the signal attenuation/transmitting distance ratio is α dB/meter, the round trip signal attenuation is thus 2α dB. An exponential parameter $A(d)$ can be multiplied to $V(d)$ to compensate signal transmission attenuation and make it outstanding from the background. The scaling function $A(d)$ can be derived based on Eq. (1.6):

$$A(d) = 10^{\frac{2\alpha d}{20}} = 10^{\frac{\alpha d}{10}} \tag{1.8}$$

1.3.9. Image analysis

Recently, computer vision techniques have drawn the attention of GPR research community for analyzing, interpreting and understanding the GPR image. Machine learning techniques were adopted for buried target detection [161]-[163] and signal classification [164]-[165]. Pattern recognition techniques [166]-[167] were utilized to detect the hyperbolas representing the buried targets in the GPR image. The popular and sparking deep learning methodologies were also explored by GPR researchers for buried target detection [168]-[172] and classification in GPR image [173]-[175]. The accuracy of the detection and classification by machine learning or deep learning techniques is primarily dependent on the amount of the training data. However, differing from computer vision applications, the images or datasets for radar applications are not often open to the academia community. Therefore, the limitation of the data source as training dataset could be an obstacle to the transition of deep learning application from computer vision to radar imaging.

1.3.10. Region of Interest Detection

For the aforementioned GPR signal processing steps, the algorithm computational cost is always an issue, especially for GPR field test data whose data size could be extremely large. In a large radargram, the targets or the scatters of interests are typically distributed sparsely in the imaging region. Therefore, reducing the data scope to sporadically distributed singular regions or region of interest (RoI) can facilitate sophisticated post-processing. The RoI detection can be integrated into any GPR signal processing steps as a pre-processing. Then the specific algorithm is only performed on the sub-regions of the GPR image, which can leverage the computation efficiency and minimize the space cost of the algorithm. For instance, for back-projection imaging algorithm, if the RoI is a prior knowledge, the BPA can just be performed on the RoI as the scene space instead of the whole GPR scanning region.

1.3.11. Summary

In this section, the typical GPR signal problems are introduced and the corresponding methodologies are reviewed. Among those problems, trace editing, rubber-banding, time-zero correction and gain adjustment already have standard processing methodologies and protocols. They have already been standardized and integrated into some commercial GPR signal processing software products, such as RADAN by GSSI [179], ObjectMapper by MALA [180], etc. For dewow, deconvolution and attribute analysis, even though no so-called standard algorithm or methodology exists, the state-of-the-art research results can already handle these problems well. Most of well functional methodologies have already been implemented and included in a free

GPR data processing tool, the MATGPR [181]. However, the clutter removal filtering, region of interest detection and image migration are still open questions lacking of very effective and efficient methodologies. Therefore, they are the major GPR signal processing problems that will be addressed in the following chapters of this dissertation. Please note, image analysis is actually a problem more relevant to computer vision and machine learning research areas, so it is not included in the topics of this dissertation even though it is essential and challenging.

1.4. Objective and Scope

The objective and focus of this dissertation is to investigate the key techniques to tackle with GPR signal processing from three perspectives: (1) Removing or suppressing the radar clutter signal; (2) Detecting the region of interest (RoI) in the GPR image; (3) Imaging the underground target to eliminate or alleviate the hyperbolic distortion and reconstructing the shape of the target with good fidelity.

The first part of this dissertation, consisting of Chapter 2 and Chapter 3, tackles with the clutter removal problems in through-the-wall radar (TWR) imaging and GPR imaging respectively. In Chapter 2, for TWR imaging, in-wall clutter data from rebars or pipes inside the wall is modeled as a low-rank matrix, while the data from the foreground target under testing is modeled as a sparse matrix that lies on top of the in-wall clutter. The in-wall clutter suppression problem for TWR image processing is then transformed into a low-rank and sparse representation optimization problem. A low-rank and sparse representation method is explored and developed to mitigate the in-wall structure reflection so as to leverage behind-wall object detection effectiveness in TWR image processing. In Chapter 3, this low-rank and sparse representation based approach is improved and extended to remove the clutter produced by rough ground surface reflection for GPR imaging applications. For rough or non-flat ground surface, the surface clutter components in different A-Scan traces are not aligned on the depth axis. To compensate for the misalignments and facilitate clutter removal, the A-Scan traces in a GPR data matrix are aligned using cross-correlation method. The low-rank and sparse representation technique is then developed to decompose the aligned GPR data matrix into two sub-matrices: a low-rank matrix whose column data records the ground clutter in A-Scan traces, and a sparse matrix that features the subsurface object.

The second part, consisting of Chapter 4 and Chapter 5, explores the methodology for detecting the region of interest (RoI) in the GPR image. Chapter 4 proposes the utilization of two-dimensional (2-D) entropy analysis to narrow down the data scope to the interested regions, which can considerably reduce the computational cost for sophisticated post data processing steps. Joint time-frequency analysis using Short Time Fourier Transform (STFT) is then performed for singular region location detection and refinement. Chapter 5 improves the entropy-based algorithm to automate and facilitate the detection of suspicious fouling ballast regions or Regions of Interest (ROI) within big GPR survey data sets. An analytic method using Hilbert Transform is developed to extract the pulse signal envelope and characterize the scattering signal power. Furthermore, an automatic layer identification method based on signal decomposition is implemented to detect and isolate the ballast region from the ground surface. Finally, the 2-D entropy analysis is performed on the scattering data corresponding to ballast region.

Such data processing approaches leverage the performance of 2-D entropy analysis and eliminate the need of STFT for singular region identification. The improved methodology can effectively facilitate the post processing and interpretation for large volume of GPR ballast inspection data.

In the third part, Chapter 6, a back-projection imaging algorithm is designed for both ground-coupled multistatic GPR and air-coupled multistatic GPR configurations. Since the refraction phenomenon at the air-ground interface is considered and the spatial offsets between the transceiver antennas are compensated in this algorithm, the data points collected by receiver antennas in time domain can be accurately mapped back to the spatial domain and the targets can be imaged in the scene space with good fidelity. Comparing to the monostatic GPR imaging and bistatic GPR imaging, the multistatic GPR imaging can produce higher signal-to-noise ratio (SNR), lower shadowing effects, high detection rate and better robustness for GPR infrastructure inspection applications.

Chapter 7 concludes that the proposed three-stage cascade signal processing methodologies can improve the performance of GPR system. The further work based on this dissertation is also remarked in Chapter 7.

1.5. References

[1] Federal Transit Administration Asset Management Guide, October 2012, FTA Report No. 0027: https://www.transit.dot.gov/sites/fta.dot.gov/files/docs/FTA_Report_No._0027.pdf

[2] Bettigole, N. and Robinson, R., "Bridge Decks," American Society of Civil Engineers, New York, (1997).

[3] 2013 Report Card for America's Infrastructure, American Society of Civil Engineers: http://2013.infrastructurereportcard.org/

[4] Jol, H.M., "Ground penetrating radar theory and applications," Elsevier, (2008).

[5] Huston, D., "Structural sensing, health monitoring, and performance evaluation", CRC Press, 117 (2010).

[6] Xia, T., Xu, X., Venkatachalam, A. and Huston, D., "Development of a High Speed UWB GPR for Rebar Detection," *Proceedings of IEEE International Conference on Ground Penetrating Radar (GPR)* (2012).

[7] Xu, X., Xia, T., Venkatachalam, A., and Huston, D., "Development of high-speed ultrawideband ground-penetrating radar for rebar detection," *Journal of Engineering Mechanics*, 139(3), 272-285 (2012).

[8] Alani, A. M., Aboutalebi, M., and Kilic, G., "Applications of ground penetrating radar (GPR) in bridge deck monitoring and assessment," *Journal of Applied Geophysics, 97,* 45-54 (2013).

[9] Wang, Z. W., Zhou, M., Slabaugh, G. G., Zhai, J., and Fang, T., "Automatic detection of bridge deck condition from ground penetrating radar images," *IEEE Transactions on Automation Science and Engineering,* 8(3), 633-640 (2011).

[10] Zhang, Y., Burns, D., Huston, D. and Xia, T., "Sand moisture assessment using instantaneous phase information in ground penetrating radar data," *Proc. SPIE 9437*, 943726 (2015).

[11] Huisman, J. A., Hubbard, S. S., Redman, J. D., and Annan, A. P., "Measuring soil water content with ground penetrating radar," *Vadose Zone Journal,* 2(4), 476-491 (2003).

[12] Al-Qadi, I.L., Xie, W., Roberts, R. and Leng, Z., "Data Analysis Techniques for GPR used for Assessing Railroad Ballast in High Radio-Frequency Environment," *Journal of Transportation Engineering, ASCE,* 136(4), 392–399 (2010).

[13] Zhang, Y., Venkatachalam, A.S., Xia, T., Xie, Y., and Wang, G., "Data analysis technique to leverage ground penetrating radar ballast inspection performance," *2014 IEEE Radar Conference,* 463-468 (2014).

[14] Zhang, Y., Venkatachalam, A.S. and Xia, T., "Ground-penetrating radar railroad ballast inspection with an unsupervised algorithm to boost the region of interest detection efficiency," *Journal of Applied Remote Sensing,* 9(1), 1-19 (2015).

[15] Gamba, P., and Lossani, S., "Neural detection of pipe signatures in ground penetrating radar images," *IEEE Transactions on Geoscience and Remote Sensing,* 38(2), 790-797 (2000).

[16] Huston, D., Xia, T., Zhang, Y., Fan, T., Orfeo, D., and Razinger, J., "Urban underground infrastructure mapping and assessment," In *SPIE Smart Structures and Materials+ Nondestructive Evaluation and Health Monitoring,* (2017).

[17] Loizos, A., and Plati, C., "Accuracy of pavement thicknesses estimation using different ground penetrating radar analysis approaches," *NDT & e International,* 40(2), 147-157 (2007).

[18] Liu, H., Birken, R., and Wang, M. L., "Automatic pavement layer identification with multichannel ground penetrating radar at traffic speed," *Journal of Applied Remote Sensing,* 10(4), (2016).

[19] Ground Penetrating Radar for Bridge Deck Inspection, Geophysical Survey Systems, Inc.: http://www.geophysical.com/bridgeinspection.htm

[20] Ground Penetrating Radar: https://en.wikipedia.org/wiki/Ground-penetrating_radar

[21] Daniels, D. J. (ed.), "Ground Penetrating Radar (2nd ed.)," Institution of Engineering and Technology (IET), (2004).

[22] Hulsenbeck, *et al.*, German Pat. No. 489434, (1926).

[23] History of Ground Penetrating Radar (GPR): https://www.obonic.de/article/ground-peentrating-radar-history/

[24] Steenson, B. O., "Radar methods for the exploration of glaciers," PhD Thesis, Calif. Inst. Tech., Pasadena, CA, USA, (1951)

[25] Evans, S., "Radio techniques for the measurement of ice thickness," *Polar Record*, 11(73), 406-410 (1963).

[26] Unterberger, R. R., "Radar and sonar probing of salt," *5th Int. Symp. On Salt*, Hamburg (Northern Ohio Geological Society), 423-437 (1979).

[27] Kadaba, P. K., "Penetration of 0.1 GHz to 1.5 GHz electromagnetic waves into the earth surface for remote sensing applications," In *Engineering in a Changing Economy*, 48-50 (1976).

[28] Cook, J. C., "Radar transparencies of mine and tunnel rocks," *Geophysics*, 40(5), 865-885 (1975).

[29] Roe, K. C., and Ellerbruch, D. A., "Development and testing of a microwave system to measure coal layer thickness up to 25 cm," *Report No. FE-8881-1; SR-723-8-79*, National Bureau of Standards, Boulder, CO (USA). Electromagnetic Fields Div., (1979).

[30] Basile, V., Carrozzo, M. T., Negri, S., Nuzzo, L., Quarta, T., and Villani, A. V., "A ground-penetrating radar survey for archaeological investigations in an urban area (Lecce, Italy)," *Journal of Applied Geophysics*, 44(1), 15-32 (2000).

[31] Slob, E., Sato, M., and Olhoeft, G., "Surface and borehole ground-penetrating-radar developments," *Geophysics, 75*(5), 75A103-75A120 (2010).

[32] Maser, K. R., "Integration of ground penetrating radar and infrared thermography for bridge deck condition evaluation," In *Non-Destructive Testing in Civil Engineering Conference, Nantes, France, June 30th-July 3rd*, (2009).

[33] Tarussov, A., Vandry, M., and De La Haza, A., "Condition assessment of concrete structures using a new analysis method: Ground-penetrating radar computer-assisted visual interpretation," *Construction and Building Materials, 38*, 1246-1254 (2013).

[34] Wilson, J. N., Gader, P., Lee, W. H., Frigui, H., and Ho, K. C., "A large-scale systematic evaluation of algorithms using ground-penetrating radar for landmine detection and discrimination," *IEEE Transactions on Geoscience and Remote Sensing*, *45*(8), 2560-2572 (2007).

[35] Gader, P., Lee, W. H., and Wilson, J. N., "Detecting landmines with ground-penetrating radar using feature-based rules, order statistics, and adaptive whitening," *IEEE Transactions on Geoscience and Remote Sensing*, *42*(11), 2522-2534 (2004).

[36] Torrione, P., and Collins, L. M., "Texture features for antitank landmine detection using ground penetrating radar," *IEEE Transactions on geoscience and remote sensing*, *45*(7), 2374-2382 (2007).

[37] Zhang, Y., Orfeo, D., Burns, D., Miller, J., Huston, D., and Xia, T., "Buried nonmetallic object detection using bistatic ground penetrating radar with variable antenna elevation angle and height," In *SPIE Smart Structures and Materials+ Nondestructive Evaluation and Health Monitoring*, (2017).

[38] Maierhofer, C., "Nondestructive evaluation of concrete infrastructure with ground penetrating radar," *Journal of Materials in Civil Engineering*, *15*(3), 287-297 (2003).

[39] Benson, A. K., "Applications of ground penetrating radar in assessing some geological hazards: examples of groundwater contamination, faults, cavities," *Journal of applied Geophysics*, *33*(1-3), 177-193 (1995).

[40] Grazzini, G., Pieraccini, M., Parrini, F., Spinetti, A., Macaluso, G., Dei, D., and Atzeni, C., "An ultra-wideband high-dynamic range GPR for detecting buried people after collapse of buildings," In *Ground Penetrating Radar (GPR), 2010 13th International Conference on*. IEEE, (2010)

[41] Fruehauf, F., Heilig, A., Schneebeli, M., Fellin, W., and Scherzer, O., "Experiments and algorithms to detect snow avalanche victims using airborne ground-penetrating radar," *IEEE Transactions on Geoscience and Remote Sensing*, *47*(7), 2240-2251 (2009).

[42] Liu, L., and Liu, S., "Remote detection of human vital sign with stepped-frequency continuous wave radar," *IEEE Journal of Selected Topics in Applied Earth Observations and Remote Sensing*, *7*(3), 775-782 (2014).

[43] Ni, S. H., Huang, Y. H., Lo, K. F., and Lin, D. C., "Buried pipe detection by ground penetrating radar using the discrete wavelet transform," *Computers and Geotechnics*, *37*(4), 440-448 (2010).

[44] Zhang, Y., Huston, D., and Xia, T., "Underground object characterization based on neural networks for ground penetrating radar data," *SPIE Smart Structures/NDE 2016*, (2016).

[45] Lester, J., and Bernold, L. E., "Innovative process to characterize buried utilities using ground penetrating radar," *Automation in Construction*, *16*(4), 546-555 (2007).

[46] Lambot, S., Slob, E. C., van den Bosch, I., Stockbroeckx, B., and Vanclooster, M., "Modeling of ground-penetrating radar for accurate characterization of subsurface electric properties," *IEEE transactions on geoscience and remote sensing*, *42*(11), 2555-2568 (2004).

[47] Degenhardt, J. J., and Giardino, J. R., "Subsurface investigation of a rock glacier using ground-penetrating radar: Implications for locating stored water on Mars," *Journal of Geophysical Research: Planets*, *108*(E4) (2003).

[48] Narayanan, R. M., Jakub, J. W., Li, D., and Elias, S. E., "Railroad track modulus estimation using ground penetrating radar measurements," *NDT & E International*, *37*(2), 141-151 (2004).

[49] Saarenketo, T., and Scullion, T., "Road evaluation with ground penetrating radar," *Journal of applied geophysics*, *43*(2), 119-138 (2000).

[50] Daniels, D. J., "Surface penetrating radar for industrial and security applications," *Microwave Journal*, *37*(12), 68-76 (1994).

[51] Withington, P., Fluhler, H., and Nag, S., "Enhancing homeland security with advanced UWB sensors," *IEEE Microwave magazine*, *4*(3), 51-58 (2003).

[52] Murray, T., Booth, A., and Rippin, D. M., "Water-content of glacier-ice: Limitations on estimates from velocity analysis of surface ground-penetrating radar surveys," *Journal of Environmental & Engineering Geophysics*, *12*(1), 87-99 (2007).

[53] Machguth, H., Eisen, O., Paul, F., & Hoelzle, M., "Strong spatial variability of snow accumulation observed with helicopter-borne GPR on two adjacent Alpine glaciers," *Geophysical research letters*, *33*(13) (2006).

[54] Rodríguez-Abad, I., Martínez-Sala, R., García-García, F., and Capuz-Lladró, R., "Non-destructive methodologies for the evaluation of moisture content in sawn timber structures: ground-penetrating radar and ultrasound techniques," *Near Surface Geophysics*, *8*(6), 475-482 (2010).

[55] Zhang, F., Xie, X., and Huang, H., "Application of ground penetrating radar in grouting evaluation for shield tunnel construction," *Tunnelling and Underground Space Technology*, *25*(2), 99-107 (2010).

[56] Venkatachalam, A. S., "RF Circuit Development for Ultra-wideband Ground Penetrating Radar Evaluating Highway Pavement and Bridge Deck Subsurface Conditions," (Master Thesis, University of Vermont), (2013).

[57] Charvat, G. L., "Small and short-range radar systems," *CRC Press*, (2014).

[58] Scheers, B., "Ultra-wideband ground penetrating radar with application to the detection of anti-personnel landmines," *Royal Military Academy, Brussels*, (2001).

[59] Ground Penetrating Radar Data Acquisition Unit – SIR 30 – GSSI: http://www.geophysical.com/sir30.htm

[60] Venkatachalam, A. S., Xu, X., Huston, D., & Xia, T., "Development of a new high speed dual-channel impulse ground penetrating radar," *IEEE Journal of Selected Topics in Applied Earth Observations and Remote Sensing*, *7*(3), 753-760 (2014).

[61] Monostatic radar – Wikipedia: https://en.wikipedia.org/wiki/Monostatic_radar

[62] Nezlin, D. V., Kostylev, V. I., Blyakhman, A. B., Ryndyk, A. G., & Myakinkov, A. V., "Bistatic radar: principles and practice," John Wiley & Sons, (2007).

[63] Chernyak, V. S., "Fundamentals of multisite radar systems: multistatic radars and multistatic radar systems," CRC Press, (1998).

[64] Multistatic radar – Wikipedia: https://en.wikipedia.org/wiki/Multistatic_radar

[65] Radar Basics – Range Resolution: http://www.radartutorial.eu/01.basics/Range%20Resolution.en.html

[66] What is GPR: A Brief Description by GSSI, Geophysical Survey Systems, Inc.: http://www.geophysical.com/whatisgpr.htm

[67] Cassidy, N. J., "Ground penetrating radar data processing, modelling and analysis," *Ground penetrating radar: theory and applications*, 141-176 (2009).

[68] Pipan, M., Baradello, L., Forte, E., Prizzon, A., and Finetti, I., "2-D and 3-D processing and interpretation of multi-fold ground penetrating radar data: a case history from an archaeological site," *Journal of Applied geophysics*, *41*(2), 271-292 (1999).

[69] Hodson, T., Gooch, D. L., & Stuart, G. W., "Structures within the surge front at Bakaninbreen, Svalbard, using ground-penetrating radar," *Annals of Glaciology*, *24*, 122-129 (1997).

[70] Leckebusch, J., "Ground-penetrating radar: a modern three-dimensional prospection method," *Archaeological prospection*, *10*(4), 213-240 (2003).

[71] Sower, G., Eberly, J., and Christy, E., "GSTAMIDS ground-penetrating radar: hardware description," In *Proc. SPIE* (Vol. 4394, p. 652) (2001).

[72] Safont, G., Salazar, A., Rodriguez, A., and Vergara, L., "On recovering missing ground penetrating radar traces by statistical interpolation methods," *Remote Sensing*, *6*(8), 7546-7565 (2014).

[73] Gerlitz, K., Knoll, M. D., Cross, G. M., Luzitano, R. D., and Knight, R., "Processing ground penetrating radar data to improve resolution of near-surface targets," In *6th EEGS Symposium on the Application of Geophysics to Engineering and Environmental Problems*, (1993).

[74] Huisman, J. A., Sperl, C., Bouten, W., and Verstraten, J. M., "Soil water content measurements at different scales: accuracy of time domain reflectometry and ground-penetrating radar," *Journal of Hydrology*, *245*(1), 48-58 (2001).

[75] Turesson, A., "Water content and porosity estimated from ground-penetrating radar and resistivity," *Journal of Applied Geophysics*, *58*(2), 99-111 (2006).

[76] Nobes, D. C., "Geophysical surveys of burial sites: a case study of the Oaro urupa," *Geophysics*, *64*(2), 357-367 (1999).

[77] Bano, M., Marquis, G., Nivière, B., Maurin, J., and Cushing, M., "Investigating alluvial and tectonic features with ground-penetrating radar and analyzing diffractions patterns," *Journal of Applied Geophysics*, *43*(1), 33-41 (2000).

[78] Sun, J., & Young, R. A., "Recognizing surface scattering in ground-penetrating radar data," *Geophysics*, *60*(5), 1378-1385 (1995).

[79] Hintz, K. J., “SNR improvements in NIITEK ground-penetrating radar,” In *Defense and Security,* International Society for Optics and Photonics, 399-408 (2004)

[80] Torrione, P., Collins, L., Clodfelter, F., Frasier, S., and Starnes, I., “Application of the LMC algorithm to anomaly detection using the Wichmann/NIITEK ground-penetrating radar,” In *Proceedings of SPIE,* 5089, 1127-1136 (2003).

[81] Ho, K. C., Carin, L., Gader, P. D., and Wilson, J. N., “An investigation of using the spectral characteristics from ground penetrating radar for landmine/clutter discrimination,” *IEEE transactions on Geoscience and Remote Sensing, 46*(4), 1177-1191 (2008).

[82] Torrione, P. A., Throckmorton, C. S., and Collins, L. M., “Performance of an adaptive feature-based processor for a wideband ground penetrating radar system,” *IEEE Transactions on Aerospace and Electronic Systems*, *42*(2), 644-658 (2006).

[83] Fisher, E., McMechan, G. A., and Annan, A. P., “Acquisition and processing of wide-aperture ground-penetrating radar data,” *Geophysics*, *57*(3), 495-504 (1992).

[84] Xia, T., Venkatachalam, A., Zhang, Y., Burns, D., and Huston, D., “Performance Enhanced High Speed UWB GPR System for Buried Rebar Detection,” In *Symposium on the Application of Geophysics to Engineering and Environmental Problems 2013,* Society of Exploration Geophysicists and Environment and Engineering Geophysical Society, 301-310 (2013).

[85] Cardimona, S. J., Clement, W. P., and Kadinsky-Cade, K., “Seismic reflection and ground-penetrating radar imaging of a shallow aquifer,” *Geophysics*, *63*(4), 1310-1317 (1998).

[86] Benson, A. K., “Applications of ground penetrating radar in assessing some geological hazards: examples of groundwater contamination, faults, cavities,” *Journal of applied Geophysics*, *33*(1-3), 177-193 (1995).

[87] Lai, W. L., Kind, T., and Wiggenhauser, H., “Using ground penetrating radar and time–frequency analysis to characterize construction materials,” *NDT & E International*, *44*(1), 111-120 (2011).

[88] Sun, Y., and Li, J., “Time–frequency analysis for plastic landmine detection via forward-looking ground penetrating radar,” *IEE Proceedings-Radar, Sonar and Navigation*, *150*(4), 253-261 (2003).

[89] Baili, J., Lahouar, S., Hergli, M., Al-Qadi, I. L., and Besbes, K., “GPR signal de-noising by discrete wavelet transform,” *NDT & E International*, 42(8), 696-703 (2009).

[90] Salvati, J. L., Chen, C. C., and Johnson, J. T., “Theoretical study of a surface clutter reduction algorithm,” In *Geoscience and Remote Sensing Symposium Proceedings, 1998. IGARSS'98. 1998 IEEE International,* 3, 1460-1462 (1998).

[91] R. Solimene, and A. Cuccaro, “Front Wall Clutter Rejection Methods in TWI,” *IEEE Geoscience and Remote Sensing Letters*, 11(6), 1158-1162 (2014).

[92] Solimene, R., and D'Alterio, A., “Entropy-based clutter rejection for intrawall diagnostics,” *International Journal of Geophysics,* (2012).

[93] Olhoeft, G. R., “Maximizing the information return from ground penetrating radar,” *Journal of Applied Geophysics,* 43(2), 175-187 (2000).

[94] Bourgeois, J. M., and Smith, G. S., “A fully three-dimensional simulation of a ground-penetrating radar: FDTD theory compared with experiment,” *IEEE Transactions on Geoscience and Remote Sensing*, *34*(1), 36-44 (1996).

[95] D. Potin, E. Duflos, and P. Vanheeghe, “Landmines Ground-Penetrating Radar Signal Enhancement by Digital Filtering,” *IEEE Transactions on Geoscience and Remote Sensing*, 44(9), 2393-2406 (2006).

[96] Y. Zhang, A. S. Venkatachalam, D. Huston, and T. Xia, “Advanced signal processing method for ground penetrating radar feature detection and enhancement,” *Proc. SPIE,* 9063, 906318 (2014).

[97] Verma, P. K., Gaikwad, A. N., Singh, D., and Nigam, M. J., “Analysis of clutter reduction techniques for through wall imaging in UWB range,” *Progress In Electromagnetics Research B,* 17, 29-48 (2009).

[98] Karlsen, B., Larsen, J., Sorensen, H. B. D., and Jakobsen, K. B., “Comparison of PCA and ICA based clutter reduction in GPR systems for anti-personal landmine detection,” In *Statistical Signal Processing, 2001. Proceedings of the 11th IEEE Signal Processing Workshop on,* 146-149 (2001).

[99] Tjora, S., Eide, E., and Lundheim, L., “Evaluation of methods for ground bounce removal in GPR utility mapping,” In *Ground Penetrating Radar, 2004. GPR 2004. Proceedings of the Tenth International Conference on,* 379-382 (2004).

[100] B. Karlsen, H. B. Sorensen, J. Larsen, and K. B. Jakobsen, “Independent component analysis for clutter reduction in ground penetrating radar data,” *Proc. SPIE* 4742, 378-389 (2002)

[101] Collins, L. M., Torrione, P. A., Munshi, V. S., Throckmorton, C. S., Zhu, Q. E., Clodfelter, J. F., and Frasier, S., “Algorithms for landmine detection using the NIITEK ground penetrating radar,” In *Proc. SPIE,* 4742, 709-718 (2002).

[102] F. H. C. Tivive, A. Bouzerdoum, and M. G. Amin, “A Subspace Projection Approach for Wall Clutter Mitigation in Through-the-Wall Radar Imaging,” *IEEE Transactions on Geoscience and Remote Sensing,* 53(4), 2108-2122 (2015).

[103] Goodman, D., “Ground-penetrating radar simulation in engineering and archaeology,” *Geophysics*, *59*(2), 224-232 (1994).

[104] Yilmaz, Ö., “Seismic data analysis: Processing, inversion, and interpretation of seismic data,” Society of exploration geophysicists, (2001).

[105] Irving, J. D., and Knight, R. J., “Removal of wavelet dispersion from ground-penetrating radar data,” *Geophysics*, *68*(3), 960-970 (2003).

[106] Richards, M. A., Scheer, J., Holm, W. A. and Melvin, W. L., “Principles of modern radar,” SciTech Pub., (2010).

[107] Annan, A. P., “Practical processing of GPR data,” *Sensors and software, Ontario*, (1999).

[108] Conyers, L. B., “Ground-penetrating radar for archaeology,” AltaMira Press, (2013).

[109] Malagodi, S., Orlando, L., and Piro, S., “Approaches to increase resolution of radar signal,” In *Proceedings of 6th international conference on ground penetrating radar. Tohoku University, Sendai,* 283-288 (1996).

[110] Savelyev, T. G., Kobayashi, T., Feng, X., and Sato, M., “Robust target discrimination with UWB GPR,” In *Ultra-Wideband, Short-Pulse Electromagnetics 7,* 732-739, Springer New York, (2007).

[111] Turner, G., “Subsurface radar propagation deconvolution,” *Geophysics*, *59*(2), 215-223 (1994).

[112] Özdemir, C., Demirci, Ş., Yiğit, E., and Yilmaz, B., “A review on migration methods in B-scan ground penetrating radar imaging,” *Mathematical Problems in Engineering, 2014,* (2014).

[113] Schneider, W. A., “Developments in seismic data processing and analysis (1968–1970),” *Geophysics*, *36*(6), 1043-1073 (1971).

[114] Gazdag, J., and Sguazzero, P., “Migration of seismic data,” *Proceedings of the IEEE*, *72*(10), 1302-1315 (1984).

[115] Ozdemir, C., Demirci, S., Yigit, E., and Kavak, A., “A hyperbolic summation method to focus B-scan ground penetrating radar images: An experimental study with a stepped frequency system,” *Microwave and Optical Technology Letters*, *49*(3), 671-676 (2007).

[116] Yilmaz, O., “Seismic data processing, volume 2 of Investigations in Geophysics,” *Society of Exploration Geophysicists,* (1987).

[117] Ozdemir, C., Demirci, S., and Yigit, E., “Practical algorithms to focus B-scan GPR images: Theory and application to real data,” *Progress In Electromagnetics Research B*, *6*, 109-122 (2008).

[118] Schneider, W. A., “Integral formulation for migration in two and three dimensions,” *Geophysics*, *43*(1), 49-76 (1978).

[119] Bleistein, N., “On the imaging of reflectors in the earth,” *Geophysics*, *52*(7), 931-942 (1987).

[120] Miller, D., Oristaglio, M., and Beylkin, G., “A new slant on seismic imaging: Migration and integral geometry,” *Geophysics*, *52*(7), 943-964 (1987).

[121] Claerbout, J. F., “Imaging the Earth's interior,” *Geophysical Journal International*, *86*(1), 217-217 (1986).

[122] Gazdag, J., “Wave equation migration with the phase-shift method,” *Geophysics*, 43(7), 1342-1351 (1978).

[123] Lecomte, I., Hamran, S. E., and Gelius, L. J., “Improving Kirchhoff migration with repeated local plane-wave imaging? A SAR-inspired signal-processing approach in prestack depth imaging,” *Geophysical Prospecting*, *53*(6), 767-785 (2005).

[124] Stolt, R. H., “Migration by Fourier transform,” *Geophysics, 43*(1), 23-48 (1978).

[125] Cafforio, C., Prati, C., and Rocca, F., “SAR data focusing using seismic migration techniques,” *IEEE transactions on aerospace and electronic systems, 27*(2), 194-207 (1991).

[126] Cafforio, C., Prati, C., and Rocca, F., “Full resolution focusing of SEASAT SAR images in the frequency-wave number domain,” *International Journal of Remote Sensing, 12*(3), 491-510 (1991).

[127] Milman, A. S., “SAR imaging by ω—κ migration,” *International Journal of Remote Sensing, 14*(10), 1965-1979 (1993).

[128] Gunawardena, A., and Longstaff, D., “Wave equation formulation of synthetic aperture radar (SAR) algorithms in the time-space domain,” *IEEE transactions on Geoscience and Remote Sensing, 36*(6), 1995-1999 (1998).

[129] Gu, K., Wang, G., and Li, J., “Migration based SAR imaging for ground penetrating radar systems,” *IEE Proceedings-Radar, Sonar and Navigation, 151*(5), 317-325 (2004).

[130] Gilmore, C., Jeffrey, I., and LoVetri, J., “Derivation and comparison of SAR and frequency-wavenumber migration within a common inverse scalar wave problem formulation,” *IEEE transactions on geoscience and remote sensing, 44*(6), 1454-1461 (2006).

[131] Zhuge, X., and Yarovoy, A., “Frequency-wavenumber domain focusing under linear MIMO array configurations,” In *Geoscience and Remote Sensing Symposium (IGARSS), 2012 IEEE International,* 2125-2128 (2012).

[132] Zhuge, X., and Yarovoy, A. G., “Three-dimensional near-field MIMO array imaging using range migration techniques,” *IEEE Transactions on Image Processing, 21*(6), 3026-3033 (2012).

[133] Yang, H., Li, T., Li, N., He, Z., and Liu, Q. H., “Efficient near-field imaging for single-borehole radar with widely separated transceivers,” *IEEE Transactions on Geoscience and Remote Sensing, 53*(10), 5327-5337 (2015).

[134] Munson, D. C., O'Brien, J. D., and Jenkins, W. K., “A tomographic formulation of spotlight-mode synthetic aperture radar,” *Proceedings of the IEEE, 71*(8), 917-925 (1983).

[135] Nilsson, S., and Andersson, L. E., “Application of fast back-projection techniques for some inverse problems of synthetic aperture radar,” In *Aerospace/Defense Sensing and Controls,* International Society for Optics and Photonics, 62-72 (1998).

[136] Soumekh, M., “*Synthetic aperture radar signal processing* (Vol. 7),” New York: Wiley, (1999).

[137] Desai, M. D., and Jenkins, W. K., “Convolution backprojection image reconstruction for spotlight mode synthetic aperture radar,” *IEEE Transactions on Image Processing, 1*(4), 505-517 (1992).

[138] Le Bastard, C., Wang, Y., Baltazart, V., and Derobert, X., "Time delay and permittivity estimation by ground-penetrating radar with support vector regression," *IEEE Geoscience and Remote Sensing Letters*, *11*(4), 873-877 (2014).

[139] Kassem, E., Chowdhury, A., Scullion, T., and Masad, E., "Application of ground-penetrating radar in measuring the density of asphalt pavements and its relationship to mechanical properties," *International Journal of Pavement Engineering*, 17(6), 503-516 (2016).

[140] Pinel, N., Le Bastard, C., Baltazart, V., Bourlier, C., and Wang, Y., "Influence of layer roughness for road survey by ground penetrating radar at nadir: theoretical study," *IET radar, sonar & navigation*, 5(6), 650-656 (2011).

[141] Shangguan, P., Al-Qadi, I., Leng, Z., Schmitt, R., and Faheem, A., "Innovative approach for asphalt pavement compaction monitoring with ground-penetrating radar," *Transportation Research Record: Journal of the Transportation Research Board*, 2347, 79-87 (2013).

[142] Willett, D. A., Mahboub, K. C., and Rister, B., "Accuracy of ground-penetrating radar for pavement-layer thickness analysis," *Journal of Transportation Engineering*, 132(1), 96-103 (2013).

[143] Lahouar, S., and Al-Qadi, I. L., "Automatic detection of multiple pavement layers from GPR data," *NDT & e International*, 41(2), 69-81 (2008).

[144] Lambot, S., Weihermüller, L., Huisman, J. A., Vereecken, H., Vanclooster, M., and Slob, E. C., "Analysis of air-launched ground-penetrating radar techniques to measure the soil surface water content," *Water resources research*, 42(11), (2006).

[145] Cassidy, N. J., "Evaluating LNAPL contamination using GPR signal attenuation analysis and dielectric property measurements: Practical implications for hydrological studies," Journal of Contaminant Hydrology, 94(1), 49-75 (2007).

[146] Li, J., Zollinger, D., and Lytton, R., "Detection of delamination in concrete pavements using ground-coupled ground-penetrating radar technique," *Transportation Research Record: Journal of the Transportation Research Board*, 2087, 68-77 (2008).

[147] Al-Qadi, I. L., Xie, W., and Roberts, R., "Scattering analysis of ground-penetrating radar data to quantify railroad ballast contamination," *NDT & E International*, 41(6), 441-447 (2008).

[148] Addison, A. D., Battista, B. M., and Knapp, C. C., "Improved hydrogeophysical parameter estimation from empirical mode decomposition processed ground penetrating radar data," *Journal of Environmental & Engineering Geophysics*, *14*(4), 171-178 (2009).

[149] Battista, B. M., Knapp, C., McGee, T., and Goebel, V., "Application of the empirical mode decomposition and Hilbert-Huang transform to seismic reflection data," *Geophysics*, *72*(2), H29-H37 (2007).

[150] Han, J., and van der Baan, M., "Empirical mode decomposition for seismic time-frequency analysis," *Geophysics,* (2013).

[151] Ghose, R., and Slob, E. C., "Quantitative integration of seismic and GPR reflections to derive unique estimates for water saturation and porosity in subsoil," *Geophysical Research Letters*, *33*(5) (2006).

[152] Lai, W. L., Kind, T., and Wiggenhauser, H., "Using ground penetrating radar and time–frequency analysis to characterize construction materials," *NDT & E International*, *44*(1), 111-120 (2011).

[153] Leng, Z., and Al-Qadi, I., "Railroad Ballast Evaluation Using Ground-Penetrating Radar: Laboratory Investigation and Field Validation," *Transportation Research Record: Journal of the Transportation Research Board*, 2159, 110-117 (2010).

[154] Liu, L., Liu, Z., & Barrowes, B. E. (2011). Through-wall bio-radiolocation with UWB impulse radar: Observation, simulation and signal extraction. *IEEE Journal of Selected Topics in Applied Earth Observations and Remote Sensing*, *4*(4), 791-798.

[155] Lester, J., and Bernold, L. E., "Innovative process to characterize buried utilities using ground penetrating radar," *Automation in Construction*, *16*(4), 546-555 (2007).

[156] Jeng, Y., Lin, C. H., Li, Y. W., Chen, C. S., and Yu, H. M., "Application of sub-image multiresolution analysis of Ground-penetrating radar data in a study of shallow structures," *Journal of Applied Geophysics*, *73*(3), 251-260 (2011).

[157] Shangguan, P., Al-Qadi, I., & Leng, Z., "Development of wavelet technique to interpret ground-penetrating radar data for quantifying railroad ballast conditions," *Transportation Research Record: Journal of the Transportation Research Board*, 2289, 95-102 (2012).

[158] Terrasse, G., Nicolas, J. M., Trouvé, E., and Drouet, É., "Application of the curvelet transform for pipe detection in GPR images," In *Geoscience and Remote Sensing Symposium (IGARSS), 2015 IEEE International*, 4308-4311, (2015, July).

[159] Tzanis, A., "The Curvelet Transform in the analysis of 2-D GPR data: Signal enhancement and extraction of orientation-and-scale-dependent information," *Journal of Applied Geophysics*, *115*, 145-170 (2015).

[160] Leucci, G., "Ground penetrating radar: the electromagnetic signal attenuation and maximum penetration depth," *Scholarly research exchange*, *2008*, (2008).

[161] Williams, R. M., Ray, L. E., Lever, J. H., and Burzynski, A. M., "Crevasse detection in ice sheets using ground penetrating radar and machine learning," *IEEE Journal of Selected Topics in Applied Earth Observations and Remote Sensing*, *7*(12), 4836-4848 (2014).

[162] Torrione, P. A., Morton, K. D., Sakaguchi, R., and Collins, L. M., "Histograms of oriented gradients for landmine detection in ground-penetrating radar data," *IEEE Transactions on Geoscience and Remote Sensing*, *52*(3), 1539-1550 (2014).

[163] Zhang, X., Bolton, J., and Gader, P., "A new learning method for continuous hidden Markov models for subsurface landmine detection in ground penetrating radar," *IEEE Journal of Selected Topics in Applied Earth Observations and Remote Sensing*, *7*(3), 813-819 (2014).

[164] Shao, W., Bouzerdoum, A., and Phung, S. L., “Signal classification for ground penetrating Radar using sparse kernel feature selection,” *IEEE Journal of Selected Topics in Applied Earth Observations and Remote Sensing*, *7*(12), 4670-4680 (2014).

[165] Camilo, J. A., Malof, J. M., and Collins, L. M., “A feature learning approach for classifying buried threats in forward looking ground penetrating radar data,” In *Proc. SPIE*, 9823, (2016).

[166] Maas, C., and Schmalzl, J., “Using pattern recognition to automatically localize reflection hyperbolas in data from ground penetrating radar,” *Computers & geosciences*, *58*, 116-125 (2013).

[167] Jiankui, Z., Zishu, H., Sellathurai, M., and Hongming, L., “Modified Hough transform for searching radar detection,” *IEEE Geoscience and Remote Sensing Letters*, *5*(4), 683-686 (2008).

[168] Besaw, L. E., and Stimac, P. J., “Deep learning algorithms for detecting explosive hazards in ground penetrating radar data,” In *Proc. SPIE*, 9072, (2014).

[169] Sakaguchi, R. T., Morton, K. D., Collins, L. M., and Torrione, P. A., “Recognizing subsurface target responses in ground penetrating radar data using convolutional neural networks,” *SPIE Defense+ Security*, *9454*, 94541A, (2015).

[170] Bralich, J., Reichman, D., Collins, L. M., and Malof, J. M., “Improving convolutional neural networks for buried threat in ground penetrating radar using transfer learning via pretraining,” In *SPIE Defense+ Security* (pp. 101820X-101820X). International Society for Optics and Photonics, (2017).

[171] Aydin, E., and Yüksel, S. E., “Buried target detection with ground penetrating radar using deep learning method,” In *Signal Processing and Communications Applications Conference (SIU), 2017 25th* (pp. 1-4). IEEE, (2017).

[172] Mason, E., Yonel, B., and Yazici, B., “Deep learning for radar,” In *Radar Conference (RadarConf), 2017 IEEE* (pp. 1703-1708). IEEE, (2017).

[173] Besaw, L. E., and Stimac, P. J., “Deep convolutional neural networks for classifying GPR B-scans,” In *SPIE Defense+ Security* (pp. 945413-945413). International Society for Optics and Photonics, (2015).

[174] Becker, J., Havens, T. C., Pinar, A., and Schulz, T. J., “Deep belief networks for false alarm rejection in forward-looking ground-penetrating radar,” In *SPIE Defense+ Security* (pp. 94540W-94540W). International Society for Optics and Photonics, (2015).

[175] Sudha, S., Vidhyalakshmi, M., Pavithra, K., Sangeetha, K., and Swaathi, V., “An automatic classification method for environment: Friendly waste segregation using deep learning,” In *Technological Innovations in ICT for Agriculture and Rural Development (TIAR), 2016 IEEE* (pp. 65-70). IEEE, (2016).

[176] Suksmono, A. B., Bharata, E., Lestari, A. A., Yarovoy, A. G., and Ligthart, L. P., “Compressive stepped-frequency continuous-wave ground-penetrating radar,” *IEEE geoscience and remote sensing letters*, *7*(4), 665-669 (2010).

[177] Zhang, Y., Wang, G., and Xia, T., "Compressive orthogonal frequency division multiplexing waveform based ground penetrating radar," In *Radar Conference (RadarCon), 2015 IEEE*, 0684-0689 (2015).

[178] Zhang, Y., and Xia, T., "Frequency domain clutter removal for compressive OFDM ground penetrating radar," In *Circuits and Systems (ISCAS), 2016 IEEE International Symposium on*, 962-965 (2016).

[179] RADAN® - GPR Software by GSSI: http://www.geophysical.com/software.htm

[180] GPR Processing Software – MALA Ground Penetrating Radar – GPR: http://www.malagpr.com.au/gpr-processing-software.html

[181] MATGPR Home: http://users.uoa.gr/~atzanis/matgpr/matgpr.html

CHAPTER 2: IN-WALL CLUTTER SUPPRESSION BASED ON LOW-RANK AND SPARSE REPRESENTATION FOR THROUGH-THE-WALL RADAR

Abstract

For Through-the-Wall radar (TWR) signal processing, there exist extensive studies on removing the wall surface reflection signal, while how to eliminate/alleviate the in-wall structure reflection is not well addressed. In many building structures, a layer of reinforced steel bars and utility pipes exist inside the wall which can cause strong clutter to overwhelmingly mask the reflection signal from the targets under test behind the wall. Such clutter cannot be mitigated using the conventional wall clutter removal methods. Thus, a new effective technique to remove the strong inside-wall rebar or pipe reflection is indispensable. Considering the correlated features of the in-wall rebar or pipes, and the spatial sparsity of the behind-wall targets under test, a low-rank and sparse representation model based in-wall clutter suppression algorithm is developed in this letter for target feature enhancement and detection. Experiments on both simulation data and field test data are performed for performance evaluation and validation.

Keywords: Through-the-wall radar; in-wall clutter suppression; low-rank representation; sparse representation.

2.1. Introduction

Through-the-Wall radar (TWR) system is widely used to detect the targets behind walls or map the structure of a building. It allows security agents, rescue personnel, first responders, and defense forces to detect, identify, classify and track the whereabouts of humans and moving objects [1]-[4].

In the TWR imaging, the strong clutter due to wall reflection often overwhelms reflection signal from the stationary targets under test behind the wall or inside the building. Many methods have been developed to mitigate the wall clutter, including subspace projection approach [5], time gating based on entropy criterion [6], spatial filtering [7]-[9], etc. The subspace projection approach [5] is based on the strength difference between the exterior wall reflection and the behind-wall targets reflection. It applies singular value decomposition to the data matrix to identify the wall subspace. Orthogonal subspace projection is then performed to remove the wall electromagnetic signature from the data matrix. Ref. [6] observes that the field reflected from a layered background medium has a strong similarity over different sensor positions. Then, an entropy-based windowing function is defined as to null the signal over instants of time where different traces exhibit high similarity. Spatial filtering method [7], [9] utilizes the strong similarity between wall EM responses from different antennas. Considering that reflection signal from targets with limited spatial extent vary from sensor to sensor, a spatial filter across the antenna scan axis is applied to mitigate the spatial zero-frequency and low-frequency components which correspond to wall reflections.

The above wall clutter removal methods are generally based on two assumptions: (1) The wall surface responses are much stronger than that of the behind-wall targets; or (2) The wall surface reflection are relatively constant signals at each antenna scan position while the target reflection is a varying signal. However, for many building structures, a layer of reinforced steel bars or utility pipes exist inside the wall, which also produce strong clutters. Such strong interference reflection may overwhelmingly mask the reflection signal from the targets under test behind the wall. However, such clutters are stronger than target responses while weaker than wall clutter. It is infeasible to determine a perfect threshold for the subspace projection approach [5] without any prior-knowledge. On the other hand, such type of clutters is also varying at each scan position, thus it cannot be distinguished from the behind-wall targets through entropy based time gating [6] or spatial filtering [7]-[9]. Therefore, a new effective method to remove the strong in-wall rebar and pipe reflection is necessary and valuable for TWR image processing.

In TWR scan, the wall surface clutter forms the stationary background signal while the behind wall target signal is considered as the foreground signal. Multiple rebars or pipes inside the wall generally show similar image patterns that are highly correlated among each other, which is the correlated background signal and named the in-wall clutter in this letter. The objective of this study is to investigate how to mitigate the in-wall clutter and enhance the feature of targets in a TWR image.

As the conventional TWR wall clutter removal methods are not effective for the in-wall clutter mitigation, the possibilities of several foreground image feature enhancement or detection methods that have been developed for ground penetrating radar (GPR) and TWR imaging systems are examined. In Ref. [10]-[11], an exponential scaling method is developed to compensate for the signal attenuation loss along the radar scan range. However, if the target is closely attached to the wall, the reflection signal of the target behind the wall and the clutter reflection due to the in-wall object are both enhanced, which inadvertently increases the difficulty of feature isolation. A pattern matching method based on the calculation of cross-correlation [12] in the TWR image can deal with the difficult case when targets and the in-wall clutter overlap in time domain. In the data processing, the signature image pattern of the in-wall object, such as rebar, is utilized as the reference for correlated matching pattern search and identification. However, when the target under test is a cylinder object of similar size with the rebar or pipes inside the wall, it results in a similar image pattern that is hard to be isolated in the detection. 2D entropy analysis [13], [14] is developed to detect the abnormal region in the radar image by characterizing the statistical distribution of the reflection signal energy distribution assuming rebars or pipes are regularly and uniformly located in the region under inspection. However, for tests where such assumptions do not hold, the effectiveness of 2D entropy analysis is degraded.

The latest mathematic theory low-rank and sparse representation [15]-[16] is able to decompose a matrix D as a superposition of a low-rank matrix L (few non-zero singular values) and a sparse matrix S (few non-zero entries). It has been applied to some research areas, such as hyperspectral image denoising [17], hyperspectral image classification [18], batch image alignment [19], and foreground extraction in video surveillance [20], etc. In TWR imaging scheme, the in-wall clutter data from rebars or pipes inside the wall forms a low-rank matrix, while the data from the foreground target under test produces a sparse matrix that lies on top of the in-wall clutter. The in-wall clutter suppression problem for TWR image processing can be transformed into a low-rank and sparse representation optimization problem. In this letter, we explore to utilize and develop low-rank and sparse representation algorithm to mitigate the in-wall structure reflection so as to leverage behind-wall object detection effectiveness in TWR image processing.

The reset sections of this chapter are organized as: Section 2.2 describes the principle of low-rank and sparse representation. Section 2.3 models the in-wall clutter suppression in TWR imaging as a low-rank and sparse representation. Section 2.4 demonstrates experiments on both the simulation data and field test TWR data. Section 2.5 summarizes the concluding remarks.

2.2. Low-Rank and Sparse Representation

The low-rank and sparse representation interprets the observed data matrix $D \in \mathbb{R}^{m\times n}$ as a superposition of a low-rank matrix $L \in \mathbb{R}^{m\times n}$ and a sparse matrix $S \in \mathbb{R}^{m\times n}$, where L represents the correlated background, while S models the foreground target features on top of the correlated background. The mathematical expression is $D = L + S$.

Decomposing the test data matrix D into L and S is an optimization problem [15]. Through Lagrangian reformulation, it can be expressed as:

$$\min_{L,S} rank(L) + \lambda\|S\|_0 \quad s.t. \;\; D = L + S \tag{2.1}$$

According to Ref. [12], in the general rectangular case, where $m \geq n$, if

$$rank(L) \leq \rho_r \frac{n}{(\log m)^2} \tag{2.2}$$

and

$$\|S\|_0 \leq 0.1 * mn \tag{2.3}$$

with the probability at least $p = 1 - cm^{-10}$, matrix L and S can be uniquely recovered by solving Eq.(2.1). In Eq. (2.2) and (2.3), ρ_r and c are positive numerical constant coefficients. Eq. (2.2) restricts the rank of the matrix L, while Eq. (2.3) defines the sparsity requirement for the matrix S. In other words, Eq. (2.2) and Eq. (2.3) specify the conditions of the matrix decomposition in Eq. (2.1).

Unfortunately, Eq. (2.1) is a highly nonconvex optimization problem with no efficient solutions. In essence, Eq. (2.1) subsumes both the low rank matrix completion problem and the l^0-minimization problem, both of which are NP-hard [21]. By replacing the l^0-norm with the l^1-norm, and the rank of L with the nuclear norm $\|L\|_* = \sum_i \sigma_i(L)$, a tractable optimization problem can be obtained [15]

$$\min_{L,S} \|L\|_* + \lambda \|S\|_1 \quad s.t. \;\; D = L + S \tag{2.4}$$

where $\|L\|_*$ is the nuclear norm or sum of singular values of matrix L, $\|S\|_1$ is the l^1-norm or sum of absolute values of the entries of S, and λ is a tuning parameter that balances the contribution of the l^1-norm term relative to the nuclear norm term. The mathematical analysis in [16] proves that the choice of $\lambda = 1/\sqrt{\max(m,n)}$ for matrices of size $m \times n$ is universal for solving the optimization problem in Eq. (2.4).

The solution of the optimization problem in Eq. (2.4) is unique and the problem is well posed if the low-rank component is not sparse, and vice versa if the sparse component does not have low rank [16]. Such condition indicates the incoherence between the matrix L and S. Under such condition, the optimization problem in Eq. (2.4) can be solved utilizing the mathematical toolbox TFOCS [22].

2.3. In-Wall Clutter Suppression for See-through-wall Radar

The TWR imaging scenario is depicted in Figure 2.1. The transceiver antennas move along the wall for imaging the object behind the wall. Generally, four types of reflection signals are collected by the receiver antenna. As shown in Figure 2.1, a_1 is the reflection signal from the exterior wall surface, a_2 is the reflection signal from the rebar or pipes inside the wall, a_3 is the reflection signal from the interior wall surface, and a_4 is the reflection signal from the object. Typically, the wall is modeled as a laterally homogeneous layer in TWR imaging scheme [6]. Thus, both the reflection signals a_1 and a_3 are both stationary background signals. The rebars or utility pipes inside the wall produce similar image patterns, while their distributions along the antenna scanning axis can be irregular. The reflection signal a_2 is called the in-wall clutter in this letter.

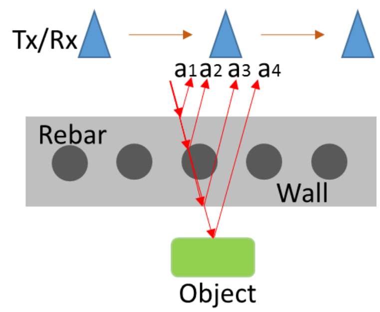

Figure 2.1: TWR imaging scenario

Based on above description, the signal collected at the n^{th} observation position can be modeled as

$$x_n(t) = b_n(t) + l_n(t) + s_n(t) \tag{2.5}$$

where $b_n(t)$ is the static background signal reflected from the wall, $l_n(t)$ is the correlated background signal produced from the in-wall rebar or pipes, and $s_n(t)$ is the object signal under detection. In TWR researches [5]-[9], various clutter removal methods have been developed to mitigate or remove the background signal $b_n(t)$. The resulting signal model upon clutter removal can be expressed as

$$d_n(t) = l_n(t) + s_n(t) \tag{2.6}$$

In this chapter, a low-rank and sparse representation based approach is investigated to suppress the correlated background signal, i.e. in-wall clutter $l_n(t)$ so as to enhance the object signal $s_n(t)$.

For TWR data processing, $d_n(t)$, $l_n(t)$ and $s_n(t)$ are recorded as $M \times 1$ vectors $\boldsymbol{d_n}$, $\boldsymbol{l_n}$, and $\boldsymbol{s_n}$ respectively. M is the number of samples collected at each scan position. Assembling the data of all N scan positions lead to the following $M \times N$ data matrices:

$$\boldsymbol{D} = [\boldsymbol{d_1}, \boldsymbol{d_2}, \boldsymbol{d_3}, \dots, \boldsymbol{d_N}] \tag{2.7}$$

$$\boldsymbol{L} = [\boldsymbol{l_1}, \boldsymbol{l_2}, \boldsymbol{l_3}, \dots, \boldsymbol{l_N}] \tag{2.8}$$

$$\boldsymbol{S} = [\boldsymbol{s_1}, \boldsymbol{s_2}, \boldsymbol{s_3}, \dots, \boldsymbol{s_N}] \tag{2.9}$$

According to Eq. (2.6),

$$\boldsymbol{D} = \boldsymbol{L} + \boldsymbol{S} \tag{2.10}$$

Since $\boldsymbol{L}$ contains the correlated background data, the rank of $\boldsymbol{L}$ matrix is low. While for the object data matrix $\boldsymbol{S}$, the object features are spatially sparse, therefore $\boldsymbol{S}$ is a sparse matrix. As shown in Figure 2.1, the object behind the wall is at different range distance from the rebar or pipes inside wall, the data matrix $\boldsymbol{D}$ can thus be inherently represented as a superposition of the low-rank matrix $\boldsymbol{L}$ and the sparse matrix $\boldsymbol{S}$. Based on the analysis elaborated in Section 2.2, as long as the target is sparser than the in-wall clutter, the object signal $\boldsymbol{S}$ can be extracted through suppressing the correlated background signal $\boldsymbol{L}$ by solving Eq. (2.4). The procedures are summarized below:

1. Pre-processing: Remove the stationary exterior and interior wall background signal using a 2-D high pass filter [9].

2. Decompose the processed TWR data matrix $\boldsymbol{D} \in \mathbb{R}^{M \times N}$ into a low-rank matrix $\boldsymbol{L} \in \mathbb{R}^{M \times N}$ and a sparse matrix $\boldsymbol{S} \in \mathbb{R}^{M \times N}$ by solving Eq. (2.4) with tuning parameter $\lambda = 1/\sqrt{\max(M, N)}$.
3. Extract the object matrix $\boldsymbol{S}$ after in-wall clutter suppression.

2.4. Experimental results

In order to validate the proposed TWR in-wall clutter suppression using low-rank and sparse representation technique, experiments are conducted. The test utilizes the data set synthesized with the simulation program GprMax [23], and field test data collected utilizing a commercial MALA CX radar system.

2.4.1. Experiment with the Synthetic Data

The geometry structure set up for producing the synthetic data is shown in Figure 2.2(a), where the TWR transceiver antennas are 2.5 cm distant from the exterior surface of the wall. The wall is modeled as a homogeneous layer of 15 cm thickness which contains 8 rebars of 1.25 cm radius unevenly placed inside. The target behind the wall is another cylinder object of 1.25 cm radius. The distance between the target and interior wall surface is 5 cm.

In the FDTD simulation, the TWR radiation signal is generated as a Ricker waveform (i.e. the normalized second derivative of a Gaussian pulse) with its center frequency being 900 MHz. During the scan, TWR data at 115 positions are uniformly collected from left to right along the horizontal direction in Figure 2.2(a). The raw B-scan image is plotted as Figure 2.2(b) and the size of the data matrix is 2036×115. In the raw image, the exterior wall reflection shows as a horizontal line, and the rebars inside the wall show hyperbolic features. In this setup, the hyperbolas in TWR image are repeatedly but not periodically distributed. The reflection signal from the target is invisible in the raw TWR image for being masked by the strong background signal.

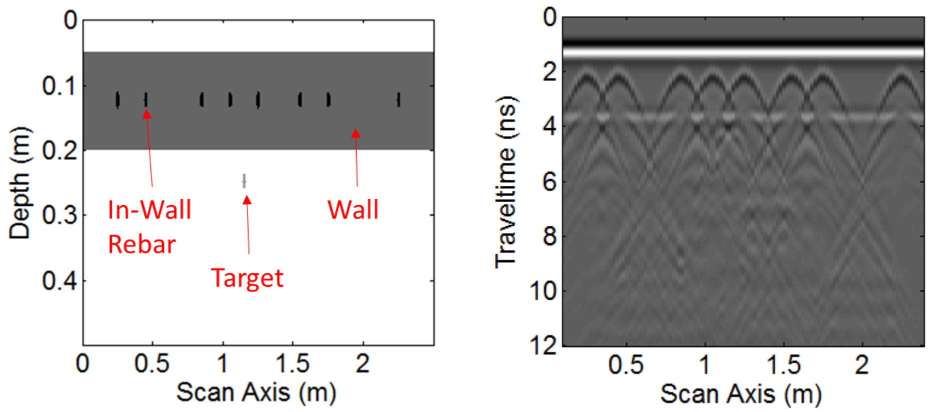

(a) (b)

Figure 2.2: Synthetic data: (a) Geometry structure; (2) Raw TWR image.

After applying the stationary background removal [9], the wall surface reflection signal is eliminated, and the pre-processed TWR is shown as Figure 2.3(a) where the target is still not visible.

For this test data processing, the tuning parameter in Eq. (2.4) is calculated as $\lambda = 1/\sqrt{\max(2036, 115)} \approx 0.022$, and the sparse object matrix is extracted from the pre-processed TWR data. The processed TWR image upon the in-wall clutter suppression is depicted as Figure 2.3(b), where the target feature clearly stands out.

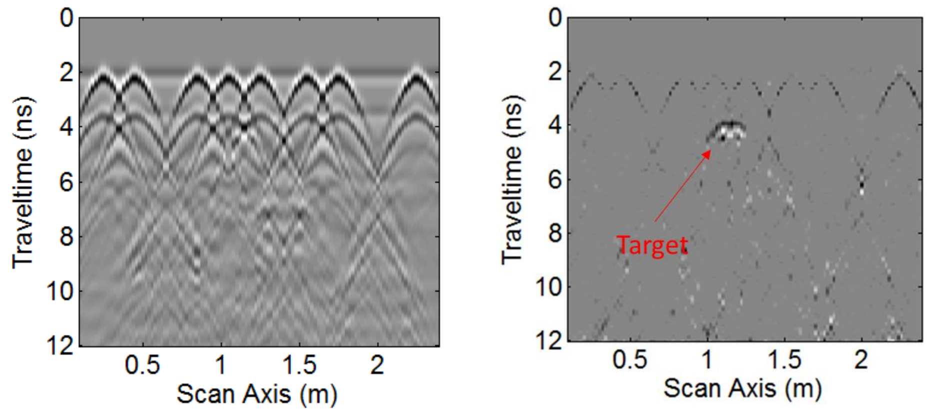

(a) (b)

Figure 2.3: Processed synthetic data: (a) Pre-processing – stationary background removal; (b) In-wall clutter removal with low-rank and sparse representation technique.

To quantitatively evaluate the performance of the in-wall clutter suppression method, signal-to-clutter ratio (SCR) is used as a metric for characterizing the power ratio between the backscattering signal from the targets under test and the clutter. Let $c_{t,n}$ be the in-wall clutter data at the time index t and scan axis n, and $s_{t,n}$ be the target reflection data at the time index t and scan axis n. The in-wall clutters are within the region $R_c = \{(t,n)|t \in (t_1, t_2), n \in (n_1, n_2)\}$, and the target reflection signals are within the region $R_s = \{(t,n)|t \in (t_3, t_4), n \in (n_1, n_2)\}$. The SCR is calculated as

$$\mathrm{SCR} = 20 \log_{10} \frac{\sum_{R_s} \|s_{t,n}\|^2}{\sum_{R_c} \|c_{t,n}\|^2} \tag{2.11}$$

For the pre-processed TWR image in Figure 2.3(a) consisting of correlated background and object signal, the SCR is calculated as -4.22 dB. While for the correlated background removed TWR image in Figure 2.3(b), the SCR is improved to 26.36 dB.

To further evaluate the algorithm performance, comparison with the cross-correlation based pattern matching method [12] is made on the synthetic data. Figure 2.4

is the TWR B-scan image obtained using pattern matching method corresponding to the synthetic data. In the TWR imaging scheme, the in-wall rebars show hyperbolic features in the TWR image. When the distance between two adjacent rebars is small, their hyperbolic patterns overlap. When the in-wall rebars are unevenly distributed inside the wall, the overlapping areas vary which results in different image patterns for different rebars. However, during the pattern matching, the same hyperbola pattern is used as the reference for cross-correlation calculation, the matching accuracy is thus not high, and undesired noises and distortions are produced upon background signal subtraction. For the processed TWR image, its SCR is calculated to be 6.00 dB only, which is much lower than 26.36 dB SCR value obtained with our proposed method.

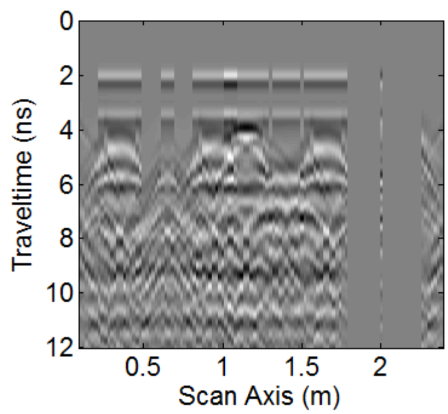

Figure 2.4: Processed simulation data using pattern matching.

2.4.2. Experiment with the Field Test Data

To further evaluate the performance of the proposed in-wall clutter suppression method, a real field TWR sensing data set is collected using a MALA CX radar system. Shown in Figure 2.5(a), in the test, a computer hard disk is put on a wood shelf leaning to the interior surface of a wall as the detection target. As depicted in Figure 2.5(b), the TWR scan is performed on the other side of the wall.

(a)

(b)

(c)

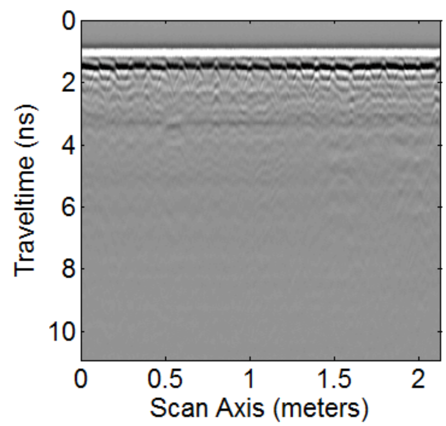

(d)

Figure 2.5: Field test data: (a) A hard disk attached on the wall; (b) TWR scanning from the other side of the wall; (c) MALA concrete imaging system; (d) Raw TWR image.

The radar system used in the test is MALA Concrete Imaging System coupled with a MALA 2.3 GHz HF Antenna, which is shown in Figure 2.5(c). TWR data are uniformly collected along the exterior wall surface at every 2.54 mm space. The raw TWR image is plotted in Figure 2.5(d). The data matrix size is 312×884. In the raw TWR image, the exterior wall reflection shows as a horizontal line at 1 ns, and the rebars inside the wall are displayed as hyperbolic features locating between 1 ns and 3 ns. The reflection signal from the hard disk at cross-section of 3 ns and 0.5 m is barely visible in the raw TWR image for being masked by the strong background signal.

The pre-processed TWR is shown as Figure 2.6(a). In the pre-processed TWR image, the wall surface reflection has been removed, however, the hard disk object feature is still obscure comparing with the strong in-wall clutter, i.e. the repeated hyperbolic features.

To solve the low-rank and sparse representation optimization problem to suppress the correlated background data, tuning parameter $\lambda = 1/\sqrt{\max(312, 884)} \approx 0.034$ is substituted into Eq. (2.4). As shown in Figure 2.6(b), the target feature is enhanced upon in-wall clutter suppression.

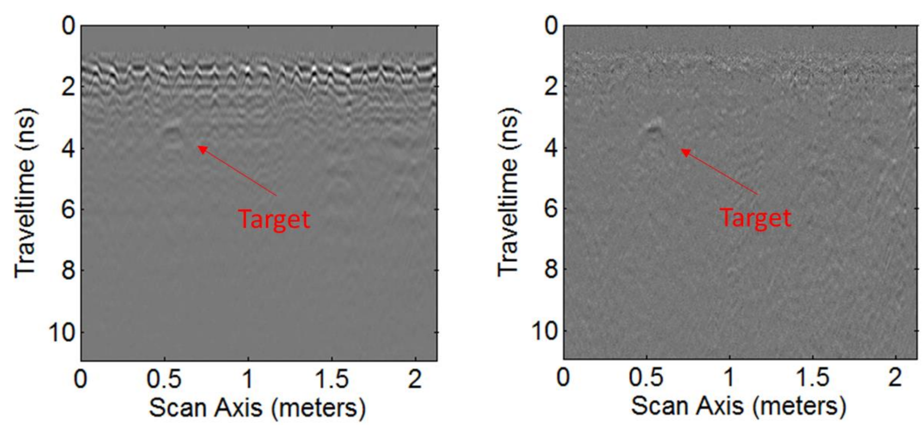

(a) (b)

Figure 2.6: Processed field test data: (a) Pre-processing – stationary background removal; (b) In-wall clutter suppression.

To quantitatively analyze the in-wall clutter suppression result, SCRs of the TWR images in the field test are calculated. For the pre-processed TWR image in Figure 2.6(a) consisting of correlated background and object signal, the SCR is -18.20 dB. While for the correlated background suppressed TWR image in Figure 2.6(b), the SCR becomes 17.75 dB. Apparently, the low-rank and sparse representation based in-wall clutter removal method improves SCR by 35.95 dB comparing with the pre-processed TWR image. The quantitative analysis results corroborate the effectiveness of the low-rank and sparse representation based in-wall clutter suppression in TWR data processing.

Similar to the simulation data processing, the field test data in Figure 2.6(a) is processed by the pattern matching method as well. The resulting image is plotted in Figure 2.7. Due to the unevenly distribution of the in-wall clutter and the test environmental noises, the in-wall clutter cannot be mitigated effectively utilizing the pattern matching approach. The SCR of the processed TWR image is as low as -13.41 dB.

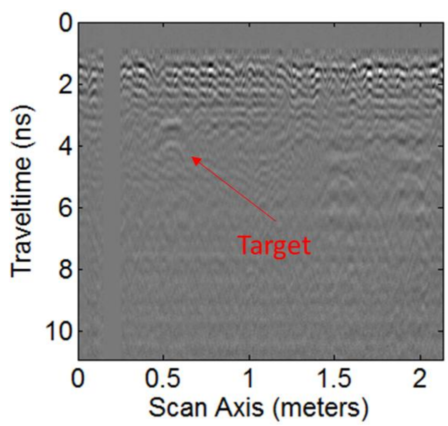

Figure 2.7: Processed field test data using pattern matching.

In sum, the proposed in-wall clutter suppression method based on low-rank and sparse representation is more robust to the uneven distribution of the in-wall rebars or pipes. Further, the proposed method does not produce fake scattering and undesired image distortion comparing with the cross-correlation based pattern matching method.

2.5. Conclusions

In this letter, the correlated TWR image background suppression using low-rank and sparse representation algorithm has been investigated, where the distribution of targets under test is significantly sparser than that of the in-wall clutter. The proposed method can automate the suppression of in-wall clutter, without the need of prior knowledge about the target under test. Also, comparing with the conventional cross-correlation based background subtraction methods, the proposed approach is insensitive to the distribution of the correlated background matrix, which makes it effective for practical use. Experiments with both the synthetic data and the field test data indicate that the proposed in-wall clutter suppression technique can effectively improve the SCR of the TWR image.

2.6. References

[1] M.G. Amin, “Through-the-Wall Radar Imaging,” CRC Press, 2011.

[2] A.S. Venkatachalam, X. Xu, D. Huston, and T. Xia, “Development of a New High Speed Dual-Channel Impulse Ground Penetrating Radar,” IEEE Journal of Selected Topics in Applied Earth Observations and Remote Sensing, vol. 7, no. 3, pp. 753-760, Mar. 2014.

[3] Y. Zhang, G. Wang, and T. Xia, “Compressive orthogonal frequency division multiplexing waveform based ground penerating radar,” 2015 IEEE Radar Conference (RadarCon), pp. 684-689, 2015.

[4] A. Ahmed, Y. Zhang, D. Burns, D. Huston, and T. Xia, “Design of UWB Antenna for Air-Coupled Impulse Ground-Penetrating Radar,” IEEE Geoscience and Remote Sensing Letters, vol. 13, no. 1, pp. 92-96, 2016.

[5] F.H.C. Tivive, A. Bouzerdoum, and M.G. Amin, “A Subspace Projection Approach for Wall Clutter Mitigation in Through-the-Wall Radar Imaging,” IEEE Transactions on Geoscience and Remote Sensing, vol. 53, no. 4, pp. 2108-2122, Apr 2015.

[6] R. Solimene and A. Cuccaro, “Front Wall Clutter Rejection Methods in TWI,” IEEE Geoscience and Remote Sensing Letters, vol. 11, no. 6, pp. 1158-1162, Jun 2014.

[7] Y.S. Yoon and M.G. Amin, "Spatial Filtering for Wall-Clutter Mitigation in Through-the-Wall Radar Imaging," IEEE Transactions on Geoscience and Remote Sensing, vol. 47, no. 9, pp. 3192-3208, Sep 2009.

[8] Y. Zhang, A.S. Venkatachalam, D. Huston, and T. Xia, "Advanced signal processing method for ground penetrating radar feature detection and enhancement," SPIE Smart Structures and Materials +Nondestructive Evaluation and Health Monitoring, pp. 1-14, 2014.

[9] D. Potin, E. Duflos, and P. Vanheeghe, "Landmines Ground-Penetrating Radar Signal Enhancement by Digital Filtering," IEEE Transactions on Geoscience and Remote Sensing, vol. 44, no. 9, pp. 2393-2406, Sep 2006.

[10] Y. Zhang, A.S. Venkatachalam, T. Xia, Y. Xie, and G. Wang, "Data analysis technique to leverage ground penetrating radar ballast inspection performance," 2014 IEEE Radar Conference, Cincinnati, OH, pp. 463-468, May 2014.

[11] L. Li, A.E. Tan, K. Jhamb, and K. Rambabu, "Buried Object Characterization Using Ultra-Wideband Ground Penetrating Radar," IEEE Transactions on Microwave Theory and Techniques, vol. 60, no. 8, pp. 2654 – 2664, Aug 2012.

[12] M. Richards, "Fundamentals of Radar Signal Processing," McGraw-Hill Education, 2005.

[13] Y. Zhang, P. Candra, G. Wang, and T. Xia, "2-D Entropy and Short-Time Fourier Transform to Leverage GPR Data Analysis Efficiency," IEEE Transactions on Instrumentation and Measurement, vol. 64, no. 1, pp. 103-111, Jan 2015.

[14] Y. Zhang, A.S. Venkatachalam, and T. Xia, "Ground-penetrating radar railroad ballast inspection with an unsupervised algorithm to boost the region of interest detection efficiency," Journal of Applied Remote Sensing, vol. 9, no. 1, pp. 1-19, 2015.

[15] J. Wright, Y. Peng, Y. Ma, A. Ganesh, and S. Rao, "Robust Principal Component Analysis: Exact Recovery of Corrupted Low-Rank Matrices by Convex Optimization," Advances in Neural Information Processing Systems, pp. 2080-2088, 2009.

[16] E.J. Candes, X. Li, Y. Ma, J. Wright, "Robust Principal Component Analysis?," Journal of the ACM, vol. 58, no. 3, article 11, pp. 1-37, May 2011.

[17] Y. Zhao and J. Yang, "Hyperspectral Image Denoising via Sparse Representation and Low-Rank Constraint," IEEE Transactions on Geoscience and Remote Sensing, vol. 53, no. 1, pp. 296-308, Jan 2015.

[18] S. Jia, X. Zhang, and Q. Li, "Spectral-Spatial Hyperspectral Image Classificatin Using $l_{1/2}$ Regularized Low-Rank Representation and Sparse Representation-Based Graph Cuts," IEEE Journal of Selected Topics in Applied Earth Observations and Remote Sensing, vol. 8, no. 6, pp. 2473-2484, Jun 2015.

[19] Y. Peng, A. Ganesh, J. Wright, W. Xu, and Y. Ma, "RASL: Robust Alignment by Sparse and Low-Rank Decomposition for Linearly Correlated Images," IEEE Transactions on Pattern Analysis and Machine Intelligence, vol. 34, no. 11, pp. 2233-2246, Nov 2012.

[20] C. Dang and H. Radha, “RPCA-KFE: Key Frame Extraction for Video Using Robust Principal Component Analysis,” IEEE Transactions on Image Processing, vol. 24, no. 11, pp. 3742-3753, Nov 2015.

[21] E. Amaldi and V. Kann, “On the approximability of minimizaing nonzero variables or unsatisfied relations in linear systems,” Theoretical Computer Science, vol. 209, no. 1-2, pp. 237-260, Dec 1998.

[22] S.R. Becker, E.J. Candes, and M.C. Grant, “Templates for convex cone problems with applications to sparse signal recovery,” Mathematical Programming Computation, vol. 3, no. 3, pp. 165-218, Sep 2011.

[23] A. Giannopoulos, “Modeling ground penetrating radar by GprMax,” Construction and Building Materials, vol. 19, no. 10, pp. 755-762, 2005.

CHAPTER 3: AIR COUPLED GROUND PENETRATING RADAR CLUTTER MITIGATION FOR ROUGH SURFACE SENSING

Abstract

Ground penetrating radar (GPR) is a non-destructive evaluation technique specifically effective for detecting buried objects. Due to the signal propagation loss, the scattering from buried objects is much weaker than the clutter signal produced by the ground surface. To extract the weak scattering from the subsurface object, removal of the strong ground surface clutter is an issue of predominance. This chapter explores a low-rank and sparse representation based signal decomposition technique to remove the clutter produced by rough ground surface for air-coupled GPR, where the time instance and the amplitude of surface clutter components in each A-Scan trace vary. The performance of the proposed clutter removal method is evaluated through simulations and laboratory experiments.

Keywords: ground penetrating radar, clutter removal, low-rank representation, sparse representation, cross-correlation, non-destructive evaluation.

3.1. Introduction

GPR is a non-destructive evaluation technique specifically effective for detecting buried objects [2]-[5]. Based on antenna configurations, GPR system can be typically classified as ground-coupled GPR and air-coupled GPR. Comparing with the ground-coupled GPR system, the air-coupled GPR sensing provides the benefit of high survey speed due to the large standoff distance between the antennas and the ground surface. Whereas the large standoff distance leads to significant propagation losses [1], the reflection signal amplitude from the subsurface object is greatly reduced. In order to extract the weak scattering from the subsurface object, removal of the strong ground surface clutter is an issue of predominance for air-coupled GPR signal processing.

Many clutter removal methods have been investigated in the literature, which generally deal with relatively flat ground surfaces. These methods include average subtraction [7], spatial filtering [8]-[9], etc. Assuming the clutter in each A-Scan shows high similarity, the average subtraction method calculates the average of different A-Scan traces as the background signal, which is then subtracted from each A-Scan to remove the clutter while enhance the target scattering signal. Spatial filtering method utilizes the same assumption to filter out the clutter data corresponding to the ground surface reflection. Considering the reflection signal from the buried object with limited spatial extent varies in different A-scan traces, a spatial filter is thus applied along the antenna moving direction to mitigate the spatial zero-frequency and low-frequency components corresponding to clutter. When the ground surface conditions are complicatedly rough, the effectiveness of average subtraction and spatial filtering clutter removal algorithms is degraded. Some other clutter removal methods can deal with rough ground surfaces, such as subspace projection approach [5], principal component analysis (PCA) [11], independent component analysis (ICA) [12], time gating [13], etc. The subspace projection approach is based on the reflection energy difference between the ground surface and the buried object. Singular value decomposition (SVD) is performed on the data matrix to identify and remove the ground surface electromagnetic signature. Unfortunately, it is infeasible to determine an appropriate threshold value for the subspace projection when no prior-knowledge about the underground structure is available. PCA and ICA methods also decompose the GPR data into subspace components, and then select a subset of components containing buried object information. However, the components selection process is performed with intensive human interventions. In the time gating method, a windowing function is defined to null the signal segments over the time intervals where different signal traces exhibit a high similarity, which facilitates clutter signal removal. However, the accuracy of time gating method is low when the target is shallowly buried where the ground clutter and target scattering overlap.

To tackle such problems, in this chapter, a low-rank and sparse representation based signal decomposition technique is explored to remove the clutter produced by rough ground surface reflection. The low-rank and sparse representation method has been proved to be effective in modeling the ground clutter data in GPR B-Scan images [14]-[18]. Those methods assume the clutter components in A-Scan signals are at the same depth level. In other words, they only deal with relatively flat ground surface. For rough or non-flat ground surface, the surface clutter components in different A-Scan traces are not aligned on the depth axis. To compensate for the misalignments so as to facilitate the clutter removal, in this chapter, the A-Scan traces in a GPR data matrix are aligned using cross-correlation method. The low-rank and sparse representation technique is then developed to decompose the aligned GPR data matrix into two sub-matrices: a low-rank matrix whose column data record the ground clutter in A-Scan traces, and a sparse matrix that features the subsurface object. This chapter is an extension of the work presented in a previous SPIE conference [19], where the preliminary study was performed. In this chapter, a Renyi entropy based analysis is developed to fine tune the clutter removal. More quantitative analysis on the methodology and experimental results are also conducted. Simulations and actual lab measurements are performed to evaluate the effectiveness of the proposed method.

The rest sections of the chapter are organized as followings. Sec. 3.2 models the clutter on rough ground surface as a low-rank and sparse representation problem, and Sec. 3.3 describes the proposed clutter removal methodology. In Sec. 3.4, the effectiveness of the proposed method is evaluated using finite-difference time-domain (FDTD) simulation and real lab experiments. Sec. 3.5 summarizes the concluding remarks.

3.2. GPR B-Scan Image Model

In GPR survey, the signal collected at the n^{th} observation position can be modeled as

$$d_n(t) = l_n(t) + s_n(t) \tag{3.1}$$

where $d_n(t)$ is the received A-Scan signal, $l_n(t)$ is the clutter due to ground surface reflection, and $s_n(t)$ is the reflection signal from the buried target.

For GPR imaging, $d_n(t)$, $l_n(t)$ and $s_n(t)$ are recorded as $M \times 1$ vectors $\boldsymbol{d_n}$, $\boldsymbol{l_n}$, and $\boldsymbol{s_n}$ respectively. M is the number of samples collected at each scan position. Assembling the data of all N scan positions leads to the following $M \times N$ data matrices:

$$\boldsymbol{D} = [\boldsymbol{d_1}, \boldsymbol{d_2}, \boldsymbol{d_3}, \dots, \boldsymbol{d_N}] \tag{3.2}$$

$$\boldsymbol{L} = [\boldsymbol{l_1}, \boldsymbol{l_2}, \boldsymbol{l_3}, \dots, \boldsymbol{l_N}] \tag{3.3}$$

$$\boldsymbol{S} = [\boldsymbol{s_1}, \boldsymbol{s_2}, \boldsymbol{s_3}, \dots, \boldsymbol{s_N}] \tag{3.4}$$

In Eq. (3.2) – Eq. (3.4), $\boldsymbol{D} \in \mathbb{R}^{M \times N}$ is the observed GPR B-Scan image data matrix, $\boldsymbol{L} \in \mathbb{R}^{M \times N}$ is the data matrix featuring the ground clutter, and $\boldsymbol{S} \in \mathbb{R}^{M \times N}$ is the data matrix featuring the buried target, where M represents the number of data points in each A-Scan trace, and N represents the total number of A-Scan traces. According to Eq. (3.1), it has

$$\boldsymbol{D} = \boldsymbol{L} + \boldsymbol{S} \tag{3.5}$$

For rough or non-flat ground surface, the surface clutter components $\boldsymbol{l_1}, \boldsymbol{l_2}, \boldsymbol{l_3}, \dots, \boldsymbol{l_N}$ in different A-Scan traces $\boldsymbol{d_1}, \boldsymbol{d_2}, \boldsymbol{d_3}, \dots, \boldsymbol{d_N}$ are not aligned on the depth axis. To compensate for these misalignments so as to facilitate clutter removal, the cross-correlation technique is applied.

The first A-Scan signal $d_1(t)$ is selected as the reference trace, and the cross-correlation between $d_1(t)$ and $d_n(t)$ is calculated to specify the time offset between the ground reflection of $d_n(t)$ and $d_1(t)$ on the depth axis [20]. Assuming the optimal time offset computed from the cross-correlation analysis is Δt_n, the alignment operation on the n^{th} A-Scan trace can be defined as

$$d_n'(t) = d_n(t - \Delta t_n) \tag{3.6}$$

Substituting Eq. (3.6) into the signal model in Eq. (3.1), the resulting signal model upon alignment can be expressed as

$$d_n'(t) = l_n'(t) + s_n'(t) \tag{3.7}$$

In this transformed model, $l_n'(t)$ is the clutter signal upon alignment adjustment, and $s_n'(t)$ is the target scattering upon alignment adjustment. Since the alignment adjustment is a linear operation, the following relation between $s_n(t)$ and $s_n'(t)$ exists:

$$s_n'(t) = s_n(t - \Delta t_n) \quad (3.8)$$

In this chapter, the low-rank and sparse representation technique is utilized to separate the correlated background clutter $l_n'(t)$ and the target signature $s_n'(t)$.

Upon the alignment adjustment, the corresponding GPR B-Scan image model in Eq. (3.5) can be expressed as

$$\boldsymbol{D}' = \boldsymbol{L}' + \boldsymbol{S}' \quad (3.9)$$

Since each column of $\boldsymbol{L}'$ is the ground clutter upon alignment adjustment, the rank of matrix $\boldsymbol{L}'$ is low. For the buried small and spatially sparse targets, it results in $\boldsymbol{S}'$ being a sparse matrix.

3.3. Low-Rank and Sparse Decomposition Based Clutter Removal

The low-rank and sparse representation [21] interprets the data matrix $\boldsymbol{D}'$ as a superposition of a low-rank matrix $\widehat{\boldsymbol{L}'} \in \mathbb{R}^{M \times N}$ and a sparse matrix $\widehat{\boldsymbol{S}'} \in \mathbb{R}^{M \times N}$, where $\widehat{\boldsymbol{L}'}$ represents the correlated clutter, while $\widehat{\boldsymbol{S}'}$ models the target features on top of the correlated clutter. The mathematical expression is $\boldsymbol{D}' = \widehat{\boldsymbol{L}'} + \widehat{\boldsymbol{S}'}$.

Decomposing the data matrix $\boldsymbol{D}'$ into $\widehat{\boldsymbol{L}'}$ and $\widehat{\boldsymbol{S}'}$ is an optimization problem. Through Lagrangian reformulation, it can be expressed as:

$$\min_{L,S} rank\left(\widehat{\boldsymbol{L}'}\right) + \lambda \left\|\widehat{\boldsymbol{S}'}\right\|_0 \quad s.t. \;\; \boldsymbol{D}' = \widehat{\boldsymbol{L}'} + \widehat{\boldsymbol{S}'} \quad (3.10)$$

Unfortunately, Eq. (3.10) is a highly nonconvex optimization problem subsuming both the low rank matrix completion and the l^0-minimization, which are both NP-hard. By replacing l^0-norm with l^1-norm, and the rank of L with the nuclear norm $\|L\|_* = \sum_i \sigma_i(L)$, a tractable optimization problem can be obtained [21]:

$$\min_{L,S} \left\|\widehat{\boldsymbol{L}'}\right\|_* + \lambda \left\|\widehat{\boldsymbol{S}'}\right\|_1 \quad s.t. \;\; \boldsymbol{D}' = \widehat{\boldsymbol{L}'} + \widehat{\boldsymbol{S}'} \quad (3.11)$$

where $\|\widehat{\boldsymbol{L}'}\|_*$ is the nuclear norm or sum of singular values of matrix $\widehat{\boldsymbol{L}'}$, $\|\widehat{\boldsymbol{S}'}\|_1$ is the l^1-norm or sum of absolute values of the entries of $\widehat{\boldsymbol{S}'}$, and λ is a tuning parameter that balances the contribution of the l^1-norm term relative to the nuclear norm term. Choice of $\lambda = 1/\sqrt{\max(M,N)}$ is universal for solving the optimization problem in Eq. (3.11).

According to Ref. [22], in the general rectangular case, where $M \geq N$, if

$$rank(\boldsymbol{L}') \leq \rho_r \frac{N}{(\log M)^2} \tag{3.12}$$

and

$$\|\boldsymbol{S}'\|_0 \leq 0.1 * MN \tag{3.13}$$

matrix $\boldsymbol{L}'$ and $\boldsymbol{S}'$ can be uniquely reconstructed by solving Eq. (3.11), which means $\boldsymbol{L}' = \widehat{\boldsymbol{L}'}$ and $\boldsymbol{S}' = \widehat{\boldsymbol{S}'}$. In Eq. (3.12), ρ_r is a positive constant coefficient, which means the rank of $\boldsymbol{L}'$ is of the order of $\frac{N}{(\log M)^2}$.

Upon the decomposition, the matrix $\boldsymbol{L}'$ contains the clutter and some subsurface background information. The subsurface background information are of interest for GPR applications, such as pavement subsurface characterization [2],[23], layer thickness measurement [24]-[25], subsurface dielectric property analysis [26], soil moisture estimation [27], etc. Since the proposed clutter removal method only aims to eliminate the clutter produced by the ground surface, the subsurface background information can be preserved and extracted in conjunction with the sparse target matrix $\boldsymbol{S}'$.

A Renyi entropy-based time gating method [5],[13],[28] is applied to extract the ground surface clutter components in the matrix $\boldsymbol{L}'$. In the low-rank matrix $\boldsymbol{L}'$, the signal envelope along the range direction is calculated with the Hilbert Transform and the produced envelope matrix is denoted as L_e. The data in L_e are normalized alone the radar cross-range direction (or the GPR scanning direction) as:

$$\tilde{L}_e(m,n) = \frac{|L_e(m,n)|^2}{\sum_{n=1}^{N}|L_e(m,n)|^2} \tag{3.14}$$

Upon the normalization, the Renyi's entropy [29] along the radar cross-range direction is calculated as:

$$E_\alpha(m) = \frac{1}{1-\alpha}\log_e\left(\sum_{n=1}^{N}\tilde{L}_e(m,n)^\alpha\right) \tag{3.15}$$

where $E_\alpha(m)$ is the entropy quantification and α is the entropy order. According to the experiments and analysis in Ref. [5], $\alpha = 3$ is the optimal configuration for GPR applications. As the ground surface clutter signal components have similar shapes, they result in large values of $E_\alpha(m)$ [13],[28]. Therefore, a windowing along the range direction that marks the ground surface clutter signals region can be determined as [28]:

$$W(m,n) = \begin{cases} 0, & if\ E_\alpha(m) \geq \beta \log_e N \\ 1, & elsewhere \end{cases} \tag{3.16}$$

β is the tuning parameter that accounts for the measurement noise in the GPR signal, which is optimized at $\beta = 0.97$ for radar applications according to the analysis in Ref. [28]. Denoting the window function $W(m)$ ranges between time instance 0 and t_d, based on the entropy analysis, the signals of time instances within 0 and t_d are considered as the ground surface clutter signals, whose values are set as zero, and the resulting matrix is recorded as $\boldsymbol{L}'_{\boldsymbol{sub}}$:

$$\boldsymbol{L}'_{\boldsymbol{sub}}(m) = \boldsymbol{L}'(m,n)W(m,n) \tag{3.17}$$

In this way, the nulling is only performed on matrix $\boldsymbol{L}'$ featuring the clutter signal, while the matrix $\boldsymbol{S}'$ featuring the buried object scattering is preserved. Comparing to traditional time gating [13] method that nulls the whole data matrix $\boldsymbol{D}'$, the proposed method does not smear the scattering data of the buried object when the object is close to the ground surface.

The overall subsurface data matrix can be expressed as:

$$\boldsymbol{S}'_{proc} = \boldsymbol{S}' + \boldsymbol{L}'_{sub} \tag{3.18}$$

Once matrix $\boldsymbol{S}'_{proc}$ is obtained, the matrix of the original object matrix$\boldsymbol{S}$ can be reconstructed by reversing the alignment adjustment process using the time offset value obtained with Eq. (3.8).

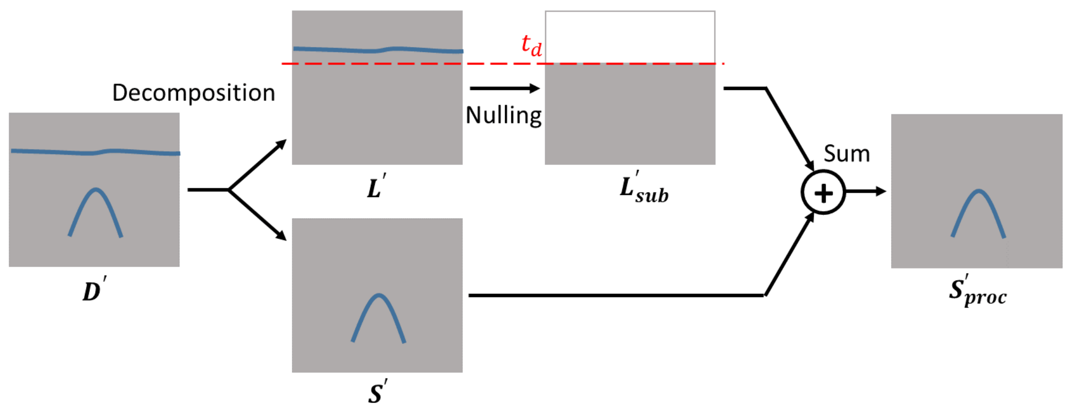

Figure 3.1: Ground clutter removal process

Finally, the clutter removal procedures for rough ground surface are summarized below:

1. Alignment: Align each A-Scan trace in the B-Scan image $\boldsymbol{D}$ using cross-correlation criterion to obtain a processed B-Scan image $\boldsymbol{D}'$.

2. Decompose the processed GPR B-Scan data matrix $\boldsymbol{D}' \in \mathbb{R}^{M\times N}$ into a low-rank matrix $\boldsymbol{L}' \in \mathbb{R}^{M\times N}$ and a sparse matrix $\boldsymbol{S}' \in \mathbb{R}^{M\times N}$ by solving Eq. (3.11) with tuning parameter $\lambda = 1/\sqrt{\max(M,N)}$.
3. Calculate the envelope of the signal in matrix $\boldsymbol{L}'$ along the range direction. Determine and null the clutter region whose depth is above t_d based on Renyi entropy analysis to obtain matrix $\boldsymbol{L}'_{\boldsymbol{sub}}$ as illustrated in Figure 3.1.
4. Compensate the subsurface medium information in matrix $\boldsymbol{L}'_{\boldsymbol{sub}}$ to the sparse matrix $\boldsymbol{S}'$ following Eq. (3.18).
5. Revere time alignment adjustment of the sparse matrix $\boldsymbol{S}'_{\boldsymbol{proc}}$ to reproduce the buried target features in the B-Scan image.

3.4. Experimental results

To evaluate the proposed clutter removal method for rough ground surface inspection, experiments are conducted with two sets of test data. The first set of data is synthesized with the GPR simulation tool GprMax [30] while the second one is the laboratory experimental data collected using a step-frequency continuous wave radar (SFCW) system. The optimization problem in Eq. (3.11) is solved utilizing the mathematical toolbox TFOCS [31].

3.4.1. Simulation Data 1: Oblique Ground Surface

In this section, two sets of simulation data are created using GprMax program. In the first simulation setup: the ground is modeled as a homogeneous layer with oblique surface whose dielectric constant is 6.0. The slope of the oblique surface is 5°. The buried target is modeled as a cylinder of 1.25 cm radius with 4.0 dielectric constant. The test geometry detail for this test case is depicted in Figure 3.2(a). The GprMax program is developed with FDTD technique. In our simulation, the GPR waveform is generated as a Ricker waveform (i.e. negative normalized second derivative of a Gaussian pulse) with its center frequency being 900 MHz. GPR A-Scan traces are collected uniformly from left to right along the horizontal direction every 2 cm distance in air-coupled mode. The standoff distance between the transceiver antennas and the ground surface is 30 cm. The separation distance between the transmitter antenna and the receiver antenna is 2.5 cm. The size of the data matrix is 962×46.

The raw GPR B-scan image is plotted in Figure 3.2(b), in which the strongest reflection between 0.5 ns and 1.3 ns time interval is the clutter due to the ground surface reflection, and the weak hyperbolic curve at 2.5 ns is the reflection signal from the buried target. Correspondingly, some A-Scan traces selected at different scan positions from the B-Scan image are plotted in Figure 3.3. As shown, the strongest peak in each A-Scan trace is the ground surface clutter, whose time index shifts among different traces. For these misaligned ground surface clutter signals in A-Scan traces, they cannot be eliminated using traditional clutter removal method, i.e. average subtraction [7]. Figure 3.2(c) shows the average subtraction method fails to improve the target feature in the B-Scan image.

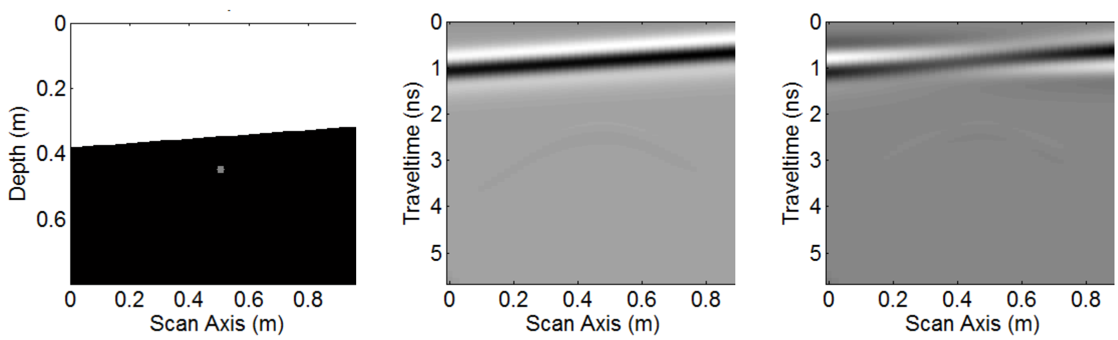

(a) (b) (c)

Figure 3.2: Synthetized oblique ground surface: (a) Geometry data; (b) Raw B-scan image; (c) Average subtraction from raw B-Scan.

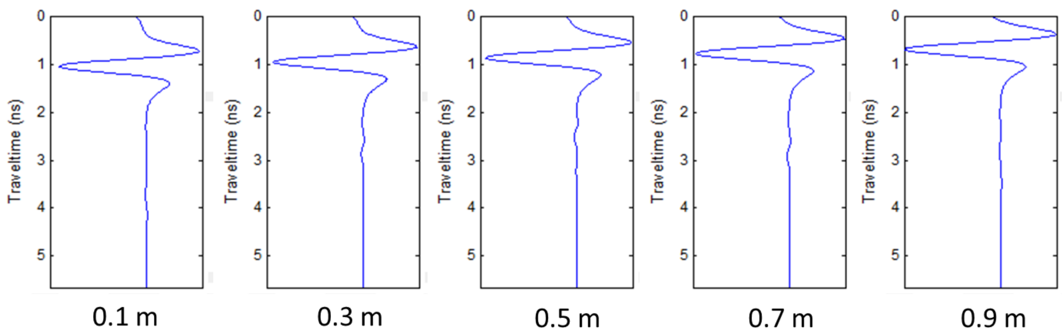

Figure 3.3: Synthesized oblique ground surface: A-Scan trace at various locations along scan axis.

By applying the alignment adjustment, the resulting GPR B-Scan image is plotted in Figure 3.4(a). Figure 3.4(b) and (c) depict the processed B-Scan images upon average subtraction and the proposed clutter removal to the aligned B-Scan image respectively. As shown in Figure 3.4(b), the average subtraction can enhance the target features, however, the residual clutter still exists around time instance 1 ns. Since the alignment is performed on the digitized data, the finest time resolution for adjustment equals the sampling time interval of the data acquisition unit (or analog-to-digital converter), which is $\Delta t = 6$ ps in this simulation test case. As the radar clutter is produced from the ground surface reflection and the radar wave propagation velocity is $c = 3 \times 10^8$ m/s in the air, the achievable depth resolution for alignment is $\Delta d = (\Delta t/2) * c = 0.9$ mm. In other words, the alignment algorithm cannot fix the depth displacement smaller than 0.9 mm.

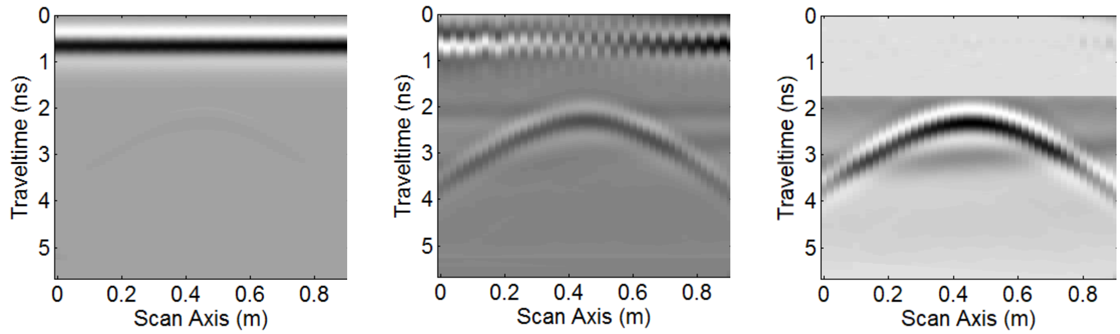

(a) (b) (c)

Figure 3.4: Synthetic oblique ground surface: (a) Aligned B-Scan; (b) Clutter removal using average subtraction; (c) Clutter removal using proposed method.

With our proposed clutter removal method, the smaller-than-resolution displacement can be processed as a low rank component within the data matrix, which can be separated and removed from the reflection signals of the underground target. Figure 3.4(c) illustrates the B-scan image upon clutter removal. As can be observed, the hyperbolic pattern corresponding to the burying cylinder is much more pronounced.

3.4.2. Simulation Data 2: Rough Ground Surface

In the second simulation setup, the ground is modeled as a homogeneous layer with wiggly surface. The heights of the wiggles vary randomly between 3 cm and 7 cm. The layer's dielectric constant is 6.0. The buried target is a reinforce bar of 2.5 cm radius and its burying depth is 10 cm. The test geometry for this test case is depicted in Figure

3.5(a). In the FDTD simulation, the same GPR waveform and scan along the horizontal direction as Simulation 1 are utilized. The data matrix dimension is 972×46.

The raw GPR B-scan image obtained is plotted in Figure 3.5(b), in which the strongest reflections between 0.5 ns and 1.2 ns time interval are the ground surface clutter, and the weak hyperbolic curve at 2 ns features the reflection signal from the buried rebar. Selected A-Scan traces at different scan locations are plotted in Figure 3.6. The foremost strong pulse in each A-Scan trace is the ground surface clutter with varying amplitude and position. Without alignment adjustment, it is infeasible to suppress such ground surface clutter. For instance, the clutter removal result with the traditional average subtraction [7] method is depicted in Figure 3.5(c). As can be observed, the hyperbolic feature is enhanced, however the clutter components remain between 1 ns and 2 ns time interval.

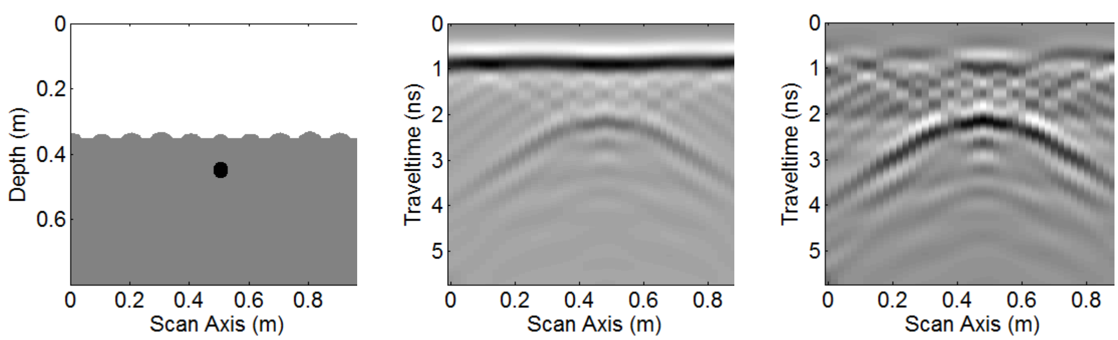

(a) (b) (c)

Figure 3.5: Synthetic rough ground surface: (a) Geometry data; (b) Raw B-scan image; (c) Average subtraction from raw B-Scan.

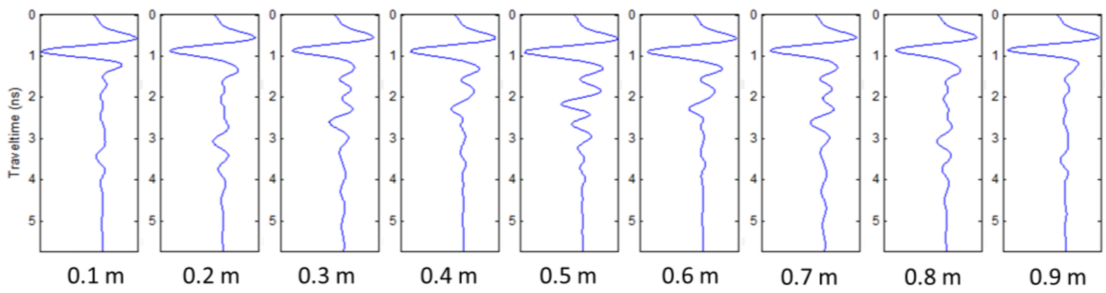

Figure 3.6: Synthesized rough ground surface: A-Scan trace at various locations along scan axis.

After the alignment adjustment, the resulting GPR B-Scan image is plotted in Figure 3.7(a). Figure 3.7(b) and (c) illustrate the processed B-Scan images upon average subtraction and proposed clutter removal. As shown in Figure 3.7(b), the average subtraction improves the target features, however is not able to remove the clutter. After applying the proposed clutter removal method, as shown in Figure 3.7(c), the hyperbolic pattern is enhanced and the clutter is largely eliminated.

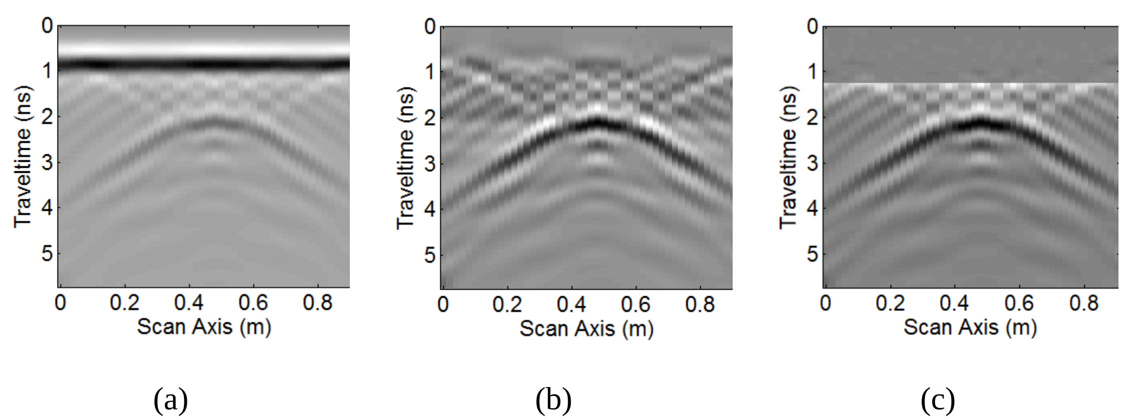

Figure 3.7: Synthetic rough ground surface: (a) Aligned B-Scan; (b) Clutter removal using average subtraction; (c) Clutter removal using the proposed method.

3.4.3. Experiment with Lab Test Data

The proposed clutter removal method is also evaluated using real experimental data collected via a step-frequency continuous wave GPR system. In this GPR system, the transmitter and data acquisition unit employed is Keysight N9917A FieldFox Microwave Analyzer whose operating frequency spans from 30 kHz to 18 GHz. The transceiver antennas are a pair of customized horn antennas [32] whose bandwidth spans from 600 MHz to 6 GHz. The test setup is depicted in Figure 3.8(a). A metal plate is buried in a sandbox as the target under test. The metal plate is 0.64 cm thick, 30.5 cm long, 20.3 cm wide and is buried 8 cm deep. Water is sprayed on sand surface to emulate moisture in real field GPR test scenario. The transmitter and receiver antennas are set 71 cm above the sand surface. The angle of incidence and angle of reflection are both 45 degree. The scan is performed along the longitudinal direction. The dimension of GPR data matrix is 400×152.

The raw GPR B-scan image is plotted in Figure 3.8(b), in which the strongest reflection at 0.45 ns is the sand surface clutter, and the hyperbolic feature at 1 ns is the reflection from the buried plate. Figure 3.8(c) shows the clutter removal result using traditional average subtraction [7] method, which even makes the target feature worse in the B-Scan image.

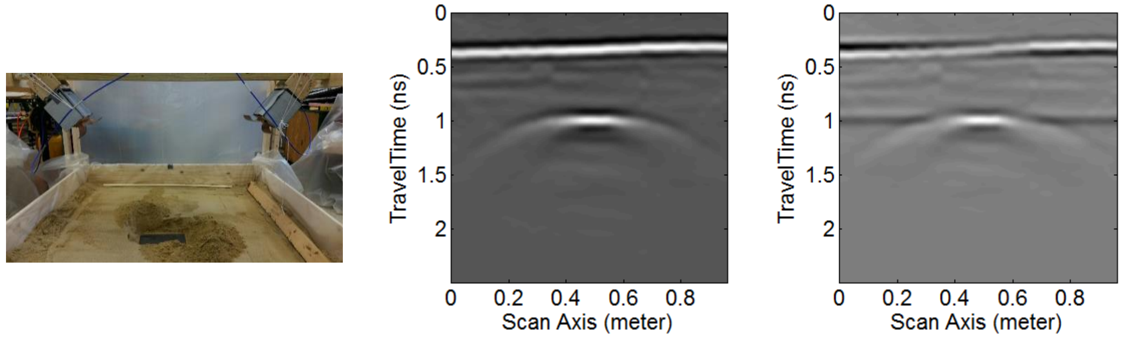

(a) (b) (c)

Figure 3.8: Lab sandbox test: (a) Geometry data; (b) Raw B-scan image; (c) Average subtraction from raw B-Scan.

Upon the alignment, the resulting GPR B-Scan image is plotted in Figure 3.9(a). Figure 3.9(b) shows the processed B-Scan image with average subtraction, where the sand surface clutter is removed, whereas additional clutter is induced around 1 ns depth as the dark horizontal line. Figure 3.9(c) shows the processed B-Scan using the proposed clutter removal method. Comparing to the average subtraction method, the proposed method can suppress the sand surface clutter while not produce any fake scattering features.

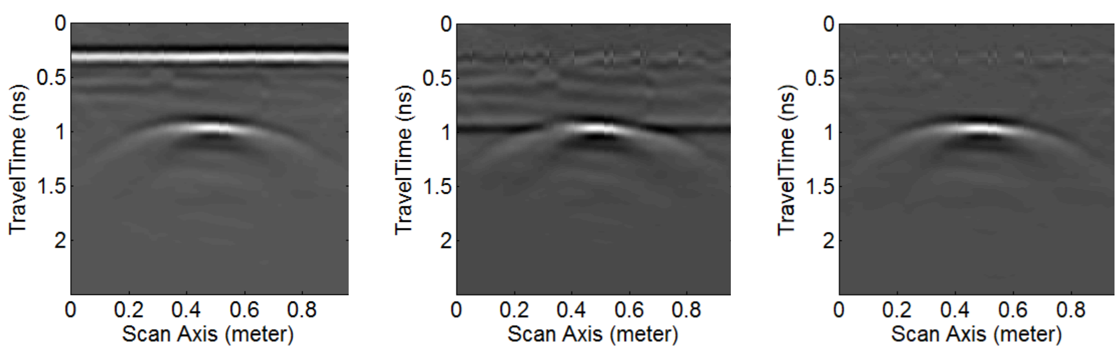

(a) (b) (c)

Figure 3.9: Lab sandbox test: (a) Aligned B-Scan; (b) Clutter removal using average subtraction; (c) Clutter removal using the proposed method.

3.4.4. Quantitative Analysis on the Processed Data

To quantitatively evaluate the clutter removal method performance, signal-to-clutter ratio (SCR) is used as a metric for characterizing the power ratio between the backscattering signal from the buried object under test and the clutter in each test case. The SCR of raw B-Scan images, the processed B-Scan image using average subtraction and the processed B-Scan image using the proposed clutter removal are calculated for all three test cases. The SCR calculation results are summarized in Table 3.1. The quantitative analysis results indicate that the proposed clutter removal method can dramatically enhance the buried object features in GPR B-Scan image, and outperforms the traditional average subtraction method.

Table 3.1: SCR of each B-Scan Image.

Test Case	SCR of Raw B-Scan (dB)	SCR of Processed B-Scan using Average Subtraction (dB)	SCR of Processed B-Scan using Proposed Method (dB)
Simulation Data 1	-22.86	6.23	14.86
Simulation Data 2	-3.75	8.75	14.58
Lab Experiment Data	2.60	7.85	23.08

3.5. Conclusions

In this chapter, a low-rank and sparse representation based clutter removal technique has been investigated. In the observed data matrix upon alignment, the clutter component produced by the rough ground surface are modeled as a low-rank matrix, and the scattering from the buried objects are modeled as a sparse matrix. The convex optimization is applied to decompose the observed data matrix into the low-rank matrix and the sparse matrix, to extract the weak scattering features from the strong clutter signal. Since the proposed method characterizes the rank of the clutter components in the data matrix instead of merely the amplitude of the clutter signal, the proposed clutter removal method can effectively suppress the clutter generated by rough ground surface in GPR field inspection. Experiments with the simulation data and lab testing data are conducted for performance validation. In the first simulation test, the proposed clutter removal method improves SCR by 37.72 dB. In the second simulation test, the proposed method improves SCR by 18.33 dB. For the lab experimental data, 20.48 dB SCR improvement is achieved.

3.6. References

[1] A. S. Venkatachalam, X. Xu, D. Huston, and T. Xia, "Development of a New High Speed Dual-Channel Impulse Ground Penetrating Radar," *IEEE Journal of Selected Topics in Applied Earth Observations and Remote Sensing* 7(3), 753-760 (2014).

[2] H. Liu, R. Birken, and M. L. Wang, "Automatic pavement layer identification with multichannel ground penetrating radar at traffic speed," *Journal of Applied Remote Sensing* 10(4), 046023 (2016).

[3] Y. Zhang, D. Burns, D. Huston, and T. Xia, "Sand moisture assessment using instantaneous phase information in ground penetrating radar data," *Proc. SPIE* 9437, 943726 (2015).

[4] H. Zhang, S. Ouyang, G. Wang, S. Wu, and F. Zhang, “Matched filtering algorithm based on phase-shifting pursuit for ground-penetrating radar signal enhancement,” *Journal of Applied Remote Sensing* 8(1), 083593 (2014).

[5] Y. Zhang, P. Candra, G. Wang, and T. Xia, “2-D entropy and short-time Fourier transform to leverage GPR data analysis efficiency,” *IEEE Transactions on Instrumentation and Measurement* 64(1), 103-111 (2015).

[6] H. M. Jol, *Ground Penetrating Radar Theory and Applications*, Elsevier (2008).

[7] G. R. Olhoeft, “Maximizing the information return from ground penetrating radar,” *Journal of Applied Geophysics* 43(2), 175-187 (2000).

[8] D. Potin, E. Duflos, and P. Vanheeghe, “Landmines Ground-Penetrating Radar Signal Enhancement by Digital Filtering,” *IEEE Transactions on Geoscience and Remote Sensing* 44(9), 2393-2406 (2006).

[9] Y. Zhang, A. S. Venkatachalam, D. Huston, and T. Xia, “Advanced signal processing method for ground penetrating radar feature detection and enhancement,” *Proc. SPIE* 9063, 906318 (2014).

[10] F. H. C. Tivive, A. Bouzerdoum, and M. G. Amin, “A Subspace Projection Approach for Wall Clutter Mitigation in Through-the-Wall Radar Imaging,” *IEEE Transactions on Geoscience and Remote Sensing* 53(4), 2108-2122 (2015).

[11] P. K. Verma, A. N. Gaikwad, D. Singh, and M. J. Nigam, “Analysis of clutter reduction techniques for through wall imaging in UWB range,” *Progress In Electromagnetics Research B* 17, 29-48 (2009).

[12] B. Karlsen, H. B. Sorensen, J. Larsen, and K. B. Jakobsen, “Independent component analysis for clutter reduction in ground penetrating radar data,” *Proc. SPIE* 4742, 378-389 (2002) [doi: 10.1117/12.479110].

[13] R. Solimene, and A. Cuccaro, “Front Wall Clutter Rejection Methods in TWI,” *IEEE Geoscience and Remote Sensing Letters* 11(6), 1158-1162 (2014).

[14] Y. Zhang, and T. Xia, “In-Wall Clutter Suppression based on Low-Rank and Sparse Representation for Through-the-Wall Radar,” *IEEE Geoscience and Remote Sensing Letters* 13(5), 671-675 (2016).

[15] Y. Zhang, and T. Xia, “Extracting sparse crack features from correlated background in ground penetrating radar concrete imaging using robust principal component analysis technique,” *Proc. SPIE* 9804, 980402 (2016).

[16] D. Kalika, M. T. Knox, L. M. Collins, P. A. Torrione, and D. Morton, “Leveraging robust principal component analysis to detect buried explosive threats in handheld ground-penetrating radar data,” *Proc. SPIE* 9454, 94541D (2015).

[17] A. Bouzerdoum, F. H. C. Tivive, and C. Abeynayake, “Target detection in GPR data using joint low-rank and sparsity constraints,” *Proc. SPIE* 9857, 98570A (2016).

[18] M. P. Masarik, J. Burns, B. T. Thelen, J. Kelly, T. C. Havens, “GPR anomaly detection with robust principal component analysis,” *Proc. SPIE* 9454, 945414 (2015).

[19] Y. Zhang, D. Burns, D. Orfeo, D. R. Huston, and T. Xia, "Rough ground surface clutter removal in air-coupled ground penetrating rdar data using low-rank and sparse representation," *SPIE Smart Structures/NDE 2017,* (2017).

[20] Y. Zhang, A. S. Venkatachalam, and T. Xia, "Ground-penetrating radar railroad ballast inspection with an unsupervised algorithm to boost the region of interest detection efficiency," *Journal of Applied Remote Sensing* 9(1), 095058 (2015).

[21] E. J. Candes, X. Li, Y. Ma, and J. Wright, "Robust Principal Component Analysis?," *Journal of the ACM* 58(3), 1-37 (2011).

[22] J. Wright, Y. Peng, Y. Ma, A. Ganesh, and S. Rao, "Robust Principal Component Analysis: Exact Recovery of Corrupted Low-Rank Matrices by Convex Optimization," *Advances in Neural Information Processing Systems* 22, 2080-2088 (2009).

[23] A. Loizos, and C. Plati, "Accuracy of Ground Penetrating Radar Horn-Antenna Technique for Sensing Pavement Subsurface," *IEEE Sensors Journal* 7(5), 842-850 (2007).

[24] I. Al-Qadi, S. Lahouar, K. Jiang, K. McGhee, D. Mokarem, "Accuracy of Ground-Penetrating Radar for Estimating Rigid and Flexible Pavement Layer Thicknesses," *Transportation Research Record: Journal of the Transportation Research Board* 1940, 69-78 (2005).

[25] D. A. Willett, K. C. Mahboub, and B. Rister, "Accuracy of Ground-Penetrating Radar for Pavement-Layer Thickness Analysis," *Journal of Transportation Engineering* 132(1), 96-103 (2006).

[26] S. Lambot, E. C. Slob, I. V. D. Bosch, B. Stockbroeckx, and M. Vanclooster, "Modeling of ground-penetrating radar for accurate characterization of subsurface electric properties," *IEEE Transactions on Geoscience and Remote Sensing* 42(11), 2555-2568 (2004).

[27] I. A. Lunt, S. S. Hubbard, and Y. Rubin, "Soil moisture content estimation using ground-penetrating radar reflection data," *Journal of Hydrology* 307(1-4), 254-269 (2005).

[28] R. Solimene, and A. D'Alterio, "Entropy-based clutter rejection for intrawall diagnostics," International Journal of Geophysics, 2012, (2012).

[29] R. G. Baraniuk, P. Flandrin, A. J. E. M. Janssen, and O. Michel, "Measuring time-frequency information content using the Renyi entropies," IEEE Transactions on Information Theory 47(4), 1391–1409 (2001).

[30] A. Giannopoulos, "Modeling ground penetrating radar by GprMax," *Construction and Building Materials* 19(10), 755-762 (2005).

[31] S. R. Becker, E. J. Candes, and M. C. Grant, "Templates for convex cone problems with applications to sparse signal recovery," *Mathematical Programming Computation* 3(3), 165-218 (2011) [doi: 10.1007/s12532-011-0029-5].

[32] A. Ahmed, Y. Zhang, D. Burns, D. Huston, and T. Xia, "Design of UWB Antenna for Air-Coupled Impulse Ground-Penetrating Radar," IEEE Geoscience and Remote Sensing Letters 13(1), 92-96 (2015).

CHAPTER 4: 2-D ENTROPY AND SHORT-TIME FOURIER TRANSFORM TO LEVERAGE GPR DATA ANALYSIS EFFICIENCY

Abstract

Accurate detection of singular region using Ground Penetrating Radar (GPR) is very useful in assessing roadway pavement, bridge deck concrete structure and railroad ballast conditions. To locate object within the large radargram, it involves extensive computational resources and time, especially when the data of interests only possess a small portion of the whole big data set. Therefore an efficient GPR signal processing technique is highly demanded. This chapter proposes the utilization of two-dimensional (2D) entropy analysis to narrow down the data scope to the interested regions, which can considerably reduce computational cost for more sophisticated post data processing. Joint time-frequency analysis using Short Time Fourier Transform (STFT) is then performed for singular region location detection and refinement. The proposed methodology is tested with different laboratory setups. The analysis results show good agreements with physical configurations.

Keywords: Radar; Signal processing; Entropy; Radar detection; Nondestructive testing.

4.1. Introduction

Impulse Ground penetrating radar (GPR) has been proven to be an effective tool in inspecting transportation infrastructures, including bridge deck [1]-[4], highway pavement and railroad ballast [5], [6], for its ability to extract subsurface information in a nondestructive manner. For GPR, one important and challenging design factor is signal processing, whose objective is to effectively analyze and extract meaningful information, and accurately interpret the measurement results. In this chapter, a new signal processing approach is developed to leverage GPR data analysis efficiency with a specific focus on singular region detection.

For transportation infrastructure survey, detecting sporadically located singular regions, such as embedded rebars is one of the basic functions for GPR subsurface structure examination. Many data processing techniques have been developed for rebar detection. In Ref. [1], an energy function is used to model and detect rebar hyperbolic signature pattern and iterative hyperbola curve fitting is applied. Although this method is effective, the long computation time limits its applicability only to small volume radar data set. Moreover, the curve fitting method is only applicable when the characteristic pattern is pre-known, and is not valid for detecting a singular region of an arbitrary shape. In Ref. [2], an approximate linear scattering model is developed utilizing the sparse nature of scatters to reconstruct the reflection signal. The reconstruction model is a double integral, and a minimization algorithm is implemented by loops of matrix multiplication. This method can precisely locate rebar. However the processing procedures are relatively complicate. In Ref. [3]-[6], rebar GPR B-scan image signature curves are characterized through a series of image processing algorithms such as image segmentation, arc detection and curve fitting. The same processing steps are performed throughout the entire scanning data even though the interested rebar data only populate a small portion of the dataset. While such approaches are meticulous, they are both costly and time consuming. Therefore to develop a method to automate the detection of sporadically distributed singular regions of arbitrary shapes for facilitating sophisticated post-processing is highly desired.

In this chapter, two-dimensional (2D) entropy analysis algorithm is developed to effectively reduce the data scope to the singular regions within the large background. In information theory, entropy is a measure of the uncertainty associated with a random variable [7]. It has been applied in several application fields such as biomedical engineering [8], [9], speech [10], information data mining [11], front wall clutter rejection [12] and color image enhancement [13]. However to date, there has been no literature utilizing entropy analysis on GPR image for detecting the sporadically distributed features. In this chapter, 2D entropy processing algorithm is developed for object extraction from the stationary background. As a result, the distinctive areas of interests can be rapidly identified, and the size of the data for post-processing can be significantly reduced. For GPR data post-processing, one important analytical approach is spectrum characterization with Fourier transform. However the main limitation is that the signal time information is lost in transforming to the frequency domain. For a stationary signal analysis, where the processed signals do not change with time, this limitation is not an issue. While in GPR scans, the premise of stationary signal does not hold. During GPR operation, the scanning antennas move continuously, thus the subsurface features under inspection change dynamically, which lead to non-stationary reflection signals being collected. In order to obtain time and spectrum information from GPR signals, the joint time-frequency (JTF) signal decomposition is employed. JTF signal decomposition is a special form of spectral analysis that aims at precise tracking frequencies of non-stationary time-varying signals. However the application of JTF analysis for GPR signal processing is very limited. A major barrier is the computational cost associated with the large data size, typically over tens of Giga-bytes (GBs). Directly performing complicate JTF analysis on such big data set is inefficient. In this chapter, with the aid of entropy characterization to narrow down the data scope, the sophisticated JTF analysis cost is considerably reduced. In the literature, there exist a variety of JTF analysis approaches, such as Gabor, wavelet, etc. [14], [15], that can achieve high time and frequency characterization resolution and accuracy. Since singular region detection does not require extremely high characterization resolution, we choose to use the basic Short Time Fourier Transform (STFT) to fulfill the application goal, which produces marginal resolution but at a relatively lower computational cost. In this chapter, the STFT analysis is applied upon 2D entropy analysis to identify the right singular region while eliminate the false ones. Even though we use GPR rebar region detection and ballast moisture region assessment as the study cases, the proposed method can be extended and combined with other processing approaches to improve processing performance for other applications.

This chapter is an extension of the work presented in [16]. In [16], preliminary study is performed to show that entropy and STFT analysis feasibility. However there are three critical limiting factors not addressed: 1). The entropy curve obtained contains high frequency noise; 2). The determination of entropy threshold values for detecting singular regions is manual and subjective; 3). Upon 2D entropy analysis, false singular region detection might be resulted. In this chapter, solutions are developed to resolve these issues. Firstly, moving average method is applied to alleviate entropy noise and smooth out entropy curve. Secondly, OTSU's thresholding algorithm [17] is developed so that singular regions identification is automated without requiring human intervention, which makes threshold determination an objective, generic and efficient process. Thirdly, STFT analysis is performed to identify the correct singular region while eliminate the false region that are not distinguishable with entropy characterization.

The remaining sections of this chapter are organized as follows: Section 4.2 introduces data acquisition, including experimental setups and data pre-processing procedures. Section 4.3 describes in detail of two computational algorithms in use: 2D Entropy analysis and Short Time Fourier Transform. Section 4.4 shows experimental results. The concluding remarks are drawn in Section 4.5.

4.2. Data Acquisition

4.2.1. System Setup

In this chapter, the experimental data are collected with our impulse GPR system developed in [18], [19], [20] and [21]. Figure 4.1(a) illustrates the system diagram. As shown, the GPR system hardware consists of five major functional units: (1) RF transmitter; (2) Ultra-wideband antennas; (3) Data acquisition unit comprising of a high speed real time digitizer, high speed data transmission and storage unit; (4) Quard-core computer (Intel core i7 3.4 GHz) (5) FPGA digital controller along with a wheel encoder.

The RF transmitter comprises of an ultra-wide bandwidth (UWB) pulse generator that generates high amplitude (up to 18 volts) 1 ns wide Gaussian pulse (Figure 4.1b) whose pulse repetition frequency (PRF) is set to 30 KHz. The digitizer employed is a high speed real-time data acquisition unit (Agilent Acqiris U1065A module) of 8 Gsps sampling rate and 10-bit resolution operating in simultaneous multi-buffer acquisition and readout (SAR) mode. The digitizer configuration details can be found in [18], [19]. For impulse signal transmission and receiving, two identical tapered wideband horn antennas, as shown in Figure 4.1(c), are designed. The antennas' operating frequencies span from 0.6 GHz to 6 GHz and S11 measurement result is contained in Figure 4.1(d).

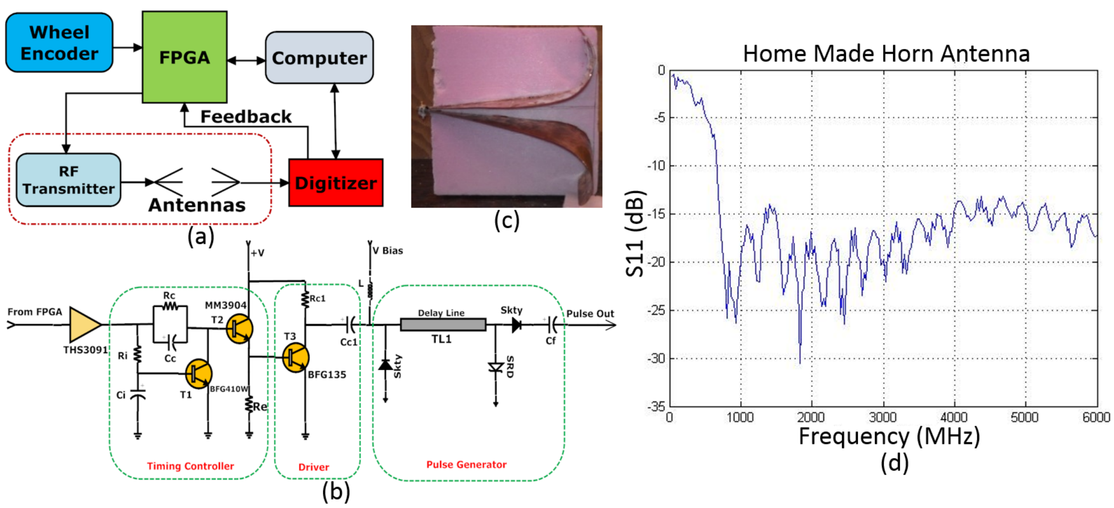

Figure 4.1: GPR system diagram: (a) High Speed UWB GPR System; (b) UWB Pulse Generator; (c) UWB Horn Antenna; (d) Reflection Loss of the UWB Horn Antenna.

4.2.2. Test Setups

In order to evaluate the performance of our GPR data analysis approaches, GPR singular region detection experiments are conducted with two types of setups. One is for rebar detections, while the other one is for ballast moisture region discovery.

For rebar detections, two different configurations are implemented: (1) A 30 mm diameter rebar is positioned in air and is placed 220 mm below antennas as shown in Figure 4.2(a); (2) Two 20 mm diameter rebars spaced by 500 mm are buried 108mm and

98.6 mm deep inside a concrete slab as shown in Figure 4.2(b). Transmitter and receiver antennas (Figure 4.2(c)) are packed inside a box which is placed 100 mm above the top surface of the concrete slab.

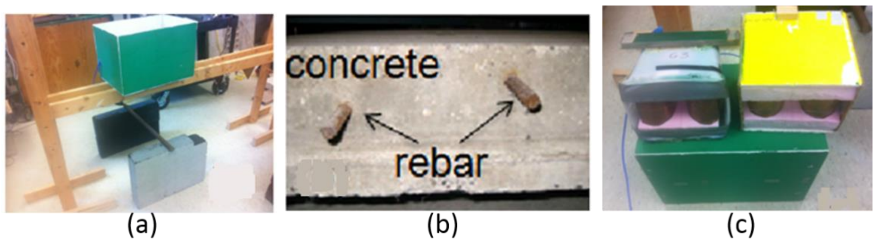

Figure 4.2: Measurement setup (a) rebar in air; (b) rebar in concrete; (c) Two horn antennas.

For ballast moisture region assessment, experiment is configured with contaminated ballasts. Figure 4.3(a) shows the test platform developed emulating the railroad structure. One portion of the ballast region is contaminated with soil and water. Figure 4.3(b) illustrates the subsurface structural configuration: (1) The ballast layer above the soil is 0.3 m thick; (2) 0.75 m apart from the left end of the platform, a region (highlighted in blue) of 0.45 m width and 0.2 m depth is filled with contaminated ballast mixed with soil and 2-gallon water, which is the fouled ballast region for GPR detection validation.

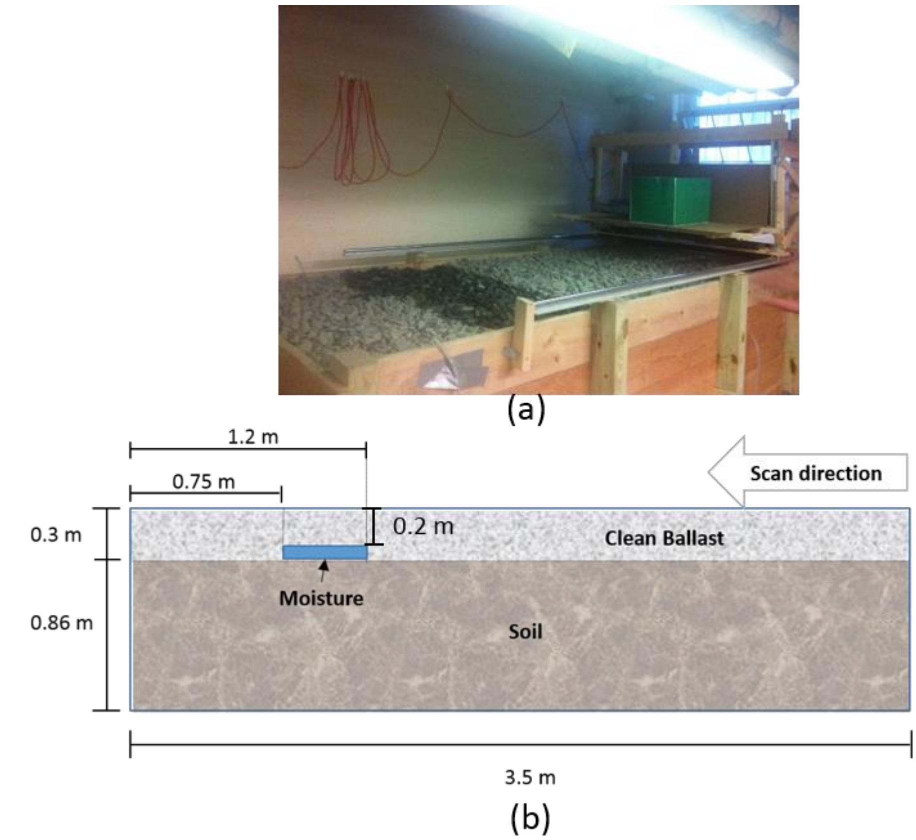

Figure 4.3: Ballast Test Configuration: (a) Test Platform; (b) Subsurface Construction.

4.2.3. GPR Data Pre-Processing

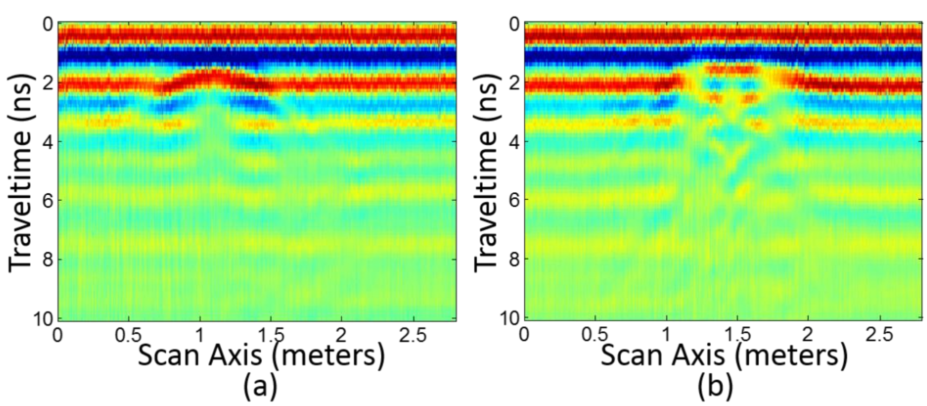

Figure 4.4: Raw B-scan images of (a) rebar in air; (b) Two rebars in a concrete slab.

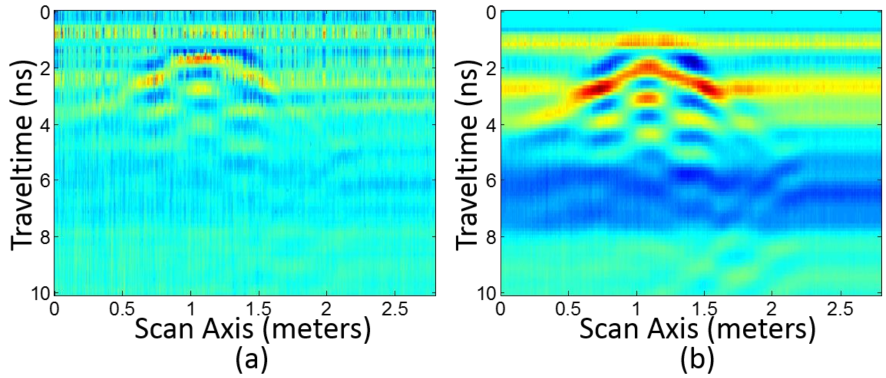

Figure 4.5: Rebar-in-Air B-scan images after preprocessing: (a) Reference trace subtraction and a LPF filtering; (b) Reference trace subtraction, LPF filtering and trace averaging operations.

During rebar scan test, GPR antennas are moved horizontally above the rebar for reflection signal collection. The obtained raw B-scan images are plotted in Figure 4.4. In these B-scan images, X-axis indicates scan distance while Y-axis specifies the radar signal travel time. The raw images contain significant background noise including floor surface reflection signal and transmitter/receiver antennas direct coupling interference signal located between time indexes 0 ns and 2 ns. To remove these undesired signals, the following data pre-processing steps are implemented: (1) Subtracting the first sampling trace from all subsequent traces to eliminate the stationary systematic interference signal. (2) Applying a 5th order 1 GHz FIR (Finite Impulse Response) low pass filter to remove off-band noise. Using rebar-in-air image as the example, the resulting images upon these processing are demonstrated in Figure 4.5(a). (3) Applying averaging operations (stacking) among every 100 traces to further alleviate random noise and to improve signal to noise ratio. The final image is illustrated in Figure 4.5(b). Note the averaging factor of 100 is selected for its effectiveness in removing noise while maintaining good image resolution.

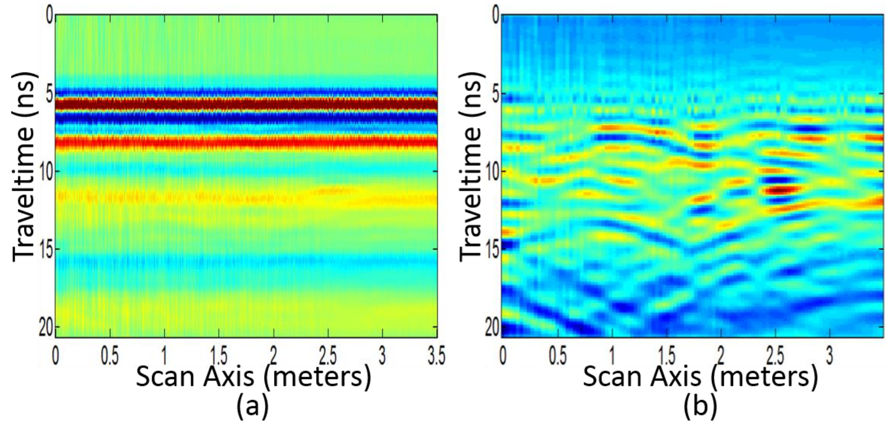

Figure 4.6: B-Scan images for ballast setup: (a) Raw B-Scan image; (b) B-Scan image upon preprocessing.

For the ballast setup configuration, Figure 4.6(a) is the raw image, and Figure 4.6(b) is the image obtained upon pre-processing. For all test configurations, 2D entropy and STFT analysis described below are applied to detect the singular regions, which are rebar region and fouled ballast region respectively.

4.3. Computational algorithms: 2-D Entropy and Short-Time Fourier Transform

4.3.1. Windowing 2D Entropy Method

In information theory, entropy is a measure of the uncertainty associated with a random variable. It quantifies the expected value of the information contained in a message. For our GPR data processing, entropy characterization is explored to identify the singular region within a large data set. In particular, a high entropy value indicates high degree of data similarity while a low entropy value highlights high degree of data singularity. Below we will elaborate our GPR data entropy analysis algorithm.

The received GPR reflection signal $Y(t)$ can be modeled with the following equation:

$$Y(t) = D(t) + S(t) \tag{4.1}$$

where $D(t)$ represents the reflection signal from the object of interest; $S(t)$ models interference and noise, including reflection signals from the background such as the concrete slab surface, and transmitter and receiver antennas direct coupling signals, etc. In calculation, power normalization is first performed with the summation of the power of the same time index data points on different traces. The normalization equation is expressed as

$$y_i(t) = \frac{\|Y_i(t)\|^2}{\sum_{i=1}^{M}\|Y_i(t)\|^2} \tag{4.2}$$

where $y_i(t)$ is the normalized signal, i denotes the trace index and M is the total number of traces included; t specifies time index of pulse data on each reflection trace waveform.

Upon power normalization, a generalized Renyi's entropy [22] is applied to assess data singularity:

$$E_\alpha(t) = \frac{1}{1-\alpha}\log_{\mathrm{e}}\langle\sum_{i=1}^{M}[y_i(t)]^\alpha\rangle \tag{4.3}$$

$E_\alpha(t)$ is the entropy quantification. α is the entropy order. When $\alpha = 1$, Eq. (4.3) transforms to the basic Shannon entropy. For analysis demonstration, Figure 4.7 shows different trace waveforms for scanning rebar-in-air setup. The scanning trace indexes are i = 1000, 1200, 1400, 1600, 1800, 2000 and 2200 respectively. Note, since rebar is a metal structure, comparing with background objects, it produces the strongest reflection corresponding to the peak pulse point on each trace waveform.

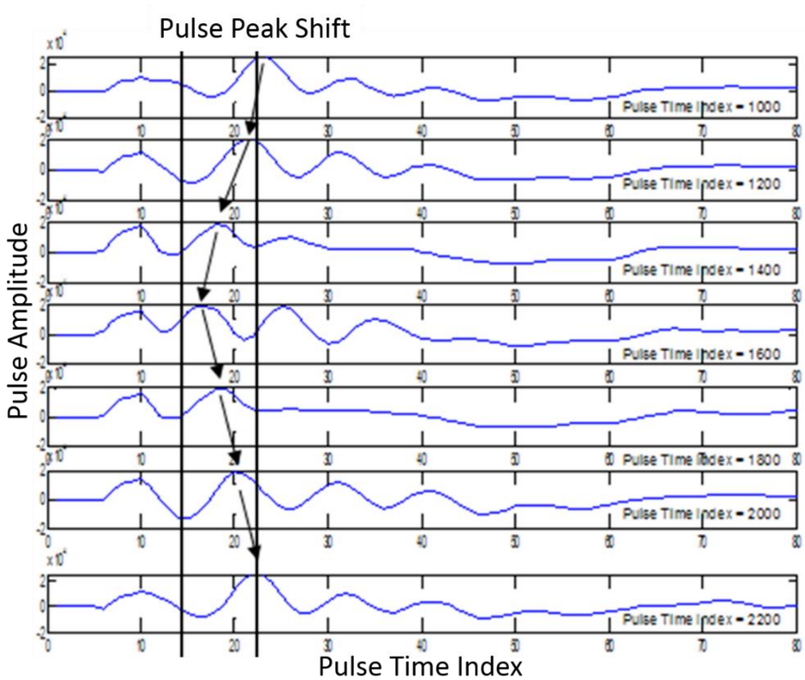

Figure 4.7: Pulse peak point shift on different trace index = 1000, 1200, 1400, 1600, 1800, 2000, 2200.

As the scanning trace index increases from i =1000 to 2200, the rebar reflection causes the time index of the peak point to initially shift toward the lower numbers and then shift back to higher ones. The lower index implies shorter signal travel distance between rebar and transceiver antennas. As antennas move away from the rebar, the pulse peak shifts to higher time indexes, indicating longer travel time. In order to identify the time index region that contains singular features such as peak shifting, entropy values are computed using Eq. (4.2) and Eq. (4.3) with $M = 4088$ scanning traces, where α is set to 3 [8], [22]. The resulting entropy curve is plotted in Figure 4.8.

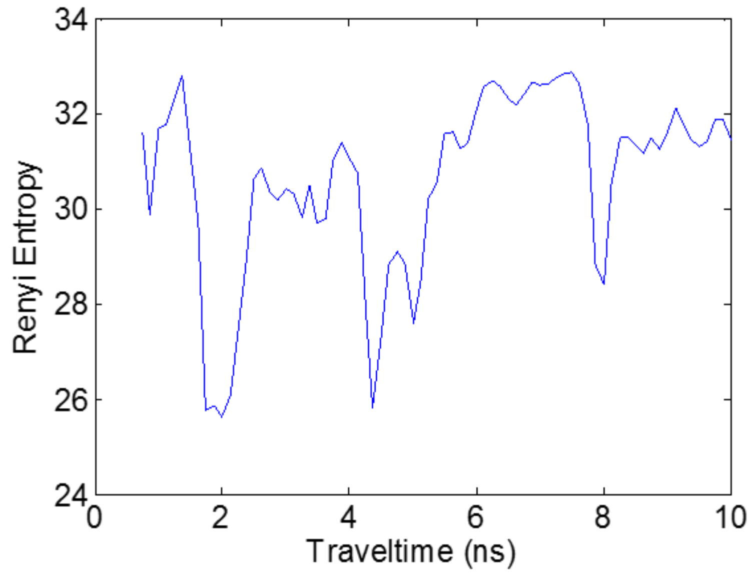

Figure 4.8: Entropy data of One Rebar in Air B-Scan.

4.3.2. Entropy Curve Smoothing Using Moving Average

To alleviate entropy value fluctuations, moving average (SMA) operation is performed to smooth out the entropy data [23]. Denoting the entropy value at index n as $E(n)$ in entropy data sequence, SMA calculates the mean of every m data points. In this chapter, m is selected to be 5% of the number of data points in $E(n)$, i.e. $m = n/20$.

$$E_{smooth}(n) = \frac{1}{m}\sum_{i=n-m+1}^{n} E(i) \tag{4.4}$$

4.3.3. Adaptive Entropy Threshold Determination

Depending on the data homogeneity, the B-scan image can be segmented into three classes of regions: singular region, stationary background region and the transition region in-between. The classification process can be made through assessing region's entropy values against two selected thresholds k_1 and k_2, where $k_1 < k_2$. The singular region entropy values are lower than threshold k_1, the stationary background region entropy values are higher than k_2. While for the transitioning region, its entropy values are between these two thresholds.

In order to appropriately determine threshold values k_1 and k_2, the automatic OTSU's thresholding method [17] is employed. OTSU's method is a classic image segmentation technique for extracting an object from its background. In principle, an image can be divided into non-overlapping regions by evaluating region's homogeneity through intensity values (i.e. pixel magnitude) variance assessment. For region classification, the intra-class intensity values are close to each other with small variances; while the inter-classes intensity values are significantly different with large variances. OTSU's method performs statistical analysis to identify appropriate thresholds so as to segment image into different regions accomplishing the criteria: the intensity values variances of the same region is minimized while the variances of different regions are maximized.

When applying OTSU's method to determine GPR B-scan image segmentation thresholds, the entropy is chosen as the intensity value. Recording the number of entropy points whose values are E_i as n_i, the total number of entropy points is $N = \sum_{E_i \in [E_{min}, E_{max}]} n_i$, where E_{min} and E_{max} specify the minimum and the maximum entropy values respectively. Statistical normalization is then performed:

$$p_i = \frac{n_i}{N},\ p_i \geq 0, \quad \sum_{E_i \in [E_{min}, E_{max}]} p_i = 1 \qquad (4.5)$$

where p_i specifies E_i value occurrence frequency or the normalized probability. With two thresholds k_1 and k_2, the entropy data set is divided into three subgroups: *group C_0:*

$[E_{min}, k_1]$, *group C_1*: (k_1, k_2), *group C_2*: $[k_2, E_{max}]$. The occurrence frequency of each subgroup can be calculated as:

$$\omega_0 = P(C_0) = \sum_{E_i \in [E_{min}, k_1]} p_i$$
$$\omega_1 = P(C_1) = \sum_{E_i \in (k_1, k_2)} p_i \tag{4.6}$$
$$\omega_2 = P(C_2) = \sum_{E_i \in [k_2, E_{max}]} p_i$$

and the group mean values are:

$$\mu_0 = \sum_{E_i \in [E_{min}, k_1]} E_i P(E_i|C_0) = \sum_{E_i \in [E_{min}, k_1]} E_i \frac{p_i}{\omega_0}$$
$$\mu_1 = \sum_{E_i \in (k_1, k_2)} E_i P(E_i|C_1) = \sum_{E_i \in (k_1, k_2)} E_i \frac{p_i}{\omega_1} \tag{4.7}$$
$$\mu_2 = \sum_{E_i \in [k_2, E_{max}]} E_i P(E_i|C_2) = \sum_{E_i \in [k_2, E_{max}]} E_i \frac{p_i}{\omega_2}$$

The overall entropy mean equals

$$\mu_T = \mu(L) = \sum_{E_i \in [E_{min}, E_{max}]} E_i p_i \tag{4.8}$$

The intra-class variances can be calculated as

$$\sigma_0^2 = \sum_{E_i \in [E_{min}, k_1]} (E_i - \mu_0)^2 P(E_i|C_0) = \sum_{E_i \in [E_{min}, k_1]} (E_i - \mu_0)^2 \frac{p_i}{\omega_0}$$
$$\sigma_1^2 = \sum_{E_i \in (k_1, k_2)} (E_i - \mu_1)^2 P(E_i|C_1) = \sum_{E_i \in (k_1, k_2)} (E_i - \mu_1)^2 \frac{p_i}{\omega_1} \tag{4.9}$$
$$\sigma_2^2 = \sum_{E_i \in [k_2, E_{max}]} (E_i - \mu_2)^2 P(E_i|C_2) = \sum_{E_i \in [k_2, E_{max}]} (E_i - \mu_2)^2 \frac{p_i}{\omega_2}$$

The inter-class variance can be measured by the following discriminate criterion

$$\sigma_B^2 = \omega_0(\mu_0 - \mu_T)^2 + \omega_1(\mu_1 - \mu_T)^2 + \omega_2(\mu_2 - \mu_T)^2 = \omega_0\omega_1(\mu_0 - \mu_1)^2$$
$$+\omega_1\omega_2(\mu_1 - \mu_2)^2 + \omega_2\omega_0(\mu_2 - \mu_0)^2 \tag{4.10}$$

which is a function of threshold variables k_1 and k_2. The optimal thresholds k_1^* and k_2^* can be determined by maximizing σ_B^2 [17]:

$$\sigma_B^2(k_1^*, k_2^*) = \max_{k_1,k_2 \in [A_{min}, A_{max}]} \sigma_B^2(k_1, k_2) \tag{4.11}$$

The adoption of these two optimal thresholds can maximize inter-group entropy variance. In the meantime, the intra-group entropy values variance is minimized [17].

4.3.4. Short Time Fourier Transform (STFT)

In essence, STFT implements local Fourier Transform on data that are evenly divided into smaller time windows. Mathematically, STFT algorithm is expressed as below:

$$X(\tau, \Omega) = \int_{-\infty}^{\infty} x(\tau) w(\tau - t) e^{-j\Omega\tau} d\tau \tag{4.12}$$

where x is the received GPR signal, Ω is the radial frequency whose resolution ($\Delta\Omega = 2\pi/N$) is determined by the number of points (N) adopted for FFT computation. In this analysis, $N = 256$. τ is the time resolution. Since our GPR digitizer's sampling frequency is 8 Gsps, τ equals 125 ps. $w(t)$ is the window function. Here a Hamming window is employed. In STFT analysis, there exists a tradeoff between time and frequency resolution when determining the window size. Through a series of iterative experiments, we select 1/10 the total number of time index to set the window size, which is proven effective in achieving a good balance between frequency and time resolution for rebar detection.

4.4. Experiment Results and Discussion

4.4.1. Rebar Test Results

Based on entropy and STFT characteristics analyzed above, this chapter proposes to perform 2-D entropy analysis first to narrow down data scope to distinctive regions, and then utilizes STFT to refine true singular region detection. For rebar in-air setup, entropy analysis Eq. (4.3) with $\alpha = 3$ is first applied to B-scan image along Y-axis, as shown in Figure 4.9. The obtained smooth entropy curve is plotted in Figure 4.9(b). Using OTSU's thresholding method, two threshold values $k_1^* = 28.96$ and $k_2^* = 31.08$ are calculated. The region between 0 and k_1^* is the singular region, while the region between k_1^* and k_2^* is the transition region. In this study, in order not to miss detecting the areas of interests, we take a conservative approach by searching for both the singular region and the transition region, where both regions have entropy values below the higher threshold $k_2^* = 31.08$. As illustrated in Figure 4.9(b), there are two regions whose entropy values are below this threshold. One locates between $t = 1.625$ ns and 5.75 ns and the other one locates between $t = 7.75$ ns and 8.625 ns.

Subsequently, Renyi's entropy calculation is applied to scanning traces along X-axis. Figure 4.10(b) plots the entropy curve. Using OTSU's thresholding method, two threshold values $k_3^* = 10.25$ and $k_4^* = 12.01$ are obtained to identify the distinctive data region in X-direction. Like the analysis along Y-axis, the region containing rebar reflection information is within the region below threshold k_4^*, which is found between $x = 0.55$ m and $x = 1.95$ m.

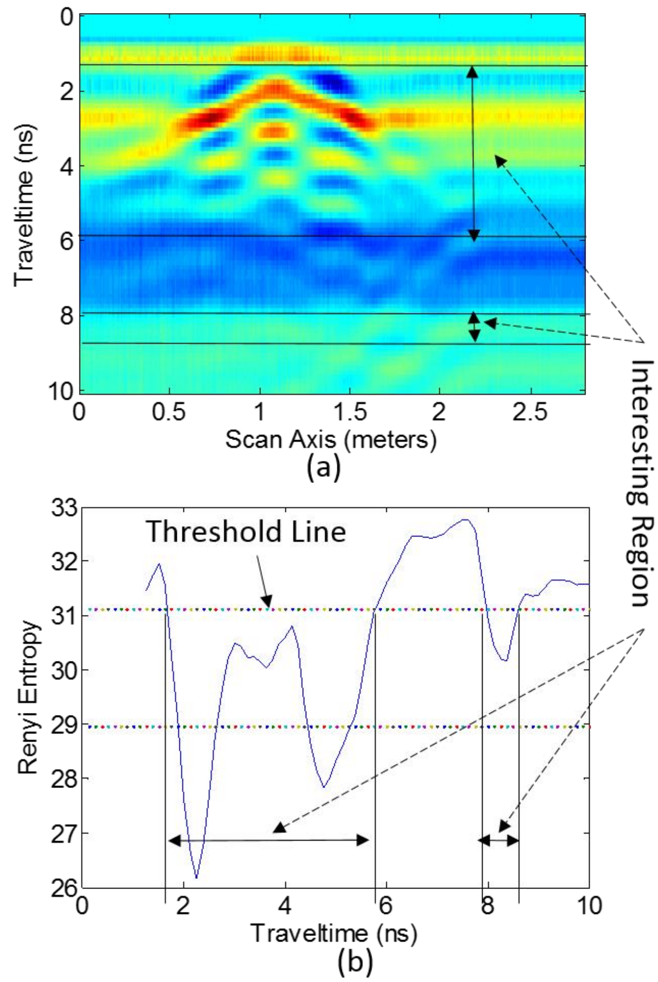

Figure 4.9: Entropy analysis along pulse time index (Y-axis) of rebar in-air data: (a) B-Scan image; (b) Entropy data.

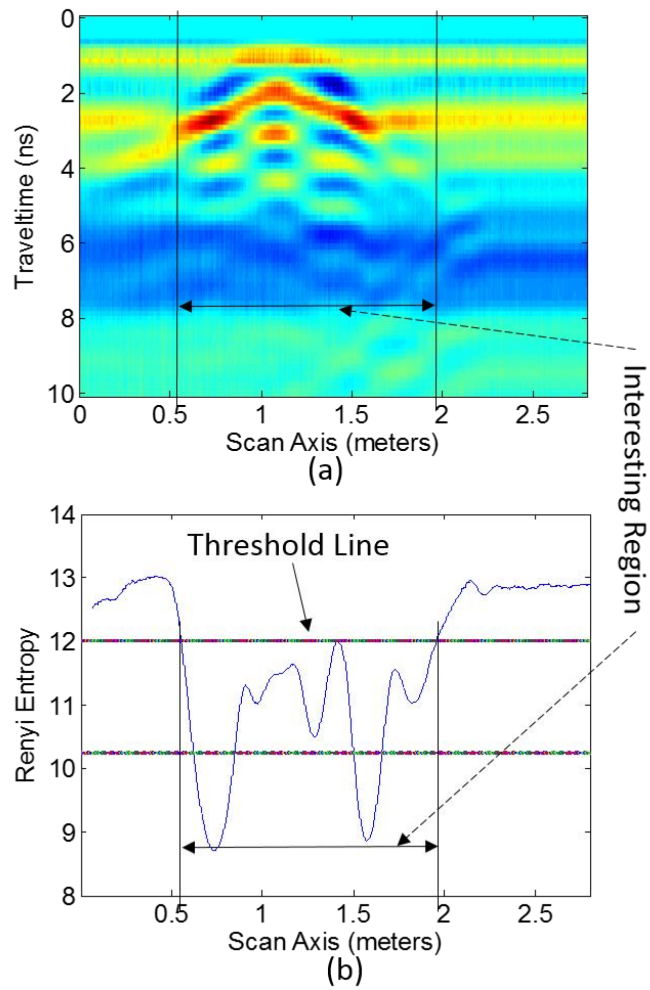

Figure 4.10: Entropy analysis along trace index (X-axis) of rebar in air B-scan: (a) B-Scan image; (b) Entropy data.

By combining both x-axis and y-axis entropy analysis results, the intersection regions are obtained. For rebar-in-air setup, the extracted regions are illustrated in Figure 4.11(a); while for rebars-in-concrete-slab setup, the extraction regions are highlighted in Figure 4.11(b). In both cases, a false region below 7 ns is also extracted. STFT analysis is then performed to refine the extraction result and eliminate the false region.

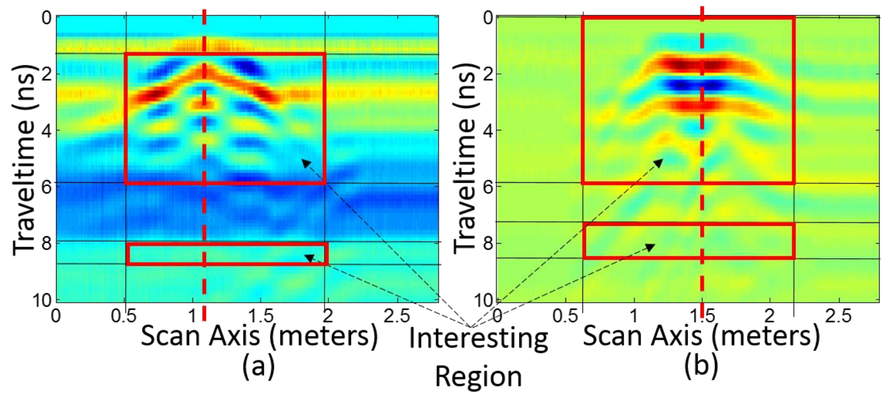

Figure 4.11: 2D entropy analysis for B-scan images of a) rebar in air and b) rebars in concrete.

For one-rebar-in-air data, STFT analysis is performed on the selected signal trace at $x = 1.1$ m across the extracted regions in Figure 4.11(a). The obtained time-spectrum is plotted in Figure 4.12(a). As shown, no strong reflection occurs between 8 ns and 10 ns, which means the second region (8 ns ~ 9 ns) in Figure 4.11(a) is the false singular region that should be eliminated. The corrected singular region extraction result is plotted in Figure 4.13(a). Similarly for two-rebar in concrete slab data, STFT analysis on the signal trace locating at x=1.5m is performed and the result is displayed in Figure 4.12(b). As shown, no strong reflection exists between 6 ns and 10 ns, which indicates the second region (between 7 ns and 9 ns) in Figure 4.11(b) is also a false region and should be eliminated. The corrected singular region extraction result is displayed as Figure 4.13(b). In both cases, the extracted rebar region comprises less than 40% of the entire scanning data volume.

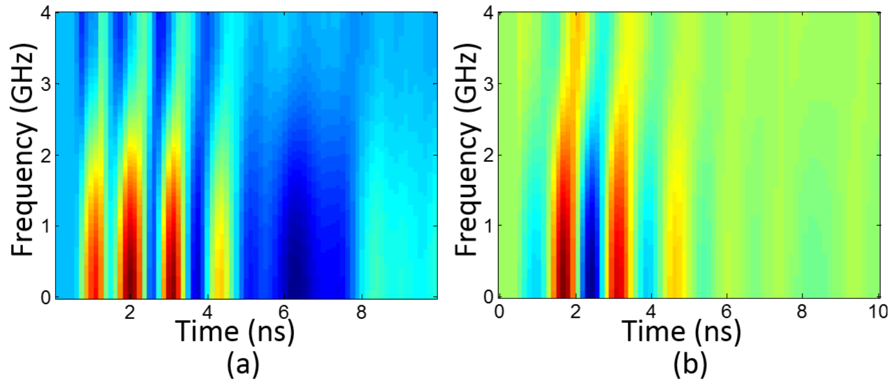

Figure 4.12: STFT analysis to correct the singular region detection: (a) STFT result of one rebar data at x=1.1m; (b) STFT result of two rebar data at x=1.5m.

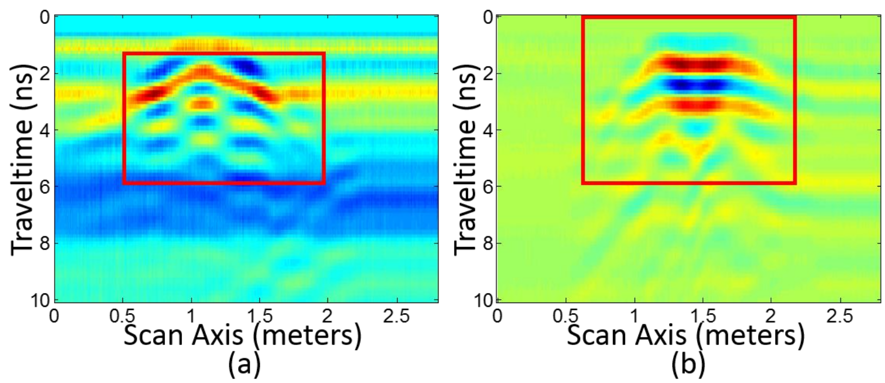

Figure 4.13: Final singular region for B-scan images of a) rebar in air and b) two rebars in concrete.

Further, STFT is operated on trace signals selected from the left side, the middle, and the right side of the rebar region respectively. The corresponding STFT analysis results are shown in Figure 4.14(b), Figure 4.14(c), and Figure 4.14(d).

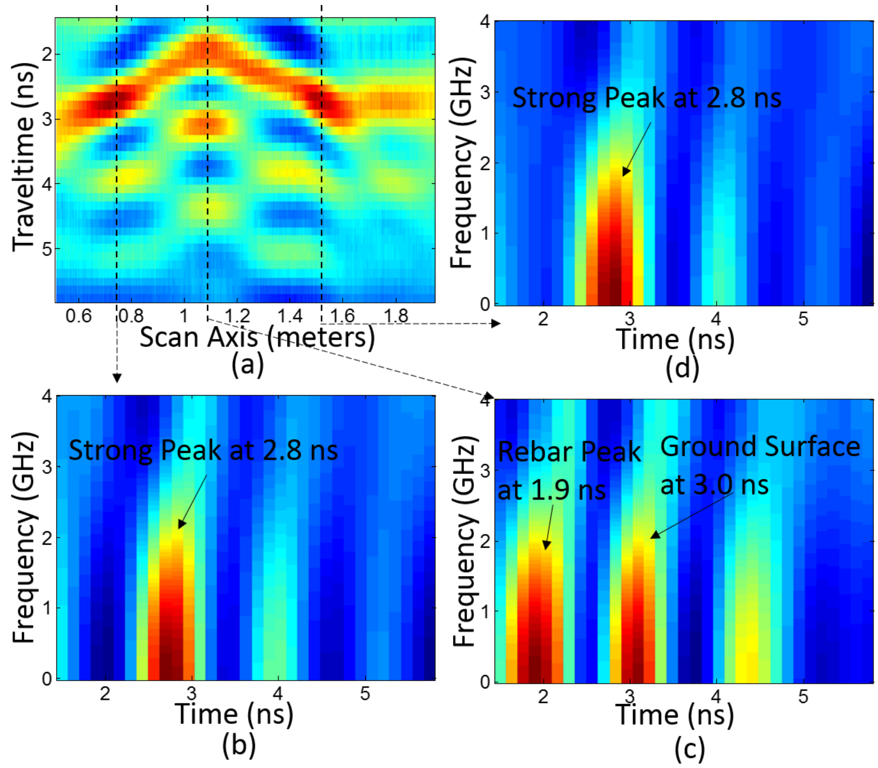

Figure 4.14: (a) Rebar in air B-scan image; 2D entropy and STFT analysis results of traces at (b) left side, (c) middle and (d) right side of rebar area.

In Figure 4.14(b), a strong peak occurs at 2.8 ns on the trace of $x = 0.75$ m when antennas are on the left side. Figure 4.14(c) shows when the antennas are right above the rebar (the trace of $x = 1.1$ m), a strong peak pulse is produced at 1.9 ns. Figure 4.14(d) depicts a strong peak at 2.8 ns on trace of $x = 1.5$ m when antennas are on the right side. In our experiments, we are able to find out that the 2.8 ns peak pulse is the reflection signal from the floor surface underneath rebar with the utilization of a large metal sheet. By covering the floor surface with a large metal sheet, a stronger reflection pulse is observed occurring at exactly the same time instant (2.8 ns), which validates the floor as the reflection source. With reference to Figure 4.4(a), the distance between antennas and the rebar can be determined through the following calculations: (1) Subtracting the time offset between antennas direct coupling pulse ($t = 0.5$ ns) (The transmitter antenna and receiver antenna are packed together inside of a box, the direct coupling pulse time is thus used as the reference time point) and the strongest STFT peak point ($t = 1.9$ ns), obtains time offset $\Delta t = 1.4$ ns; (2) Inserting Δt to the following equation

$$V = d/(\frac{\Delta t}{2}) \tag{4.13}$$

where d is the distance, V is the speed of light in air ($3\text{x}10^8$ m/s), and ($\Delta t/2$) indicates one way signal travel time from rebar to the receiver antenna. The distance d is thus calculated to be 210 mm, which agrees well with the physical setup described in section 4.2.1, where antennas are placed 220 mm above the rebar.

For two rebars in a concrete slab setup, Figure 4.15(a) extracts the intersected B-scan image section that focuses on rebars. Both STFT images of the left side trace (the trace at $x = 1.25$ m) (Figure 4.15(b)) and right side trace (the trace at $x = 1.7$ m) (Figure 4.15(c)) show two strong peaks (in red color) at 1.75 ns and 3.125 ns. These peak time values are used to compute rebars burying depths inside the concrete slab. The radar signal two-way travel time between concrete and rebars is calculated to be 3.125 ns – 1.75 ns = 1.375 ns. The electromagnetic (EM) wave travel velocity V_c inside concrete needs to be taken into account, which equals:

$$V_c = V/\sqrt{\varepsilon_c} \tag{4.14}$$

ε_c is the relative dielectric constant of the concrete which equals about 4.1 according to our measurements conducted in [18], [19], [20] and [21]. V is the speed of light in air. V_c is calculated to be $1.48\text{x}10^8$ m/s. Using Eq. (4.13) with Δt = 1.375 ns, the rebar burying depth from concrete surface is computed to be 102 mm approximately, which is in good agreement with the physical setups (98.6/108 mm depths) described in Section 4.2.

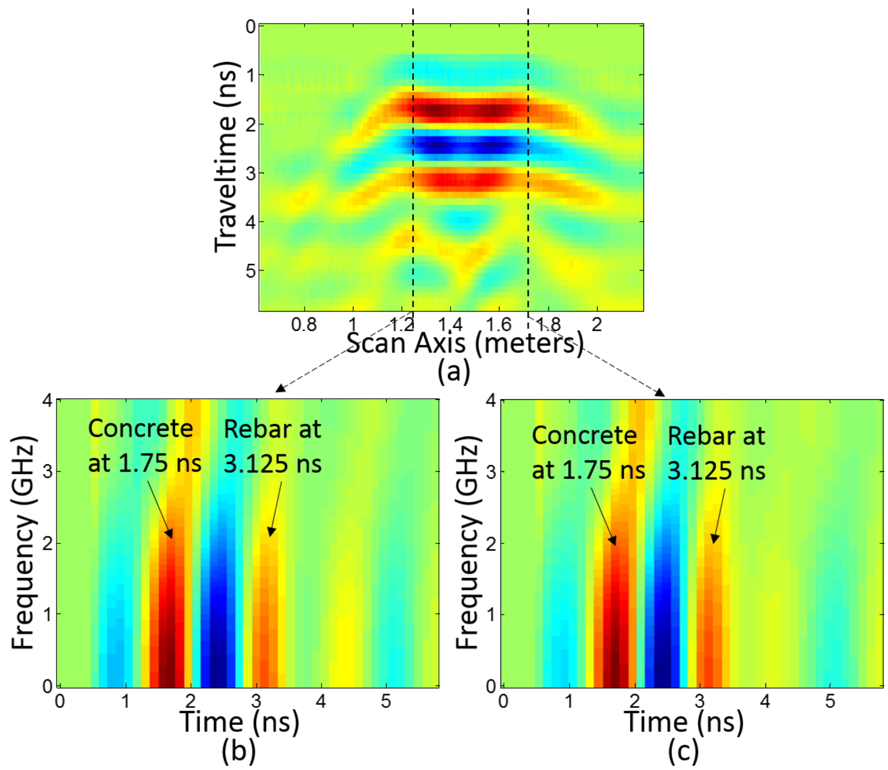

Figure 4.15: (a) Rebars in concrete B-scan image; 2D entropy and STFT analysis at (b) left rebar and (c) right rebar.

4.4.2. Ballast Test Results

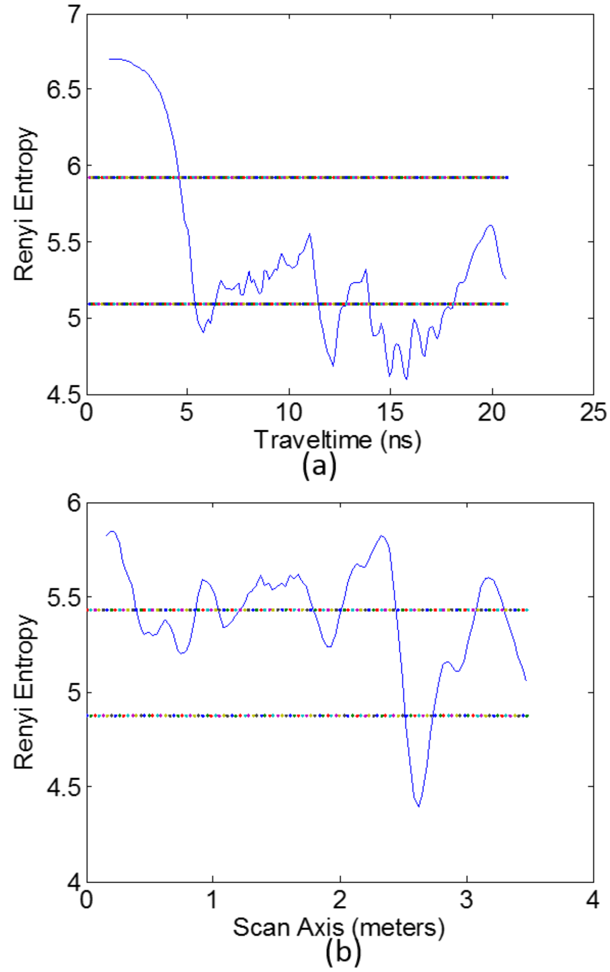

Figure 4.16: Entropy analysis of ballast data: (a) Entropy along Travel time index (Y-axis); (b) Entropy along Scan Axis (X-axis).

For ballast platform setup, entropy analysis is first applied to the B-scan image along Y-axis, as shown in Figure 4.16(a). Using OTSU's thresholding method, two threshold values $k_1^* = 5.08$ and $k_2^* = 5.92$ are calculated. The singular regions have entropy values below threshold k_1^*. As illustrated in Figure 4.16(a), there are three regions whose entropy values are below this threshold. The first one locates between $t = 5.125$

ns and 6.00 ns, the second locates between $t = 11.00$ ns and 12.50 ns, and the third one locates between $t = 14.25$ ns and 17.50 ns.

Subsequently, Renyi's entropy is computed along X-axis. Figure 4.16(b) plots the obtained curve. Using OTSU's thresholding method, two threshold values $k_3^* = 4.88$ and $k_4^* = 5.43$ are obtained. Similar to the analysis along Y-axis, the singular region is below threshold k_3^*, which locates between $x = 2.35$ m and $x = 2.75$ m. By combining both the x-axis and y-axis entropy analysis results, the intersection regions in the B-scan image are obtained. For the ballast platform setup, the extracted region is illustrated in Figure 4.17.

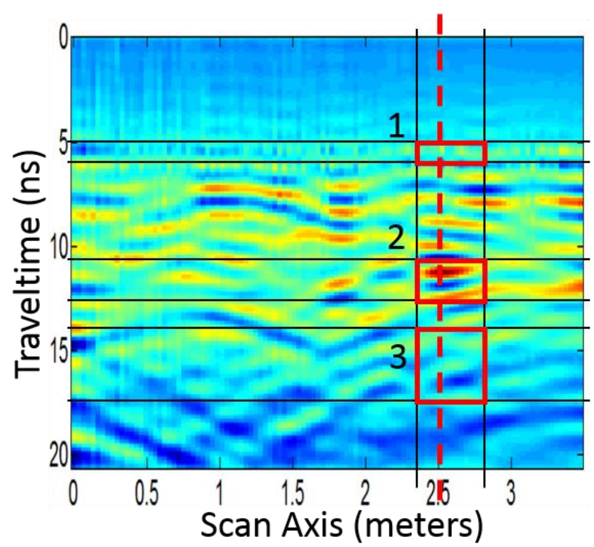

Figure 4.17: 2-D entropy analysis for B-Scan image of ballast platform.

To refine region identification, windowing STFT analysis is performed on a trace signal across three regions locating at $x = 2.5$ m. The corresponding STFT analysis result is shown in Figure 4.18.

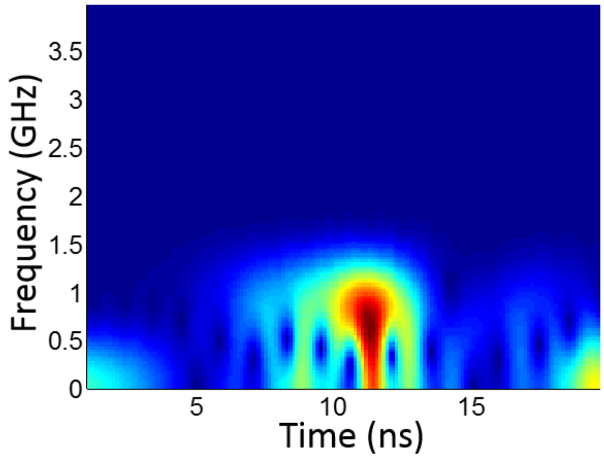

Figure 4.18: STFT analysis result of trace at x = 2.5 m.

As shown in Figure 4.18, a strong peak occurs only between 11 ns and 12 ns. This result indicates that region 2 in Figure 4.17 is the true singular region while regions 1 and 3 are false ones. Combining the results of entropy analysis and STFT analysis, the correct fouled ballast region is singled out in Figure 4.19. In this test case, the extracted region comprises less than 5% of the entire scanning data volume.

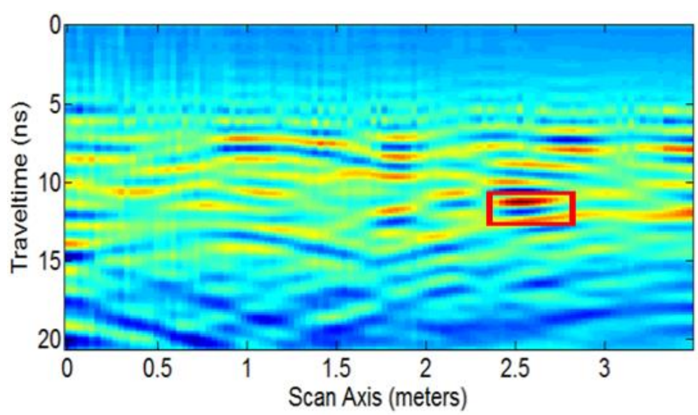

Figure 4.19: Final moisture region detection result based on entropy and STFT analysis.

To validate the detection result, the fouled ballast region depth is computed in a similar way as the rebar test. The ground surface reflection signal locates at $t = 8.5$ ns in Figure 4.6(a), and the detected region top side locates at $t = 11.0$ ns, therefore the two-way travel time of radar incident signal between ground surface and moisture region is 11.0 ns – 8.5 ns = 2.5 ns. Substituting the measured dielectric constant of clean ballast $\varepsilon_c = 3$ into Eq. (4.14), V_c is calculated as 1.73x10^8 m/s. Using Eq. (4.13) with $\Delta t = 1.25$ ns, the depth of the fouled ballast region is computed as 0.216 m approximately. This value agrees well with the actual physical setups (0.2 m depth).

4.5. Conclusions

This chapter has demonstrated the integration of 2D entropy and STFT analytical methods to leverage GPR data processing efficiency. By computing radargram 2D entropy and OTSU's thresholds, singular areas within large background data can be effectively extracted. The utilization of entropy analysis effectively reduces the data volume for implementing more sophisticated post-processing algorithms. In our test experiments, around 60% data compression rate is achieved for rebar detection and 95% data compression rate is achieved for fouled ballast region detection. STFT is then applied for time-frequency characterization to leverage region detection accuracy and screen out false results. Note there are other more sophisticated JTF analysis methods, such as Gabor transform, wavelet, fractional Fourier transform, etc., that are capable of more advanced characterizations when the data scope is more focused with the assistance of entropy calculation. STFT is generally sufficient for these applications that require marginal detection resolutions.

4.6. References

[1] Z.W. Wang, M. Zhou, G.G. Slabaugh, J. Zhai, and T. Fang, "Automatic Detection of Bridge Deck Condition From Ground Penetrating Radar Images," IEEE Transactions on Automation Science and Engineering, Vol. 8, No. 3, pp 633-640, 2011

[2] F. Soldovieri, R. Solimene, L. Lo Monte, M. Bavusi, and A. Loperte, "Sparse Reconstruction From GPR Data With Applications to Rebar Detection," IEEE Transactions on Instrumentation and Measurement, Vol. 60, No. 3, pp. 1070-1079, 2011

[3] V. Krause, I. Abdel-Qader, O. Abudayyeh , and S. Yehia, "An Image Segmentation Algorithm for the Detection of Rebar in Bridge Decks from GPR Scans," Proceedings of IEEE International Conference on Electro/Inforation Technology, Vol. 7, 2007, pp 114-119.

[4] A. Simi, G. Manacorda, and A. Benedetto, "Bridge deck survey with high resolution Ground Penetrating Radar," 14th International Conference on GPR, 2012, pp 489-495.

[5] J.S. Lee, C. Nguyen, and T. Scullion, "A Novel, Compact, Low-Cost, Impulse Ground-Penetrating Radar for Nondestructive Evaluation of Pavements," IEEE Transactions on Instrumentation and Measurement, Vol. 53, No. 6, pp1502-1509, 2004

[6] W.L. Lai, C.S. Poon, "GPR data analysis in time-frequency domain," 14th International Conference on GPR, 2012, pp 362-366.

[7] https://www.princeton.edu/~achaney/tmve/wiki100k/docs/Entropy_%28information_theory%29.html

[8] W. Zhi and F. Chin, "Entropy-Based Time Window for Artifact Removal in UWB Imaging of Breast Cancer Detection," IEEE Signal Processing Letters, Vol. 13, No. 10, 2006, pp 585-588.

[9] M. Ferrario, M. G. Signorini, G. Magenes, and S. Cerutti, "Comparison of Entropy-Based Regularity Estimators: Application to the Fetal Heart Rate Signal for the Identification of Fetal Distress," IEEE Transactions on biomedical engineering, Vol. 53, No. 1, pp 119-125, 2006

[10] H. You, Q. Zhu, and A. Alwan. "Entropy-based variable frame rate analysis of speech signals and its application to ASR," IEEE Acoustics, Speech, and Signal Processing, 2004, Vol.1, pp 549-52.

[11] E.C. Kenley and Y-R Cho, "Entropy-Based Graph Clustering: Application to Biological and Social Networks," IEEE International Conference Data Mining, 2011, pp 1116-1121

[12] R. Solimene and A. Cuccaro, "Front Wall Clutter Rejection Methods in TWI," Geoscience and Remote Sensing Letters, IEEE , vol.11, no.6, pp.1158,1162, June 2014

[13] M. Hanmandlu, O.P. Verma, N.K. Kumar, and M. Kulkarni, “A Novel Optimal Fuzzy System for Color Image Enhancement using Bacterial Foraging,” IEEE Transactions on Instrumentation and Measurement, vol. 58, no. 8, 2009, pp 2867-2879.

[14] T. P. Zielinski, “Joint Time-Frequency Resolution of signal Analysis Using Gabor Transform,” IEEE Transactions on Instrumentation and Measurement. vol. 50, No. 5. 2001. pp. 1436-1444.

[15] Z. Li and M. J. Crocker, “A Study of Joint Time-Frequency Analysis-Based Modal Analysis,” IEEE Transactions on Instrumentation and Measurement. vol. 55, No. 6. 2006. pp. 2335-2342.

[16] P. Candra, T. Xia, D. Huston, and G.A. Wang, "Two dimensional entropy and short time Fourier Transform application on ground penetrating radar data analysis," Proc. SPIE 8694, Nondestructive Characterization for Composite Materials, Aerospace Engineering, Civil Infrastructure, and Homeland Security 2013, 86940J (April 24, 2013); doi:10.1117/12.2010224.

[17] N. Otsu, “A Threshold Selection Method from Gray-Level Histograms,” IEEE Transactions on Systems, Man and Cybernetics, vol. 9, Issue: 1, 1979, pp 62 – 66.

[18] A. Venkatachalam, X.L. Xu, D. Huston, and T. Xia, "Development of a New High Speed Dual-Channel Impulse Ground Penetrating Radar," IEEE Journal of Selected Topics in Applied Earth Observations and Remote Sensing. Vol. 6, No. 6, Dec. 2013.

[19] T. Xia, XL. Xu, A. Venkatachalam, and D. Huston, "Development of a High Speed UWB GPR for Rebar Detection," Proceedings of IEEE International Conference on Ground Penetrating Radar (GPR) 2012.

[20] T. Xia, A. S. Venkatachalam, and D. Huston, "A High Performance Low Ringing Ultra-Wideband Monocycle Pulse Generator," IEEE Transactions on Instrumentation and Measurement. vol. 61, Issue 1. 2012. pp. 261-266.

[21] X.L. Xu, T. Xia, A. Venkatachalam, and D. Huston, “Development of High-Speed Ultrawideband Ground-Penetrating Radar for Rebar Detection,” Journal of Engineering Mechanics, vol. 139, no. 3, 2012, pp 272-285.

[22] R. G. Baraniuk, P. Flandrin, A. J. E. M. Janssen, and O. Michel, “Measuring time-frequency information content using the Rényi entropies,” IEEE Trans. Inf. Theory, vol. 47, no. 4, May 2001, pp. 1391–1409.

[23] S. W. Smith, “The Scientist and Engineer's Guide to Digital Signal Processing,” Second Edition, California Technical Publishing, San Diego, 1999.

CHAPTER 5: GROUND PENETRATING RADAR RAILROAD BALLAST INSPECTION WITH AN UNSUPERVISED ALGORITHM TO BOOST THE REGION OF INTEREST DETECTION EFFICIENCY

Abstract

Railroad ballast inspection is critical for the safety of both passenger and freight rail. Ground penetrating radar (GPR) has been utilized as a highly efficient non-destructive evaluation (NDE) and structural health monitoring technique in bridge and roadway inspection for many years. However, the development of robust GPR technologies for railroad ballast inspection is still at its early stage due to the complex scattering characteristics of ballast and the lack of efficient algorithms to process big GPR data. In this study, an efficient unsupervised method for detecting the region of interest in ballast layer based on Hilbert Transform and Renyi entropy analysis is proposed and tested extensively using an indoor platform emulating the railroad structure. Based on the lab test results, this unsupervised analysis approach is utilized to characterize 300 GB field test data collected at Massachusetts Bay Transit Authority (MBTA) and Metro St. Louis. The data interpretation results demonstrate that the developed region of interest detection algorithm is an efficient and valuable tool for GPR data processing.

Keywords: ground penetrating radar, information entropy, Hilbert transform, railroad ballast inspection, automatic detection, region of interest.

5.1. Introduction

Typical railroad subsurface defects include cavity, fouled ballast, high degree of moisture, etc. Although railroad subsurface structure safety is critical, its inspection is very challenging. Traditional inspection methods such as drilling test and acoustic/hammer test are either destructive or inefficient, labor intensive, time consuming, disturbing to the normal traffic, etc. As a non-destructive and highly efficient test method, GPR has been widely used for concrete bridge decks inspection [1], asphalt pavement monitoring [2], highway rebar detection [3], railroad ballast condition assessment [4], soil moisture estimation [5], etc. Among these applications, railroad ballast condition assessment is especially challenging due to the complex scattering characteristics of the ballast. Although a number of studies have been conducted, the application of GPR for railroad structure inspections is still in its early stage.

For applying GPR to railroad inspections, a major challenge is how to effectively process and interpret GPR data. There are sophisticated processing algorithms [6]-[9] that can effectively characterize subsurface structural features. Sparse representation is utilized in Ref. [6] to extract the feature of the A-Scan trace signal, and Support Vector Machine (SVM) technique [7] is applied for the GPR A-Scan traces classification based on a prior knowledge. Discrete wavelet transform is used in Ref. [8] to extract the texture feature in GPR B-Scan image and similarity measurement is performed to compare the tested B-Scan image and known B-Scan image pattern for ballast of various fouling condition. Similarly, discrete wavelet transform and fractional Fourier transform [9] are developed to extract features of each GPR A-Scan trace, and these features are supplied to SVM classifiers to identify the underground objects. Nearly all existing GPR ballast data interpretation methods share the same data processing scheme: 1. producing priori knowledge about various fouling ballast patterns; 2. applying the feature extraction method to GPR data to extract test patterns; 3. using a classifier to categorize the test data in accordance to fouling ballast patterns.

Such supervised methods can achieve high classification accuracy, however they are computationally complex. For large scale GPR survey, the collected inspection data is typically over hundred Giga Bytes (GB), making the direct application of these sophisticated data processing methods difficult and sometimes even infeasible. On the other hand, the structural composition of field ballast layer is very complex as some other scatters or material can be mixed within the ballast. Even the prior knowledge can be obtained using some ballast test with various fouling conditions, the feature pattern of field test ballast cannot be guaranteed to exist in the known training pattern due to its complex material composition. Therefore, developing an unsupervised and automatic GPR data processing method that can effectively and rapidly identify suspicious features from big radargram is critically desirable, which will facilitate advanced radar data post processing, such as the sophisticated feature extraction and pattern recognition.

In our previous work, an entropy analysis and short-time Fourier transform (STFT) based unsupervised algorithm has been developed and demonstrated to boost GPR signal processing efficiency [10]. By computing radargram 2D entropy and OTSU's thresholds, singular areas within large background data can be effectively extracted. The utilization of entropy analysis effectively reduces the data volume for implementing more sophisticated post-processing algorithms. STFT performs time-frequency characterization to leverage region detection accuracy and screen out false results.

In this chapter, the customized entropy-based algorithm is improved to automate and facilitate the detection of suspicious fouling ballast regions or Regions of Interest (ROI) within big GPR survey data sets. Considering the GPR transmitting signal is a high order (2nd order or higher) Gaussian pulse, the backscattering A-scan signal shows multiple peaks, which increases the difficulty to identify the feature of scatters. In this research, an analytic method using Hilbert Transform is developed to extract the pulse signal envelope so as to characterize the scattering signal power. Furthermore, an automatic layer identification method based on signal decomposition is implemented to detect and isolate the ballast region from the ground surface. Finally, the 2D entropy analysis is performed on the scattering data corresponding to ballast region. Such data processing approaches leverage 2D entropy analysis effectiveness and eliminate the need of STFT for singular region identification, so as to facilitate large volume GPR ballast inspection data post processing and interpretation.

To validate data processing effectiveness, extensive laboratory experiments are first conducted employing our Ultra Wideband (UWB) air-coupled impulse GPR system [11]. Further analysis is conducted on large volume (overall 20 miles) railroad field test data sets collected during the field test at Metro St. Louis and Massachusetts Bay Transit Authority (MBTA).

5.2. GPR System Configuration

In this chapter, the experimental data are collected with our air-coupled impulse GPR system developed in Ref. [3], [11] and [12]. Figure 5.1 illustrates the system diagram. As shown in Figure 5.1, the GPR system hardware consists of five major functional units: (1) RF transmitter; (2) Ultra-wideband antennas; (3) Data acquisition unit comprising of a high speed real time digitizer, high speed data transmission and storage unit; (4) Quard-core computer (Intel core i7 3.4 GHz) (5) FPGA digital controller along with a wheel encoder.

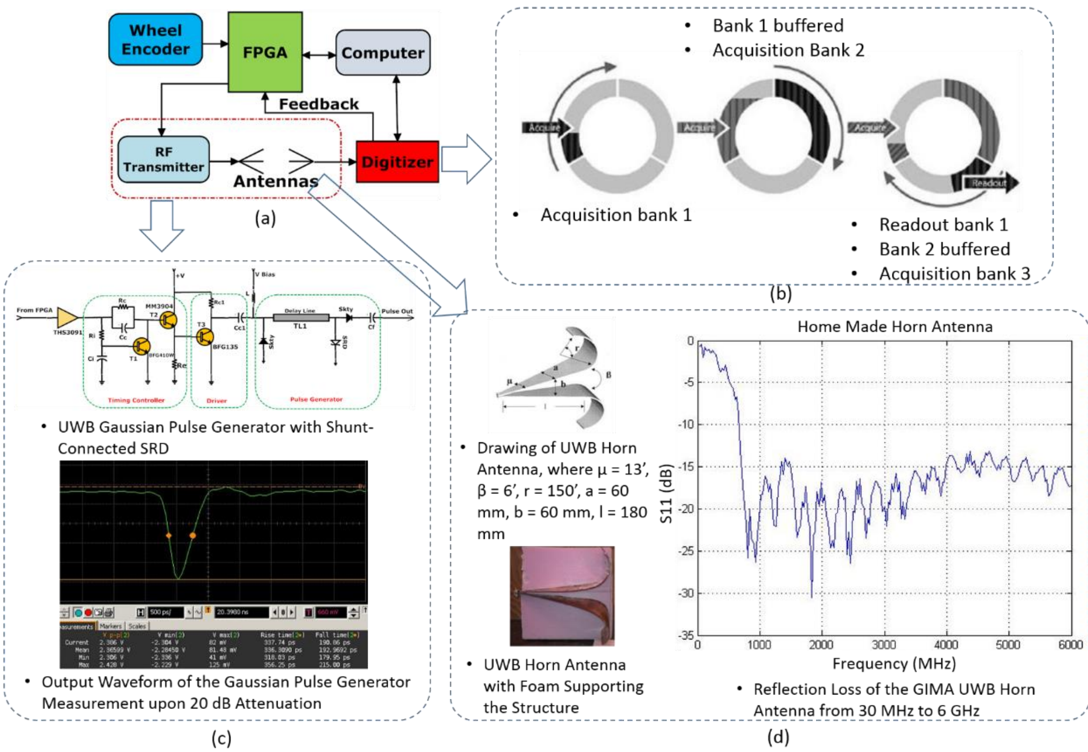

Figure 5.1: GPR system diagram: (a) High Speed UWB GPR System; (b) Digitizer Configured in SAR Mode; (c) UWB Pulse Generator; (d) UWB Antenna.

The RF transmitter comprises a UWB pulse generator that generates high-amplitude Gaussian pulses with the Pulse Repetition Frequency (PRF) controlled by the

FPGA. The high-speed digitizer contains a 10-bit 8 GSPS real-time sampling Analog-to-Digital Converter (ADC), which also includes a high-throughput data transmission unit connected to the multi-core computer via Peripheral Component Interconnect express (PCIe) bus. The computer streams the GPR data from the digitizer and tags the data with header information. The optical encoder measures the travel distance and generates quadrature pulses correspondingly. The FPGA receives the wheel encoder pulses and triggers GPR scans. The travel distance information is transmitted to the computer for data location registration. The antennas have a compact size and good impedance matching over a wide bandwidth from 600 MHz to 6 GHz for effective signal transmission and reception. Some selected key specifications of this GPR system are summarized in Table 1.1.More design details are elaborated in Ref. [3], [11]-[13].

Table 5.1: Air-coupled Impulse GPR System Specifications.

Data acquisition unit	8 Gsps, 10-bit resolution
GPR reflection pulse sampling window width	40 ns
Pulse repetition frequency	0 to 30 kHz tunable
Horizontal resolution	1 cm at 100 km/h survey speed
Signal bandwidth	600 MHz to 2 GHz tunable
Penetrating capability	Up to 1 meter

5.3. Unsupervised GPR ROI Detection Method

The flow chart of the proposed unsupervised GPR signal processing methods for detecting region of interest is illustrated in Figure 5.2. Stacking and low pass filtering are first performed on raw B-scan image for noise reduction. Hilbert transform is then utilized to extract the scattering signal envelope and characterize the signal power, based on which, the A-Scan decomposition is conducted to identify interfacing layers between different materials and to locate the ballast region for data interpretation. Clutter removal and stacking are then performed to enhance the ballast region image. Finally, the statistical 2D entropy analysis is applied to quickly detect the singular region of interest. Details of each step are elaborated in the following subsections.

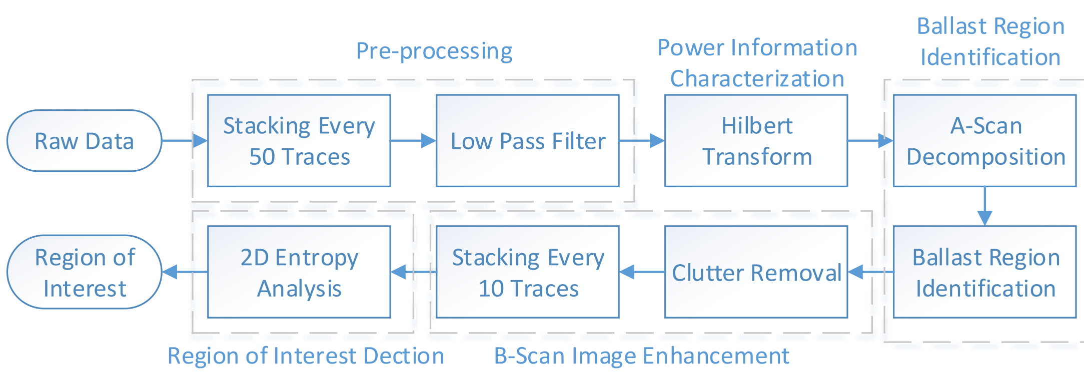

Figure 5.2: Unsupervised algorithm for detecting region of interest in ballast layer.

5.3.1. Pre-processing

To enhance the raw B-Scan images quality, a two-step pre-processing is implemented:

Step 1: Stack every 50 A-scan traces to calculate the average to boost the signal-to-noise ratio (SNR) [14].

The GPR signal transmitter is triggered in distance. The perimeter of the hi-rail SUV wheel used in GPR test is 0.77 m, and the wheel encoder has 10000 triggers per rotation. Thus, the distance interval between two pulses are 0.77m/10000 = 0.077 mm. Stacking every 50 traces results in 0.077mm*50 = 3.85 mm distance interval between two pulses, which assures the good spatial scanning resolution as well as improves the SNR of GPR A-Scan trace.

Step 2: Apply Low Pass Filtering (LPF) with a 2 GHz cutoff frequency. In the test, our GPR pulse signal spectrum is tuned as a monocycle pulse with 1 GHz center frequency, and the amplitude spectrum of received GPR A-Scan trace is shown in Figure 5.3. A 2 GHz LPF is employed to filter out the out-of-band high frequency noise.

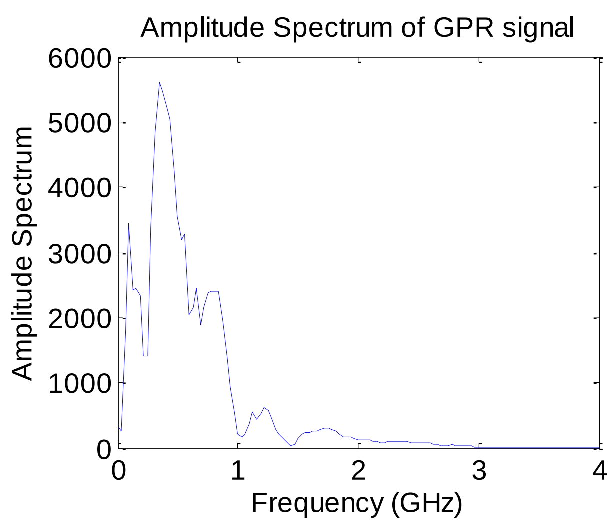

Figure 5.3: Amplitude spectrum of GPR A-Scan trace.

5.3.2. Power Information Characterization

Hilbert Transform is often used in communication system for baseband signal demodulation and extraction. In our GPR system, Hilbert Transform is implemented to extract the pulse envelope that measures the signal power [15].

The Hilbert Transform of signal $s(t)$ can be considered as the convolution of $s(t)$ with the function $h(t) = \frac{1}{\pi t}$, which can be expressed as

$$\hat{s}(t) = \mathcal{H}\{s\} = h(t) * s(t) = \int_{-\infty}^{\infty} s(\tau)h(t-\tau)d\tau = \frac{1}{\pi}\int_{-\infty}^{\infty} \frac{s(\tau)}{t-\tau}d\tau \quad (5.1)$$

To eliminate the singularities, such as $\tau = t$ and $\tau = \pm\infty$, Hilbert Transform is defined using the Cauchy principal value. Correspondingly, the Hilbert Transform of $s(t)$ is given by

$$\hat{s}(t) = \mathcal{H}\{s\} = -\frac{1}{\pi}\lim_{\varepsilon \downarrow 0}\int_{\varepsilon}^{\infty} \frac{s(t+\tau)-s(t-\tau)}{\tau}d\tau \quad (5.2)$$

Applying Hilbert transform to GPR signal $s(t)$, the analytic signal is obtained as

$$s_a(t) = s(t) + i\hat{s}(t) \quad (5.3)$$

where $\hat{s}(t)$ is the direct output of the Hilbert Transform of $s(t)$. The magnitude of $s_a(t)$ equals

$$|s_a(t)| = \sqrt{s(t)^2 + \hat{s}(t)^2} \quad (5.4)$$

$|s_a(t)|$ is the envelope of $s(t)$, which facilitates the signal power characterization.

Figure 5.4 demonstrates signal power characterization using Hilbert transform. The signal in Figure 5.4(a) is a GPR A-Scan waveform produced from two scatters. In the A-Scan waveform, the first pulse is the antennas' direct coupling, while the second and third pulses are the reflection signal from the 1st and 2nd scatters correspondingly.

As the transmitting pulse signal is the Ricker wavelet (the second order derivatives of Gaussian function), the backscattering pulse from each object or layer interface shows three peaks. Figure 5.4(b) shows the waveform produced by the Hilbert transform where the three peaks become much more discernible.

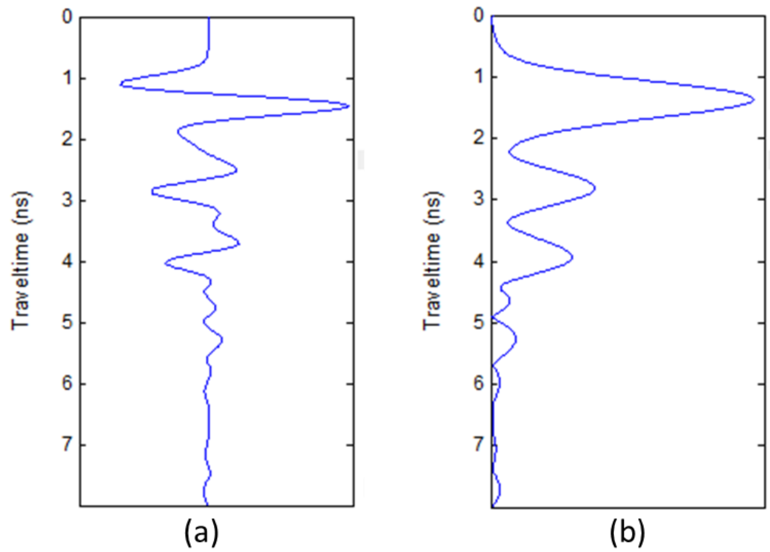

Figure 5.4: Hilbert transform for signal power characterization: (a) GPR A-Scan trace; (b) GPR A-Scan envelope.

5.3.3. Identification of Ballast Region

Prior to 2D entropy analysis, an A-Scan decomposition is performed to remove clutters that are produced due to various sources, such as antenna direct coupling, cross-ties reflection, etc, and to isolate ballast layer for more sophisticated post processing.

For signal decomposition, the transmitter and receiver antennas' direct coupling pulse is utilized as the reference signal which preserves the transmitted pulse signal shape. Cross-correlation is a measure of similarity of two signal sequences as a function of the lag of one relative to the other. Denoting the reference GPR A-Scan trace as $f[t]$

and the target GPR A-Scan trace as $g[t]$, the cross-correlation for these two real signal sequences is defined as:

$$CrossCor(f,g)[\tau] \stackrel{\text{def}}{=} \sum_{t=-\infty}^{\infty} f[t]g[t+\tau] \tag{5.5}$$

The scattering is located at the time shift τ which is determined as

$$\tau = arg\max_{\tau}|CrossCor(f,g)[\tau]| \tag{5.6}$$

By performing iterative cross correlations [16], an A-Scan waveform is decomposed into the combinations of multiple pulses of varying amplitude and phases characterizing the reflection signals from different scatters (i.e. objects or layers). Based on the decomposition result, the signal component corresponding to the ballast layer is picked out and the scope of data analysis is narrowed down to the ballast region.

Figure 5.5 demonstrates the process of A-Scan decomposition. In Figure 5.5(a), the direct coupling signal with amplitude A_1 at time instance t_1 is chosen as the reference signal. As shown in Figure 5.5(b), by performing cross correlation between the reference signal and the A-Scan trace following t_1 time instant, a maximum correlation value is identified at time instance t_2 which corresponds to the first backscattering pulse. Continuing the cross correlation calculation, another backscattering pulse is identified at time instance t_3 as shown in Figure 5.5(c). Finally, the A-Scan trace is decomposed into combinations of three pulses of varying amplitudes and time delays.

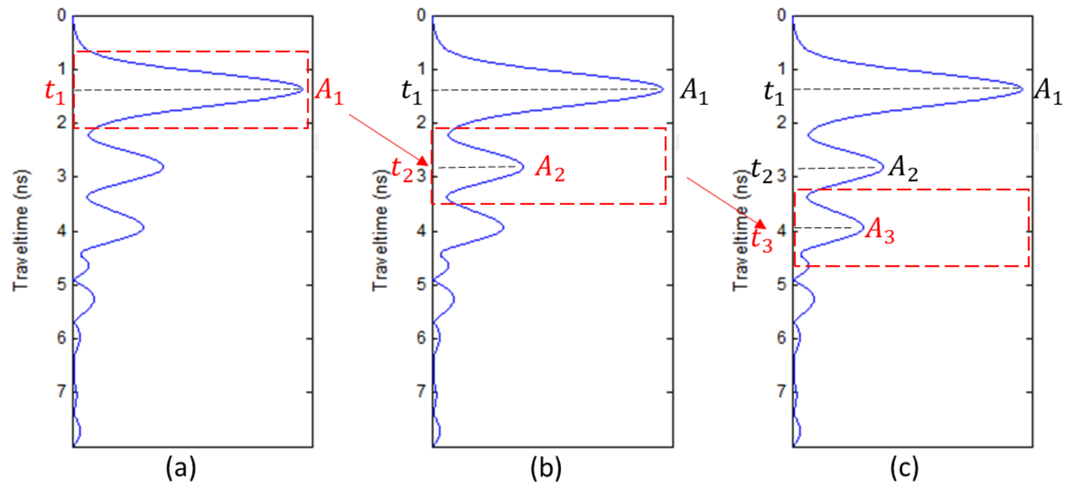

Figure 5.5: Signal decomposition for identification of backscattering from different sources: (a) Direct coupling signal; (b) 1st backscattering pulse; (c) 2nd backscattering pulse.

5.3.4. B-Scan Image Enhancement

Upon ballast region identification, the resultant B-Scan image is further enhanced:

Step 1: Remove the background signals (i.e. air-ground surface reflection signals) using a 2-Dimensional (2D) High Pass Filter (HPF) [17]-[18]. The basic principle of this filtering is that in the B-scan image's horizontal direction, the frequency bandwidth of the background clutter is much narrower than that of subsurface scattering signals.

Step 2: After clutter removal, every 10 A-scan traces are grouped to perform the averaging calculation to further improve signal SNR as well as reduce data volume and redundancy.

5.3.5. Entropy Based Region of Interest (ROI) Detection

Our automatic ROI detection method computes 2D Renyi entropy to characterize data singularity so as to effectively identify and detect the structural features of interest.

In information theory, entropy is a measure of the uncertainty associated with a random variable. For our GPR data processing, entropy characterization is explored to identify singular regions within a large data set. In particular, a high entropy value indicates high degree of data similarity while a low entropy value specifies high degree of data singularity.

The received GPR backscattering signal $Y(t)$ can be modeled with the following equation:

$$Y(t) = D(t) + S(t) \tag{5.7}$$

where $D(t)$ represents the reflection signal from objects of interest, and $S(t)$ models background signals, clutters or other interference signals. For entropy analysis, a power normalization is first performed which can be expressed as

$$y_i(t) = \frac{\|Y_i(t)\|^2}{\sum_{i=1}^{M}\|Y_i(t)\|^2} \tag{5.8}$$

where $y_i(t)$ is the normalized signal, i denotes the trace index, M is the total number of traces included, and t specifies the time index of data points on each reflection trace waveform. Upon the power normalization, a generalized Renyi's entropy [19] is computed to assess the data singularity as:

$$E_\alpha(t) = \frac{1}{1-\alpha}\log_e\langle\sum_{i=1}^{M}[y_i(t)]^\alpha\rangle \tag{5.9}$$

where $E_\alpha(t)$ is the entropy quantification and α is the entropy order. Based on the study in Ref. [10], α = 3 can accomplish optimal performance.

Fouled ballast mixed with sand and fouled ballast of diverse moisture levels produce distinct features of reflection [15], which can be characterized from entropy data values for detecting the singular data regions. Following this idea, an automatic ROI detection method is developed, which consists of the following data processing steps:

Step 1: 2D Renyi entropy calculations in accordance to Eq. (5.9).

Step 2: Entropy curve smoothing using a moving average method [20].

$$E_{smooth}(n) = \frac{1}{m}\sum_{i=n-m+1}^{n} E(i) \tag{5.10}$$

In Eq. (5.10), $E(i)$ denotes the entropy value of index i in entropy data sequence. The moving average method calculates the mean of every m data points to eliminate noise and smooth out the entropy data array. In our analysis, m is selected as 5% of the total number of entropy data points to accomplish optimal smoothing performance as well as preserve the data resolution.

Step 3: Adaptive entropy threshold determination using OTSU's method.

Depending on the data characteristics, regions in a B-scan image can be classified into three categories: singular region, stationary background region and the transition region. The classification of a region can be done through assessing its entropy values against two thresholds K_1 and K_2 ($K_1 < K_2$). Singular regions have entropy values lower than threshold K_1, and stationary background regions have entropy values higher than K_2. For transition regions, their entropy values are amid of these two thresholds. In order to appropriately determine threshold values K_1 and K_2, the automatic OTSU's thresholding method [21] is employed. OTSU's method is a classic image segmentation technique for extracting an object from its background. In principle, an image can be divided into non-overlapping regions by evaluating region's homogeneity through intensity values (i.e. pixel magnitude) variance assessment. For region classification, the intra-class intensity values are close to each other with small variances; while the inter-classes intensity values are significantly different with large variances. OTSU's method performs statistical analysis to identify appropriate thresholds so as to segment image into different regions accomplishing the criteria: the intensity values variances of the same region is minimized while the variances of different regions are maximized.

5.4. Lab Experiment

5.4.1. Test Configuration

To test and verify our automatic ROI region detection method, a test platform is produced emulating a railroad segment as shown in Figure 5.6(a). The test platform is 3.5 meters long, 1.2 meters tall and 1.5 meters wide. It is filled with sand and ballast. One portion of the ballast region is filled with the fouled ballast mixed with sand and water. Figure 5.6(b) illustrates the platform structure: (1) The ballast layer of 0.3 meters thickness is laid above the soil; (2) 0.75 meters apart from the left end of the platform, an area (highlighted in blue) of 0.45 meters length and 0.2 meters depth is filled with the fouled ballast, which is a mixture of sand, ballast, and water. This fouled ballast region is used to evaluate the effectiveness of our GPR system and ROI detection algorithms.

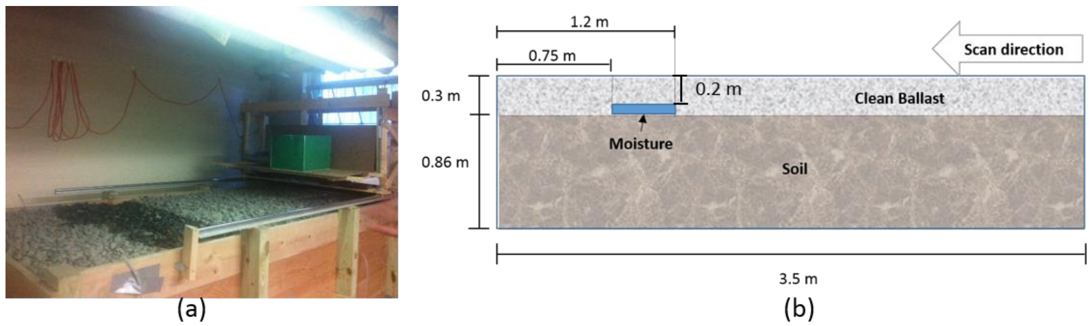

Figure 5.6: Railroad ballast lab test configuration: (a) Test platform; (b) Subsurface structure.

5.4.2. ROI Detection

The GPR raw B-scan image of the test platform is plotted in Figure 5.7(a). Figure 5.7(b) shows the pre-processed B-Scan image upon de-noising with stacking and low pass filtering. The air-ballast interface reflection appears at 8.5 ns, and the ballast-soil interface reflection appears at 12 ns. The two-way travel time of radar incident signal within the clean ballast region equals Δt = 12 ns – 8.5 ns = 3.5 ns, and the one-way travel time is 1.75 ns. Substituting the dielectric constant of clean ballast $\varepsilon_c = 3.2$ [22] into equation $V_c = V/\sqrt{\varepsilon_c}$, where V is the speed of light in air, V_c is calculated as 1.68×10^8 m/s. Using $V_c = d/(\frac{\Delta t}{2})$, the thickness of clean ballast region is computed as 0.294 m approximately. This value agrees well with the actual setup on the test platform in Figure 5.6(b), where the thickness of clean ballast region is 0.3 m.

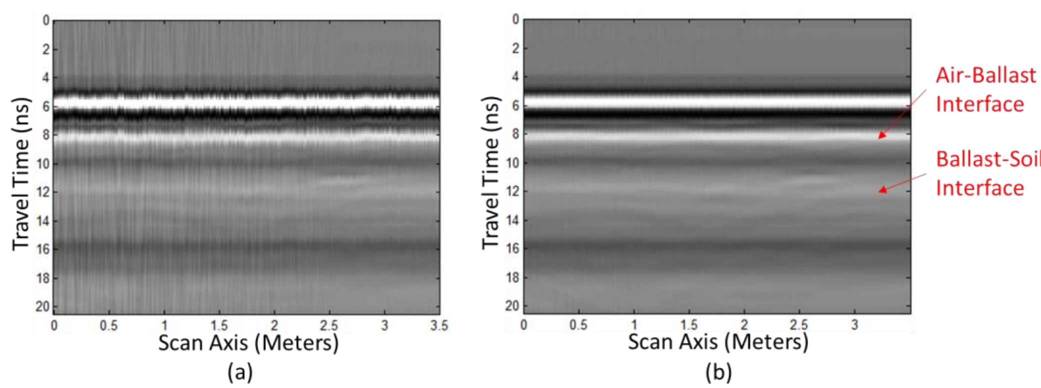

Figure 5.7: B-Scan image from lab tests: (a) Raw B-Scan image; (b) Pre-processed B-Scan image.

After applying the Hilbert transform, the new B-Scan image Figure 5.8(a) is plotted in accordance to signal magnitude envelop, which characterizes the power distribution of the reflection signal. Figure 5.8(c) depicts a sample A-scan waveform, wherein the first pulse corresponds to the direct coupling between the transmitter and receiver antennas, and the second one corresponds to the ground surface reflection signal. Utilizing signal decomposition method, these systematic background signals can be effectively identified and singled out. As shown in Figure 5.8(b), the first white line represents the antennas direct coupling signal (the reference signal), and the ground surface reflection signal is highlighted as the gray line. The ballast region can be located as the region below the ground surface reflection, and is extracted in Figure 5.9(a) separately. Since our interest is only in the ballast layer in this study, the development of the automatic ROI detection method focuses on characterizing the ballast layer, while other layers above it are eliminated. The ballast region data are further enhanced using 2D high pass filtering and 10-trace stacking to improve signal to noise ratio SNR. The resulting B-Scan image is depicted in Figure 5.9(b).

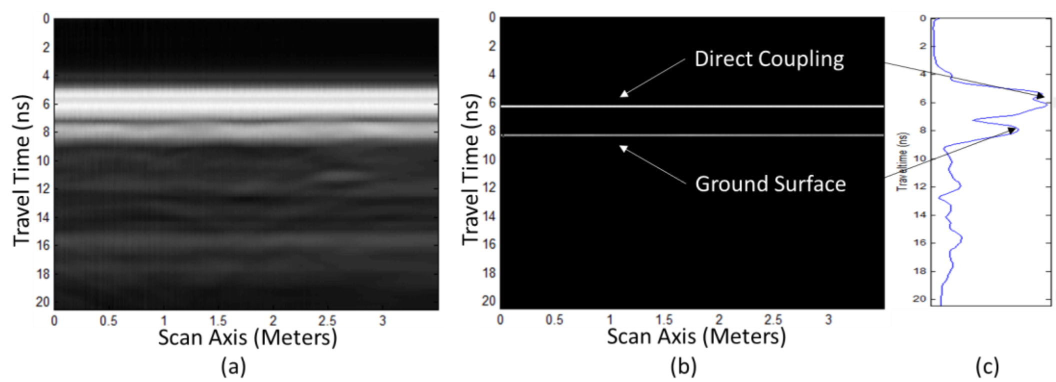

Figure 5.8: Signal Magnitude Characterization through Hilbert Transform: (a) B-Scan image plotted using signal magnitude data; (b) Systematic background signals identified through decomposition method; (c) A sample A-Scan trace waveform.

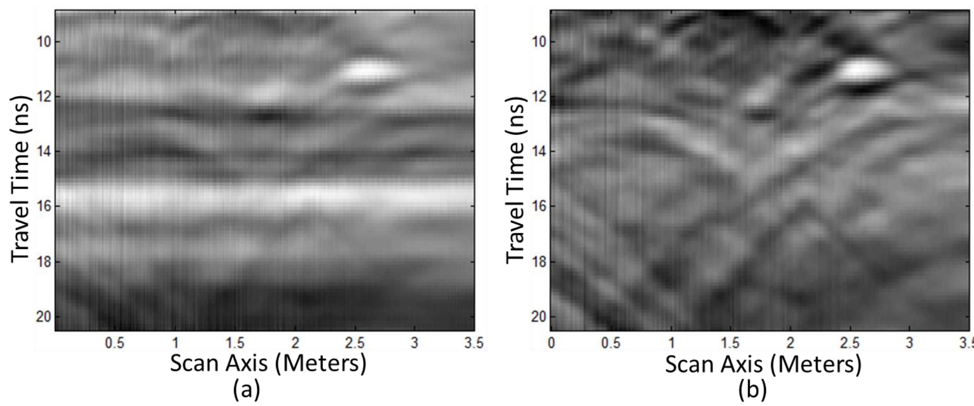

Figure 5.9: B-Scan image for ballast layer: (a) Ballast layer; (b) Enhanced ballast layer.

After obtaining Figure 5.9(b), 2D entropy analysis is calculated, and the resulting curves are shown in Figure 5.10.

For the y-axis entropy curve shown in Figure 5.10(a), two threshold values $K_1 = 5.78$ and $K_2 = 6.22$ are calculated using the OTSU's thresholding method. As illustrated in Figure 5.10(a), there is one region with entropy values smaller than K_1, which locates between $t = 10.80$ ns and 12.30 ns. Similarly, two other threshold values $K_1' = 4.48$ and $K_2' = 4.80$ are also computed for the x-axis entropy curve shown in Figure 5.10(b). A singular region is identified based on threshold K_1', which is located between $x = 2.55$ m and $x = 2.80$ m. Combining both the x-axis and y-axis entropy analysis results, one singular area is marked in Figure 5.11 specifying the fouled ballast area.

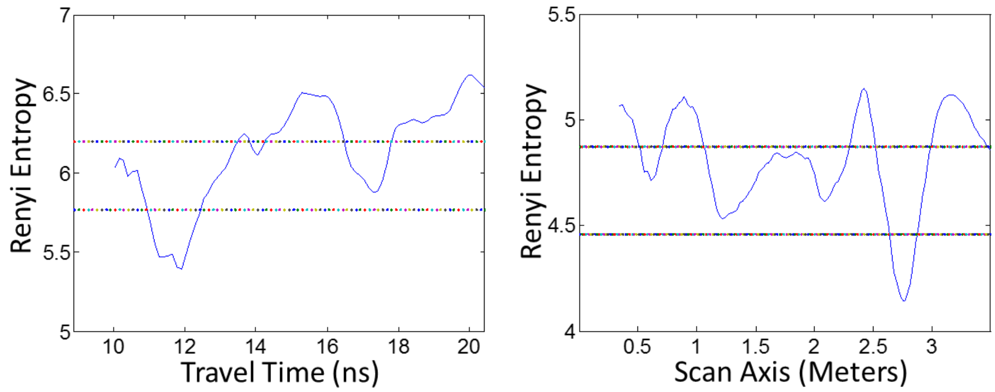

Figure 5.10: Entropy analysis of ballast data of Figure 5.8(b): (a) Entropy along Travel time index (y-axis); (b) Entropy along Scan Axis (x-axis).

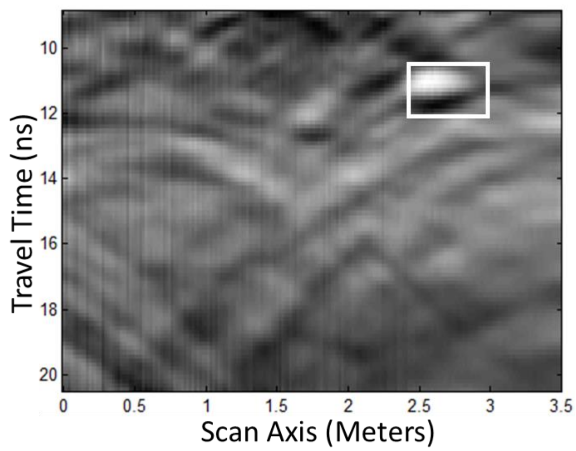

Figure 5.11: 2D entropy analysis of the B-Scan image collected from the test platform.

The depth of the fouled ballast region is computed as follows: In raw B-Scan image Figure 5.7(a), the air-ground surface reflection signal is located at $t = 8.5$ ns, and the top edge of the detected singular region is located at $t = 10.80$ ns. Hence, the two-way travel time of radar incident signal between the air-ground surface and the fouled ballast region equals Δt = 10.80 ns – 8.5 ns = 2.3 ns, and the one-way travel time is 1.15 ns. Substituting the dielectric constant of clean ballast $\varepsilon_c = 3.2$ [22] into equation $V_c =$

$V/\sqrt{\varepsilon_c}$, where V is the speed of light in air, V_c is calculated as 1.68×10^8 m/s. Using $V_c = d/(\frac{\Delta t}{2})$, the depth of the fouled ballast region is computed as 0.193 m approximately. This value agrees well with the actual setup on the test platform in Figure 5.6(b), where the depth of fouled ballast region is 0.2 m. The detection error is only (0.2 - 0.193)/0.2 = 3.5%.

Horizontally, the fouled ballast region spans from 2.4 m to 2.8 m, which is also consistent with the actual setup on the test platform (from 2.55 m to 2.80 m) in Figure 5.6(b). These results validate that the automatic ROI detection method can correctly identify the fouled ballast region. As shown in Figure 5.11, the extracted fouled ballast region comprises less than 5% of the entire data volume, which can significantly reduce computation complexity for other more sophisticated post-processing.

5.5. Inspection of Railroad Ballast

5.5.1. Test Configuration

Table 5.2: Key Parameters Used in the GPR Field Tests.

Data acquisition unit	8 Gsps, 10-bit resolution
Vehicle moving speed	5 miles/h according to railway service regulation
Pulse repetition frequency	Triggered in distance, 10000 triggers per wheel rotation
Vehicle wheel Perimeter	0.77 meter
Signal bandwidth	1.5 GHz
Penetrating capability	1 meter

In August 2013, the research team conducted several field tests at Boston MBTA Green and Red Lines as well as St. Louis Metro Red and Blue Lines. The GPR system is mounted on a hi-rail SUV as shown in Figure 5.12 and the key parameters used in the GPR tests are listed in Table 5.2.

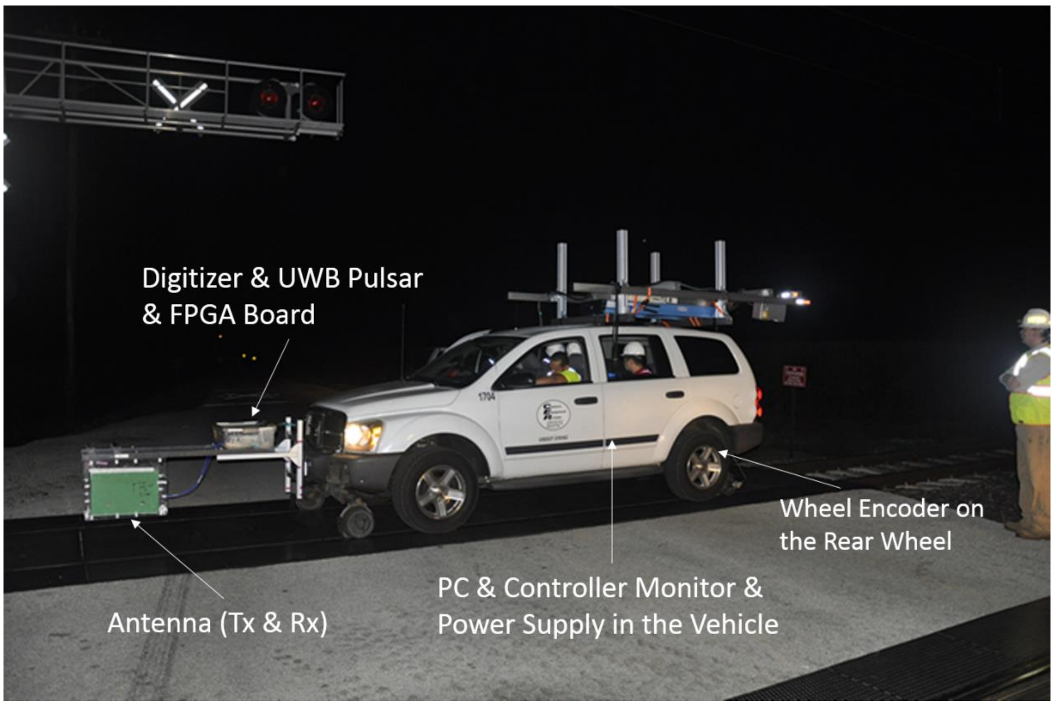

Figure 5.12: GPR System configuration during field tests.

Field tests at Boston MBTA: On August 15th, 2013, the GPR was utilized to scan approximately 2.4 miles of MBTA Green line from Blandford Rd to Summit Ave traveling westbound. On August 16th, 2013, about 3 miles of MBTA Red line from Mattapan Station to Cedar Grove Station traveling eastbound was inspected with GPR.

Field tests at Metro St. Louis: During the night of August 19th and the early morning of August 20th, 2013, the team collected GPR data along MetroLink Red line from Shiloh-Scott Station to Belleville Station for approximately 6 miles. In the night of August 20th and the early morning of August 21st, 2013, the team tested the GPR system along MetroLink Blue line from Forest Park Station to Sunnen Station for approximately 6 miles.

These field tests generate about 300 GB of GPR data. For processing the big data of such volume, the aforementioned GPR signal processing algorithms are applied to automatically detect singular regions of potential interests. In this chapter, a segment of GPR data from Metro St. Louis MetroLink Blue line (about 8 meters long) is used to demonstrate our automatic ROI detection algorithm. Figure 5.13 shows two pictures of the site where the sample GPR data were collected.

(a) (b)

Figure 5.13: Site pictures: (a) Metro St. Louis MetroLink Blue line; (b) Railroad ballast.

5.5.2. ROI Detection

The same pre-processing steps detailed in the preceding sections are implemented for the field test data. The raw B-Scan image is shown in Figure 5.14(a), and the pre-processing result is plotted in Figure 5.14(b).

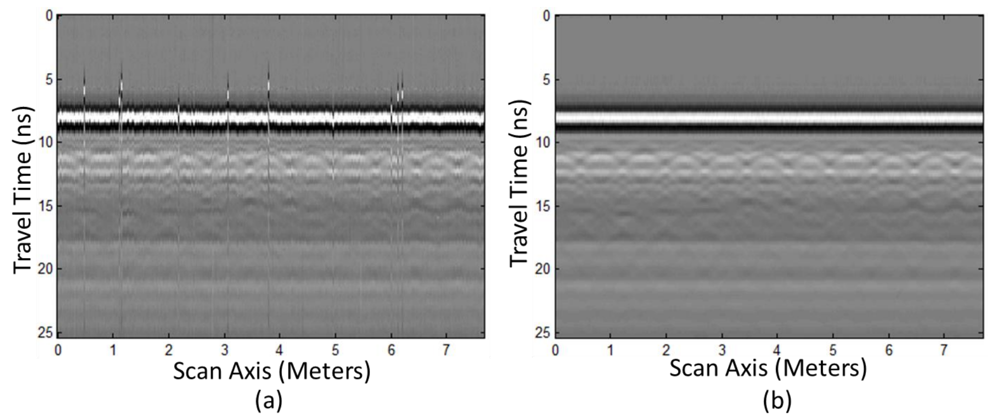

Figure 5.14: (a) Field test raw B-Scan image; (b) Pre-processed B-Scan image.

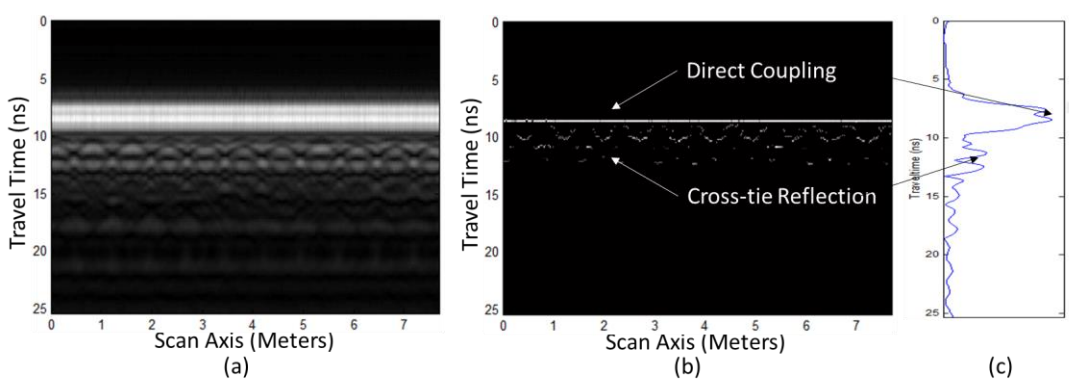

Figure 5.15: (a) Field test B-Scan image obtained from signal magnitude ; (b) cross-tie marked by signal decomposition; (c) A-Scan signal at x = 3.8 m.

Utilizing the Hilbert transform, the envelope of the field test B-Scan image is plotted in Figure 5.15(a), which characterizes the power distribution of the reflection signal. To separate the ballast layer and the cross-tie layer, the first step is to choose the transmitter and receiver antennas' direct coupling pulse as the reference signal, which is the first pulse in Figure 5.15(c). By performing cross correlation using the reference pulse signal, each A-Scan waveform in the B-Scan image (Figure 5.15(a)) is decomposed into combinations of pulses of varying amplitude and time delays representing the reflection signals from different scatters. As shown in Figure 5.15(b) and (c), the second scatter in the B-Scan image (Figure 5.15(a)) is detected as the cross-tie (or sleeper). By removing these two sections, the ballast layer is obtained in Figure 5.16(a).

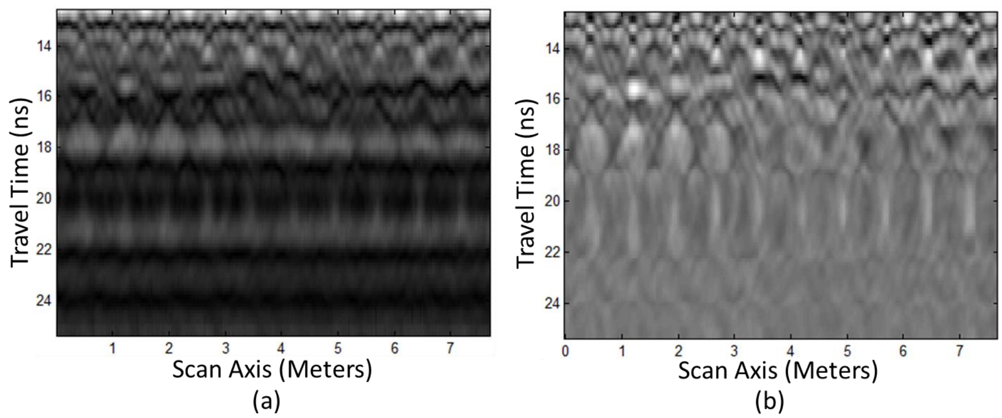

Figure 5.16: B-Scan image for ballast layer: (a) Ballast layer; (b) Enhanced ballast layer.

The ballast region image is further enhanced by clutter removal using 2D high pass filtering and averaging by stacking operation of every 10 traces. The enhanced ballast B-Scan image is shown in Figure 5.16(b).

The 2D entropy characterization algorithm is then utilized to detect singular features. As in the laboratory GPR data processing, high entropy values characterizes high data similarity, while low entropy values specify high degree of singularity.

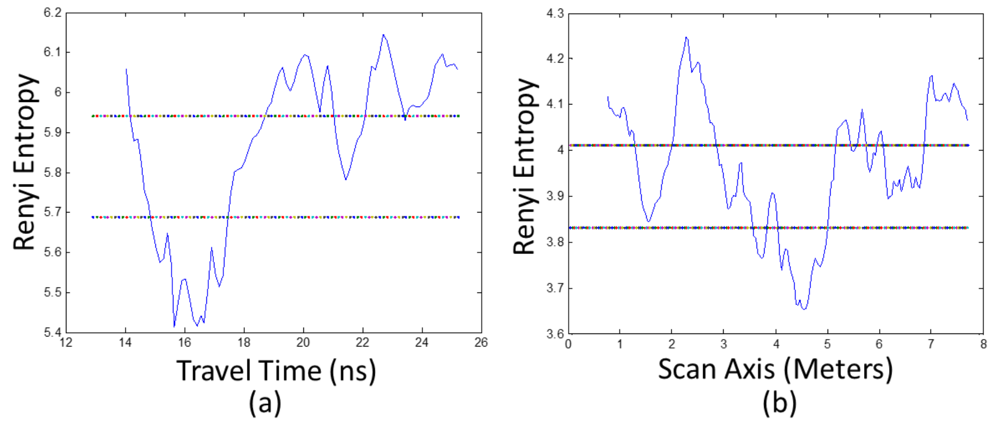

Figure 5.17: Entropy analysis of ballast data of Figure 5.15(b) along: (a) Travel time axis and (b) Scan Distance axis.

As shown in Figure 5.17, the smoothed entropy curves are calculated. Using the OTSU's method, the thresholds for vertical entropy data are computed as $K_1 = 5.69$ and $K_2 = 5.94$ respectively as shown in Figure 5.17(a), and the thresholds for horizontal entropy data are $K_1' = 3.82$ and $K_2' = 4.01$ respectively as shown in Figure 5.17(b). In each direction, regions with entropy values below threshold K_1 or K_1' are considered as the ROI. By combining the entropy analysis results along the vertical and horizontal directions, the automatic ROI detection results are marked out with white rectangles in Figure 5.18. The suspicious fouled ballast region data occupies about 5% of the entire data volume. By narrowing down the data scope, the automatic ROI detection method can remarkably decrease computation complexity and storage space for more sophisticated post-processing. The developed algorithm has been applied to the whole GPR data collected from the field tests at Boston MBTA and Metro St. Louis. Due to the chapter length constraints, only some selected results are presented in this chapter.

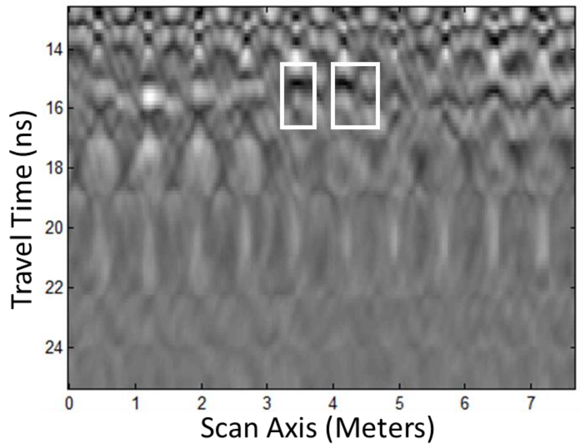

Figure 5.18: Automatic suspicious fouled ballast regions marked by white rectangle.

5.6. Discussion and Conclusions

The advancements in microelectronics technologies have made it possible to design high-speed and high-resolution GPR circuit hardware for large-scale railroad structural inspections. However, the field employments of these GPR technologies unavoidably produce big survey data volume, which challenges data processing. How to effectively detect sporadically distributed singular regions of interest within a big data set is a critical problem for GPR railroad inspections. Although sophisticated GPR data processing methods exist in the literature, most of which are supervised and computationally demanding. The unsupervised automatic ROI detection method developed in this study provides a promising solution to leverage computation efficiency. Moreover it can effectively identify regions of interest in the ballast layer for further in-depth analysis. The proposed unsupervised automatic GPR data processing algorithm has been effectively applied to laboratory and field test data. The analysis results prove that the proposed algorithm can correctly identify the fouled ballast region and can accurately measure the region's location. According to our experiments, the fouled ballast data scope is significantly reduced to less than 5% of the whole data set for both laboratory and field tests. After narrowing down the data scope, sophisticated and computational demanding post-processing can be performed effectively.

5.7. References

[1] D. Huston, J.Q. Hu, K. Maser, W. Weedon, and C. Adam, "GIMA Ground Penetrating Radar System for Monitoring Concrete Bridge Decks," *Journal of Applied Geophysics*, 43(2-4), 139-146 (2000).

[2] P. Shangguan, I.L. Al-Qadi, Z. Leng, R. Schmitt, and A. Faheem, "Innovative Approach for Asphalt Pavement Compaction Monitoring using Ground-Penetrating Radar," *Transportation Research Record: Journal of the Transportation Research Board*, 2347, 79-87 (2013).

[3] X. Xu, T. Xia, A.S. Venkatachalam, and D. Huston, "The Development of a High Speed Ultrawideband Ground Penetrating Radar for Rebar Detection," *ASCE Journal of Engineering Mechanics*, 139(3), 272-285 (2013).

[4] I.L. Al-Qadi, W. Xie, R. Roberts, and Z. Leng, "Data Analysis Techniques for GPR used for Assessing Railroad Ballast in High Radio-Frequency Environment," *ASCE Journal of Transportation Engineering*, 136(4), 392–399 (2010).

[5] W. T. S. Crooks and R. A. Cheke, "Soil moisture assessments for brown locust Locustana pardalina breeding potential using synthetic aperture radar," *Journal of Applied Remote Sensing*, 8(1), 1-22 (2014).

[6] W. Shao, A. Bouzerdoum, and S.L. Phung, "Sparse Representation of GPR Traces with Application to Signal Classification," *IEEE Transactions on Geoscience and Remote Sensing*, 51(7), 3922-3930 (2013).

[7] G. Cervone and B. Haack, "Supervised machine learning of fused RADAR and optical data for land cover classification," *Journal of Applied Remote Sensing*, **6**(1), 1-18 (2012).

[8] P. Shangguan, I.L. Al-Qadi, "Content-based Image Retrieval Approaches to interpret ground penetrating radar data," *Construction and Building Materials*, 69, 10-17 (2014).

[9] Q. Lu, J. Pu, and Z. Liu, "Feature Extraction and Automatic Material Classification of Underground Objects from Ground Penetrating Radar Data," *Journal of Electrical and Computer Engineering*, 2014, 1-10 (2014).

[10] Y. Zhang, P. Candra, G. Wang, and T. Xia. "2-D Entropy and Short-Time Fourier Transform to Leverage GPR Data Analysis Efficiency," *IEEE Transactions on Instrumentation and Measurement*, 64(1), 103-111 (2015).

[11] A.S. Venkatachalam, X. Xu, D. Huston, and T. Xia. "Development of a New High Speed Dual-Channel Impulse Ground Penetrating Radar," *IEEE Journal of Selected Topics in Applied Earth Observations and Remote Sensing*, **7**(3), 753-760 (2014).

[12] T. Xia, X. Xu, A. Venkatachalam and D. Huston, "Development of a High Speed UWB GPR for Rebar Detection," in *Proceedings of IEEE International Conference on Ground Penetrating Radar (GPR) 2012*, 66-70 (2012).

[13] T. Xia, A. S. Venkatachalam, D. Huston, "A High Performance Low Ringing Ultra-Wideband Monocycle Pulse Generator," *IEEE Transactions on Instrumentation and Measurement*, 61(1), 261-266 (2012).

[14] S.K. Mitra, *Digital Signal Processing: A Computer-Based Approach, 4th edition*, McGraw-Hill, New York (2010).

[15] Y. Zhang, A.S. Venkatachalam, Y. Xie, G. Wang, and T. Xia, "Data Analysis Techniques to Leverage Ground Penetrating Radar Ballast Inspection Performance," in *2014 IEEE Radar Conference*, 463 - 468 (2014).

[16] H. Zhang, S. Ouyang, G Wang, S. Wu, and F. Zhang, "Matched filtering algorithm based on phase-shifting pursuit for ground-penetrating radar signal enhancement," *Journal of Applied Remote Sensing*, 8(1), 1-9 (2014).

[17] D. Potin, E. Duflos and P. Vanheeghe, "Landmines Ground-Penetrating Radar Signal Enhancement by Digital Filtering," *IEEE Transactions on Geoscience and Remote Sensing*, 44(9), 2393-2406 (2006).

[18] Y. Zhang, A.S. Venkatachalam, D. Huston, and T. Xia, "Advanced Signal Processing Method for Ground Penetrating Radar Feature Detection and Enhancement," *Proc. SPIE 9063 Nondestructive Characterization for Composite Materials, Aerospace Engineering, Civil Infrastructure, and Homeland Security 2014*, 1-14 (2014).

[19] W. Zhi and F. Chin, "Entropy-Based Time Window for Artifact Removal in UWB Imaging of Breast Cancer Detection," *IEEE Signal Processing Letters*, 13(10), 585-588 (2006).

[20] S.W. Smith, *The Scientist and Engineer's Guide to Digital Signal Processing, Second Edition*, California Technical Publishing, San Diego, 1999.

[21] N. Otsu, "A Threshold Selection Method from Gray-Level Histograms," *IEEE Transactions on Systems, Man and Cybernetics*, 9(1), 62-66 (1979).

[22] Z. Leng and I. L. Al-Qadi, "Dielectric Constant Measurement of Railroad Ballast and Application of STFT for GPR Data Analysis," in *NDTCE'09, Non-Destructive Testing in Civil Engineering, Nantes, France*, 1-6 (2009).

CHAPTER 6: MULTISTATIC GROUND PENETRATING RADAR IMAGING USING BACK-PROJECTION ALGORITHM

6.1. Introduction

Multistatic GPR system contains multiple spatially diverse monostatic radar or bistatic radar components with a shared area of coverage [1]. Each of the components pairs involves a different bistatic angle and target radar cross section. Upon the data fusion between each component pair, the spatial diversity afforded by the multistatic GPR system allows for different aspects of a target being viewed simultaneously. The information gained from various antenna pairs and multiple radar cross sections can give rise to a number of advantages over conventional monostatic or bistatic GPR systems, such as higher signal-to-noise ratio (SNR), signal-to-clutter ratio (SCR), high detection rate, better robustness, etc.

High Signal-to-Noise Ratio (SNR): The multiple measurements at a target from the variety of antenna locations afford the integration of the target scattering signals. While for the measurement noises, the measurements from different antenna locations would cancel each other. Thus, the multistatic GPR imaging can attain a higher SNR comparing to monostatic GPR and bistatic GPR.

High Signal-to-Clutter Ratio (SCR): Multiple looks at a target from the variety of antenna spacings make the GPR easier to distinguish targets of interest from clutter [2]. The clutter characteristic can be affected many parameters, such as bistatic geometry of radar, frequency of transmitting signal, meteorological conditions, polarization of antenna, etc. It has been proven that the magnitude of clutter varies significantly as a function of bistatic geometry [3]. The variety of bistatic geometry and diversity in reflectivity within the multistatic GPR system can alleviate the clutter signal.

High Detection Rate. Many targets only reflect radar energy away to certain angles of narrow range, such as a small target buried beneath a large target, so the monostatic GPR or bistatic GPR may not be able to capture the reflection signal from those targets. Multistatic receivers look at the target from multiple angles so they could have a higher chance to catch the reflection signal.

High Robustness. A fault or malfunction in either transmitter or receiver for a monostatic or bistatic system will lead to a complete loss of radar functionality. While for multistatic GPR system, multiple pairs of transmitters and receivers increase the overall stability and robustness of the system functionality.

The back-projection imaging algorithm is developed for both ground-coupled multistatic GPR and air-coupled multistatic GPR configurations in this chapter. The rest sections of this chapter are organized as following. Sec. 6.2 introduces two popular GPR migration algorithms (Stolt migration and back-projection) for monostatic system and discusses their potential to be extended for multistatic GPR system. Sec. 6.3 describes the development of back-projection algorithm for ground-coupled multistatic GPR imaging, which accounts for the spatial offsets between the transmitter antennas and receiver antennas. Sec. 6.4 proposes the back-projection algorithm for air-coupled multistatic GPR imaging, which deliberates the heights of the antenna platform and the refraction phenomenon at the air-ground interface. In Sec. 6.5, experiments on simulated GPR data are conducted to evaluate the effectiveness of the back-projection algorithm for multistatic GPR imaging application. Concluding remarks are summarized in Sec. 6.6.

6.2. Stolt Migration Algorithm and Back-Projection Algorithm

Among the aforementioned GPR migration methodologies in Sec. 1.3.6, the Stolt migration algorithm (SMA) and back-projection algorithm (BPA) are two most popular and functional algorithms. The development of conventional SMA and BPA as well as comparison between them are described in the subsequent sections.

6.2.1. SMA for Ground-Coupled Monostatic GPR

6.2.1.1. Implementation Method 1

Assuming the subsurface media is homogeneous, the implementation of the SMA for ground-coupled monostatic GPR can be summarized as follows [4]:

(1) Collect the 2-D scattered field B-Scan data $s(x,t)$.

(2) Perform the 2-D Fourier Transform on $s(x,t)$ to transform the data into the wavenumber-frequency domain as $s(k_x,f)$ and normalize it to get $\bar{s}(k_x,f)$. On the cross-range direction, the k_x varies linearly from $-\pi/\Delta x$ to $\pi/\Delta x$, where Δx is the distance interval between two adjacent A-Scan traces in time domain.

(3) Substitute $k_r = \omega/v = 2\pi f/v$ into $\bar{s}(k_x,f)$ to obtain the data in wavenumber-wavenumber domain as $\bar{s}(k_x,k_r)$, where v is the wave propagating velocity in subsurface media. For a homogeneous subsurface media of dielectric constant ε_r, the wave propagating velocity is $v = c/\sqrt{\varepsilon_r}$, where c is the light speed in air.

(4) Map the data from $k_x - k_r$ domain to $k_x - k_z$ domain using

$$k_z = \sqrt{4k_r^2 - k_x^2} \tag{6.1}$$

and do interpolation to produce the uniformly spaced rectangular mesh data as $\tilde{s}(k_x, k_z)$.

(5) Take the 2-D Inverse Fourier Transform on $\tilde{s}(k_x, k_z)$ to produce the final migrated 2-D GPR image $s_{image}(x, z)$ in the scene space under Cartesian coordinates.

6.2.1.2. Implementation Method 2

Recently, another implementation of the SMA was introduced as range migration algorithm (RMA) [5]-[6] for ground-coupled monostatic GPR imaging applications. The implementation of the RMA can be summarized as follows:

(1) Collect the 2-D scattered field B-Scan data $s(x, t)$.

(2) Range and Cross-Range Fourier Transform: Calculate the 2-D Discrete Fourier Transform (DFT) of the GPR data matrix $s(x, t)$ resulting in the wavenumber-frequency domain data matrix $s(k_x, f)$, where the k_x varies linearly from $-\pi/\Delta x$ to $\pi/\Delta x$. In addition to the DFT, the substitution $k_r = 2\pi f / v_{half-way}$ is made to produce the GPR data matrix in wavenumber-wavenumber domain as $s(k_x, k_r)$, where $v_{half-way}$ is the half-way wave propagating velocity in subsurface media. Since in the GPR data collection, the time instance along the range direction actually is the two-way wave propagating time from the target to GPR antenna. However, the GPR image in scene space should show the real depth (or one-way distance) of the target in range direction. Thus, when calculating the wave propagating velocity in the substitution, the RMA utilizes the half-way velocity $v_{half-way} = v/2$, where v is the wave propagating velocity in the media. For a homogeneous subsurface media of dielectric constant ε_r, the wave propagating velocity is $v = c/\sqrt{\varepsilon_r}$.

(3) Stolt Interpolation: Stolt interpolation transforms the 2-D GPR data matrix $s(k_x, k_r)$ from the spatial wavenumber and frequency wavenumber domain $k_x - k_r$, to the spatial wavenumber and spatial wavenumber domain $k_x - k_z$. The Stolt relationship between k_z, k_r and k_x is

$$k_z = \sqrt{k_r^2 - k_x^2} \tag{6.2}$$

Upon this, a 1-D interpolation is applied across all the wavenumber k_r to map them onto k_z resulting in the Stolt interpolated GPR data matrix $\tilde{s}(k_x, k_z)$.

(4) Inverse Fourier Transform to Scene Domain: To convert the Stolt GPR data matrix $\tilde{s}(k_x, k_z)$ into scene domain $s_{image}(x, z)$, a rectangle subsection completely filled with data of the Stolt interpolated data matrix $\tilde{s}(k_x, k_z)$ is taken. For some narrow band GPR imaging application, such rectangle subsection can't be found so all elements with no value in the $\tilde{s}(k_x, k_z)$ would be set to 0. The 2-D Inverse Discrete Fourier Transform (IDFT) is then applied on the rectangle subsection to produce the final migrated 2-D GPR image $s_{image}(x, z)$ in the scene space.

6.2.1.3. Comparison between Two Implementations

Theoretically, the two implementations of SMA in Sec. 6.2.1.1 and 6.2.1.2 are identical. The only difference is the mapping equation. In the first implementation, mapping $k_z = \sqrt{4k_r^2 - k_x^2}$ is performed while the second implementation utilizes the mapping $k_z = \sqrt{k_r^2 - k_x^2}$. The reason is that in the first implementation, $k_r = \omega/v$ is calculated using the normal wave propagating speed $v = c/\sqrt{\varepsilon_r}$. While in the second implementation, $k_r = \omega/v_{half-way}$ is formulated using the half-way wave velocity. The same result of $k_z = \sqrt{4\,\omega^2\varepsilon_r/c^2 - k_x^2}$ will be obtained if the two velocity definitions are substituted into the two mapping equations respectively. This explanation just tries to eliminate the confusion when readers survey the relevant SMA literatures.

6.2.2. Improved SMA for Ground-Coupled Bistatic GPR

Based on phase shift of samples and the wave equation, the traditional SMA interpolates the samples in the frequency-wavenumber (F-K) domain to obtain the reconstructed target in scene space. The F-K domain of samples in SMA can be easily generated by fast Fourier transform (FFT) on the radar range and cross range direction, which has high efficiency. Unfortunately, the traditional SMA or RMA fails to consider the impact of separation between the transmitter and receiver antennas, so the SAR imaging result has object shape distortion and range calculation error for bistatic GPR or multistatic GPR imaging application.

In the bistatic GPR configuration, the transmitter and receiver antennas can be modeled as Figure 6.1. The range direction is denoted as z-axis which indicates the depth in the GPR inspection, while the cross range direction is denoted as x-axis which presents the horizontal GPR survey distance. The coordinate of the receiver antenna during the survey is $(x_R, z_R = 0)$, and that of the transmitter antenna is $(x_T, z_T = 0)$. The separation distance between the transmitter antenna and the receiver antenna is denoted as d, so $x_T = x_R + d$. The coordinate of the target is (x, z). When $d \geq 0.64z$ in the GPR configuration, the separation between the transceiver antennas increases the minimum travel distance of the transmitted signal by 5% at least, which will lead to obvious error in the estimation of target locations for traditional SMA [7].

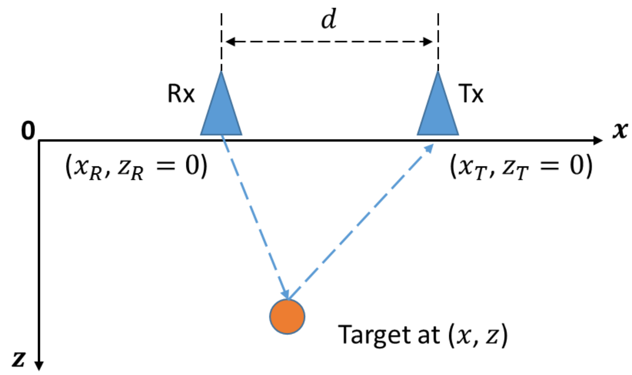

Figure 6.1: One pair of transceiver antennas in multi-static GPR configuration.

A new interpolation scheme in F-K domain that accounts for the widely separated transceivers (WST) has recently been investigated to reconstruct the targets under testing in Ref. [7], which is summarized as follows.

To compensate the impact of the d on the performance of the GPR migration, the 2-D GPR data matrix $s_0(x,t)$ is first converted into a 3-D data matrix $s(x_R, x_T, t)$. The mapping between those two matrices are:

$$\begin{cases} s(x_R, x_T, t) = s_0(x_R, t), \text{ when } x_T = x_R + d \\ s(x_R, x_T, t) = 0, \text{ otherwise} \end{cases} \tag{6.3}$$

If we denote the signal at location (x, z) and time instance t in the EM field as $s_{t,z}(x_R, x_T, t)$, where x_R and x_T are regarded as two independent location variables, the signal collected by the receiver antenna during the movement of the transceivers along the x-axis is $s_{t,z=0}(x_R, x_T, t)$, the data inside which are identical with the 3-D data matrix $s(x_R, x_T, t)$. The time domain signal $s_{t,z=0}(x_R, x_T, t)$ and its F-K domain form $S_{t,z=0}(k_{x_R}, k_{x_T}, \omega)$ can be transformed between each other via the 3-D Fourier transform:

$$S_{t,z=0}(k_{x_R}, k_{x_T}, \omega) = \iiint s_{t,z=0}(x_R, x_T, t) e^{-j(k_{x_R}x_R + k_{x_T}x_T + \omega t)}\, dx_R\, dx_T\, dt \tag{6.4}$$

$$s_{t,z=0}(x_R, x_T, t) = \frac{1}{(2\pi)^3} \iiint S_{t,z=0}\left(k_{x_R}, k_{x_T}, \omega\right) e^{j(k_{x_R} x_R + k_{x_T} x_T + \omega t)}\, dk_{x_R}\, dk_{x_T}\, d\omega$$

(6.5)

where k_{x_R} and k_{x_T} are the wavenumbers of the transmitter and receiver respectively. ω is the angular frequency. When the target coordinate is (x, z), the EM wave field at the target position can be modeled as $s_{t,z}(x_R, x_T, t)$, which is a phase shifted version of $s_{t,z=0}(x_R, x_T, t)$ in F-K domain:

$$s_{t,z}(x_R, x_T, t) = \frac{1}{(2\pi)^3} \iiint S_{t,z=0}\left(k_{x_R}, k_{x_T}, \omega\right) e^{j(k_{x_R} x_R + k_{x_T} x_T + k_{z_R} z + k_{z_T} z + \omega t)}\, dk_{x_R}\, dk_{x_T}\, d\omega \qquad (6.6)$$

Therefore, the target feature in the imaging space is $s_{t=0,z}(x_R, x_T, z) = s_{t,z}(x_R, x_T, t)|t = 0$, i.e.

$$s_{t=0,z}(x_R, x_T, z) = \frac{1}{(2\pi)^3} \iiint S_{t,z=0}\left(k_{x_R}, k_{x_T}, \omega\right) e^{j(k_{x_R} x_R + k_{x_T} x_T + k_{z_R} z + k_{z_T} z)}\, dk_{x_R}\, dk_{x_T}\, d\omega \qquad (6.7)$$

Due to the Maxwell's equations, the target reflection signal should meet the following conditions:

$$\frac{\partial^2 s}{\partial^2 x_R^2} + \frac{\partial^2 s}{\partial^2 z_R^2} - \frac{1}{v^2}\frac{\partial^2 s}{\partial^2 t^2} = 0 \qquad (6.8)$$

$$\frac{\partial^2 s}{\partial^2 x_T^2} + \frac{\partial^2 s}{\partial^2 z_T^2} - \frac{1}{v^2}\frac{\partial^2 s}{\partial^2 t^2} = 0 \qquad (6.9)$$

where v is the signal velocity in the underground medium. If the dielectric constant of the medium is ε_r, the velocity is $v = c/\sqrt{\varepsilon_r}$. The above conditions lead to the following relations between the wavenumbers and angular frequency:

$$k_{x_R}^2 + k_{Z_R}^2 - \omega^2/v^2 = 0 \qquad (6.10)$$

$$k_{x_T}^2 + k_{z_T}^2 - \omega^2/v^2 = 0 \tag{6.11}$$

Denoting that $k_z = k_{z_R} + k_{z_T}$, the angular frequency ω can be expressed in form of k_z as

$$\omega(k_z) = sgn(k_z)\frac{v}{2}\sqrt{2\left(k_{x_R}^2 + k_{x_T}^2\right) + k_z^2 + (k_{x_R}^2 - k_{x_T}^2)^2/k_z^2} \tag{6.12}$$

where $sgn(k_z)$ is the positive or negative sign of k_z. Using the function $\omega(k_z)$, $S_{t,z=0}\left(k_{x_R}, k_{x_T}, \omega\right)$ can be interpolated and projected into a 3-D data matrix $S_{t=0,z}(k_{x_R}, k_{x_T}, k_z(\omega))$ in new coordinate system $(x_R, x_{T,} z)$, which is migrated data in the target space domain or imaging area domain. Substituting Eq. (6.12) into Eq. (6.7), the follow relation between $s_{t=0,z}(x_R, x_T\,, z)$ and $S_{t=0,z}(k_{x_R}, k_{x_T}, k_z)$ can be obtained:

$$s_{t=0,z}(x_R, x_T\,, z) =$$

$$\frac{1}{(2\pi)^3}\iiint S_{t=0,z}(k_{x_R}, k_{x_T}, k_z(\omega))\, g(k_z) e^{j(k_{x_R}x_R + k_{x_T}x_T + k_z z)}\, dk_{x_R}\, dk_{x_T}\, dk_z \tag{6.13}$$

where the weighting coefficients are

$$g(k_z) = \frac{sgn(k_z)v\left(k_z - \left(k_{x_R}^2 - k_{x_T}^2\right)^2/k_z^3\right)}{2\sqrt{2\left(k_{x_R}^2 + k_{x_T}^2\right) + k_z^2 + \left(k_{x_R}^2 - k_{x_T}^2\right)^2/k_z^2}} \tag{6.14}$$

Eq. (6.13) indicates that $S_{t=0,z}(k_{x_R}, k_{x_T}, k_z(\omega))$ is the 3-D inverse Fourier transform of $s_{t=0,z}(x_R, x_T\,, z)$.

Finally, the B-Scan image can be produced as

$$s_{\mathrm{mig}}(x, z) = s_{t=0,z}(x_R, x_R + d, z)\big|_{x = x_R + d} \tag{6.15}$$

The flow chart of the WST-SMA is summarized as

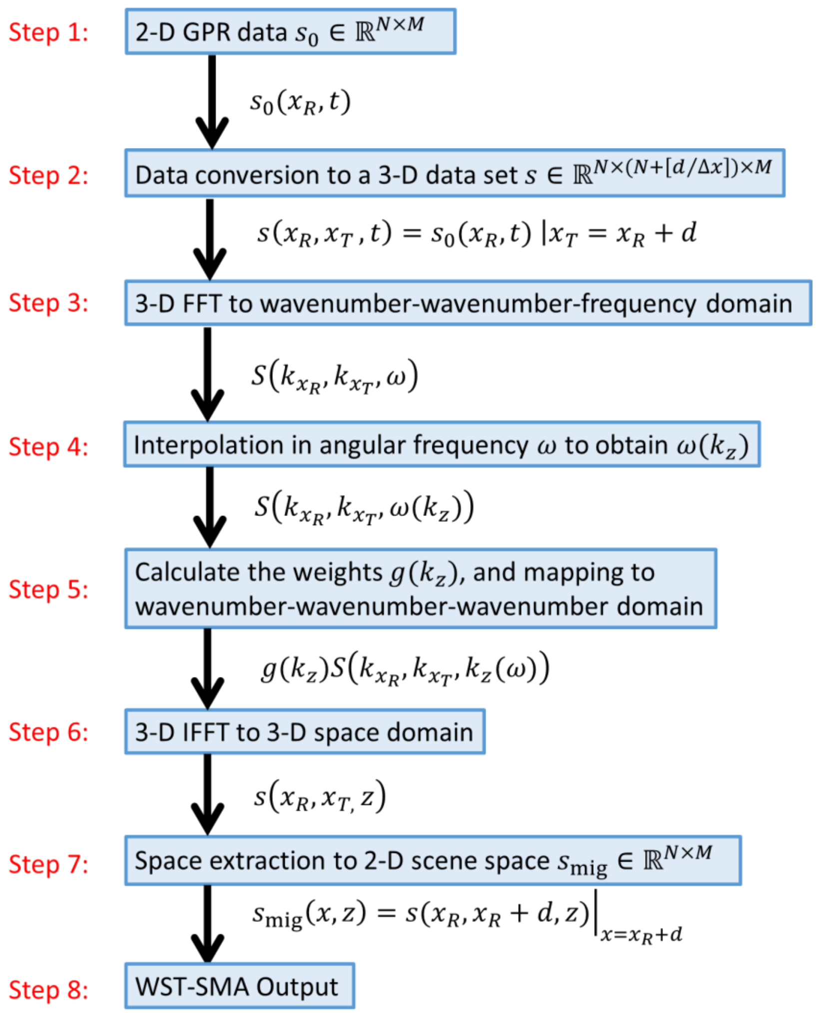

Figure 6.2: WST-SMA Migration Flow Chart.

The WST-SMA accounts for the separation between the transmitter antenna and receiver antenna, so it is an improved version of the traditional SMA for bistatic GPR imaging application. Nevertheless, since the WST-SMA performs all the computations on a 3-D data matrix instead of the original 2-D data matrix, this algorithm sacrifices both computational efficiency and space complexity for achieving a good imaging performance, which could be an issue when processing large GPR data matrix, especially the GPR field test data.

6.2.3. BPA for Ground-Coupled Monostatic GPR

6.2.3.1. Principle

Assuming the subsurface media is homogeneous, the physical principle of the BPA for ground-coupled monostatic GPR can be elaborated as follows [8]-[9]:

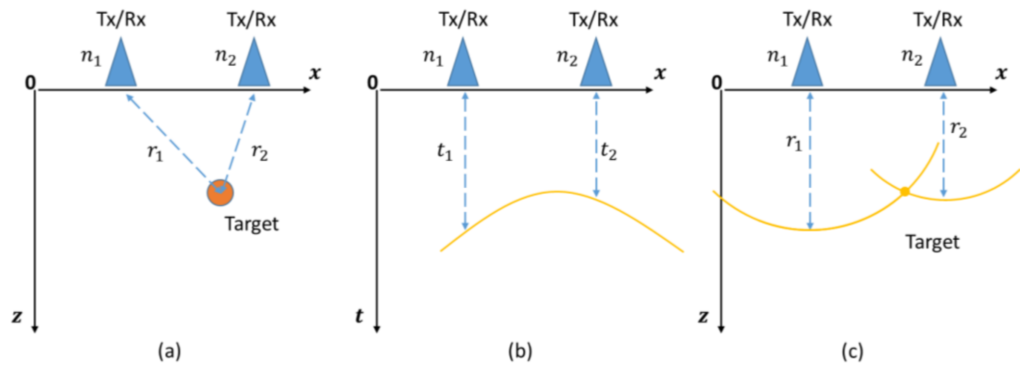

Figure 6.3: Principle of BPA for monostatic GPR: (a) Distance between antenna and target in scene space; (b) Wave propagating time from antenna to target; (c) Time domain data points back projected to scene space.

(1) Collect the 2-D scattered field B-Scan data $s(x, t)$. There are N A-Scan traces in the 2-D GPR data corresponding to signals received at N antenna locations.

(2) Consider the received signal from the target at different antenna locations n_i ($i = 1, 2, \dots, N$). The physical setup is illustrated in Figure 6.3(a), in which two antenna locations are plotted as example. In scene space, the distance between the target and each antenna location is r_i ($i = 1, 2, \dots, N$).

(3) Based on the distance between the target and each antenna location in scene space, the two-way wave propagating time between each antenna location and the target is

$$t_i = \frac{2r_i}{v} \tag{6.16}$$

where v is the wave propagating velocity in the subsurface media. This process is illustrated in Figure 6.3(b).

(4) The scattering source can be located on a semicircle around each antenna location with radius $\bar{r}_i = vt_i/2$, where t_i is the wave propagating time calculated in Step (3) for each antenna position. As an example, in Figure 6.3(c), the semicircles with radius $\bar{r}_1$ and $\bar{r}_2$ are generated in two individual images respectively. Then those two images are superposed to the final migrated GPR image. In the final resulted image, the section where the semicircles overlap will have a strong reflection while the other data points have weak or zero reflection.

(5) Repeat the Step (3) and (4) for all antenna positions and superpose corresponding semicircles on the migrated GPR image. The strong scattering in the migrated image will be considered as the target while the weak scattering considered as the noise or background.

The principle of the BPA indicates that, as long as the wave propagating path between the antenna and the target can be determined, the wave propagating time can be calculated. Further, the data points in the scene space can be reconstructed from the collected data matrix in time domain. Therefore, the BPA algorithm has the potential to be modified and extended for bistatic GPR and multistatic GPR imaging applications.

6.2.3.2. Implementation Method 1

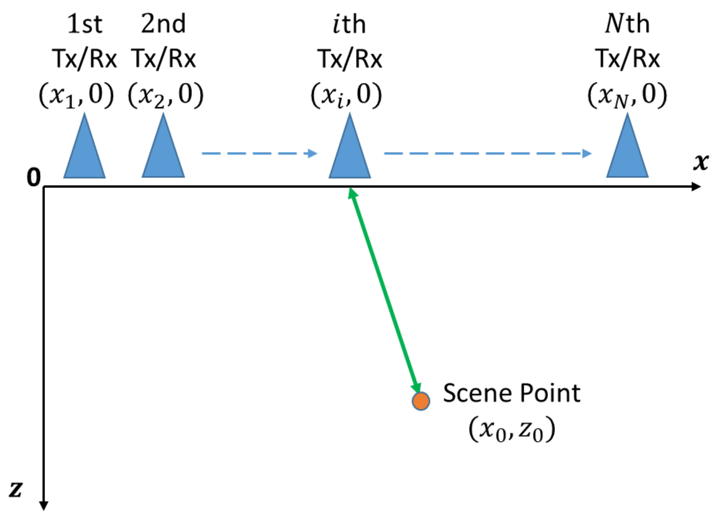

Figure 6.4: Implementation of BPA for ground-coupled monostatic GPR

The monostatic GPR configuration is plotted in Figure 6.4. The implementation of the BPA for ground-coupled monostatic can be described as follows [10]-[11]:

(1) Collect the 2-D scattered field B-Scan data $s(x, t)$. There are N A-Scan traces in the 2-D GPR data corresponding to signals received at N antenna locations. For the ith antenna location, the coordinate of the antenna is $(x_i, 0)$.

(2) For a given scene point $P(x_0, z_0)$ in the GPR testing scenario, the GPR signal transmits from the antenna, propagates to the scene point, and reflects back to the antenna.

(3) For the ith antenna location, the round-trip distance between the antenna at $(x_i, 0)$ and the scene point P at (x_0, z_0) can be calculated as:

$$d_{P,i} = 2\sqrt{(x_0 - x_i)^2 + z_0^2} \tag{6.17}$$

The two-way wave propagating time is

$$t_{P,i} = \frac{d_{P,i}}{v} = \frac{2\sqrt{(x_0 - x_i)^2 + z_0^2}}{v} = \frac{2\sqrt{(x_0 - x_i)^2 + z_0^2}}{c/\sqrt{\varepsilon_r}} \tag{6.18}$$

where ε_r is the dielectric constant of the subsurface media. Here we assume that the subsurface is a homogeneous media.

(4) For this given scene point P, calculate the two-way wave propagating time from P to each of the antenna position as $\{t_{P,1}, t_{P,2}, \dots, t_{P,N}\}$.

(5) The scattering signal of scene point P is recorded in all the N received signals at the N antenna locations. Denote the A-Scan trace signal at ith antenna is $s_i(t)$. Interpolate in the $s_i(t)$ to obtain the scattering from point P in the ith A-Scan trace:

$$S_{P,i} = s_i(\tau)|_{\tau = t_{P,i}} \tag{6.19}$$

(6) Perform interpolation and Eq. (6.19) on all the A-Scan traces, the scattering from point P in each A-Scan trace can be obtained as $\{S_{P,1}, S_{P,2}, \dots, S_{P,N}\}$. If point P is out of the illuminated area of the kth antenna location, then $S_{P,k}$ is set to 0.

(7) The final value of the point $P(x_0, z_0)$ in the scene space can be formulated as:

$$S_{image}(x_0, z_0) = \sum_{i=1}^{N} S_{P,i} \tag{6.20}$$

(8) Repeat Step (2)-(7) for all the points in the scene space to produce the migrated GPR image.

Considering the interpolation is the most time consuming computation in this implementation, let us quantify how many interpolations are performed to complete this migration process. For GPR data matrix or the imaging region of size $M \times N$, signals are recorded at N antenna locations as N A-Scan traces, and each A-Scan trace consists of M data points. Assume we set a scene space of size $M_0 \times N_0$. In this implementation of

BPA, a point P in the scene space is given and the scattering signal of this point in each A-Scan trace is calculated by interpolation. Then the scattering signals recorded in each A-Scan traces are projected back to the point P. So N interpolations are required for one data point in the scene space. This process will be repeated for all data points in the GPR imaging scene space for M_0N_0 times. Finally, M_0N_0N times of interpolation are computed during the BPA migration process.

6.2.3.3. Implementation Method 2

An alternative implementation was proposed in Ref. [12] comprising less times of interpolation:

(1) Collect the 2-D scattered field B-Scan data $s(x,t)$. There are N A-Scan traces in the 2-D GPR data corresponding to signals received at N antenna locations. For the ith antenna location, the coordinate of the antenna is $(x_i, 0)$. Initialize the migrated GPR image as $S_{image}(x,z)$ consisting of $M_0 \times N_0$ scene points. For a given scene point $P(x_0, z_0)$ in the GPR testing scenario, the GPR signal transmits from the antenna, propagates to the scene point, and reflects back to the antenna.

(2) For the ith antenna location, the round-trip distance between the antenna at $(x_i, 0)$ and the scene point P at (x_0, z_0) can be calculated as:

$$d_{P,i} = 2\sqrt{(x_0 - x_i)^2 + z_0^2} \tag{6.21}$$

The two-way wave propagating time is

$$t_{P,i} = \frac{d_{P,i}}{v} = \frac{2\sqrt{(x_0-x_i)^2+z_0^2}}{v} = \frac{2\sqrt{(x_0-x_i)^2+z_0^2}}{c/\sqrt{\varepsilon_r}} \tag{6.22}$$

where ε_r is the dielectric constant of the subsurface media. Here we assume that the subsurface is a homogeneous media.

(3) For the ith antenna location, calculate the two-way wave propagating time from it to each of the scene points in the scene space $S_{image}(x, z)$ as a matrix:

$$T_i = \begin{bmatrix} t_i(x_1, z_1) & \cdots & t_i(x_{N_0}, z_1) \\ \vdots & \ddots & \vdots \\ t_i(x_1, z_{M_0}) & \cdots & t_i(x_{N_0}, z_{M_0}) \end{bmatrix} \tag{6.23}$$

(4) The ith A-Scan trace at the ith antenna location records the scattering signal from all the scene points in $S_{image}(x, z)$. Denote the A-Scan trace signal collected at ith antenna location is $s_i(t)$. Interpolate in the $s_i(t)$ to obtain the scattering from point $P(x_n, z_m)$ that recorded in the ith A-Scan trace, and project this scattering back to the scene space:

$$S_i(x_n, z_m) = s_i(\tau)|_{\tau = t_i(x_n, z_m)} \tag{6.24}$$

Eq. (6.24) represents the contribution $S_i(x, z)$ of the ith A-Scan trace to the migrated image in scene space. For those scene points out of the illuminated area of the ith antenna location, their corresponding values in $S_i(x, z)$ are set to 0.

(5) Repeat Step (2)-(4) on all the A-Scan traces, the contribution of each A-Scan trace to the migrated image can be obtained as $\{S_1(x, z), S_2(x, z), \dots, S_N(x, z)\}$. Finally, the migrated image can be formulated as:

$$S_{image}(x, z) = \sum_{i=1}^{N} S_i(x, z) \tag{6.25}$$

In this implementation of BPA, an A-Scan trace received at the ith antenna location is given and the scattering signals from all the scene points recorded in this A-Scan trace are calculated by interpolation. Then the scattering signals from all the scene points recorded in this A-Scan trace are projected back to the scene space. So just one interpolation is applied when calculating the contribution of the ith A-Scan signal to the scene space. This process will be repeated for all antenna locations by N times. Totally, only N times of interpolation are computed during the BPA migration process.

6.2.3.4. Comparison between Two Implementations

Comparing to the implement in Sec. 6.2.3.2, the implementation in Sec. 6.2.3.3 has three advantages:

(1) Since much less times of interpolation are performed, this implementation of BPA has much lower computational cost.

(2) The data in each A-Scan are only accessed within one single loop, so the process or computation on each A-Scan signal is independent to each other, which benefits the parallel processing and computing.

(3) The A-Scan is used as a unit in each loop within the implementation, so, highly vectorized programming scheme can be utilized in MATLAB to implement the algorithm with concise and efficient code.

Therefore, the implementation of BPA described in Sec. 6.2.3.3 is a better option from multiple aspects. All the discussions on BPA in the following sections of this chapter will be based on this implementation.

6.2.4. Comparison between SMA and BPA

Comparisons between the SMA and BPA for GPR imaging are summarized as follows:

Image Quality: The range resolutions of the SMA and BPA are nearly the same for experimental measurements [13]. On the other hand, the effects of the antenna's finite beam-width is incorporated in the BPA, since the back-projection is only performed on the scene points that fall inside the antenna's illuminated area. Thus, BPA performs better than SMA when dealing with the antenna's side-lobes.

Computational Cost: The time complexity of BPA is $\mathcal{O}(N^3)$. The time complexity of conventional SMA for monostatic GPR imaging is only $\mathcal{O}(N^2)$, while for bistatic GPR imaging, the improved SMA described in Sec. 6.2.2 also has time complexity of $\mathcal{O}(N^3)$. Thus, for potential multistatic GPR imaging, the time complexity of BPA and SMA are close to each other. However, BPA lends itself naturally to parallel processing [12]. Firstly, BPA can be performed on any selected sub-region of the scene space, so the scene space can be divided into several sub-region and each sub-region can be imaged separately on different hardware processors. Secondly, the BPA processes each A-Scan signal individually, so the GPR data matrix can be divided into several groups of A-Scan traces and each group can be processed parallel on separated processors. Thus, BPA is suitable for parallel computation. Overall speaking, the computational cost of BPA is not a severe issue for multistatic GPR imaging.

Real-Time Application: For some GPR applications, especially multistatic GPR applications such as landmine detection [15]-[17], the real-time GPR imaging is urgently demanded. Since the BPA processes each A-Scan signal individually, so it can generate the GPR image as collecting the data. While for the SMA, all the measurements have to be record as a B-Scan since cross range FFT is one of the steps in SMA, so SMA has to wait until the whole GPR inspection is completed. Therefore, the BPA is more suitable for real-time GPR imaging than SMA.

Geometry Configuration: Due to the FFT operation, SMA requires a uniform spatial sampling along the cross range direction, which limits its geometry configuration. This could be an issue for multistatic GPR. The increments in the separation distances between different transmitter antennas and receiver antennas may not be uniform, so the overall spatial distribution of the GPR measurements from all bistatic pairs is not uniform for the data fusion process. Therefore, the geometry configuration requirement of SMA limits its utilization in multistatic GPR application. While for the BPA, as long as the coordinates of bistatic pairs are known, the data points can be accurately projected back to the scene space.

In summary, BPA is more suitable for multistatic GPR imaging than SMA from above four perspectives. A BPA imaging algorithm would be developed in this chapter for multistatic GPR imaging application in the following sections.

6.3. Ground-Coupled Multistatic GPR Imaging Methodology

As a starting point, back-projection imaging algorithm for ground-coupled multistatic GPR is described in this section. It is a special and simplified case of air-coupled multistatic imaging algorithm.

6.3.1. System Configuration

Given a multistatic GPR system with M transmitter antennas and N receiver antennas depicted as Figure 6.5, there are totally $M \times N$ bistatic pairs or transceiver antennas pairs. The antennas are assembled on an antenna platform. During the GPR survey, the antenna platform moves along the cross-range direction and records signals at K positions. At each data collection location, all transmitter antennas are switched on sequentially. When one transmitter antenna is on, N A-Scan traces are recorded by N receiver antennas respectively and simultaneously. After switching between all M transmitter antennas, totally $M \times N$ A-Scan traces are recorded by the GPR system. This data acquisition step is repeat at every antenna platform scanning position. Finally, $M \times N \times K$ A-Scan traces are recorded and assembled into one GPR data matrix for this GPR inspection job.

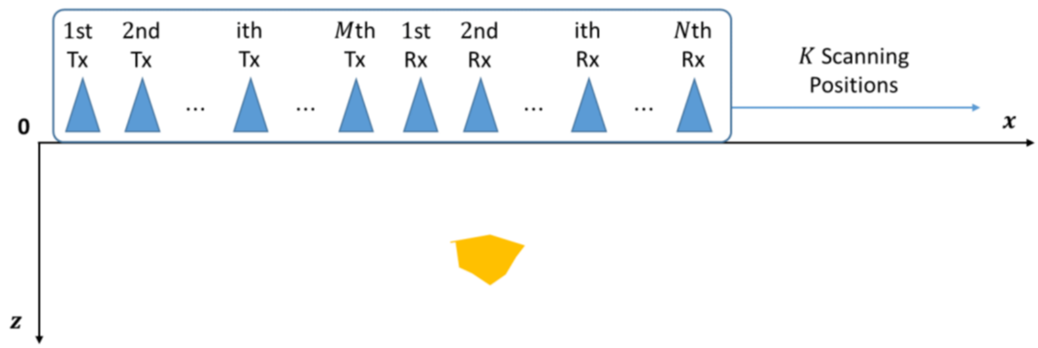

Figure 6.5: Ground-coupled multistatic GPR configuration.

6.3.2. BPA for Ground-Coupled Multistatic GPR Imaging

The back-projection based multistatic GPR imaging algorithm aims to fuse the $M \times N \times K$ A-Scan traces from different bistatic pairs and signal measurement locations into one B-Scan image. The imaging configuration of ground-coupled multistatic GPR is illustrated in Figure 6.6. A 2-D coordinate in scene space is constructed and all the bistatic pairs share the same coordinate system. The x-axis is the cross-range direction or the GPR scanning direction. Antenna platform consisting of M transmitter antennas and

N receiver antennas is moving along the x-axis during the GPR survey. The z-axis is the range direction or the penetrating depth. Assume the subsurface media is a homogenous media of dielectric constant ε_r.

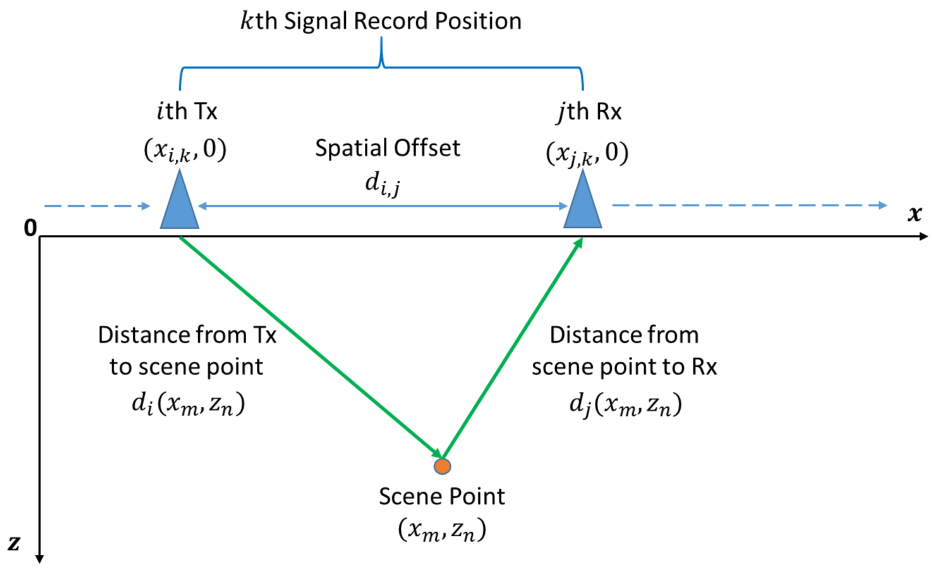

Figure 6.6: Ground-coupled multistatic GPR imaging.

As an example, one bistatic pair at one antenna platform scanning location is plotted in Figure 6.6. When the antenna platform is at the kth scanning location ($k = 1, 2, \dots, K$), the coordinate of the ith transmitter antenna ($i = 1, 2, \dots, M$) is $(x_{i,k}, 0)$ and the coordinate of the jth receiver antenna ($j = 1, 2, \dots, N$) is $(x_{j,k}, 0)$. In this example, the ith transmitter antenna and the jth receiver antenna form a bistatic pair (i, j), and the spatial offset between them is $d_{i,j}$ which is a fixed value during the GPR survey.

Define the scene region as $S \in \mathbb{R}^{M_0 \times N_0}$ consisting of $M_0 \times N_0$ scene points. For a scene point $P(x_m, z_n)$ where $m = 1, 2, \dots, M_0$ and $N = 1, 2, \dots, N_0$, the GPR signal transmits from the ith transmitter antenna to it and then reflects back to the jth receiver antenna at the kth scanning position. The wave propagating distance between the ith transmitter antenna at $(x_{i,k}, 0)$ and the scene point P at (x_m, z_n) can be calculated as:

$$d_{i,k}(x_m, z_n) = \sqrt{(x_m - x_{i,k})^2 + z_n^2} \tag{6.26}$$

The corresponding wave propagating time for $d_{i,k}(x_m, z_n)$ is:

$$t_{i,k}(x_m, z_n) = \frac{d_{i,k}(x_m, z_n)}{v} = \frac{\sqrt{(x_m - x_{i,k})^2 + z_n^2}}{v} = \frac{\sqrt{(x_m - x_{i,k})^2 + z_n^2}}{c/\sqrt{\varepsilon_r}} \tag{6.27}$$

Similarly, the wave propagating distance from the scene point P at (x_m, z_n) to the jth receiver antenna at $(x_{j,k}, 0)$ and corresponding propagating time can be formulated as:

$$d_{j,k}(x_m, z_n) = \sqrt{(x_m - x_{j,k})^2 + z_n^2} \tag{6.28}$$

$$t_{j,k}(x_m, z_n) = \frac{d_{j,k}(x_m, z_n)}{v} = \frac{\sqrt{(x_m - x_{j,k})^2 + z_n^2}}{v} = \frac{\sqrt{(x_m - x_{j,k})^2 + z_n^2}}{c/\sqrt{\varepsilon_r}} \tag{6.29}$$

Adding Eq. (6.27) and Eq. (6.29) together, the round-trip wave propagating time between the scene point $P(x_m, z_n)$ and the bistatic pair (i, j) is expressed as:

$$\begin{aligned} t_{(i,j),k}(x_m, z_n) &= t_{i,k}(x_m, z_n) + t_{j,k}(x_m, z_n) \\ &= \frac{\sqrt{(x_m - x_{i,k})^2 + z_n^2}}{c/\sqrt{\varepsilon_r}} + \frac{\sqrt{(x_m - x_{j,k})^2 + z_n^2}}{c/\sqrt{\varepsilon_r}} \end{aligned} \tag{6.30}$$

For the bistatic pair (i, j), calculate the two-way wave propagating times between it and each of the scene points in the scene space S as a matrix:

$$T_{(i,j),k}(x, z) = \begin{bmatrix} t_{(i,j),k}(x_1, z_1) & \cdots & t_{(i,j),k}(x_1, z_{N_0}) \\ \vdots & \ddots & \vdots \\ t_{(i,j),k}(x_{M_0}, z_1) & \cdots & t_{(i,j),k}(x_{M_0}, z_{N_0}) \end{bmatrix} \tag{6.31}$$

The A-Scan trace measured by bistatic pair (i, j) at the kth antenna platform location $s_{(i,j),k}(t)$ records the scattering signal from all the scene points in $S_{image}(x, z)$.

Interpolate in the $s_{(i,j),k}(t)$ to obtain the scattering from point $P(x_n, z_m)$ that recorded by the bistatic pair (i, j) at the kth antenna platform location, and project this scattering back to the scene space:

$$S_{(i,j),k}(x_n, z_m) = s_{(i,j),k}(\tau)|_{\tau=t_{(i,j),k}(x_n,z_m)} \tag{6.32}$$

The contribution $S_{(i,j),k}(x, z)$ of the bistatic pair (i, j) at kth antenna platform location to the migrated image in scene space can be formulated as:

$$S_{(i,j),k}(x, z) = \begin{bmatrix} S_{(i,j),k}(x_1, z_1) & \cdots & S_{(i,j),k}\left(x_1, z_{N_0}\right) \\ \vdots & \ddots & \vdots \\ S_{(i,j),k}\left(x_{M_0}, z_1\right) & \cdots & S_{(i,j),k}\left(x_{M_0}, z_{N_0}\right) \end{bmatrix} \tag{6.33}$$

For those scene points out of the illuminated area of the bistatic pair (i, j) at the kth location, their corresponding values in $S_{(i,j),k}(x, z)$ are set to 0.

Repeating above processing for the bistatic pair (i, j) on the A-Scan traces at every platform location, the contribution of A-Scan traces at each antenna platform location to the migrated image can be obtained as $\left\{S_{(i,j),1}(x, z), S_{(i,j),2}(x, z), \dots, S_{(i,j),K}(x, z)\right\}$. The imaging data matrix produced by the static pair (i, j) can be formulated as:

$$S_{(i,j)}(x, z) = \sum_{k=1}^{K} S_{(i,j),k}(x, z) \tag{6.34}$$

Repeating above processing for every bistatic pair in the multistatic GPR system, the imaging data matrix for each bistatic pair can be obtained as $S_{(i,j)}(x, z)$ where $i = 1, 2, \dots, M$ and $j = 1, 2, \dots, N$. The final migrated GPR image can be formulated as the superposition of the $S_{(i,j)}(x, z)$ from each bistatic pair:

$$S_{\text{image}}(x, z) = \sum_{i=1}^{M} \sum_{j=1}^{N} S_{(i,j)}(x, z) \tag{6.35}$$

For algorithm development and elaboration purpose, we set $S_{\mathrm{image}}(x, z)$ as a gridded rectangle. However, for real GPR imaging application, $S_{\mathrm{image}}(x, z)$ can be subsurface region of arbitrary shape that the GPR operator would like to inspect.

6.4. Air-Coupled Multistatic GPR Imaging Methodology

The back-projection imaging algorithm for air-coupled multistatic GPR is described in this section. Based on the ground-couple version, the air-couple multistatic GPR imaging methodology accounts for the height of the antenna platform and the refraction phenomenon of the propagating signal at the air-ground interface.

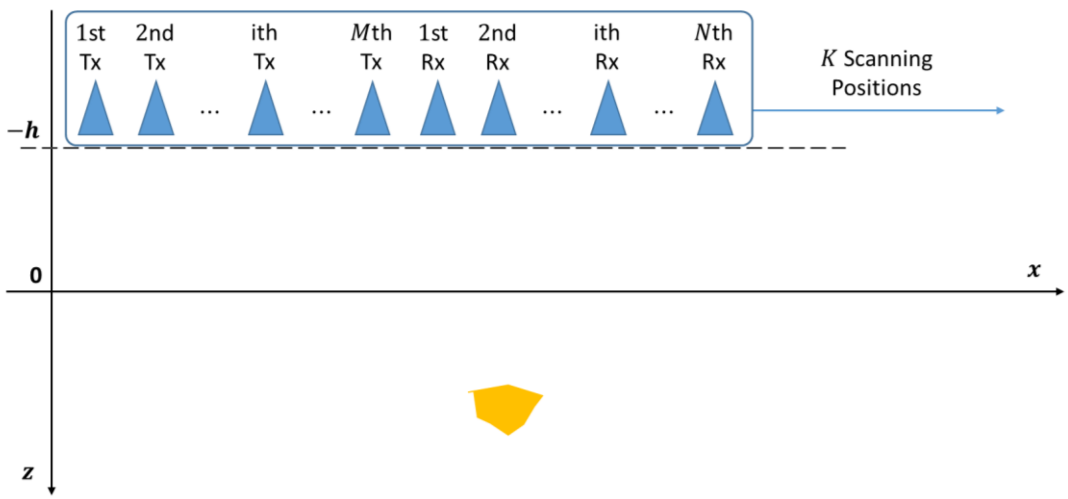

Figure 6.7: Air-coupled multistatic GPR configuration.

The system configuration of the air-couple multistatic GPR is almost the same as ground-coupled multistatic GPR. The only difference is the antenna platform is above the ground surface with a height of h as depicted in Figure 6.7. The configuration of the array of the transmitter antennas and receiver antennas in Figure 6.7 is just for demonstration purpose. In practical hardware design, the sequence, heights and spatial offsets of the antennas can be adjusted to achieve different system specifications [18]-[21].

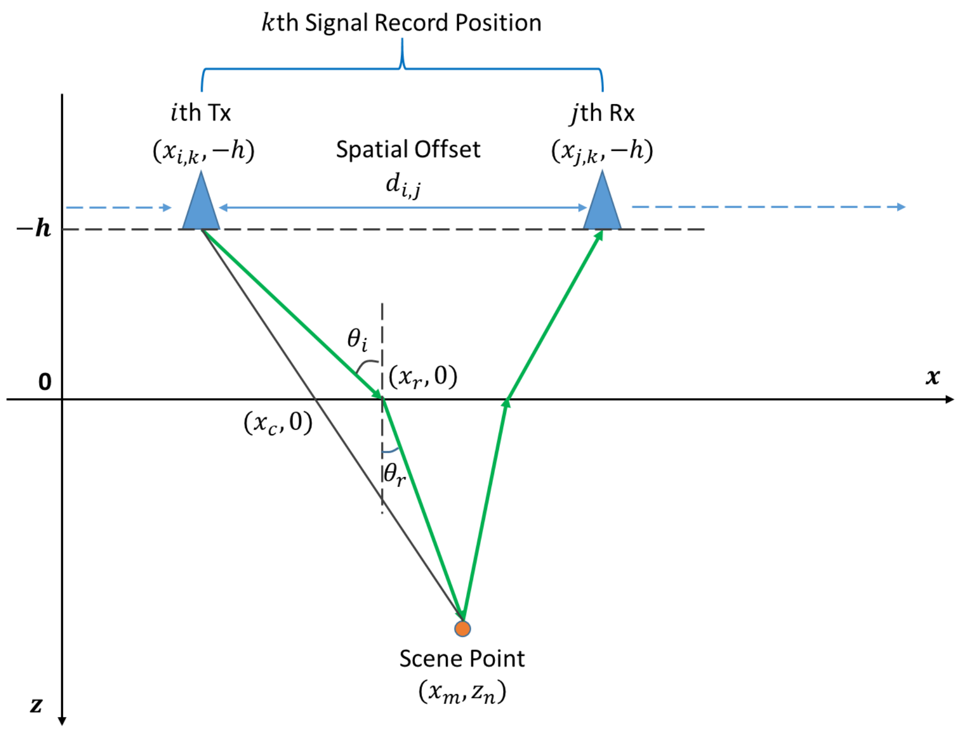

Figure 6.8: Air-coupled multistatic GPR imaging.

One bistatic pair at one antenna platform scanning location is plotted in Figure 6.8. When the antenna platform is at the kth scanning location ($k = 1, 2, \dots, K$), the coordinate of the ith transmitter antenna ($i = 1, 2, \dots, M$) is $(x_{i,k}, -h)$ and the coordinate of the jth receiver antenna ($j = 1, 2, \dots, N$) is $(x_{j,k}, -h)$. In this example, the ith transmitter antenna and the jth receiver antenna form a bistatic pair (i, j), and the spatial offset between them is $d_{i,j}$ which is a fixed value during the GPR survey.

Define the scene region as $S \in \mathbb{R}^{M_0 \times N_0}$ consisting of $M_0 \times N_0$ scene points. For a scene point $P(x_m, z_n)$ where $m = 1, 2, \dots, M_0$ and $N = 1, 2, \dots, N_0$, the GPR signal transmits from the ith transmitter antenna to the air-ground interface, refracts into the ground, reaches the scene point P, reflects back to the ground-air interface, refracts out of the ground and then propagates back to the jth receiver antenna at the kth scanning position.

The wave propagating path is displayed in Figure 6.8. In the path from the transmitter antenna to the scene point, the EM wave refracts at point $(x_{r,(i,k),(x_m,z_n)}, 0)$ on the air-ground interface. To determine the wave propagating path, the value of $x_{r,(i,k),(x_m,z_n)}$ should be solved. The angle of incidence is θ_i and the angle of refraction is θ_r, whose values satisfy the Snell's law:

$$\frac{\sin\theta_i}{\sin\theta_r} = \sqrt{\varepsilon_r} \tag{6.36}$$

According to the geometry, the angle of incidence θ_i and angle of refraction θ_r can also be expressed as:

$$\sin\theta_i = \frac{|x_{r,(i,k),(x_m,z_n)} - x_{i,k}|}{\sqrt{(x_{r,(i,k),(x_m,z_n)} - x_{i,k})^2 + h^2}} \tag{6.37}$$

$$\sin\theta_r = \frac{|x_m - x_{r,(i,k),(x_m,z_n)}|}{\sqrt{(x_m - x_{r,(i,k),(x_m,z_n)})^2 + z_n^2}} \tag{6.38}$$

Substituting Eq. (6.37) and Eq. (6.38) into Eq. (6.36), the following quartic equation can be obtained:

$$\frac{|x_{r,(i,k),(x_m,z_n)} - x_{i,k}|}{\sqrt{(x_{r,(i,k),(x_m,z_n)} - x_{i,k})^2 + h^2}} \cdot \frac{\sqrt{\left(x_m - x_{r,(i,k),(x_m,z_n)}\right)^2 + z_n^2}}{|x_m - x_{r,(i,k),(x_m,z_n)}|} = \sqrt{\varepsilon_r} \tag{6.39}$$

which is equivalent to:

$$\frac{(x_{r,(i,k),(x_m,z_n)} - x_{i,k})^2}{(x_{r,(i,k),(x_m,z_n)} - x_{i,k})^2 + h^2} \cdot \frac{\left(x_m - x_{r,(i,k),(x_m,z_n)}\right)^2 + z_n^2}{(x_m - x_{r,(i,k),(x_m,z_n)})^2} = \varepsilon_r \tag{6.40}$$

$x_{r,(i,k),(x_m,z_n)}$ can be solved from Eq. (6.40). Solving a quartic equation is a time consuming computation. Considering there are $M \times N$ bistatic pairs in the system and K antenna platform scanning positions, for a single scene point, the quartic equation in Eq. (6.40) will be solved for $M \times N \times K$ times. To alleviate the computational cost, the approximate value of $x_{r,(i,k),(x_m,z_n)}$ will be applied in this multistatic GPR imaging method instead of solving the quartic equation (6.40).

Denote the intersection point of the x-axis and the direct line from the antenna $(x_{i,k}, -h)$ to the scene point (x_m, z_n) is $(x_{c,(i,k),(x_m,z_n)}, 0)$. According to geometry of the setup, the following relation on $(x_{i,k}, -h)$, $(x_{c,(i,k),(x_m,z_n)}, 0)$ and (x_m, z_n) can be formulated:

$$\frac{x_{c,(i,k),(x_m,z_n)} - x_{i,k}}{x_m - x_{c,(i,k),(x_m,z_n)}} = \frac{h}{z_n} \tag{6.41}$$

Thus, the value of $x_{c,(i,k),(x_m,z_n)}$ can be calculated by

$$x_{c,(i,k),(x_m,z_n)} = \frac{z_n x_{i,k} + h x_0}{z_n + h} \tag{6.42}$$

Once $x_{c,(i,k),(x_m,z_n)}$ is known, according to the derivation in Ref. [22]-[23], the approximation of $x_{r,(i,k),(x_m,z_n)}$ can be formulated as:

$$x_{r,(i,k),(x_m,z_n)} =$$

$$\begin{cases} x_m + (x_{c,(i,k),(x_m,z_n)} - x_m)/\sqrt{\varepsilon_r}\,, & |x_{i,k} - x_m| < (z_n + h)\sqrt{\varepsilon_r/(\varepsilon_r - 1)} \\ x_m + z_n/\sqrt{\varepsilon_r - 1}\,, & x_{i,k} - x_m \geq (z_n + h)\sqrt{\varepsilon_r/(\varepsilon_r - 1)} \\ x_m - z_n/\sqrt{\varepsilon_r - 1}\,, & x_{i,k} - x_m \leq -(z_n + h)\sqrt{\varepsilon_r/(\varepsilon_r - 1)} \end{cases} \tag{6.43}$$

Once x_r is solved, the wave path from the ith transmitter antenna at $(x_{i,k}, 0)$ to the scene point P at (x_m, z_n) when the antenna platform is at the kth location can be determined. The wave propagating time on this path can be calculate as:

$$t_{i,k}(x_m, z_n) = \frac{\sqrt{\left(x_{r,(i,k),(x_m,z_n)} - x_{i,k}\right)^2 + h^2}}{c} + \frac{\sqrt{\left(x_m - x_{r,(i,k),(x_m,z_n)}\right)^2 + z_n^2}}{c/\sqrt{\varepsilon_r}} \qquad (6.44)$$

Similarly, when antenna platform is at the kth location, for the wave propagating path from the scene point P at (x_m, z_n) to the jth receiver antenna at $(x_{j,k}, 0)$, the intersection point $(x_{c,(j,k),(x_m,z_n)}, 0)$ and the refraction point $(x_{r,(j,k),(x_m,z_n)}, 0)$ can be determined as:

$$x_{c,(j,k),(x_m,z_n)} = \frac{z_n x_{j,k} + h x_0}{z_n + h} \qquad (6.45)$$

$$x_{r,(j,k),(x_m,z_n)} =$$

$$\begin{cases} x_m + (x_{c,(j,k),(x_m,z_n)} - x_m)/\sqrt{\varepsilon_r}\,, & \left|x_{j,k} - x_m\right| < (z_n + h)\sqrt{\varepsilon_r/(\varepsilon_r - 1)} \\ x_m + z_n/\sqrt{\varepsilon_r - 1}\,, & x_{j,k} - x_m \geq (z_n + h)\sqrt{\varepsilon_r/(\varepsilon_r - 1)} \\ x_m - z_n/\sqrt{\varepsilon_r - 1}\,, & x_{j,k} - x_m \leq -(z_n + h)\sqrt{\varepsilon_r/(\varepsilon_r - 1)} \end{cases} \qquad (6.46)$$

Once the refraction point $(x_{r,(j,k),(x_m,z_n)}, 0)$ is obtained, the wave propagating time on this path can be calculate as

$$t_{j,k}(x_m, z_n) = \frac{\sqrt{\left(x_{r,(j,k),(x_m,z_n)} - x_{j,k}\right)^2 + h^2}}{c} + \frac{\sqrt{\left(x_m - x_{r,(j,k),(x_m,z_n)}\right)^2 + z_n^2}}{c/\sqrt{\varepsilon_r}} \qquad (6.47)$$

Adding Eq. (6.44) and Eq. (6.47) together, the round-trip wave propagating time between the scene point $P(x_m, z_n)$ and the bistatic pair (i, j) is expressed as:

$$t_{(i,j),k}(x_m, z_n) = t_{i,k}(x_m, z_n) + t_{j,k}(x_m, z_n)$$

$$= \frac{\sqrt{\left(x_{r,(i,k),(x_m,z_n)} - x_{i,k}\right)^2 + h^2} + \sqrt{\left(x_{r,(j,k),(x_m,z_n)} - x_{j,k}\right)^2 + h^2}}{c}$$

$$+\frac{\sqrt{\left(x_m-x_{r,(i,k),(x_m,z_n)}\right)^2+z_n^2}+\sqrt{\left(x_m-x_{r,(j,k),(x_m,z_n)}\right)^2+z_n^2}}{c/\sqrt{\varepsilon_r}} \tag{6.48}$$

For the bistatic pair (i,j), calculate the two-way wave propagating times between it and each of the scene points in the scene space S as a matrix:

$$T_{(i,j),k}(x,z)=\begin{bmatrix} t_{(i,j),k}(x_1,z_1) & \cdots & t_{(i,j),k}\left(x_1,z_{N_0}\right) \\ \vdots & \ddots & \vdots \\ t_{(i,j),k}\left(x_{M_0},z_1\right) & \cdots & t_{(i,j),k}\left(x_{M_0},z_{N_0}\right) \end{bmatrix} \tag{6.49}$$

The A-Scan trace measured by bistatic pair (i,j) at the kth antenna platform location $s_{(i,j),k}(t)$ records the scattering signal from all the scene points in $S_{image}(x,z)$. Interpolate in the $s_{(i,j),k}(t)$ to obtain the scattering from point $P(x_n,z_m)$ that recorded by the bistatic pair (i,j) at the kth antenna platform location, and project this scattering back to the scene space:

$$S_{(i,j),k}(x_n,z_m)=s_{(i,j),k}(\tau)|_{\tau=t_{(i,j),k}(x_n,z_m)} \tag{6.50}$$

The contribution $S_{(i,j),k}(x,z)$ of the bistatic pair (i,j) at kth antenna platform location to the migrated image in scene space can be formulated as:

$$S_{(i,j),k}(x,z)=\begin{bmatrix} S_{(i,j),k}(x_1,z_1) & \cdots & S_{(i,j),k}\left(x_1,z_{N_0}\right) \\ \vdots & \ddots & \vdots \\ S_{(i,j),k}\left(x_{M_0},z_1\right) & \cdots & S_{(i,j),k}\left(x_{M_0},z_{N_0}\right) \end{bmatrix} \tag{6.51}$$

For those scene points out of the illuminated area of the bistatic pair (i,j) at the kth location, their corresponding values in $S_{(i,j),k}(x,z)$ are set to 0.

Repeating above processing for the bistatic pair (i,j) on the A-Scan traces at all K platform locations, the contribution of A-Scan traces at each antenna platform location to the migrated image can be obtained as $\left\{S_{(i,j),1}(x,z),S_{(i,j),2}(x,z),\dots,S_{(i,j),K}(x,z)\right\}$. The imaging data matrix produced by the static pair (i,j) can be formulated as:

$$S_{(i,j)}(x,z) = \sum_{k=1}^{K} S_{(i,j),k}(x,z) \tag{6.52}$$

Repeating above processing for every bistatic pair in the multistatic GPR system, the imaging data matrix for each bistatic pair can be obtained as $S_{(i,j)}(x,z)$ where $i = 1, 2, \ldots, M$ and $j = 1, 2, \ldots, N$. The final migrated GPR image can be formulated as the superposition of the $S_{(i,j)}(x,z)$ from each bistatic pair:

$$S_{\text{image}}(x,z) = \sum_{i=1}^{M} \sum_{j=1}^{N} S_{(i,j)}(x,z) \tag{6.53}$$

The difference of this air-coupled multistatic GPR imaging method and the ground-coupled version is the way to calculate the wave propagating time between the scene point and the antennas.

6.5. Experimental Results

To evaluate the back-projection based multistatic GPR imaging method, experiments are conducted with four sets of test data that are synthesized with the GPR simulation tool GprMax [24]. In the first and second test cases, a ground-coupled multistatic GPR is simulated. An air-coupled multistatic GPR is simulated in the third and fourth test cases.

6.5.1. Ground-Coupled GPR Imaging Experiments

In this section, two sets of simulation data are created using GprMax program. In our simulation, the GPR waveform is generated as a Ricker waveform (i.e. negative normalized second derivative of a Gaussian pulse) with its center frequency being 2 GHz. The multistatic configuration consists of one transmitter antenna and six receiver antennas. Spatial offsets between the transmitter antenna and six receiver antennas are 5 cm, 10 cm, 20 cm, 30 cm, 40 cm and 50 cm respectively. The antenna platform is close to the ground surface simulating the ground-coupled configuration. The antenna platform moves uniformly from left to right along the horizontal direction and records the received signal at 100 positions. The distance interval between two adjacent platform locations is 2 cm.

6.5.1.1. Simulation Data 1: Three Targets

In the first simulation setup, the subsurface media is modeled as a homogeneous layer whose dielectric constant is 6.0. As depicted in Figure 6.9, three targets are buried underground whose dielectric constants are all set to 8.0. The purpose of this test case is to evaluate the effectiveness of the proposal multistatic GPR imaging method on targets of various shapes. The dimensional specifications of the targets are listed as follows:

- Pipe (cylinder object) – depth: 7.5 cm; diameter: 2.5 cm.
- Man-made shape object – depth of top surface: 10 cm; depth of bottom surface: 20 cm; width of top part: 10 cm; width of bottom part: 20 cm; thickness of top part: 5 cm; thickness of bottom part: 5 cm.
- Plate – depth: 8.5 cm; width: 15 cm; thickness: 0.5 cm.

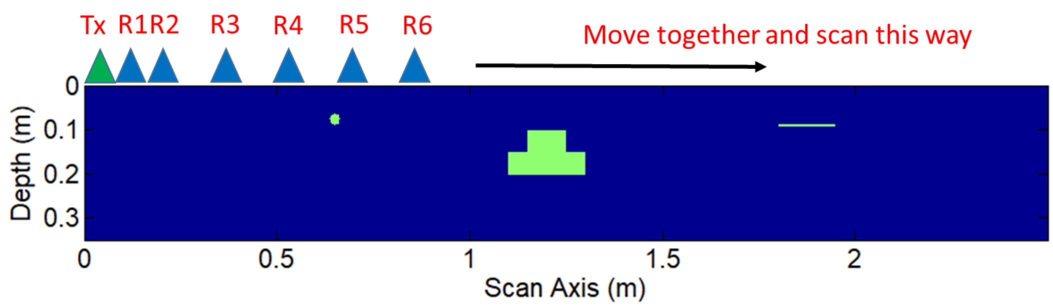

Figure 6.9: Ground-coupled multistatic GPR testing setup – three buried targets.

The multistatic system in this simulation consists of one transmitter antenna and six receiver antennas, so six GPR data matrices are produced by six bistatic pairs. The raw B-Scan images produced by the Tx1-Rx1 pair and Tx1-Rx5 pair are plotted as Figure 6.10(a) and (b) respectively.

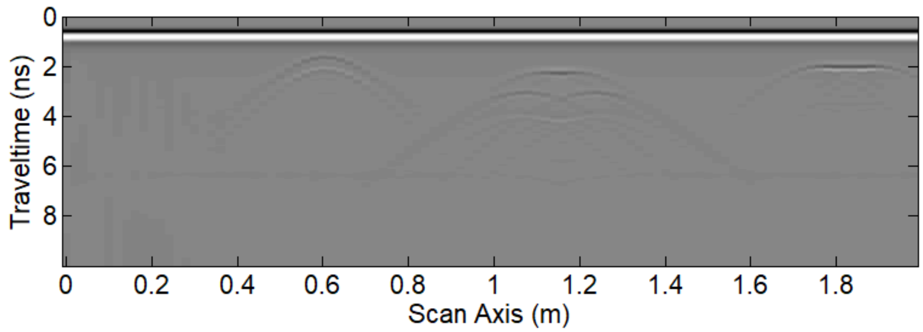

(a)

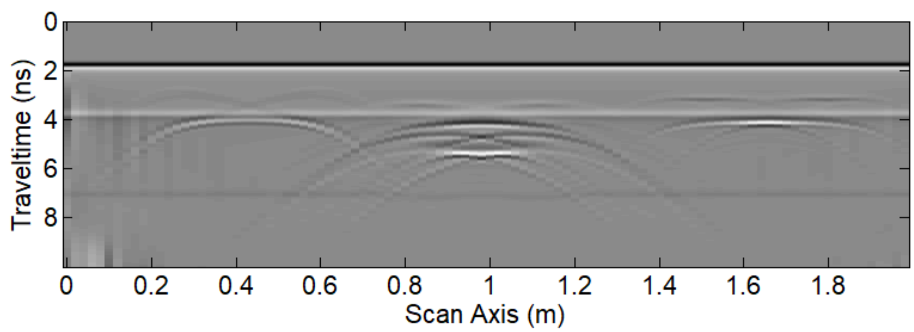

(b)

Figure 6.10: Ground-coupled multistatic GPR raw B-Scan – three buried targets: (1) Tx1-Rx1 pair; (2) Tx1-Rx5 pair.

If each bistatic pair is regarded as an individual GPR system, the migrated B-Scan images generated by the proposed algorithm are displayed in Figure 6.11(a) and (b) for pair Tx1-Rx1 and Tx1-Rx5 respectively. As shown in Figure 6.11(a), for the B-Scan produced by bistatic pair Tx1-Rx1, the resolution of the targets is good, nevertheless, the bottom of the man-made shape target can't be detected and the SCR is low. As depicted in Figure 6.11(b), for the B-Scan image obtained from bistatic pair Tx1-Rx5, the bottom of the middle target can be reconstructed accurately and the SCR is high, however, the resolution is not good comparing to bistatic pair Tx1-Rx1. Because of the variety of spatial offsets in different bistatic antenna pairs, the characteristics of both the target and clutter vary.

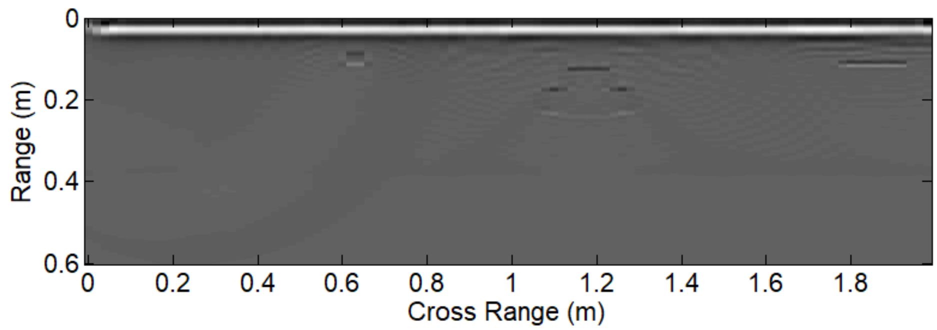

(a)

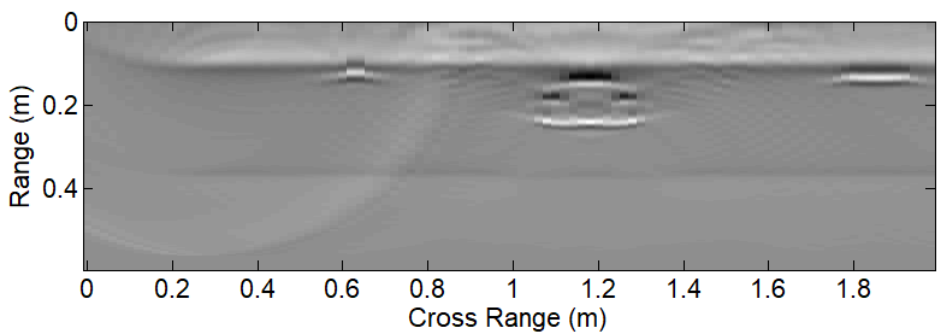

(b)

Figure 6.11: Ground-coupled multistatic GPR migrated B-Scan – three buried targets: (1) Tx1-Rx1 pair; (2) Tx1-Rx5 pair.

Now considering all six bistatic pairs as a multistatic system, the GPR data matrix is processed by the proposed multistatic GPR imaging method, and the resulted GPR image is plotted as Figure 6.12. The imaging result is consistent with the geometry setup depicted in Figure 6.9. It combines the advantages of all bistatic pairs, in which, the resolution is good and the shapes of the targets are reconstructed accurately. Moreover, this migrated GPR image testifies to the discussion in Sec. 6.1 that the radar imaging specifications, such as SNR and SCR, benefit from the multistatic configuration because of information gained from various antenna pairs and multiple radar cross sections.

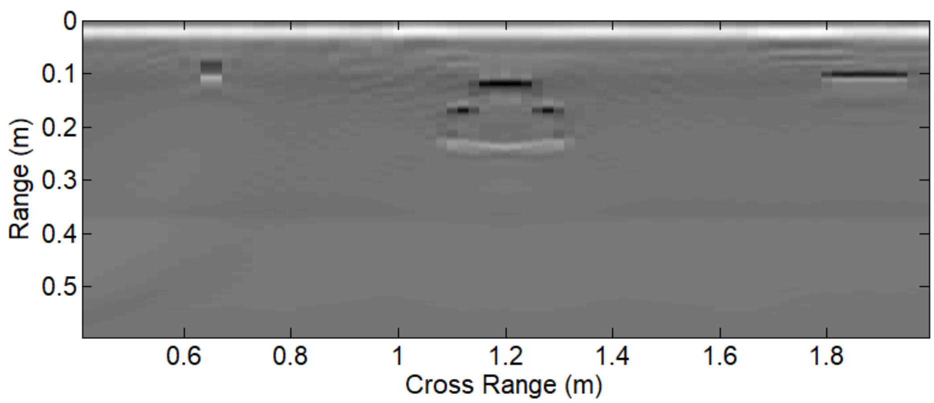

Figure 6.12: Ground-coupled multistatic GPR migrated B-Scan using proposed multistatic imaging method – three buried targets

6.5.1.2. Simulation Data 2: Congested Pipes

In the second simulation setup for ground-coupled multistatic GPR inspection, the subsurface media is also modeled as a homogeneous layer whose dielectric constant is 6.0. As depicted in Figure 6.13, three groups of congested pipes are buried underground whose dielectric constants are all set to 8.0. The diameters of the pipes are all 2.5 cm. This test case simulates the complex testing scenario of GPR underground utility sensing and mapping application. The dimensional specifications of the targets are listed as follows:

- Left group – three pipes are at the same x-coordinate while different depth. The depths of them are 8.5 cm, 16 cm and 23.5 cm respectively.
- Middle group – five pipes construct a "W" shape. The depths of the top three pipes are 10.5 cm. The depths of the bottom two pipes are 20.5 cm. The horizontal spatial separation between two adjacent pipes is 10 cm.
- Right group – Depths of all three pipes are 15 cm. The separation between two adjacent ones is 10 cm.

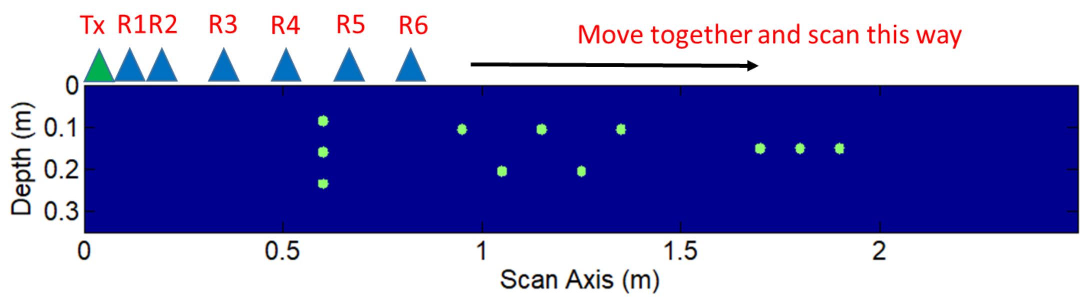

Figure 6.13: Ground-coupled multistatic GPR testing setup – three buried targets.

If individual antenna pair is selected for GPR imaging processing, the raw B-Scan images produced by the Tx1-Rx1 pair and Tx1-Rx5 pair are plotted in Figure 6.14(a) and (b) respectively as two examples. Their corresponding migrated B-Scan images reconstructed by the proposed algorithm are shown in Figure 6.15(a) and (b) respectively. Similar to the first test case in Sec. 6.5.1.1, for the B-Scan produced by bistatic pair with small spatial offset, the resolution of the targets is good, while the SCR is low. For the B-Scan image obtained from bistatic pair with large spatial offset, the SCR is high while the resolution, especially the cross range resolution is not good.

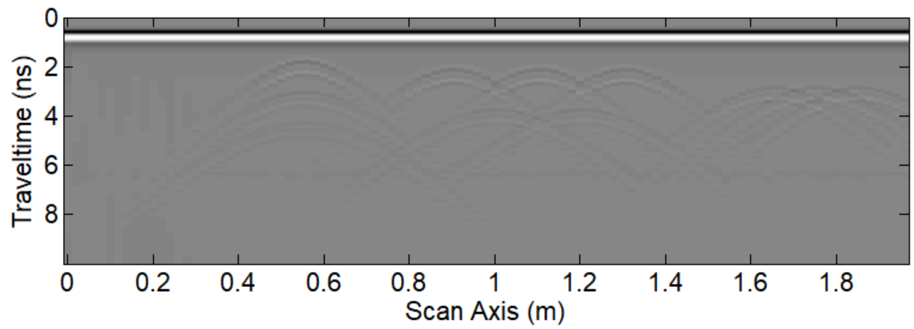

(a)

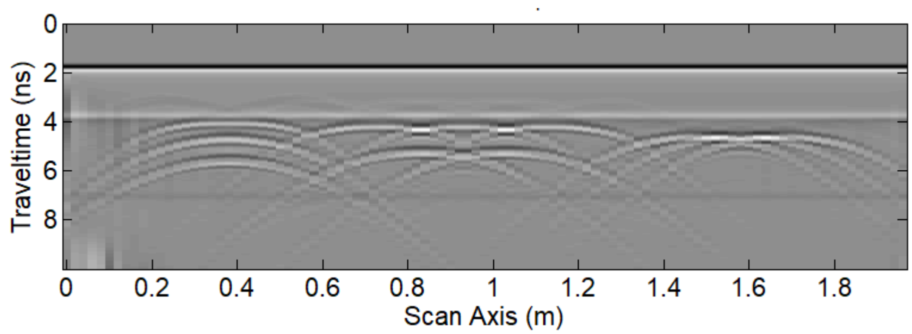

(b)

Figure 6.14: Ground-coupled multistatic GPR raw B-Scan – congested pipes: (1) Tx1-Rx1 pair; (2) Tx1-Rx5 pair.

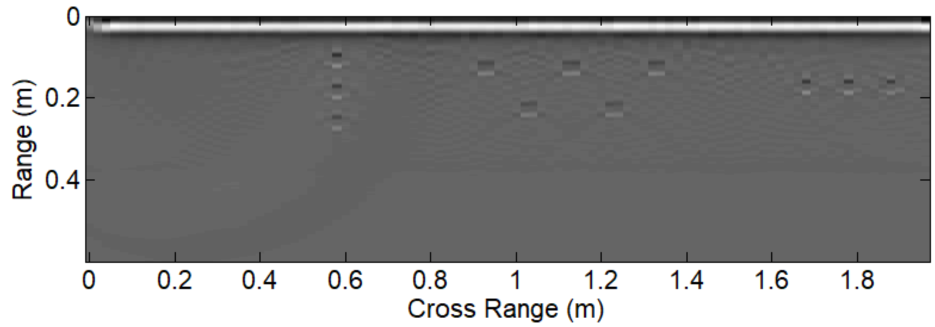

(a)

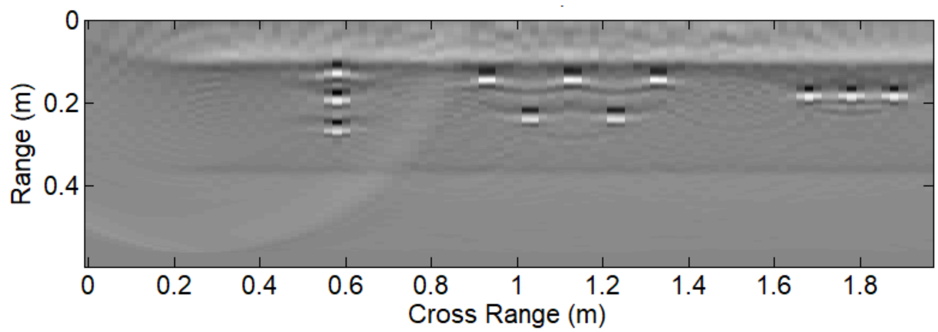

(b)

Figure 6.15: Ground-coupled multistatic GPR migrated B-Scan – congested pipes: (1) Tx1-Rx1 pair; (2) Tx1-Rx5 pair.

Now performing the multistatic GPR imaging algorithm on the GPR data collected by all six bistatic pairs, the resulted GPR image is plotted as Figure 6.16, which is consistent with the geometry setup depicted in Figure 6.13. The migrated GPR image from multistatic measurement data benefits from the multiple looks at the targets. It has high reconstruction accuracy, resolution, and SCR.

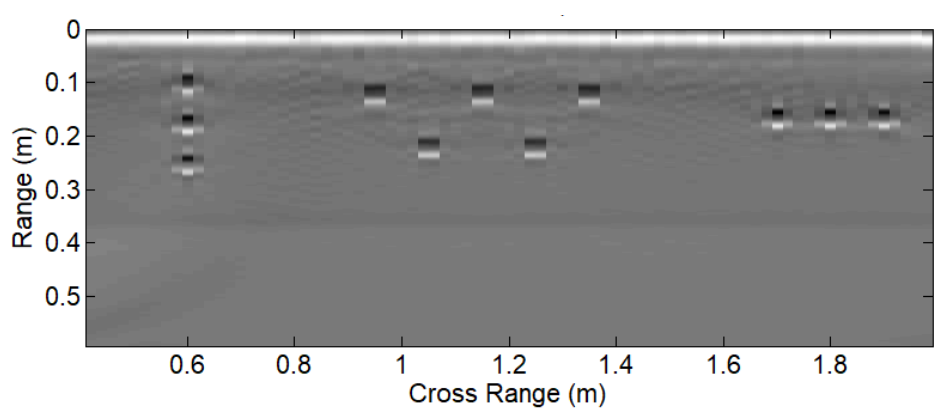

Figure 6.16: Ground-coupled multistatic GPR migrated B-Scan using proposed multistatic imaging method – congested pipes.

6.5.2. Air-Coupled GPR Imaging Experiments

In this section, two sets of simulation data are created using GprMax program using the same transmitting waveform. The multistatic configuration is similar to the ground-coupled setup described in 6.5.1. The only difference is the antenna platform is 0.5 m high above the ground surface to simulate an air-coupled antenna configuration.

6.5.2.1. Simulation Data 1: Three Targets

The geometry setup of the subsurface region and targets is illustrated in Figure 6.17, which is identical to the setup in Sec. 6.5.1.1.

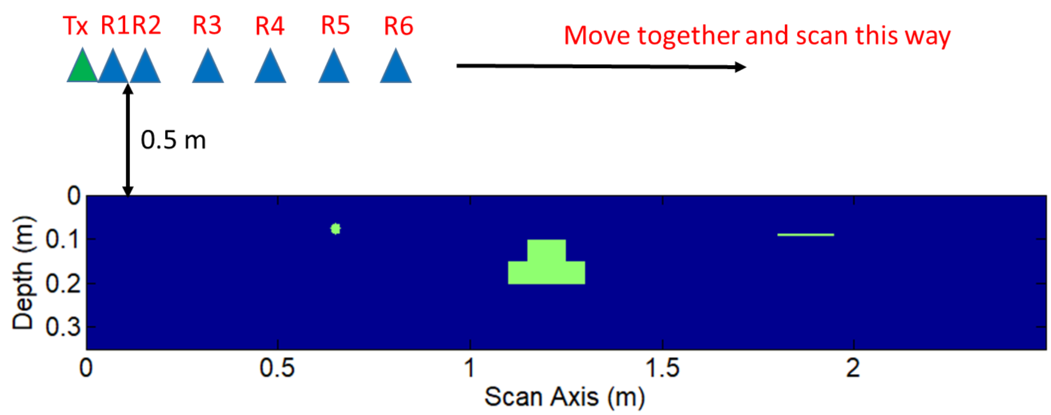

Figure 6.17: Air-coupled multistatic GPR testing setup – three buried targets.

The GPR data are processed by the proposed multistatic GPR imaging method and the resulted GPR image is plotted in Figure 6.18. Due to the large signal propagation loss in air-couple GPR system [25], the clutter removal is performed to enhance the target features. The B-Scan image upon clutter removal processing is depicted in Figure 6.19, in which the three targets are all reconstructed accurately as the geometry setup.

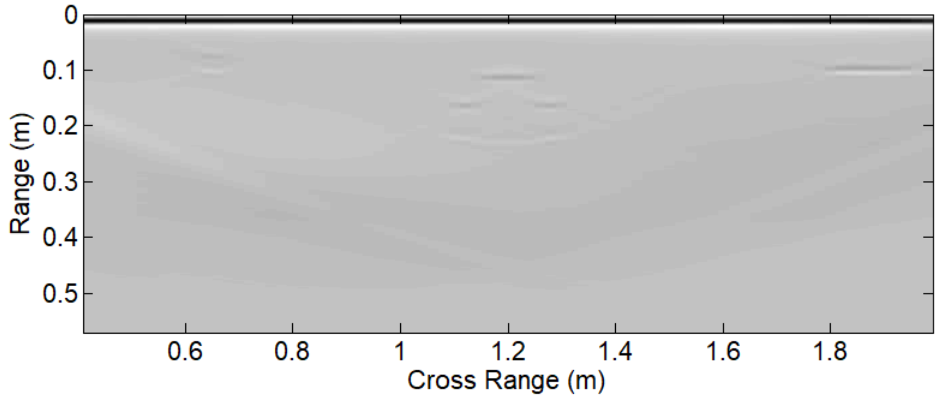

Figure 6.18: Air-coupled multistatic GPR migrated B-Scan using proposed multistatic imaging method – three buried targets

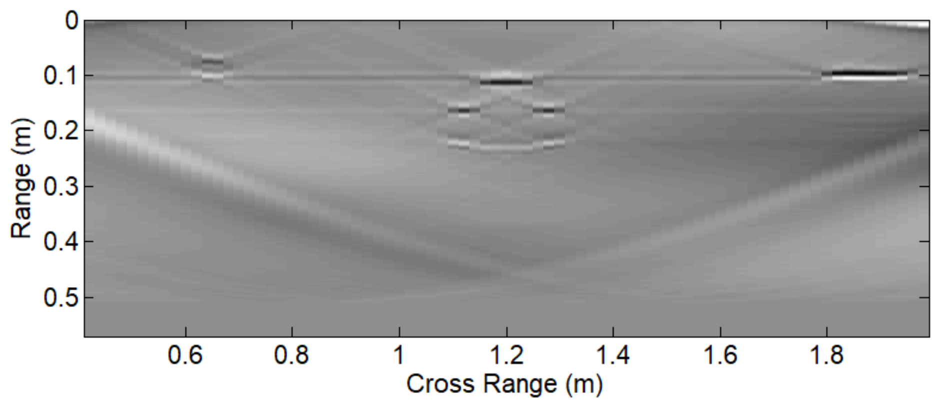

Figure 6.19: Air-coupled multistatic GPR migrated B-Scan upon clutter removal – three buried targets

6.5.2.2. Simulation Data 2: Congested Pipes

The geometry setup of the subsurface region and targets is illustrated in Figure 6.20, which is similar to the setup in Sec. 6.5.1.2.

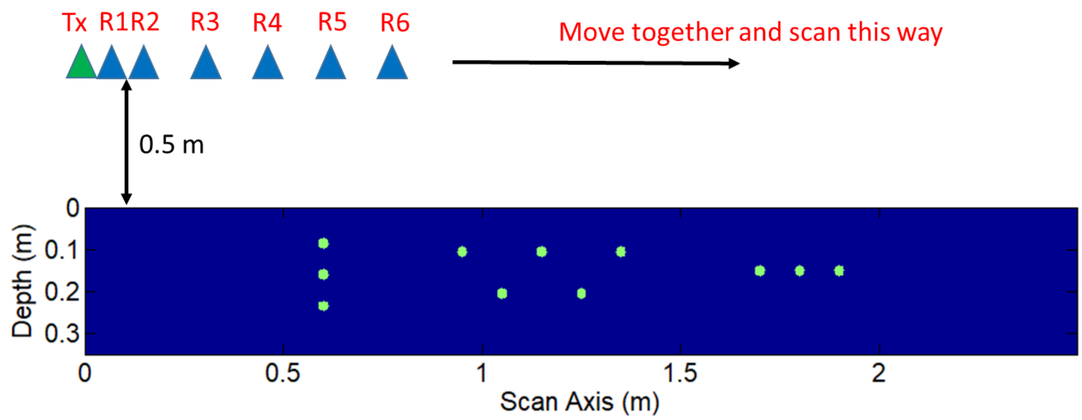

Figure 6.20: Air-coupled multistatic GPR testing setup – congested pipes.

The GPR data processed by the proposed multistatic GPR imaging method is plotted in Figure 6.21. Due to large signal propagation loss of air-couple GPR system, the clutter removal is necessary to improve the image equality. The B-Scan image upon clutter suppression is depicted in Figure 6.22, in which all the pipes are imaged on the accurate coordinates defined by the geometry setup.

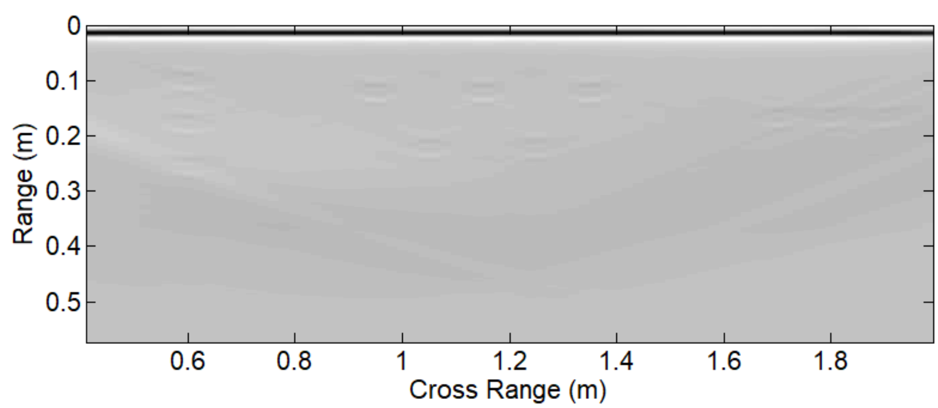

Figure 6.21: Air-coupled multistatic GPR migrated B-Scan using proposed multistatic imaging method – congested pipes.

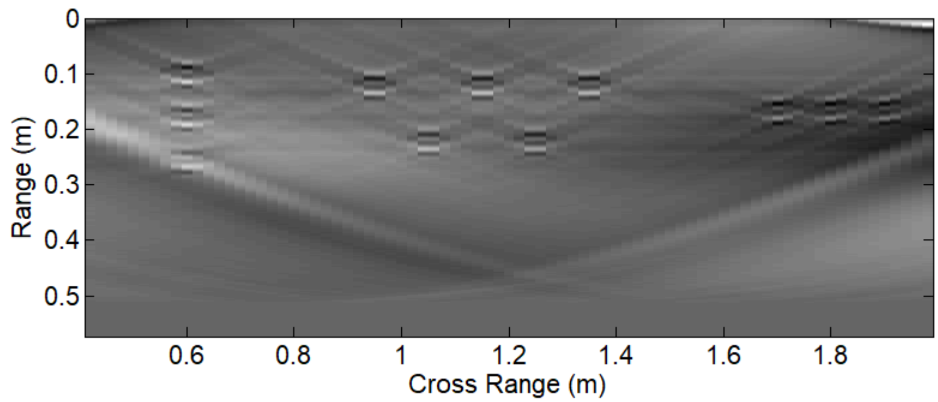

Figure 6.22: Air-coupled multistatic GPR migrated B-Scan upon clutter removal – congested pipes.

6.6. Conclusions

In this chapter, back-projection based imaging techniques are developed for both ground-coupled multistatic GPR and air-coupled multistatic GPR systems. This multistatic imaging method accounts for the height offsets of the antennas, spatial offsets between antennas and refraction phenomenon at the air-ground interface. It fuses the scattering signals gained from various antenna pairs and multiple radar cross sections to produce migrated GPR image with higher SNR and SCR over conventional monostatic or bistatic GPR systems. Experiments with simulation data indicate that the proposed multistatic imaging method can effectively reconstruct the targets from raw GPR data.

6.7. References

[1] Multistatic Radar – Wikipedia: https://en.wikipedia.org/wiki/Multistatic_radar

[2] Counts, T., Gurbuz, A. C., Scott, W. R., McClellan, J. H., and Kim, K., "Multistatic ground-penetrating radar experiments," *IEEE Transactions on Geoscience and Remote Sensing*, *45*(8), 2544-2553 (2007).

[3] Inggs, M., Griffiths, H., Fioranelli, F., Ritchie, M., and Woodbridge, K., "Multistatic radar: System requirements and experimental validation," In *Radar Conference (Radar), 2014 International*, 1-6 (2014).

[4] Yigit, E., Demirci, S., Ozdemir, C., and Kavak, A., "A synthetic aperture radar-based focusing algorithm for B-Scan ground penetrating radar imagery," Microwave and Optical Technology Letters, 49(10), 2534 -2540 (2007).

[5] Charvat, G. L., "Small and short-range radar systems," CRC Press, (2014).

[6] Charvat, G. L., "A Low-Power Radar Imaging System," *Ph.D. dissertation, Dept. of Electrical and Computer Engineering, Michigan State University, East Lansing, MI*, (2007).

[7] Yang, H., Li, T., Li, N., He, Z., and Liu, Q. H., "Efficient Near-Field Imaging for Single-Borehole Radar with Widely Separated Transceivers," IEEE Transactions on Geoscience and Remote Sensing, 53(10), 5327-5337 (2015).

[8] Vargas, J. M. M., "Signal processing techniques for radar based subsurface and through wall imaging," Doktora Tezi, University of Alberta, Edmonton, (2012).

[9] Demirci, S., Yigit, E., Eskidemir, I. H., and Ozdemir, C., "Ground penetrating radar imaging of water leaks from buried pipes based on back-projection method," NDT & E International, 47, 35-42 (2012).

[10] Halman, J. I., Shubert, K. A., and Ruck, G. T., "SAR processing of ground-penetrating radar data for buried UXO detection: results from a surface-based system," IEEE Transactions on Antennas and Propagation, 46(7), 1023-1027 (1998).

[11] Carin, L., Geng, N., McClure, M., Sichina, J., and Nguyen, L., "Ultra-wide-band synthetic-aperture radar for mine-field detection," IEEE Antennas and Propagation Magazine, 41(1), 18-33 (1999).

[12] Gorham, L. A., and Moore, L. J., "SAR image formation toolbox for MATLAB," In Proc. SPIE, 7699, (2010).

[13] Yigit, E., Demirci, S., Özdemir, C., and Tekbaş, M, "Short-range ground-based synthetic aperture radar imaging: performance comparison between frequency-wavenumber migration and back-projection algorithms," *Journal of Applied Remote Sensing*, *7*(1), 073483-073483 (2013).

[14] Zhuge, X., Savelyev, T. G., Yarovoy, A. G., Ligthart, L. P., and Levitas, B., "Comparison of different migration techniques for UWB short-range imaging," In *Radar Conference, 2009. EuRAD 2009. European*, 184-187 (2009).

[15] Chambers, D. H., Paglieroni, D. W., Mast, J. E., and Beer, N. R. "*Real-Time Vehicle-Mounted Multistatic Ground Penetrating Radar Imaging System for Buried Object Detection*," (No. LLNL-TR-615452). Lawrence Livermore National Laboratory (LLNL), Livermore, CA, (2013).

[16] Fischer, C., Herschlein, A., Younis, M., and Wiesbeck, W., "Detection of antipersonnel mines by using the factorization method on multistatic ground-penetrating radar measurements," *IEEE transactions on geoscience and remote sensing*, *45*(1), 85-92 (2007).

[17] Kim, K., Gurbuz, A. C., Scott Jr, W. R., and McClellan, J. H., "A multi-static ground-penetrating radar with an array of resistively loaded vee dipole antennas for landmine detection," In *Defense and Security* (pp. 495-506). International Society for Optics and Photonics, (2005).

[18] Paglieroni, D. W., Chambers, D. H., Mast, J. E., Bond, S. W., and Beer, N. R., "Imaging modes for ground penetrating radar and their relation to detection performance," *IEEE Journal of Selected Topics in Applied Earth Observations and Remote Sensing*, *8*(3), 1132-1144 (2015).

[19] Karim, M. N. A., Malek, M. F. A., Jamlos, M. F., Seng, L. Y., and Saudin, N., "Design of ground penetrating radar antenna for buried object detection," In *RF and Microwave Conference (RFM), 2013 IEEE International,* 253-257 (2013).

[20] Labarthe, C., Mutzig, J. P., Jecko, B., Hamieh, H., Martinod, E., Feix, N., and Vergnault, R, "An Ultra-Wideband radar concept for the detection of buried victims beneath building rubble," In *Radar Conference-Surveillance for a Safer World, 2009. RADAR. International,* 1-6 (2009).

[21] Kim, K., and Scott, W. R., "Investigation of resistive vee antennas for a multi-static ground-penetrating radar," In *Antennas and Propagation Society International Symposium, 2005 IEEE,* 96-99 (2005).

[22] Zhou, L., Huang, C., and Su, Y., "A fast back-projection algorithm based on cross correlation for GPR imaging," *IEEE Geoscience and Remote Sensing Letters,* 9(2), 228-232 (2012).

[23] Johansson, E. M., and Mast, J. E., "Three-dimensional ground penetrating radar imaging using synthetic aperture time-domain focusing," In *Proc. SPIE,* 2275, 205-214 (1994).

[24] Giannopoulos, A., "Modelling ground penetrating radar by GprMax," *Construction and building materials*, *19*(10), 755-762 (2005).

[25] Zhang, Y., Burns, D., Orfeo, D., Huston, D. R., and Xia, T., "Rough ground surface clutter removal in air-coupled ground penetrating radar data using low-rank and sparse representation," In *SPIE Smart Structures and Materials+ Nondestructive Evaluation and Health Monitoring,* 1016904, (2017).

CHAPTER 7: CONCLUSIONS AND FUTURE WORKS

7.1. Conclusions

In this dissertation, the three-stage cascade signal processing methodologies were proposed to tackle with GPR signal processing from three perspectives: (1) Suppressing the radar clutter signal through a low-rank and sparse representation based approach. (2) Detecting the region of interest in the GPR image using Hilbert Transform and 2-D Renyi entropy based statistical analysis to reduce the computational cost for further sophisticated GPR data processing, such as back-projection migration. (3) Imaging the underground target for both ground-coupled multistatic GPR and air-coupled multistatic GPR configurations by back-projection imaging techniques. Experiments on both the simulation and lab measurement data validate that the proposed three-stage cascade signal processing methodologies can improve the performance of GPR system.

7.2. Future Work

The future work based on the materials presented in this dissertation can be focused on a few directions.

In Chapter 2 and 3, the clutter removal problem is formulated as a low-rank and sparse decomposition problem:

$$\min_{L,S} \|L\|_* + \lambda \|S\|_1 \quad s.t. \;\; D = L + S \tag{7.1}$$

The success of this decomposition is primarily dependent on how low the rank of matrix L is and how sparse the matrix S is. Some pre-processing steps can be applied to improve the quality of the data prior to the decomposition and transform the decomposition problem to the following one:

$$\min_{L,S} \|L\|_* + \lambda \|S\|_1 \quad s.t. \quad D = L \circ \tau + S \circ \rho \tag{7.2}$$

where τ is the operator manipulating the clutter component in the GPR data to have lower rank, and ρ is the operator making the target component more sparse. The methodology presented in Chapter 3 proposed the cross-correlation as the operator τ to align the ground surface reflection and decrease the rank of the clutter matrix. A recent work in Ref. [1] testified that instead of decomposing the raw GPR data, migration imaging can be applied first to focus target response so that the sparsity and the strength of target response are enhanced, which is a kind of the operator ρ in Eq. (7.2). The future direction on the low-rank and sparse representation based clutter removal can focus on optimizing and implementing the operator τ and ρ simultaneously for the GPR data matrix.

In Chapter 4 and 5, 2-D Renyi entropy analysis was performed on the amplitude and phase information of the GPR data. For GPR underground sensing application, most of the targets are objects with certain shapes, so geometry structure and morphological information reside inside the GPR data matrix. The 2-D entropy analysis methodology can be further explored and applied on the data features extracted from morphological transformation, such as Curvelet Transform [2]-[5] to afford more comprehensive region of interest detection.

For GPR migration problem, the propagating velocity of the EM wave in subsurface media is a vital input, which is associated with the dielectric constant of the subsurface media. Unfortunately, this is usually not prior information for real field GPR testing. The approaches for measuring or estimating the dielectric constant and wave velocity information have been investigated by some research work [6]-[8] for homogeneous subsurface media. However, for most of the real GPR testing scenarios, the subsurface media is inhomogeneous. Moreover, Ref. [9]-[10] claims that the systematic errors in the migration techniques may lead to poor image reconstruction and inaccurate target position estimation even if the exact velocity distribution is used as the prior knowledge. Therefore, autofocusing technique for GPR imaging is highly demanded and will be investigated in the future work.

7.3. References

[1] Song, X., Xiang, D., Zhou, K., & Su, Y. (2017). Improving RPCA-Based Clutter Suppression in GPR Detection of Antipersonnel Mines. IEEE Geoscience and Remote Sensing Letters.

[2] Terrasse, G., Nicolas, J. M., Trouvé, E., & Drouet, É. (2015, July). Application of the curvelet transform for pipe detection in GPR images. In *Geoscience and Remote Sensing Symposium (IGARSS), 2015 IEEE International* (pp. 4308-4311). IEEE.

[3] Tzanis, A. (2015). The Curvelet Transform in the analysis of 2-D GPR data: Signal enhancement and extraction of orientation-and-scale-dependent information. *Journal of Applied Geophysics*, *115*, 145-170.

[4] Temlioglu, E., & Erer, I. (2016). Clutter removal in ground-penetrating radar images using morphological component analysis. *IEEE Geoscience and Remote Sensing Letters*, *13*(12), 1802-1806.

[5] Bao, Q. Z., Li, Q. C., & Chen, W. C. (2014). GPR data noise attenuation on the curvelet transform. *Applied Geophysics*, *11*(3), 301-310.

[6] Soldovieri, F., Prisco, G., & Persico, R. (2009). A strategy for the determination of the dielectric permittivity of a lossy soil exploiting GPR surface measurements and a cooperative target. *Journal of Applied Geophysics*, *67*(4), 288-295.

[7] Huston, D. (2010). *Structural sensing, health monitoring, and performance evaluation*. CRC Press.

[8] Brown, J., Nichols, J., Steinbronn, L., & Bradford, J. (2009). Improved GPR interpretation through resolution of lateral velocity heterogeneity: example from an archaeological site investigation. *Journal of Applied Geophysics*, *68*(1), 3-8.

[9] Black, J. L., & Brzostowski, M. A. (1994). Systematics of time-migration errors. *Geophysics*, *59*(9), 1419-1434.

[10] Wei, X., & Zhang, Y. (2014). Autofocusing techniques for GPR data from RC bridge decks. *IEEE Journal of Selected Topics in Applied Earth Observations and Remote Sensing*, *7*(12), 4860-4868.

BIBLIOGRAPHY

2013 Report Card for America's Infrastructure, American Society of Civil Engineers: http://2013.infrastructurereportcard.org/

Addison, A. D., Battista, B. M., & Knapp, C. C. (2009). Improved hydrogeophysical parameter estimation from empirical mode decomposition processed ground penetrating radar data. Journal of Environmental & Engineering Geophysics, 14(4), 171-178.

Ahmed, A., Zhang, Y., Burns, D., Huston, D., & Xia, T. (2016). Design of UWB antenna for air-coupled impulse ground-penetrating radar. IEEE Geoscience and Remote Sensing Letters, 13(1), 92-96.

AI-Qadi, I., Lahouar, S., Jiang, K., McGhee, K., & Mokarem, D. (2005). Accuracy of ground-penetrating radar for estimating rigid and flexible pavement layer thicknesses. Transportation Research Record: Journal of the Transportation Research Board, (1940), 69-78.

Alani, A. M., Aboutalebi, M., & Kilic, G. (2013). Applications of ground penetrating radar (GPR) in bridge deck monitoring and assessment. Journal of Applied Geophysics, 97, 45-54.

Al-Qadi, I. L., Xie, W., & Roberts, R. (2008). Scattering analysis of ground-penetrating radar data to quantify railroad ballast contamination. NDT & E International, 41(6), 441-447.

Al-Qadi, I. L., Xie, W., Roberts, R., & Leng, Z. (2010). Data analysis techniques for GPR used for assessing railroad ballast in high radio-frequency environment. Journal of transportation engineering, 136(4), 392-399.

Amaldi, E., & Kann, V. (1998). On the approximability of minimizing nonzero variables or unsatisfied relations in linear systems. Theoretical Computer Science, 209(1-2), 237-260.

Amin, M. G. (Ed.). (2016). Through-the-wall radar imaging. CRC press.

Annan, A. P. (1999). Practical processing of GPR data. Sensors and software, Ontario.

Aydin, E., & Yüksel, S. E. (2017, May). Buried target detection with ground penetrating radar using deep learning method. In Signal Processing and Communications Applications Conference (SIU), 2017 25th (pp. 1-4). IEEE.

Baili, J., Lahouar, S., Hergli, M., Al-Qadi, I. L., & Besbes, K. (2009). GPR signal de-noising by discrete wavelet transform. Ndt & E International, 42(8), 696-703.

Bano, M., Marquis, G., Nivière, B., Maurin, J., & Cushing, M. (2000). Investigating alluvial and tectonic features with ground-penetrating radar and analyzing diffractions patterns. Journal of Applied Geophysics, 43(1), 33-41.

Bao, Q. Z., Li, Q. C., & Chen, W. C. (2014). GPR data noise attenuation on the curvelet transform. Applied Geophysics, 11(3), 301-310.

Baraniuk, R. G., Flandrin, P., Janssen, A. J., & Michel, O. J. (2001). Measuring time-frequency information content using the Rényi entropies. IEEE Transactions on Information Theory, 47(4), 1391-1409.

Basile, V., Carrozzo, M. T., Negri, S., Nuzzo, L., Quarta, T., & Villani, A. V. (2000). A ground-penetrating radar survey for archaeological investigations in an urban area (Lecce, Italy). Journal of Applied Geophysics, 44(1), 15-32.

Battista, B. M., Knapp, C., McGee, T., & Goebel, V. (2007). Application of the empirical mode decomposition and Hilbert-Huang transform to seismic reflection data. Geophysics, 72(2), H29-H37.

Becker, J., Havens, T. C., Pinar, A., & Schulz, T. J. (2015, May). Deep belief networks for false alarm rejection in forward-looking ground-penetrating radar. In SPIE Defense+ Security (pp. 94540W-94540W). International Society for Optics and Photonics.

Becker, S. R., Candès, E. J., & Grant, M. C. (2011). Templates for convex cone problems with applications to sparse signal recovery. Mathematical programming computation, 3(3), 165-218.

Benson, A. K. (1995). Applications of ground penetrating radar in assessing some geological hazards: examples of groundwater contamination, faults, cavities. Journal of applied Geophysics, 33(1-3), 177-193.

Besaw, L. E., & Stimac, P. J. (2014, May). Deep learning algorithms for detecting explosive hazards in ground penetrating radar data. In Proc. SPIE (Vol. 9072, p. 90720Y).

Besaw, L. E., & Stimac, P. J. (2015, May). Deep convolutional neural networks for classifying GPR B-scans. In SPIE Defense+ Security (pp. 945413-945413). International Society for Optics and Photonics.

Bettigole, N., & Robinson, R. (1997). Bridge Decks. American Society of Civil Engineers, New York.

Black, J. L., & Brzostowski, M. A. (1994). Systematics of time-migration errors. Geophysics, 59(9), 1419-1434.

Bleistein, N. (1987). On the imaging of reflectors in the earth. Geophysics, 52(7), 931-942.

Bourgeois, J. M., & Smith, G. S. (1996). A fully three-dimensional simulation of a ground-penetrating radar: FDTD theory compared with experiment. IEEE Transactions on Geoscience and Remote Sensing, 34(1), 36-44.

Bouzerdoum, A., Tivive, F. H. C., & Abeynayake, C. (2016, May). Target detection in GPR data using joint low-rank and sparsity constraints. In SPIE Commercial+ Scientific Sensing and Imaging (pp. 98570A-98570A). International Society for Optics and Photonics.

Bralich, J., Reichman, D., Collins, L. M., & Malof, J. M. (2017, May). Improving convolutional neural networks for buried threat in ground penetrating radar using transfer learning via pretraining. In SPIE Defense+ Security (pp. 101820X-101820X). International Society for Optics and Photonics.

Brown, J., Nichols, J., Steinbronn, L., & Bradford, J. (2009). Improved GPR interpretation through resolution of lateral velocity heterogeneity: example from an archaeological site investigation. Journal of Applied Geophysics, 68(1), 3-8.

Cafforio, C., Prati, C., & Rocca, F. (1991). Full resolution focusing of SEASAT SAR images in the frequency-wave number domain. International Journal of Remote Sensing, 12(3), 491-510.

Cafforio, C., Prati, C., & Rocca, F. (1991). SAR data focusing using seismic migration techniques. IEEE transactions on aerospace and electronic systems, 27(2), 194-207.

Camilo, J. A., Malof, J. M., & Collins, L. M. (2016, May). A feature learning approach for classifying buried threats in forward looking ground penetrating radar data. In Proc. SPIE (Vol. 9823, p. 98231I).

Candès, E. J., Li, X., Ma, Y., & Wright, J. (2011). Robust principal component analysis?. Journal of the ACM (JACM), 58(3), 11.

Candra, P., Xia, T., Huston, D., & Wang, G. (2013, April). Two dimensional entropy and short time Fourier transform application on ground penetrating radar data analysis. In SPIE Smart Structures and Materials+ Nondestructive Evaluation and Health Monitoring (pp. 86940J-86940J). International Society for Optics and Photonics.

Cardimona, S. J., Clement, W. P., & Kadinsky-Cade, K. (1998). Seismic reflection and ground-penetrating radar imaging of a shallow aquifer. Geophysics, 63(4), 1310-1317.

Carin, L., Geng, N., McClure, M., Sichina, J., & Nguyen, L. (1999). Ultra-wide-band synthetic-aperture radar for mine-field detection. IEEE Antennas and Propagation Magazine, 41(1), 18-33.

Cassidy, N. J. (2007). Evaluating LNAPL contamination using GPR signal attenuation analysis and dielectric property measurements: Practical implications for hydrological studies. Journal of Contaminant Hydrology, 94(1), 49-75.

Cassidy, N. J. (2009). Ground penetrating radar data processing, modelling and analysis. Ground penetrating radar: theory and applications, 141-176.

Cervone, G., & Haack, B. (2012). Supervised machine learning of fused RADAR and optical data for land cover classification. Journal of Applied Remote Sensing, 6(1), 063597-063597.

Chambers, D. H., Paglieroni, D. W., Mast, J. E., & Beer, N. R. (2013). Real-Time Vehicle-Mounted Multistatic Ground Penetrating Radar Imaging System for Buried Object Detection (No. LLNL-TR-615452). Lawrence Livermore National Laboratory (LLNL), Livermore, CA.

Charvat, G. L. (2007). A Low-Power Radar Imaging System (Doctoral dissertation, Michigan State University).

Charvat, G. L. (2014). Small and short-range radar systems. CRC Press.

Chernyak, V. S. (1998). Fundamentals of multisite radar systems: multistatic radars and multistatic radar systems. CRC Press.

Claerbout, J. F. (1986). Imaging the Earth's interior. Geophysical Journal International, 86(1), 217-217.

Collins, L. M., Torrione, P. A., Munshi, V. S., Throckmorton, C. S., Zhu, Q. E., Clodfelter, J. F., & Frasier, S. (2002, August). Algorithms for landmine detection using the NIITEK ground penetrating radar. In Proc. SPIE (Vol. 4742, pp. 709-718).

Conyers, L. B. (2013). Ground-penetrating radar for archaeology. AltaMira Press.

Cook, J. C. (1975). Radar transparencies of mine and tunnel rocks. Geophysics, 40(5), 865-885.

Counts, T., Gurbuz, A. C., Scott, W. R., McClellan, J. H., & Kim, K. (2007). Multistatic ground-penetrating radar experiments. IEEE Transactions on Geoscience and Remote Sensing, 45(8), 2544-2553.

Crooks, W. T., & Cheke, R. A. (2014). Soil moisture assessments for brown locust Locustana pardalina breeding potential using synthetic aperture radar. Journal of Applied Remote Sensing, 8(1), 084898-084898.

Dang, C., & Radha, H. (2015). RPCA-KFE: Key frame extraction for video using robust principal component analysis. IEEE Transactions on Image Processing, 24(11), 3742-3753.

Daniels, D. J. (1994). Surface penetrating radar for industrial and security applications. Microwave Journal, 37(12), 68-76.

Daniels, D. J. (ed.). (2004) Ground Penetrating Radar (2nd ed.). Institution of Engineering and Technology (IET).

Degenhardt, J. J., & Giardino, J. R. (2003). Subsurface investigation of a rock glacier using ground-penetrating radar: Implications for locating stored water on Mars. Journal of Geophysical Research: Planets, 108(E4).

Demirci, S., Yigit, E., Eskidemir, I. H., & Ozdemir, C. (2012). Ground penetrating radar imaging of water leaks from buried pipes based on back-projection method. NDT & E International, 47, 35-42.

Desai, M. D., & Jenkins, W. K. (1992). Convolution backprojection image reconstruction for spotlight mode synthetic aperture radar. IEEE Transactions on Image Processing, 1(4), 505-517.

Entropy (information theory): https://www.princeton.edu/~achaney/tmve/wiki100k/docs/Entropy_%28information_theory%29.html

Evans, S. (1963). Radio techniques for the measurement of ice thickness. Polar Record, 11(73), 406-410.

Federal Transit Administration Asset Management Guide, October 2012, FTA Report No. 0027: https://www.transit.dot.gov/sites/fta.dot.gov/files/docs/FTA_Report_No._0027.pdf

Ferrario, M., Signorini, M. G., Magenes, G., & Cerutti, S. (2006). Comparison of entropy-based regularity estimators: application to the fetal heart rate signal for the identification of fetal distress. IEEE Transactions on Biomedical Engineering, 53(1), 119-125.

Fischer, C., Herschlein, A., Younis, M., & Wiesbeck, W. (2007). Detection of antipersonnel mines by using the factorization method on multistatic ground-penetrating radar measurements. IEEE transactions on geoscience and remote sensing, 45(1), 85-92.

Fisher, E., McMechan, G. A., & Annan, A. P. (1992). Acquisition and processing of wide-aperture ground-penetrating radar data. Geophysics, 57(3), 495-504.

Fruehauf, F., Heilig, A., Schneebeli, M., Fellin, W., & Scherzer, O. (2009). Experiments and algorithms to detect snow avalanche victims using airborne ground-penetrating radar. IEEE Transactions on Geoscience and Remote Sensing, 47(7), 2240-2251.

Gader, P., Lee, W. H., & Wilson, J. N. (2004). Detecting landmines with ground-penetrating radar using feature-based rules, order statistics, and adaptive whitening. IEEE Transactions on Geoscience and Remote Sensing, 42(11), 2522-2534.

Gamba, P., & Lossani, S. (2000). Neural detection of pipe signatures in ground penetrating radar images. IEEE Transactions on Geoscience and Remote Sensing, 38(2), 790-797.

Gazdag, J. (1978). Wave equation migration with the phase-shift method. Geophysics, 43(7), 1342-1351.

Gazdag, J., & Sguazzero, P. (1984). Migration of seismic data. Proceedings of the IEEE, 72(10), 1302-1315.

Gerlitz, K., Knoll, M. D., Cross, G. M., Luzitano, R. D., & Knight, R. (1993, April). Processing ground penetrating radar data to improve resolution of near-surface targets. In 6th EEGS Symposium on the Application of Geophysics to Engineering and Environmental Problems.

Ghose, R., & Slob, E. C. (2006). Quantitative integration of seismic and GPR reflections to derive unique estimates for water saturation and porosity in subsoil. Geophysical Research Letters, 33(5).

Giannopoulos, A. (2005). Modelling ground penetrating radar by GprMax. Construction and building materials, 19(10), 755-762.

Gilmore, C., Jeffrey, I., & LoVetri, J. (2006). Derivation and comparison of SAR and frequency-wavenumber migration within a common inverse scalar wave problem formulation. IEEE transactions on geoscience and remote sensing, 44(6), 1454-1461.

Goodman, D. (1994). Ground-penetrating radar simulation in engineering and archaeology. Geophysics, 59(2), 224-232.

Gorham, L. A., & Moore, L. J. (2010, April). SAR image formation toolbox for MATLAB. In Proc. SPIE (Vol. 7699, p. 769906).

GPR Processing Software – MALA Ground Penetrating Radar – GPR: http://www.malagpr.com.au/gpr-processing-software.html

Grazzini, G., Pieraccini, M., Parrini, F., Spinetti, A., Macaluso, G., Dei, D., & Atzeni, C. (2010, June). An ultra-wideband high-dynamic range GPR for detecting buried people after collapse of buildings. In Ground Penetrating Radar (GPR), 2010 13th International Conference on (pp. 1-6). IEEE.

Ground Penetrating Radar Data Acquisition Unit – SIR 30 – GSSI: http://www.geophysical.com/sir30.htm

Ground Penetrating Radar for Bridge Deck Inspection, Geophysical Survey Systems, Inc.: http://www.geophysical.com/bridgeinspection.htm

Ground Penetrating Radar: https://en.wikipedia.org/wiki/Ground-penetrating_radar

Gu, K., Wang, G., & Li, J. (2004). Migration based SAR imaging for ground penetrating radar systems. IEE Proceedings-Radar, Sonar and Navigation, 151(5), 317-325.

Gunawardena, A., & Longstaff, D. (1998). Wave equation formulation of synthetic aperture radar (SAR) algorithms in the time-space domain. IEEE transactions on Geoscience and Remote Sensing, 36(6), 1995-1999.

Halman, J. I., Shubert, K. A., & Ruck, G. T. (1998). SAR processing of ground-penetrating radar data for buried UXO detection: results from a surface-based system. IEEE Transactions on Antennas and Propagation, 46(7), 1023-1027.

Han, J., & van der Baan, M. (2013). Empirical mode decomposition for seismic time-frequency analysis. Geophysics.

Hanmandlu, M., Verma, O. P., Kumar, N. K., & Kulkarni, M. (2009). A novel optimal fuzzy system for color image enhancement using bacterial foraging. IEEE Transactions on Instrumentation and Measurement, 58(8), 2867-2879.

Hintz, K. J. (2004, September). SNR improvements in NIITEK ground-penetrating radar. In Defense and Security (pp. 399-408). International Society for Optics and Photonics.

History of Ground Penetrating Radar (GPR): https://www.obonic.de/article/ground-peentrating-radar-history/

Ho, K. C., Carin, L., Gader, P. D., & Wilson, J. N. (2008). An investigation of using the spectral characteristics from ground penetrating radar for landmine/clutter discrimination. IEEE transactions on Geoscience and Remote Sensing, 46(4), 1177-1191.

Hodson, T., Gooch, D. L., & Stuart, G. W. (1997). Structures within the surge front at Bakaninbreen, Svalbard, using ground-penetrating radar. Annals of Glaciology, 24, 122-129.

Huisman, J. A., Hubbard, S. S., Redman, J. D., & Annan, A. P. (2003). Measuring soil water content with ground penetrating radar. Vadose zone journal, 2(4), 476-491.

Huisman, J. A., Sperl, C., Bouten, W., & Verstraten, J. M. (2001). Soil water content measurements at different scales: accuracy of time domain reflectometry and ground-penetrating radar. Journal of Hydrology, 245(1), 48-58.

Hulsenbeck, et al. (1926) German Pat. No. 489434.

Huston, D. (2010). Structural sensing, health monitoring, and performance evaluation. CRC Press.

Huston, D., Hu, J. Q., Maser, K., Weedon, W., & Adam, C. (2000). GIMA ground penetrating radar system for monitoring concrete bridge decks. Journal of Applied Geophysics, 43(2), 139-146.

Huston, D., Xia, T., Zhang, Y., Fan, T., Orfeo, D., & Razinger, J. (2017, April). Urban underground infrastructure mapping and assessment. In SPIE Smart Structures and Materials+ Nondestructive Evaluation and Health Monitoring (pp. 101680M-101680M). International Society for Optics and Photonics.

Inggs, M., Griffiths, H., Fioranelli, F., Ritchie, M., & Woodbridge, K. (2014, October). Multistatic radar: System requirements and experimental validation. In Radar Conference (Radar), 2014 International (pp. 1-6). IEEE.

Irving, J. D., & Knight, R. J. (2003). Removal of wavelet dispersion from ground-penetrating radar data. Geophysics, 68(3), 960-970.

Jeng, Y., Lin, C. H., Li, Y. W., Chen, C. S., & Yu, H. M. (2011). Application of sub-image multiresolution analysis of Ground-penetrating radar data in a study of shallow structures. Journal of Applied Geophysics, 73(3), 251-260.

Jia, S., Zhang, X., & Li, Q. (2015). Spectral–Spatial Hyperspectral Image Classification Using $\ell_ {1/2} $ Regularized Low-Rank Representation and Sparse Representation-Based Graph Cuts. IEEE Journal of Selected Topics in Applied Earth Observations and Remote Sensing, 8(6), 2473-2484.

Jiankui, Z., Zishu, H., Sellathurai, M., & Hongming, L. (2008). Modified Hough transform for searching radar detection. IEEE Geoscience and Remote Sensing Letters, 5(4), 683-686.

Johansson, E. M., & Mast, J. E. (1994, September). Three-dimensional ground penetrating radar imaging using synthetic aperture time-domain focusing. In Proc. SPIE (Vol. 2275, pp. 205-214).

Jol, H. M. (Ed.). (2008). Ground penetrating radar theory and applications. elsevier.

Kadaba, P. K. (1976). Penetration of 0.1 GHz to 1.5 GHz electromagnetic waves into the earth surface for remote sensing applications. In Engineering in a Changing Economy (pp. 48-50).

Kalika, D., Knox, M. T., Collins, L. M., Torrione, P. A., & Morton, K. D. (2015, May). Leveraging robust principal component analysis to detect buried explosive threats in handheld ground-penetrating radar data. In SPIE Defense+ Security (pp. 94541D-94541D). International Society for Optics and Photonics.

Karim, M. N. A., Malek, M. F. A., Jamlos, M. F., Seng, L. Y., & Saudin, N. (2013, December). Design of ground penetrating radar antenna for buried object detection. In RF and Microwave Conference (RFM), 2013 IEEE International (pp. 253-257). IEEE.

Karlsen, B., Larsen, J., Sorensen, H. B. D., & Jakobsen, K. B. (2001). Comparison of PCA and ICA based clutter reduction in GPR systems for anti-personal landmine detection. In Statistical Signal Processing, 2001. Proceedings of the 11th IEEE Signal Processing Workshop on (pp. 146-149). IEEE.

Karlsen, B., Sørensen, H. B. D., Larsen, J., & Jackobsen, K. B. (2002, August). Independent component analysis for clutter reduction in ground penetrating radar data. In Proceedings of the SPIE, AeroSense (pp. 378-389).

Kassem, E., Chowdhury, A., Scullion, T., & Masad, E. (2016). Application of ground-penetrating radar in measuring the density of asphalt pavements and its relationship to mechanical properties. International Journal of Pavement Engineering, 17(6), 503-516.

Kenley, E. C., & Cho, Y. R. (2011, December). Entropy-based graph clustering: Application to biological and social networks. In Data Mining (ICDM), 2011 IEEE 11th International Conference on (pp. 1116-1121). IEEE.

Kim, K., & Scott, W. R. (2005, July). Investigation of resistive vee antennas for a multi-static ground-penetrating radar. In Antennas and Propagation Society International Symposium, 2005 IEEE (Vol. 3, pp. 96-99). IEEE.

Kim, K., Gurbuz, A. C., Scott Jr, W. R., & McClellan, J. H. (2005, June). A multi-static ground-penetrating radar with an array of resistively loaded vee dipole antennas for landmine detection. In Defense and Security (pp. 495-506). International Society for Optics and Photonics.

Krause, V., Abdel-Qader, I., Abudayyeh, O., & Yehia, S. (2007, May). An image segmentation algorithm for the detection of rebar in bridge decks from GPR scans. In Electro/Information Technology, 2007 IEEE International Conference on (pp. 114-119). IEEE.

Labarthe, C., Mutzig, J. P., Jecko, B., Hamieh, H., Martinod, E., Feix, N., ... & Vergnault, R. (2009, October). An Ultra-Wideband radar concept for the detection of buried victims beneath building rubble. In Radar Conference-Surveillance for a Safer World, 2009. RADAR. International (pp. 1-6). IEEE.

Lahouar, S., & Al-Qadi, I. L. (2008). Automatic detection of multiple pavement layers from GPR data. NDT & e International, 41(2), 69-81.

Lai, W. L., & Poon, C. S. (2012, June). GPR data analysis in time-frequency domain. In Ground Penetrating Radar (GPR), 2012 14th International Conference on (pp. 362-366). IEEE.

Lai, W. L., Kind, T., & Wiggenhauser, H. (2011). Using ground penetrating radar and time–frequency analysis to characterize construction materials. NDT & E International, 44(1), 111-120.

Lambot, S., Slob, E. C., van den Bosch, I., Stockbroeckx, B., & Vanclooster, M. (2004). Modeling of ground-penetrating radar for accurate characterization of subsurface electric properties. IEEE transactions on geoscience and remote sensing, 42(11), 2555-2568.

Lambot, S., Weihermüller, L., Huisman, J. A., Vereecken, H., Vanclooster, M., & Slob, E. C. (2006). Analysis of air-launched ground-penetrating radar techniques to measure the soil surface water content. Water resources research, 42(11).

Le Bastard, C., Wang, Y., Baltazart, V., & Derobert, X. (2014). Time delay and permittivity estimation by ground-penetrating radar with support vector regression. IEEE Geoscience and Remote Sensing Letters, 11(4), 873-877.

Leckebusch, J. (2003). Ground-penetrating radar: a modern three-dimensional prospection method. Archaeological prospection, 10(4), 213-240.

Lecomte, I., Hamran, S. E., & Gelius, L. J. (2005). Improving Kirchhoff migration with repeated local plane-wave imaging? A SAR-inspired signal-processing approach in prestack depth imaging. Geophysical Prospecting, 53(6), 767-785.

Lee, J. S., Nguyen, C., & Scullion, T. (2004). A novel, compact, low-cost, impulse ground-penetrating radar for nondestructive evaluation of pavements. IEEE Transactions on Instrumentation and Measurement, 53(6), 1502-1509.

Leng, Z., & Al-Qadi, I. (2010). Railroad Ballast Evaluation Using Ground-Penetrating Radar: Laboratory Investigation and Field Validation. Transportation Research Record: Journal of the Transportation Research Board, (2159), 110-117.

Leng, Z., & Al-Qadi, I. L. (2009). Dielectric constant measurement of railroad ballast and application of STFT for GPR data analysis. Non-Destructive Testing in Civil Engineering Nantes, sn.

Lester, J., & Bernold, L. E. (2007). Innovative process to characterize buried utilities using ground penetrating radar. Automation in Construction, 16(4), 546-555.

Leucci, G. (2008). Ground penetrating radar: the electromagnetic signal attenuation and maximum penetration depth. Scholarly research exchange, 2008.

Li, J., Zollinger, D., & Lytton, R. (2008). Detection of delamination in concrete pavements using ground-coupled ground-penetrating radar technique. Transportation Research Record: Journal of the Transportation Research Board, (2087), 68-77.

Li, L., Tan, A. E. C., Jhamb, K., & Rambabu, K. (2012). Buried object characterization using ultra-wideband ground penetrating radar. IEEE Transactions on Microwave Theory and Techniques, 60(8), 2654-2664.

Li, Z., & Crocker, M. J. (2006). A study of joint time-frequency analysis-based modal analysis. IEEE transactions on instrumentation and measurement, 55(6), 2335-2342.

Liu, H., Birken, R., & Wang, M. L. (2016). Automatic pavement layer identification with multichannel ground penetrating radar at traffic speed. Journal of Applied Remote Sensing, 10(4), 046023-046023.

Liu, L., & Liu, S. (2014). Remote detection of human vital sign with stepped-frequency continuous wave radar. IEEE Journal of Selected Topics in Applied Earth Observations and Remote Sensing, 7(3), 775-782.

Liu, L., Liu, Z., & Barrowes, B. E. (2011). Through-wall bio-radiolocation with UWB impulse radar: Observation, simulation and signal extraction. IEEE Journal of Selected Topics in Applied Earth Observations and Remote Sensing, 4(4), 791-798.

Loizos, A., & Plati, C. (2007). Accuracy of ground penetrating radar horn-antenna technique for sensing pavement subsurface. IEEE Sensors Journal, 7(5), 842-850.

Loizos, A., & Plati, C. (2007). Accuracy of pavement thicknesses estimation using different ground penetrating radar analysis approaches. NDT & e International, 40(2), 147-157.

Lu, Q., Pu, J., & Liu, Z. (2014). Feature extraction and automatic material classification of underground objects from ground penetrating radar data. Journal of Electrical and Computer Engineering, 2014, 28.

Lunt, I. A., Hubbard, S. S., & Rubin, Y. (2005). Soil moisture content estimation using ground-penetrating radar reflection data. Journal of Hydrology, 307(1), 254-269.

Maas, C., & Schmalzl, J. (2013). Using pattern recognition to automatically localize reflection hyperbolas in data from ground penetrating radar. Computers & geosciences, 58, 116-125.

Machguth, H., Eisen, O., Paul, F., & Hoelzle, M. (2006). Strong spatial variability of snow accumulation observed with helicopter-borne GPR on two adjacent Alpine glaciers. Geophysical research letters, 33(13).

Maierhofer, C. (2003). Nondestructive evaluation of concrete infrastructure with ground penetrating radar. Journal of Materials in Civil Engineering, 15(3), 287-297.

Malagodi, S., Orlando, L., & Piro, S. (1996, September). Approaches to increase resolution of radar signal. In Proceedings of 6th international conference on ground penetrating radar. Tohoku University, Sendai (pp. 283-288).

Masarik, M. P., Burns, J., Thelen, B. T., Kelly, J., & Havens, T. C. (2015, May). GPR anomaly detection with robust principal component analysis. In Proc. SPIE (Vol. 9454, pp. 945414-945414).

Maser, K. R. (2009, June). Integration of ground penetrating radar and infrared thermography for bridge deck condition evaluation. In Non-Destructive Testing in Civil Engineering Conference, Nantes, France, June 30th-July 3rd.

Mason, E., Yonel, B., & Yazici, B. (2017, May). Deep learning for radar. In Radar Conference (RadarConf), 2017 IEEE (pp. 1703-1708). IEEE.

MATGPR Home: http://users.uoa.gr/~atzanis/matgpr/matgpr.html

Miller, D., Oristaglio, M., & Beylkin, G. (1987). A new slant on seismic imaging: Migration and integral geometry. Geophysics, 52(7), 943-964.

Milman, A. S. (1993). SAR imaging by ω—κ migration. International Journal of Remote Sensing, 14(10), 1965-1979.

Mitra, S. K., & Kuo, Y. (2006). Digital signal processing: a computer-based approach (Vol. 2). McGraw-Hill Higher Education.

Monostatic radar – Wikipedia: https://en.wikipedia.org/wiki/Monostatic_radar

Multistatic radar – Wikipedia: https://en.wikipedia.org/wiki/Multistatic_radar

Munson, D. C., O'Brien, J. D., & Jenkins, W. K. (1983). A tomographic formulation of spotlight-mode synthetic aperture radar. Proceedings of the IEEE, 71(8), 917-925.

Murray, T., Booth, A., & Rippin, D. M. (2007). Water-content of glacier-ice: Limitations on estimates from velocity analysis of surface ground-penetrating radar surveys. Journal of Environmental & Engineering Geophysics, 12(1), 87-99.

Narayanan, R. M., Jakub, J. W., Li, D., & Elias, S. E. (2004). Railroad track modulus estimation using ground penetrating radar measurements. NDT & E International, 37(2), 141-151.

Nezlin, D. V., Kostylev, V. I., Blyakhman, A. B., Ryndyk, A. G., & Myakinkov, A. V. (2007). Bistatic radar: principles and practice. John Wiley & Sons.

Ni, S. H., Huang, Y. H., Lo, K. F., & Lin, D. C. (2010). Buried pipe detection by ground penetrating radar using the discrete wavelet transform. Computers and Geotechnics, 37(4), 440-448.

Nilsson, S., & Andersson, L. E. (1998, September). Application of fast back-projection techniques for some inverse problems of synthetic aperture radar. In Aerospace/Defense Sensing and Controls (pp. 62-72). International Society for Optics and Photonics.

Nobes, D. C. (1999). Geophysical surveys of burial sites: a case study of the Oaro urupa. Geophysics, 64(2), 357-367.

Olhoeft, G. R. (2000). Maximizing the information return from ground penetrating radar. Journal of Applied Geophysics, 43(2), 175-187.

Otsu, N. (1979). A threshold selection method from gray-level histograms. IEEE transactions on systems, man, and cybernetics, 9(1), 62-66.

Ozdemir, C., Demirci, S., & Yigit, E. (2008). Practical algorithms to focus B-scan GPR images: Theory and application to real data. Progress In Electromagnetics Research B, 6, 109-122.

Ozdemir, C., Demirci, S., Yigit, E., & Kavak, A. (2007). A hyperbolic summation method to focus B-scan ground penetrating radar images: An experimental study with a stepped frequency system. Microwave and Optical Technology Letters, 49(3), 671-676.

Özdemir, C., Demirci, Ş., Yiğit, E., & Yilmaz, B. (2014). A review on migration methods in B-scan ground penetrating radar imaging. Mathematical Problems in Engineering, 2014.

Paglieroni, D. W., Chambers, D. H., Mast, J. E., Bond, S. W., & Beer, N. R. (2015). Imaging modes for ground penetrating radar and their relation to detection performance. IEEE Journal of Selected Topics in Applied Earth Observations and Remote Sensing, 8(3), 1132-1144.

Peng, Y., Ganesh, A., Wright, J., Xu, W., & Ma, Y. (2012). RASL: Robust alignment by sparse and low-rank decomposition for linearly correlated images. IEEE Transactions on Pattern Analysis and Machine Intelligence, 34(11), 2233-2246.

Pinel, N., Le Bastard, C., Baltazart, V., Bourlier, C., & Wang, Y. (2011). Influence of layer roughness for road survey by ground penetrating radar at nadir: theoretical study. IET radar, sonar & navigation, 5(6), 650-656.

Pipan, M., Baradello, L., Forte, E., Prizzon, A., & Finetti, I. (1999). 2-D and 3-D processing and interpretation of multi-fold ground penetrating radar data: a case history from an archaeological site. Journal of Applied geophysics, 41(2), 271-292.

Potin, D., Duflos, E., & Vanheeghe, P. (2006). Landmines ground-penetrating radar signal enhancement by digital filtering. IEEE Transactions on Geoscience and Remote Sensing, 44(9), 2393-2406.

RADAN® - GPR Software by GSSI: http://www.geophysical.com/software.htm

Radar Basics – Range Resolution: http://www.radartutorial.eu/01.basics/Range%20Resolution.en.html

Richards, M. A. (2005). Fundamentals of radar signal processing. Tata McGraw-Hill Education.

Rodríguez-Abad, I., Martínez-Sala, R., García-García, F., & Capuz-Lladró, R. (2010). Non-destructive methodologies for the evaluation of moisture content in sawn timber structures: ground-penetrating radar and ultrasound techniques. Near Surface Geophysics, 8(6), 475-482.

Roe, K. C., & Ellerbruch, D. A. (1979). Development and testing of a microwave system to measure coal layer thickness up to 25 cm (No. FE-8881-1; SR-723-8-79). National Bureau of Standards, Boulder, CO (USA). Electromagnetic Fields Div..

Saarenketo, T., & Scullion, T. (2000). Road evaluation with ground penetrating radar. Journal of applied geophysics, 43(2), 119-138.

Safont, G., Salazar, A., Rodriguez, A., & Vergara, L. (2014). On recovering missing ground penetrating radar traces by statistical interpolation methods. Remote Sensing, 6(8), 7546-7565.

Sakaguchi, R. T., Morton, K. D., Collins, L. M., & Torrione, P. A. (2015). Recognizing subsurface target responses in ground penetrating radar data using convolutional neural networks. SPIE Defense+ Security, 9454, 94541A.

Salvati, J. L., Chen, C. C., & Johnson, J. T. (1998, July). Theoretical study of a surface clutter reduction algorithm. In Geoscience and Remote Sensing Symposium Proceedings, 1998. IGARSS'98. 1998 IEEE International (Vol. 3, pp. 1460-1462). IEEE.

Savelyev, T. G., Kobayashi, T., Feng, X., & Sato, M. (2007). Robust target discrimination with UWB GPR. In Ultra-Wideband, Short-Pulse Electromagnetics 7 (pp. 732-739). Springer New York.

Scheer, J., & Holm, W. A. (2010). Principles of modern radar. M. A. Richards, & W. L. Melvin (Eds.). SciTech Pub..

Scheers, B. (2001). Ultra-wideband ground penetrating radar with application to the detection of anti personnel landmines. Royal Military Academy, Brussels.

Schneider, W. A. (1971). Developments in seismic data processing and analysis (1968–1970). Geophysics, 36(6), 1043-1073.

Schneider, W. A. (1978). Integral formulation for migration in two and three dimensions. Geophysics, 43(1), 49-76.

Shangguan, P., & Al-Qadi, I. L. (2014). Content-based image retrieval approaches to interpret ground penetrating radar data. Construction and Building Materials, 69, 10-17.

Shangguan, P., Al-Qadi, I., & Leng, Z. (2012). Development of wavelet technique to interpret ground-penetrating radar data for quantifying railroad ballast conditions. Transportation Research Record: Journal of the Transportation Research Board, (2289), 95-102.

Shangguan, P., Al-Qadi, I., Leng, Z., Schmitt, R., & Faheem, A. (2013). Innovative approach for asphalt pavement compaction monitoring with ground-penetrating radar. Transportation Research Record: Journal of the Transportation Research Board, (2347), 79-87.

Shao, W., Bouzerdoum, A., & Phung, S. L. (2013). Sparse representation of GPR traces with application to signal classification. IEEE transactions on geoscience and remote sensing, 51(7), 3922-3930.

Shao, W., Bouzerdoum, A., & Phung, S. L. (2014). Signal classification for ground penetrating Radar using sparse kernel feature selection. IEEE Journal of Selected Topics in Applied Earth Observations and Remote Sensing, 7(12), 4670-4680.

Simi, A., Manacorda, G., & Benedetto, A. (2012, June). Bridge deck survey with high resolution ground penetrating radar. In Ground Penetrating Radar (GPR), 2012 14th International Conference on (pp. 489-495). IEEE.

Slob, E., Sato, M., & Olhoeft, G. (2010). Surface and borehole ground-penetrating-radar developments. Geophysics, 75(5), 75A103-75A120.

Smith, S. W. (1997). The scientist and engineer's guide to digital signal processing.

Soldovieri, F., Prisco, G., & Persico, R. (2009). A strategy for the determination of the dielectric permittivity of a lossy soil exploiting GPR surface measurements and a cooperative target. Journal of Applied Geophysics, 67(4), 288-295.

Soldovieri, F., Solimene, R., Monte, L. L., Bavusi, M., & Loperte, A. (2011). Sparse reconstruction from GPR data with applications to rebar detection. IEEE transactions on instrumentation and measurement, 60(3), 1070-1079.

Solimene, R., & Cuccaro, A. (2014). Front wall clutter rejection methods in TWI. IEEE Geoscience and Remote Sensing Letters, 11(6), 1158-1162.

Solimene, R., & D'Alterio, A. (2012). Entropy-based clutter rejection for intrawall diagnostics. International Journal of Geophysics, 2012.

Song, X., Xiang, D., Zhou, K., & Su, Y. (2017). Improving RPCA-Based Clutter Suppression in GPR Detection of Antipersonnel Mines. IEEE Geoscience and Remote Sensing Letters.

Soumekh, M. (1999). Synthetic aperture radar signal processing (Vol. 7). New York: Wiley.

Sower, G., Eberly, J., & Christy, E. (2001). GSTAMIDS ground-penetrating radar: hardware description. In Proc. SPIE (Vol. 4394, p. 652).

Steenson, B. O. (1951). Radar methods for the exploration of glaciers (Doctoral dissertation, California Institute of Technology).

Stolt, R. H. (1978). Migration by Fourier transform. Geophysics, 43(1), 23-48.

Sudha, S., Vidhyalakshmi, M., Pavithra, K., Sangeetha, K., & Swaathi, V. (2016, July). An automatic classification method for environment: Friendly waste segregation using deep learning. In Technological Innovations in ICT for Agriculture and Rural Development (TIAR), 2016 IEEE (pp. 65-70). IEEE.

Suksmono, A. B., Bharata, E., Lestari, A. A., Yarovoy, A. G., & Ligthart, L. P. (2010). Compressive stepped-frequency continuous-wave ground-penetrating radar. IEEE geoscience and remote sensing letters, 7(4), 665-669.

Sun, J., & Young, R. A. (1995). Recognizing surface scattering in ground-penetrating radar data. Geophysics, 60(5), 1378-1385.

Sun, Y., & Li, J. (2003). Time–frequency analysis for plastic landmine detection via forward-looking ground penetrating radar. IEE Proceedings-Radar, Sonar and Navigation, 150(4), 253-261.

Tarussov, A., Vandry, M., & De La Haza, A. (2013). Condition assessment of concrete structures using a new analysis method: Ground-penetrating radar computer-assisted visual interpretation. Construction and Building Materials, 38, 1246-1254.

Temlioglu, E., & Erer, I. (2016). Clutter removal in ground-penetrating radar images using morphological component analysis. IEEE Geoscience and Remote Sensing Letters, 13(12), 1802-1806.

Terrasse, G., Nicolas, J. M., Trouvé, E., & Drouet, É. (2015, July). Application of the curvelet transform for pipe detection in GPR images. In Geoscience and Remote Sensing Symposium (IGARSS), 2015 IEEE International (pp. 4308-4311). IEEE.

Tivive, F. H. C., Bouzerdoum, A., & Amin, M. G. (2015). A subspace projection approach for wall clutter mitigation in through-the-wall radar imaging. IEEE Transactions on Geoscience and Remote Sensing, 53(4), 2108-2122.

Tjora, S., Eide, E., & Lundheim, L. (2004, June). Evaluation of methods for ground bounce removal in GPR utility mapping. In Ground Penetrating Radar, 2004. GPR 2004. Proceedings of the Tenth International Conference on (Vol. 1, pp. 379-382). IEEE.

Torrione, P. A., Morton, K. D., Sakaguchi, R., & Collins, L. M. (2014). Histograms of oriented gradients for landmine detection in ground-penetrating radar data. IEEE Transactions on Geoscience and Remote Sensing, 52(3), 1539-1550.

Torrione, P. A., Throckmorton, C. S., & Collins, L. M. (2006). Performance of an adaptive feature-based processor for a wideband ground penetrating radar system. IEEE Transactions on Aerospace and Electronic Systems, 42(2), 644-658.

Torrione, P., & Collins, L. M. (2007). Texture features for antitank landmine detection using ground penetrating radar. IEEE Transactions on geoscience and remote sensing, 45(7), 2374-2382.

Torrione, P., Collins, L., Clodfelter, F., Frasier, S., & Starnes, I. (2003, April). Application of the LMC algorithm to anomaly detection using the Wichmann/NIITEK ground-penetrating radar. In Proceedings of SPIE (Vol. 5089, pp. 1127-1136).

Turesson, A. (2006). Water content and porosity estimated from ground-penetrating radar and resistivity. Journal of Applied Geophysics, 58(2), 99-111.

Turner, G. (1994). Subsurface radar propagation deconvolution. Geophysics, 59(2), 215-223.

Tzanis, A. (2015). The Curvelet Transform in the analysis of 2-D GPR data: Signal enhancement and extraction of orientation-and-scale-dependent information. Journal of Applied Geophysics, 115, 145-170.

Unterberger, R. R. (1979). Radar and sonar probing of salt. The Northern Geological Society.

Vargas, J. M. M. (2012). Signal processing techniques for radar based subsurface and through wall imaging. Doktora Tezi, University of Alberta, Edmonton.

Venkatachalam, A. S. (2013). RF Circuit Development for Ultra-wideband Ground Penetrating Radar Evaluating Highway Pavement and Bridge Deck Subsurface Conditions (Master thesis, University of Vermont).

Venkatachalam, A. S., Xu, X., Huston, D., & Xia, T. (2014). Development of a new high speed dual-channel impulse ground penetrating radar. IEEE Journal of Selected Topics in Applied Earth Observations and Remote Sensing, 7(3), 753-760.

Verma, P. K., Gaikwad, A. N., Singh, D., & Nigam, M. J. (2009). Analysis of clutter reduction techniques for through wall imaging in UWB range. Progress In Electromagnetics Research B, 17, 29-48.

Wang, Z. W., Zhou, M., Slabaugh, G. G., Zhai, J., & Fang, T. (2011). Automatic detection of bridge deck condition from ground penetrating radar images. IEEE transactions on automation science and engineering, 8(3), 633-640.

Wei, X., & Zhang, Y. (2014). Autofocusing techniques for GPR data from RC bridge decks. IEEE Journal of Selected Topics in Applied Earth Observations and Remote Sensing, 7(12), 4860-4868.

What is GPR: A Brief Description by GSSI, Geophysical Survey Systems, Inc.: http://www.geophysical.com/whatisgpr.htm

Willett, D. A., Mahboub, K. C., & Rister, B. (2006). Accuracy of ground-penetrating radar for pavement-layer thickness analysis. Journal of Transportation Engineering, 132(1), 96-103.

Williams, R. M., Ray, L. E., Lever, J. H., & Burzynski, A. M. (2014). Crevasse detection in ice sheets using ground penetrating radar and machine learning. IEEE Journal of Selected Topics in Applied Earth Observations and Remote Sensing, 7(12), 4836-4848.

Wilson, J. N., Gader, P., Lee, W. H., Frigui, H., & Ho, K. C. (2007). A large-scale systematic evaluation of algorithms using ground-penetrating radar for landmine detection and discrimination. IEEE Transactions on Geoscience and Remote Sensing, 45(8), 2560-2572.

Withington, P., Fluhler, H., & Nag, S. (2003). Enhancing homeland security with advanced UWB sensors. IEEE Microwave magazine, 4(3), 51-58.

Wright, J., Ganesh, A., Rao, S., Peng, Y., & Ma, Y. (2009). Robust principal component analysis: Exact recovery of corrupted low-rank matrices via convex optimization. In Advances in neural information processing systems (pp. 2080-2088).

Xia, T., Venkatachalam, A. S., & Huston, D. (2012). A high-performance low-ringing ultrawideband monocycle pulse generator. IEEE Transactions on Instrumentation and Measurement, 61(1), 261-266.

Xia, T., Venkatachalam, A., Zhang, Y., Burns, D., & Huston, D. (2013, March). Performance Enhanced High Speed UWB GPR System for Buried Rebar Detection. In Symposium on the Application of Geophysics to Engineering and Environmental Problems 2013 (pp. 301-310). Society of Exploration Geophysicists and Environment and Engineering Geophysical Society.

Xia, T., Xu, X., Vekatachalam, A., & Huston, D. (2012, June). Development of a high speed UWB GPR for rebar detection. In Ground Penetrating Radar (GPR), 2012 14th International Conference on (pp. 66-70). IEEE.

Xu, X., Xia, T., Venkatachalam, A., & Huston, D. (2012). Development of high-speed ultrawideband ground-penetrating radar for rebar detection. Journal of Engineering Mechanics, 139(3), 272-285.

Yang, H., Li, T., Li, N., He, Z., & Liu, Q. H. (2015). Efficient near-field imaging for single-borehole radar with widely separated transceivers. IEEE Transactions on Geoscience and Remote Sensing, 53(10), 5327-5337.

Yigit, E., Demirci, S., Ozdemir, C., & Kavak, A. (2007). A synthetic aperture radar-based focusing algorithm for B-scan ground penetrating radar imagery. Microwave and Optical Technology Letters, 49(10), 2534-2540.

Yigit, E., Demirci, S., Özdemir, C., & Tekbaş, M. (2013). Short-range ground-based synthetic aperture radar imaging: performance comparison between frequency-wavenumber migration and back-projection algorithms. Journal of Applied Remote Sensing, 7(1), 073483-073483.

Yilmaz, O. (1987). Seismic data processing, volume 2 of Investigations in Geophysics. Society of Exploration Geophysicists.

Yilmaz, Ö. (2001). Seismic data analysis: Processing, inversion, and interpretation of seismic data. Society of exploration geophysicists.

Yoon, Y. S., & Amin, M. G. (2009). Spatial filtering for wall-clutter mitigation in through-the-wall radar imaging. IEEE Transactions on Geoscience and Remote Sensing, 47(9), 3192-3208.

You, H., Zhu, Q., & Alwan, A. (2004, May). Entropy-based variable frame rate analysis of speech signals and its application to ASR. In Acoustics, Speech, and Signal Processing, 2004. Proceedings.(ICASSP'04). IEEE International Conference on (Vol. 1, pp. I-549). IEEE.

Zhang, F., Xie, X., & Huang, H. (2010). Application of ground penetrating radar in grouting evaluation for shield tunnel construction. Tunnelling and Underground Space Technology, 25(2), 99-107.

Zhang, H., Ouyang, S., Wang, G., Wu, S., & Zhang, F. (2014). Matched filtering algorithm based on phase-shifting pursuit for ground-penetrating radar signal enhancement. Journal of Applied Remote Sensing, 8(1), 083593-083593.

Zhang, X., Bolton, J., & Gader, P. (2014). A new learning method for continuous hidden Markov models for subsurface landmine detection in ground penetrating radar. IEEE Journal of Selected Topics in Applied Earth Observations and Remote Sensing, 7(3), 813-819.

Zhang, Y., & Xia, T. (2016). In-Wall Clutter Suppression Based on Low-Rank and Sparse Representation for Through-the-Wall Radar. IEEE Geoscience and Remote Sensing Letters, 13(5), 671-675.

Zhang, Y., & Xia, T. (2016, April). Extracting sparse crack features from correlated background in ground penetrating radar concrete imaging using robust principal component analysis technique. In Nondestructive Characterization and Monitoring of Advanced Materials, Aerospace, and Civil Infrastructure 2016 (Vol. 9804).

Zhang, Y., & Xia, T. (2016, May). Frequency domain clutter removal for compressive OFDM ground penetrating radar. In Circuits and Systems (ISCAS), 2016 IEEE International Symposium on (pp. 962-965). IEEE.

Zhang, Y., Burns, D., Huston, D., & Xia, T. (2015, April). Sand moisture assessment using instantaneous phase information in ground penetrating radar data. In Proc. SPIE (Vol. 9437, p. 943726).

Zhang, Y., Burns, D., Orfeo, D., Huston, D. R., & Xia, T. (2017, April). Rough ground surface clutter removal in air-coupled ground penetrating radar data using low-rank and sparse representation. In SPIE Smart Structures and Materials+ Nondestructive Evaluation and Health Monitoring (pp. 1016904-1016904). International Society for Optics and Photonics.

Zhang, Y., Candra, P., Wang, G., & Xia, T. (2015). 2-D entropy and short-time Fourier transform to leverage GPR data analysis efficiency. IEEE Transactions on Instrumentation and Measurement, 64(1), 103-111.

Zhang, Y., Huston, D., & Xia, T. (2016). Underground object characterization based on neural networks for ground penetrating radar data. SPIE Smart Structures/NDE 2016.

Zhang, Y., Orfeo, D., Burns, D., Miller, J., Huston, D., & Xia, T. (2017, April). Buried nonmetallic object detection using bistatic ground penetrating radar with variable antenna elevation angle and height. In SPIE Smart Structures and Materials+ Nondestructive Evaluation and Health Monitoring (pp. 1016908-1016908). International Society for Optics and Photonics.

Zhang, Y., Venkatachalam, A. S., & Xia, T. (2015). Ground-penetrating radar railroad ballast inspection with an unsupervised algorithm to boost the region of interest detection efficiency. Journal of Applied Remote Sensing, 9(1), 095058-095058.

Zhang, Y., Venkatachalam, A. S., Huston, D., & Xia, T. (2014, March). Advanced signal processing method for ground penetrating radar feature detection and enhancement. In Proc. SPIE (Vol. 9063, p. 906318).

Zhang, Y., Venkatachalam, A. S., Xia, T., Xie, Y., & Wang, G. (2014, May). Data analysis technique to leverage ground penetrating radar ballast inspection performance. In Radar Conference, 2014 IEEE (pp. 0463-0468). IEEE.

Zhang, Y., Wang, G., & Xia, T. (2015, May). Compressive orthogonal frequency division multiplexing waveform based ground penetrating radar. In Radar Conference (RadarCon), 2015 IEEE (pp. 0684-0689). IEEE.

Zhao, Y. Q., & Yang, J. (2015). Hyperspectral image denoising via sparse representation and low-rank constraint. IEEE Transactions on Geoscience and Remote Sensing, 53(1), 296-308.

Zhi, W., & Chin, F. (2006). Entropy-based time window for artifact removal in UWB imaging of breast cancer detection. IEEE Signal Processing Letters, 13(10), 585-588.

Zhou, L., Huang, C., & Su, Y. (2012). A fast back-projection algorithm based on cross correlation for GPR imaging. IEEE Geoscience and Remote Sensing Letters, 9(2), 228-232.

Zhuge, X., & Yarovoy, A. (2012, July). Frequency-wavenumber domain focusing under linear MIMO array configurations. In Geoscience and Remote Sensing Symposium (IGARSS), 2012 IEEE International (pp. 2125-2128). IEEE.

Zhuge, X., & Yarovoy, A. G. (2012). Three-dimensional near-field MIMO array imaging using range migration techniques. IEEE Transactions on Image Processing, 21(6), 3026-3033.

Zhuge, X., Savelyev, T. G., Yarovoy, A. G., Ligthart, L. P., & Levitas, B. (2009, September). Comparison of different migration techniques for UWB short-range imaging. In Radar Conference, 2009. EuRAD 2009. European (pp. 184-187). IEEE.

Zielinski, T. P. (2001). Joint time-frequency resolution of signal analysis using Gabor transform. IEEE Transactions on Instrumentation and Measurement, 50(5), 1436-1444.